Linear and Nonlinear Optical Properties and Ultrafast Dynamics of Hybrid Lead Halide Perovskites

A Thesis
Submitted in Partial Fulfillment of the Requirements
for the Degree of

Doctor of Philosophy

By

Shabnum Maqbool

(20173507)

Department of Chemistry,
Indian Institute of Science Education and Research (IISER)
Pune, India - 411008

December 2022

To the little girl in the valley surrounded by snow-clad mountains,

with dreams in her eyes and undying hope in her heart, and to all

those who helped her realize her dreams.

Verily, with every difficulty comes ease.

Quran 94:5

CERTIFICATE

I certify that the work incorporated in the thesis entitled "**Linear and Nonlinear Optical Properties and Ultrafast Dynamics of Hybrid Lead Halide Perovskites**" submitted by **Ms. Shabnum Maqbool** was carried out by the candidate, under my supervision. The work presented here or any part of it has not been included in any other thesis submitted previously for the award of any degree or diploma from any other university or institution. For the completion of the thesis, a few results are taken from collaborators after their permissions and are clearly mentioned in the thesis.

Date: 30-12-2022

Dr. Pankaj Mandal
(Research Supervisor)

DECLARATION

I declare that this written submission represents my ideas in my own words and wherever others' ideas have been included, I have adequately cited and referenced the original sources. I also declare that I have adhered to all principles of academic honesty and integrity and have not misrepresented, fabricated or falsified any idea/data/fact/source in my submission. I understand that violation of the above will be cause for disciplinary action by the Institute and can also evoke penal action from the sources which have thus not been properly cited or from whom proper permission has not been taken when needed.

Date: 30-12-2022

Shabnum Maqbool

(ID: 20173507)

Acknowledgements

First and foremost, I would like to express my sincere thanks and gratitude to my thesis supervisor, Dr. Pankaj Mandal. It has been almost six years since you provided me an opportunity to work with you in the amazing world of fundamental sciences. I must admit it has been a roller-coaster of a journey. You always provided freedom while doing the experiments, new initiatives and designing the projects. You have been an example of patience, reliability and took time to explain scientific points whenever situations arose. I endure to achieve the depths of understanding for my research projects as guided by you and to have the dedication to look for the bigger picture in every situation.

I am indebted to the members of my Research Advisory Committee, Dr. Angshuman Nag and Dr. Sayan Bagchi for their constant support, critical discussions and suggestions. They put tremendous effort to inculcate the scientific fervor and rational approach on different research projects over the course of my Ph.D. I am highly thankful to both of them for being my advocates and supporters whenever needed, be it for conference fundings or postdoc applications. I am grateful to Dr. Sayan Bagchi for providing the lab space during the down-time of our laser system.

My collaborators at IISER Pune, Dr. Angshuman Nag, Dr. Prasenjit Ghosh, Dr. Bhoomi Shankar have been incredible collaborators and I have really enjoyed collaborating with their groups. Tariq Sheikh, Rayan Chakraborty, Parikshit Rajput, Ziyad Thekkayil, Garvit Bansal, Swati Deswal have proven amazing colleagues and were always eager to discuss the collaborative projects.

Indian Institute of Science Education and Research Pune has been my sanctuary and safe space where I grew tremendously, personally as well as professionally over the past six years. It would not be far-fetched to say that I had not imagined to have a belonging to such a prestigious institution for the most crucial stage of my scientific journey. The peace, freedom, and safety I felt in IISER Pune is somewhat I had not dreamt of before in my life. The collaborations and friendships developed are for life. The state-of-art research facilities and atmosphere provided at IISER Pune is due to its diligent management by former and present Directors and Chairs of Chemistry. I would also like to thank IISER Pune and DST INSPIRE for the research fellowship.

List of Abbreviations

0D: Zero dimensional

1D: One dimensional

2D: Two dimensional

3D: Three dimensional

BA: Butylammonium

CB: Conduction band

CBM: Conduction band minimum

EQE: External quantum efficiency

FA: Formamidinium

FESEM: Field emission scanning electron microscopy

FWHM: Full width at half maximum

PLE: Photoluminescence excitation

IRF: Instrument response function

LED: Light-emitting diode

MA: Methylammonium

NIR: Near-infrared

OA: Octylammonium

PCE: Power conversion efficiency

PEA: Phenethylammonium

PMT: Photomultiplier tube

PXRD: Powder X-ray diffraction

SCXRD: Single crystal X-ray diffraction

SHG: Second harmonic generation

STE: Self-trapped exciton

VB: Valance band

VBM: Valance band maximum

THz: Terahertz

OPTP: Optical pump THz probe

LD: Lower dimensional

FE: Free exciton

STE: Self-trapped exciton

OKE: Optical Kerr effect

LIDT: Laser induced damage threshold

THz-TDS: Terahertz time-domain spectroscopy

TRTS: Time-resolved terahertz spectroscopy

TEM: Transmission electron microscopy

BBO: Beta barium borate

TFISH: THz field induced second harmonic

OPA: Optical parametric amplifier

PCA: Photoconductive antenna

OR: Optical rectification

ABCD: Air-biased coherent detection/ air-breakdown coherent detection

HDPE: High density polyethylene

OD: Optical density

THG: Third harmonic generation

SHG: Second harmonic generation

SFG: Sum frequency generation

LHP: Lead halide perovskite

DFT: Density functional theory

EDAX: Energy Dispersive X-Ray

UV: Ultraviolet

Synopsis

Lead halide perovskites have shown a diversity of functionalities and applications based on compositional flexibility. By relaxing the restricted choice of cations in 3D perovskites, lower dimensional perovskites are easily synthesized. Cations not only bring dimensionality changes; rather multiple functionalities have been incorporated in lead halide perovskites by careful choice of cations. Using organic cations enables perovskites to show dual properties arising from both organic and inorganic components.

The principal aim of this thesis is to explore the effects of cations on the multitude of photophysical properties shown by lead halide perovskites. In the 3D regime, organic cations modify the excited state and hence affect the charge carrier recombination, coupling mechanisms, and carrier transport processes. The semiconducting properties desirable for photovoltaic applications, such as mobility and diffusion lengths, are also therefore affected by the choice of cations in 3D lead halide perovskites. We explored these effects by utilizing time domain and time-resolved terahertz spectroscopy. When larger organic cations are incorporated in 3D perovskites, lower dimensional lead halide systems are obtained, such as 2D, 1D, and 0D. This dimensional diversity brings diverse properties based on quantum and dielectric confinement effects. The adjacent octahedral connectivity also gets modified from corner to edge or face sharing or a mix of these. The incorporation of bulky organic cations leads to bandgap tunability and desirable properties such as moisture resistance. The linear optical properties also get tempered, with the absorption edge shifting to higher energy and the emission getting highly red-shifted from the band edge, which is assigned to exciton self-trapping. To understand the role of cation in the exciton self-trapping, we utilized optical Kerr effect spectroscopy and DFT calculations. By tracing the phonon modes in the excited and the ground state, we observed that phonon modes involving cation motions play a significant role in exciton self-trapping. Since emission is affected by a variation in temperature, we also performed temperature-dependent PL measurements to study the role of phase change, dynamic disorder and anharmonicity in the emission due to exciton self-trapping. The non-linear optical properties also get affected by dimensionality reduction. We observed wavelength-tunable THG output and increased optical stability in the 1D pyridinium lead halide ($PyPbX_3$) system. By cation engineering, we achieved a highly enhanced, wavelength-tunable THG response from diisopropylammonium lead iodide ($DipaPbI_3$). Both 1D systems show selective enhancement of THG output due to band-edge resonance. The interplay of phase stability and polarizability was observed to affect the THG output upon incorporating mixed halide ions.

Synopsis

Chapter 1: Introduction

In this chapter, we provide an introduction to lead halide perovskites and their relevance to the requirements of the energy consumption of the current world. We then discuss the electronic band structure and the defect-tolerant nature of perovskites which make them suitable for optoelectronic and photovoltaic applications. Tuning the bandgap and emission properties by the quantum confinement effect is further discussed. The amazing and diverse applications of perovskites are due to their amazing excited state properties, and we discuss how time-resolved spectroscopic techniques can be utilized to understand the excited state properties of lead halide perovskites. This is followed by a discussion of lower dimensional perovskites and their optical properties arising from the dimensionality reduction, such as highly red-shifted PL due to exciton self-trapping. We then discuss exciton self-trapping and how to explore its origins spectroscopically. Further, we discuss the non-linear optical properties in lower dimensional perovskites, which are affected due to quantum and dielectric confinement.

Chapter 2: Ultrafast Charge Carrier Dynamics in Formamidinium Lead Bromide Nanocrystal Film: Time-resolved Terahertz Spectroscopic Study

This chapter discusses the effect of formamidinium (FA) cation on the excited state properties of 3D lead halide perovskites (FaPbBr$_3$ NC thin films) by utilizing time-resolved optical pump terahertz probe (OPTP) spectroscopy. In the time-domain THz absorbance spectrum, we obtain a phonon feature due to the FA cation. Thus, we speculate that the FA cation might affect the carrier-phonon coupling interactions and recombination dynamics.
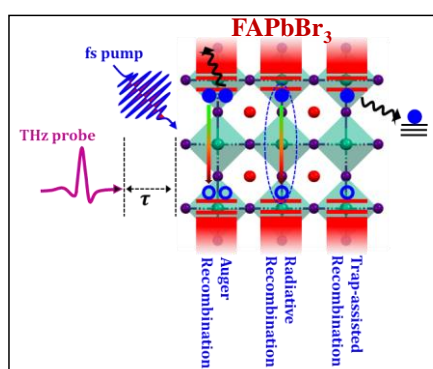
Figure 1. Schematic showing the creation of excited state by femtosecond pump pulses and tracing of this excited state by the THz probe pulses. Using THz pulses, various recombination mechanisms and carrier backscattering mechanisms were explored.

Frequency-averaged THz transients revealed that three types of recombination pathways i.e., Auger, bimolecular and trap-assisted are active for carrier recombination. Excited states were created, with carriers having excess energy of 185 meV by 480 nm excitation and minimum or no excess energy by 517 nm excitation. We observed different rate constants for both excitations after global fitting by kinetic equation, indicating different natures of excited states. The frequency-resolved THz spectra were fitted to the Drude Smith Anderson model to explore the nature of carrier-phonon coupling, charge transport, and semiconducting properties. Anderson's model, which depicts the localization effects due to backscattering from photo-induced lattice fluctuations, explains well the carrier transport mechanism in $FAPbBr_3$ NC thin films.

Chapter 3: Direct Probing of the Origins of Exciton Self-trapping in 1D Perovskite

In this chapter, we focus on exploring the fundamental origins of exciton self-trapping in 1D pyridinium lead bromide ($PyPbBr_3$) single crystals. The $PyPbBr_3$ single crystals show highly red-shifted and broad PL emission from the band-edge at room temperature. The excitons which undergo self-trapping are strongly coupled to the polarizable phonon modes. Band structure calculations show pyridinium cation orbitals are predominantly present in the conduction band minima. Thus, pyridinium cation can affect optical properties such as PL emission.
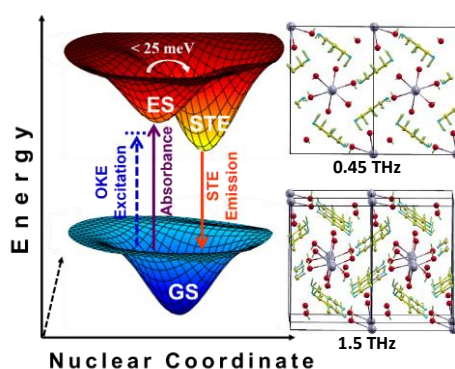
Figure 2. Schematic of the ground and excited state potential energy surfaces explored using OKE spectroscopy in $PyPbBr_3$ single crystals. DFT calculations unraveled these phonon modes as observed by the OKE spectroscopy.

We utilized ultrafast optical Kerr effect (OKE) spectroscopy to divulge the details of the composition of these phonon modes responsible for exciton self-trapping and the role of the cation. By performing optical excitations creating the pre-resonant (400 nm) and the non-

resonant (800 nm) states, we obtain the spectral density plots of the transient state close to the first excited state and the ground state. A red-shift in multiple phonon modes in the excited state compared to the ground state indicates these modes are leading to exciton self-trapping. DFT calculations helped us to visualize these affected modes. Phonon modes with significant contribution from pyridinium motions were the phonon modes affected by excitation, thus responsible for exciton-self trapping.

Chapter 4: Third Harmonic Up-Conversion in Lower Dimensional 1D Pyridinium Lead Iodide Perovskite

This chapter explores the effects of dimensionality reduction on the non-linear optical properties of lower dimensional 1D pyridinium lead iodide ($PyPbI_3$) single crystals. Due to increased quantum and dielectric confinement, $PyPbI_3$ shows enhanced third harmonic up-conversion as compared to its 2D or 3D counterparts. An extensive probe of THG properties was performed, and a wavelength-tunable THG output was observed. The THG output was selectively enhanced due to bang-edge resonance. Additionally, a very high LIDT was observed for $PyPbI_3$ under intense laser excitation.
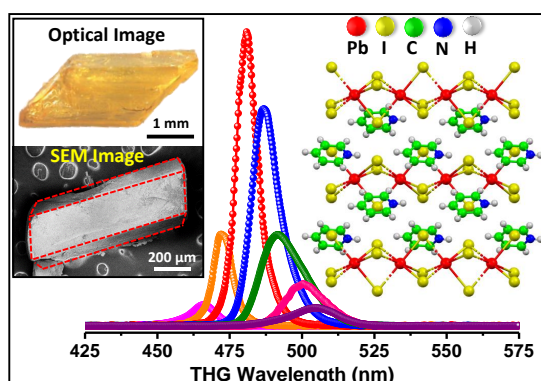
Figure 3. Wavelength tunable THG output obtained from 1D $PyPbI_3$ single crystals.

Chapter 5: 1D Diisopropylammonium Lead Iodide Perovskite Shows Exceptional Optical Stability and Third-Order Nonlinearity

The polarizability of a system is directly related to the non-linear susceptibility. By incorporating diisopropylammonium cation in 1D lead iodide perovskites ($DipaPbI_3$), leading to high bulk polarizability, exceptionally high THG output and LIDT was observed. High LIDT is partly due to the dynamic disorder due to the cation motions, which helps in the dissipation

of the local heating. The DipaPbI$_3$ system shows stability in ambient conditions for extended periods and thus is a potential candidate for commercial applications.
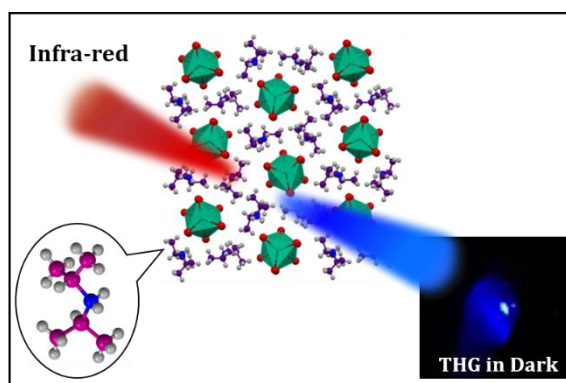
Figure 4. A schematic showing strongly enhanced THG emission from highly polarizable 1D DipaPbI$_3$ perovskite system.

Appendix 1: Interplay of Phase Stability and Polarizability in the Third Harmonic Up Conversion Process in Pyridinium Lead Mixed Halides

In this appendix chapter, the effect of variation of halide composition on NLO properties was explored. Pyridinium lead mixed halide systems were synthesized with bandgap varying between pure iodide and bromide compositions. Extensive NLO studies were performed by varying wavelength, power, and polarization of the incident IR pulses. The mixed halide composition induces lattice strain, and thus, a complex THG behavior was obtained. These systems show selective enhancement of THG far from the band edge due to lattice strain effects. Easily achievable wavelength-tunability was observed by incorporating mixed halides in pyridinium lead halide perovskites.
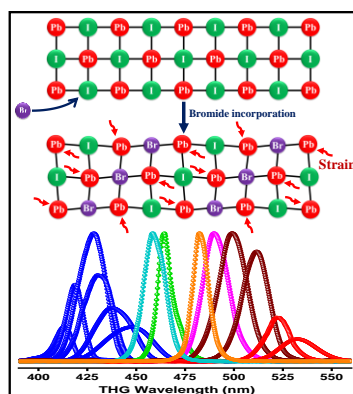
Figure 5. Wide wavelength-tunable THG output from mixed halide perovskite systems affected by lattice strain effects.

Appendix 2: Anharmonicity and Dynamic-Disorder Driven Self-Trapped Excitonic Emission in Pyridinium Lead Iodide Single Crystals

In this appendix chapter, we extended our exploration of STE formation in face-shared pyridinium lead iodide perovskite. We performed temperature-dependent PL measurements to study the evolution of exciton self-trapping (STE). We observed a negligible thermal barrier between free exciton and the STE state. Highly red-shifted STE emission was observed up to ~5K. In these lower dimensional perovskites, the STE emission is governed by the relative contribution of high anharmonicity and dynamic disorder present.
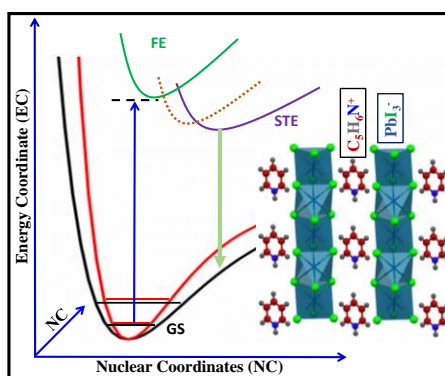
Figure 6. Schematic showing the mechanism of STE formation from the temperature-dependent PL studies in PyPbI$_3$ single crystals.

Thesis Summary and Future Outlook

In this section, we summarize the major findings of this thesis. We explain how small cations have big effects on the properties and applications of lead halide perovskites. We explain how different spectroscopic techniques can help us to explore different optoelectronic properties of various lead halide perovskites. Finally, a future outlook is provided wherein we propose how exploring organic cations with chirality can help us approach the spin-quantum effects. We suggest various spectroscopic techniques that can help us explore these spin-filtering effects in lead halide perovskites.

Table of Contents

Table of Contents

Table of Contents

Table of Contents

Chapter 1

Introduction

Chapter 1

Introduction

1.1 Energy crisis and renewable energy

The development, wealth, and prosperity of a society are governed by the availability and affordability of energy. The supply of non-renewable sources of energy, such as fossil fuels, is limited and expected to extinguish in the nearest future.[1] Not just the limited supply, the by-products of combustion of fossil fuels has wreaked havoc on the climate, leading to catastrophes such as global warming, ozone layer depletion, rising sea levels, extinction of vital species, and further disastrous consequences.[1-2] At present, the Earth is the only habitable place for living organisms, particularly the human race. However, the indiscriminate use of energy and unbalanced consumption of natural resources are making the Earth inhabitable.

Sun is the major source of energy on Earth, in addition to other renewable sources such as wind, geothermal, or biomass. Natural systems like plants and algae are highly capable of utilizing solar energy for their complete survival. Unfortunately, we humans are still lagging far behind in this direction. The main reason is the unavailability of cheap materials capable of harvesting solar energy efficiently.[3]

1.2 Solar energy harvesting and semiconductors

Solar energy is one of the most abundant sources of renewable energy on the surface of Earth. The solar energy incident on Earth's surface is ~1.4 kW/m^2.[4] The available solar energy incident on Earth, if harvested efficiently, can power human consumption for endless time. Such a huge amount of renewable energy can be trapped by utilizing materials that absorb sunlight and convert it into electricity. Semiconductors have long been used for trapping solar energy and providing electricity.[5] However, the semiconducting materials used so far in solar light harvesting are severely limited either due to the processing technologies and cost or the inefficiency in the solar light conversion.[3] Thus, there is an unending attempt to engineer semiconducting materials showing the best solar energy conversion efficiency. At present, silicon-based photovoltaics (PV) have the highest share within the PV sector.[6] However, silicon has an indirect bandgap and hence is a poor absorber and emitter of light. Recently, a new class of materials known as perovskites has emerged as efficient solar light absorbers.[7] These materials, in addition to increased conversion efficiencies, have additional benefits over traditional semiconductors, such as easy and cost-effective processibility and material flexibility. However, these perovskites are still evolving regarding their commercialization, the main reason being their instability at ambient conditions.

2

1.3 Lead halide perovskites

Lead halide perovskites have emerged as potential candidates for their outstanding performance in photovoltaics, LEDs, lasers, and other optoelectronic devices.[8-18] For example, the power conversion efficiency of perovskite solar cells has reached to 25.7%.[19-20] Lead halide perovskites are a class of materials with the chemical formula ABX_3, where A is a monovalent cation such as Cs^+, methylammonium ($CH_3NH_3^+$ or MA), Formamidinium ($CH(NH_2)_2^+$ or FA), B is a divalent metal cation, i.e., Pb^{2+}, and X is a halide anion such as Cl^-, Br^- or I^-, as shown in Figure 1.1. These novel materials can be synthesized by wet chemical processes or physical deposition by thermal evaporation. Usually, solution-processed materials have high defect densities, which is detrimental to their performance. Perovskites, however, show minimal effect of defects despite their solution-based route of synthesis. This defect tolerance of perovskites offers a great advantage over the traditional semiconductors that require significantly high temperatures for producing highly crystalline materials with good semiconducting properties. Additionally, these perovskites show an amazing dimensional diversity, due to which tunable size effects can be incorporated. Quantum dots, nanoplatelets, nanowires, and further morphologies can be easily obtained by solution processing. At present, perovskites are already trying to occupy commercial space for various applications such as X-ray imaging,[21-22] and are being sent to space for potential explorations in spacecrafts[23-24].
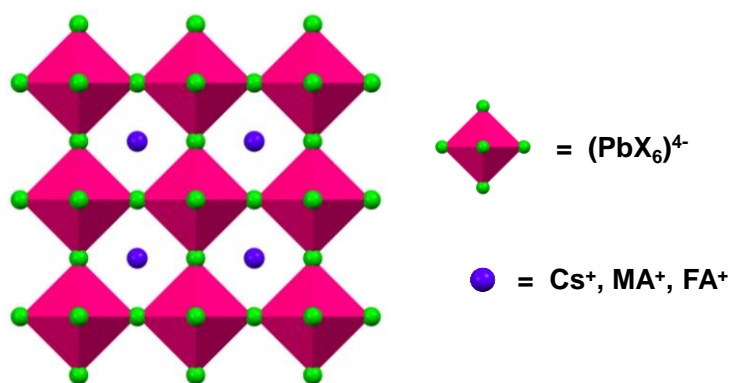
Figure 1.1: Schematic of the crystal structure of a lead halide perovskite. The corners are occupied by halide ions, while the lead cation sits in the center of the octahedra. The monovalent A-site cation occupies the voids created by adjacent octahedra.

1.3.1 Electronic band structure and defect tolerance

The steep rise in performance of lead halide perovskites is ascribed to its unique band structure, which is defect tolerant. Upon device fabrication, a possible large density of defects can

emerge, thereby compromising the device's performance. But the defects in lead halide perovskites are either shallow or intra-band trap states and hence do not contribute significantly to non-radiative recombination-based loss pathways.[25] The conduction band minima and the valence band maxima of lead halide perovskites are comprised of anti-bonding orbitals, and hence the defect states originating from non-bonding electrons are well within the bands or close to them, as shown in Figure 1.2. This is a significant blessing for perovskites compared to traditional semiconductors, which are usually defect-intolerant and have significant mid-gap trap-states. The defects of the perovskite nanocrystals are therefore less detrimental to the electronic and optical properties. This advantage of defect insensitivity is responsible for the high quantum yield, narrow bandwidth, high carrier mobilities, and large diffusion lengths in these lead halide perovskites.
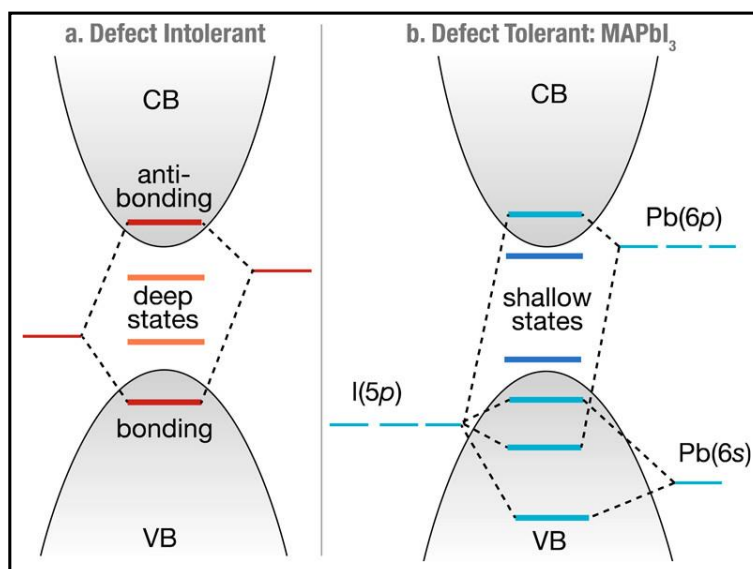
Figure 1.2: Schematic showing the comparison of the band structure of the defect intolerant, conventional semiconductors such as CdSe, GaAs and the defect-tolerant perovskites such as MAPbI$_3$. The figure is reprinted from reference 25 with permission. Copyright © 2017, American Chemical Society.

The wide popularity of lead halide perovskites can also be ascribed to their bandgap tunability. A simple modification of the monovalent cation or the halide ion allows for a wide tuning of the bandgap energy.[12] As clearly seen in Figure 1.3, bandgap tunability over the entire visible spectrum from ~ 400 nm to ~800 nm can be achieved by facile synthesis. Additionally, narrow PL bandwidth and reduced PL blinking make them ideal for LEDs with high color purity and

efficiency. Not only the composition, but the variation in size also introduces the band gap tunability by size or shape-dependent quantum confinement, as discussed in the next section.
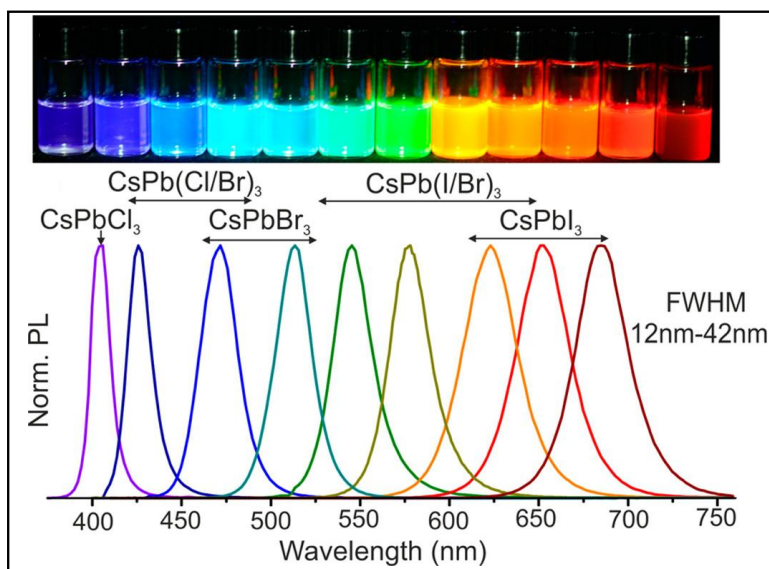
Figure 1.3: Top panel shows the colloidal lead halide perovskites dispersed in toluene after UV excitation. The bottom panel shows the representative PL spectra for various compositions of 3D lead halide perovskites. The figure is reprinted with permission from reference 12. Copyright © 2015, American Chemical Society.

1.3.2 Quantum confinement

The band structure of semiconductors is comprised of valence and conduction bands separated by an energy barrier, i.e., a band gap.[26] Bulk semiconductors have a fixed bandgap, but by reducing their size below their excitonic Bohr diameter, the band gap shows a dependence on the size of semiconductor NCs.[27] This is known as the quantum confinement effect. The quantum confinement and the bandgap increase with a decrease in NC size. For a significantly small NC, atom-like quantized states become more prominent rather than a continuum of energy (Figure 1.4a). Quantum confinement affects optical transitions such as absorption and emission. With an increase in the quantum confinement, the absorption coefficient increases, and the photoluminescence (PL) lifetime gets affected.

The huge success of lead halide perovskites as promising optoelectronic material lies in its facile synthesis. By changing the reaction conditions such as temperature, reaction time, solvents, and precursors, different variations of sizes and shapes are easily achievable.[12, 16] By variations in sizes, tunable quantum confinement can be incorporated in lead halide

perovskites, as shown in Figure 1.4a. It is to be noted that the compositional changes, such as halide variation, can also lead to the band gap tunability in lead halide perovskites, as shown in Figure 1.4b.
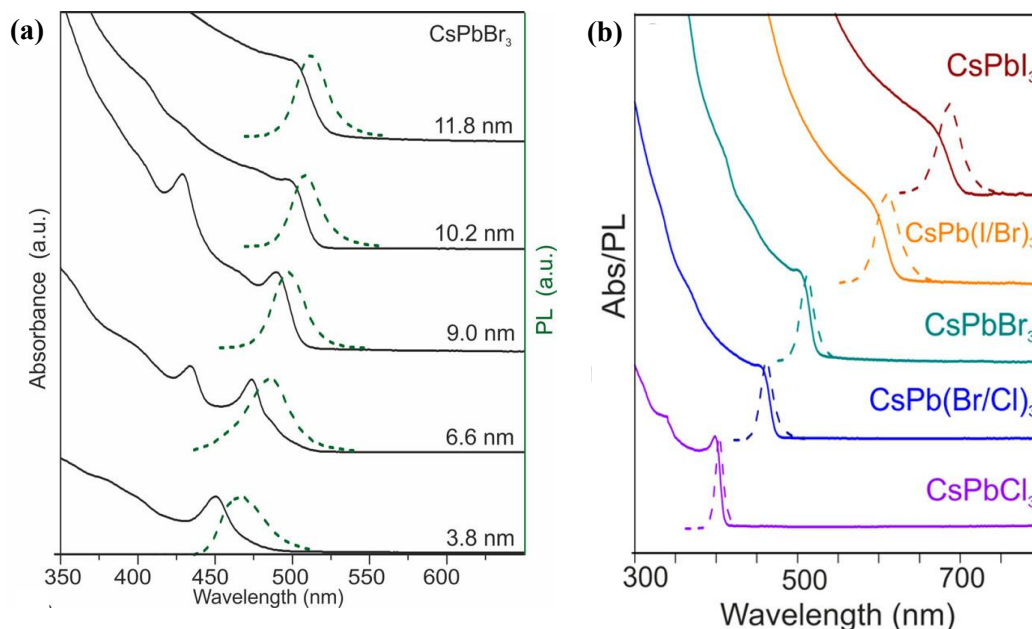
Figure 1.4: Tuning the band gap and PL emission in $CsPbX_3$ by tuning the a) NC size and b) halide composition. These figures are reprinted from reference 12. with permission. Copyright © 2015, American Chemical Society.

1.4 Excited state properties

As discussed earlier, lead halide perovskites show near-unity PL quantum yield, narrow emission bandwidth, high solar cell efficiencies, etc.[12, 16, 19] All these properties are controlled by the nature and dynamics of the excited states. For an exclusive understanding of a one-to-one correlation between excited state dynamics and the material properties, we use different time-resolved, pump-probe spectroscopic techniques. In a pump-probe spectroscopic technique, firstly, a pump pulse with energy equal to or more than the bandgap of the material excites the sample, creating charge carriers in the excited state. After a time delay, a probe pulse interacts with the charge carriers and extracts information about the charge carrier transport, recombination dynamics, and carrier phonon interactions, as schematically presented in Figure 1.5.
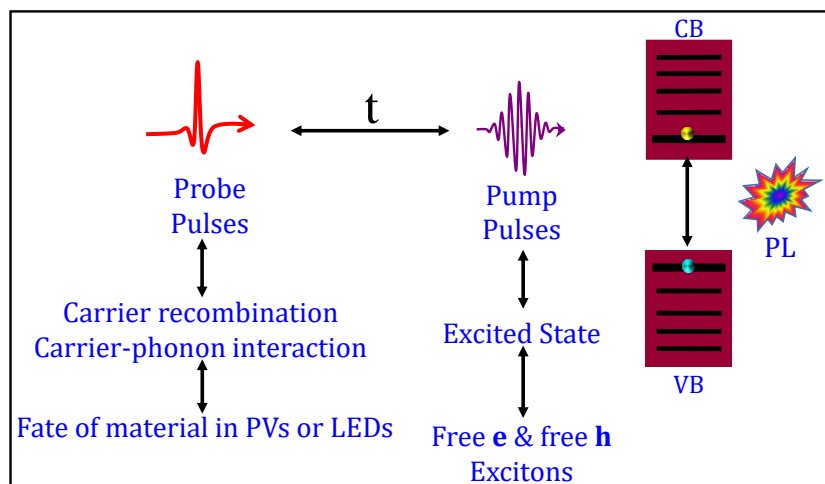
Figure 1.5: Schematic of a time-resolved spectroscopic experiment. Pump pulses create the charge carriers in the excited state. These charge carriers are then traced by the probe pulses, which arrive after a time delay.

Various pump-probe techniques, such as transient absorption[28-29], time-resolved microwave spectroscopies[30-31], etc., have been utilized to explore the excited state properties. However, these techniques do not provide any information about conductivity, mobility, and other related parameters. Recently, terahertz (THz) pulses have been used as probe pulses for studying the optically excited systems[14-15, 32-36], and the spectroscopic technique is known as optical pump THz probe (OPTP) spectroscopy.[37] THz spectroscopy provides a contact-free measurement of conductivity and is most suited for studying nanocrystals where external contacts cannot be made.[37-39]

1.5 Lower dimensional perovskites

3D lead halide perovskite crystal structure comprises corner shared $[PbX_6]^{4-}$ octahedra.[12] The A-site cation sits in the coordination site in the middle of eight such octahedra. The A-site cation interacts with the lead halide network via ion-ion, ion-dipole, and hydrogen-bonding interactions. The size of the A-site cation is crucial for the stability of the 3D crystal structure (ABX_3), as dictated by the Gold-Schmidt tolerance factor (T),[40-41] T is given by $(R_A+R_X)/\sqrt{2}(R_B + R_X)$ where R_A, R_B and R_X are the ionic radii of A, B and X respectively, and it provides an idea of not only the geometric stability but also the distortion of crystal structures in terms of the constituent ionic packing. When bigger organic cations are incorporated in the lattice, deviation from 3D (T = 1) structure occurs, and lower dimensional (LD) lead halide perovskites (T $\neq$ 1) such as 2D, 1D, or 0D systems are generated[42-43], as represented in Figure 1.6. These

LD perovskites are not limited by the Gold-Schmidt tolerance factor and hence, offer an immense diversity by incorporation of organic cations with a variety of functionalities.
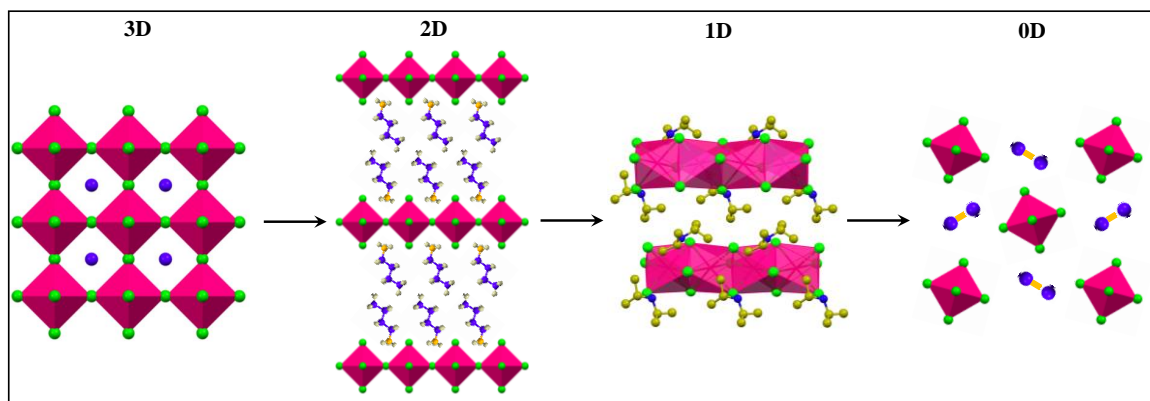
Figure 1.6: Schematic representation of different dimensionalities present in lead halide perovskites. In 3D perovskites octahedra are connected along all three dimensions; in 2D, along one dimension, the organic cation slides these 3D layers forming a 2D structure. In 1D perovskites, lead halide octahedra are connected in only one direction, and these chains are connected by the bulky organic cations whereas in 0D perovskites, the lead halide octahedra are isolated.

In 2D lead halide perovskites, infinite 2D slabs of lead halide octahedra are separated by large organic spacer cations leading to a quantum-well structure. 1D metal halides comprises of infinite 1D chains of lead halide octahedra surrounded by organic cations. In 2D and 1D perovskites or perovskitoids, in addition to corner-sharing connectivity, edge-sharing and face-sharing are also found. In 0D structures, individual lead halide octahedra can be seen isolated within a large number of organic cations. This further allows for tunability of the bandgap in these LD perovskites. The change in dimensionality leads to the quantum confinement with charge carrier movement getting restricted to two (2D) or one (1D) dimension only.[43] In addition to quantum confinement, dielectric confinement is also prevalent in these LD perovskites, which arises due to the contrast of the dielectric constants between the organic and the inorganic layers. Interestingly, the presence of large hydrophobic cations in these LD perovskites makes them moisture-resistant comparative to their 3D counterparts.[44]

1.5.1 Dimensionality reduction and optical properties

The crystal structure has a strong impact on the optoelectronic landscape in perovskites.[16] Any change in structure incurred by a change in composition or dimensionality will affect the

optical properties of perovskites. Dimensionality reduction changes the crystal structure significantly. This change in the crystal structure not only affects the linear optical properties, but also the nonlinear optical response.[45-47] In the linear optical regime, excitonic features become prominent, and a larger bandgap is observed compared to the 3D counterparts. The PL emission from LD perovskites is also quite unique and different from the 3D counterparts. The emission is mostly broad and hugely red-shifted from the band-edge due to a process known as exciton self-trapping.[48-54]

1.5.2 Exciton self-trapping

Usually, semiconductors show PL emission close to the band edge, by a direct band-to-band transition, by the radiative recombination of free excitons (FE) (Figure 1.7a).[16-17, 55] However, the LD lead halide perovskites shows a broad and highly-redshifted PL emission (Figure 1.b).[55] arising due to exciton self-trapping. In LD lead halide perovskites, FE gets trapped in deformities, which could be intrinsic, extrinsic, or defect-mediated (Figure 1.8, left panel).[56] This leads to a coupling between the FE and the phonon modes of the material in the excited state, leading to stabilization of the FE, and is known as self-trapped excitons (STE).

(a)   Band to Band PL   (b)   STE Emission
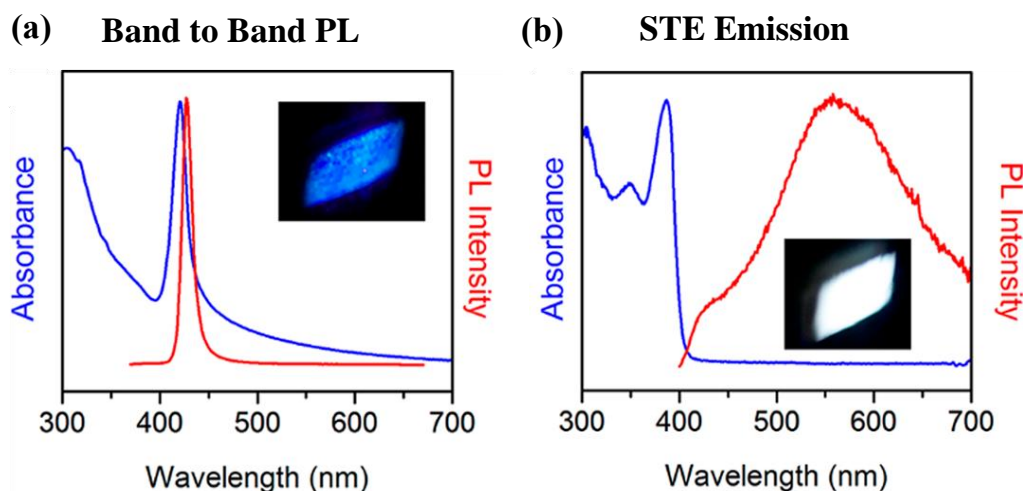
Figure 1.7: (a) The PL emission close to the band edge for a usual perovskite semiconductor. (b) An unusual, highly red-shifted, and broad PL emission from 1D perovskite, known as STE emission. The figure is taken from reference 55. with permission. Copyright © 2014. American Chemical Society.

The stabilization of the FE occurs along certain nuclear coordinates (Figure 1.8b right panel).[57] Earlier literature suggests that the nuclear coordinate along which the coupling occurs is mostly

comprised of the Pb-X sublattice deformations.[58] But this is not completely true; rather, a complex mix of phonon modes due to the Pb-X sublattice and the cation may possibly be responsible for the STE formation. Moreover, there could be multiple STE states formed, giving rise to a broad STE emission. In Chapter three of this thesis, we explored the composition of these nuclear coordinates along which exciton self-trapping takes place in 1D pyridinium lead bromide perovskites.
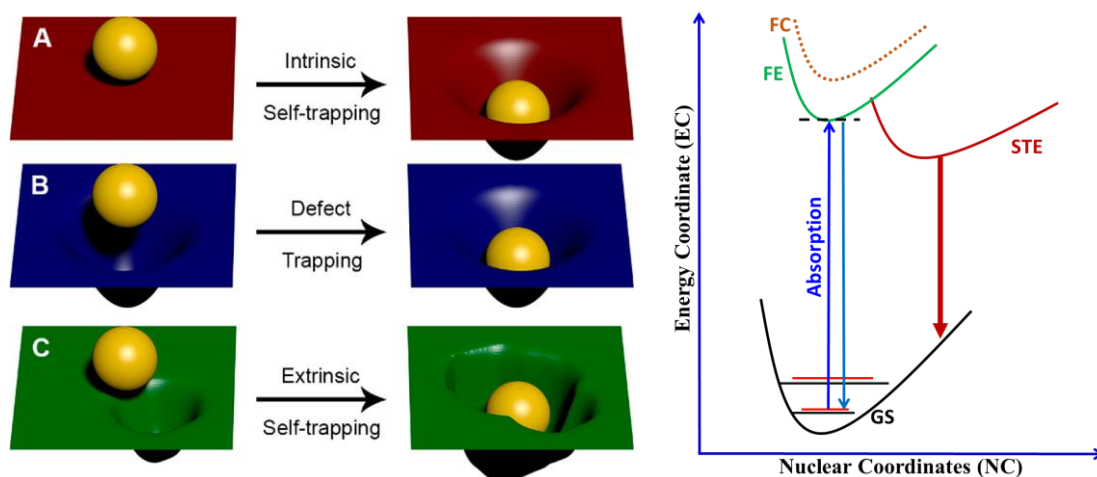
Figure 1.8: On the left is the schematic of self-trapping of excitons due to intrinsic, defect, or extrinsic trapping processes. The right panel shows the PL emission obtained from exciton self-trapping along certain nuclear coordinates. The figure 8a is reprinted with permission from reference 56, Copyright © 2018, American Chemical Society.

Exciton is a polarizable quasi-particle.[59] The coupling of the wave function of this exciton during the STE formation would be very strong with the polarizable Raman active modes of the 1D perovskites. The polarizable Raman active modes can be traced by Optical Kerr Effect (OKE) spectroscopy which traces the depolarized Raman active modes in a system.[58, 60] The OKE spectroscopy can provide information about the cation phonon modes in addition to the phonon modes of the lead halide backbone.

1.6 Nonlinear optical properties

3D lead halide perovskites have shown promising applications in the NLO regime, such as low-threshold lasing and energy upconversion processes (Figure 1.9).[61-62] Nonlinear optics (NLO) deals with the behavior of highly intense light in a nonlinear medium where the polarization of the medium responds non-linearly with the electric field of incident light.[63]

Upon interacting with a nonlinear material, some part of the fundamental light gets converted into lower and higher frequencies. Nonlinear materials with significant NLO efficiencies are required to extend the limit of the wavelength range directly accessible by laser sources. Having high-energy sources of radiation from X-ray to terahertz opens a huge field of investigation and application.
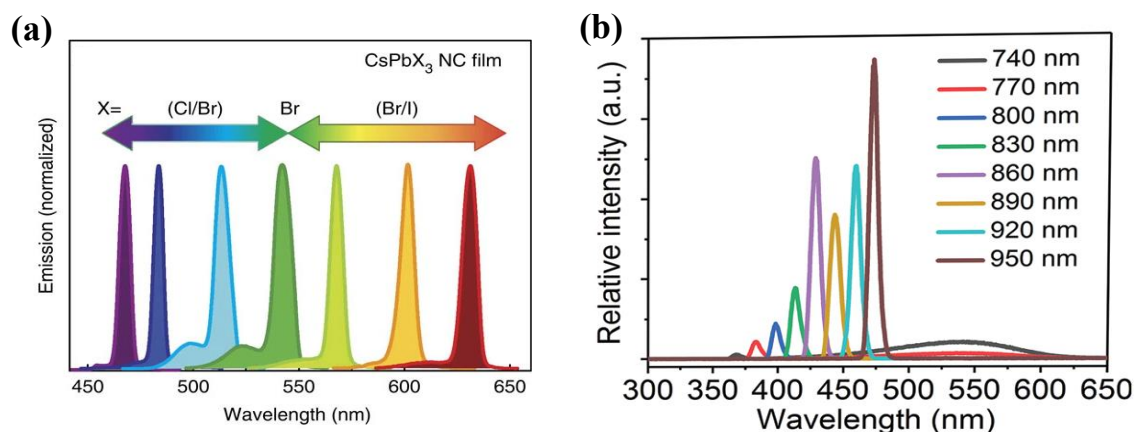
Figure 1.9: (a) Low-threshold lasing observed from 3D perovskites over a large wavelength range. (b) Second harmonic generation from 3D perovskites. The figures are reprinted with permission from reference 61, Copyright © 2017, Nature Publishing Group, and reference 62, Copyright © 2018, American Chemical Society.

Because of strong quantum and dielectric confinement effects, LD perovskites are ideal materials for efficient NLO output, which is further enhanced by their strong excitonic resonances. Additionally, tunability in the composition leads to the further diversification of NLO responses. The laser-induced damage threshold (LIDT), which determines the optical stability of the material under intense laser excitation, is also enhanced in LD perovskites. Thus, LD perovskites find potential applications in IR visualizing equipment and as efficient upconverters for lasing in a broad wavelength range.

1.7 Thesis summary and scope

As the sunlight helps us to see what is on the surface of the Earth, the spectroscopic techniques help us to unravel what is on the surface of the materials, their composition, and how the constituent particles such as electrons, atoms, molecules or ions bond and move around. Different spectroscopies help us to visualize the environment, composition, and nature of various systems. Despite promising applications of lead halide perovskites, an understanding

of the fundamental photophysics responsible for such excellent properties is yet maturing. This is partly because of the immensely complex and diverse optoelectronic properties shown by perovskites. In this thesis, various ultrafast spectroscopic techniques have been utilized to understand the myriad of properties shown by lead halide perovskites.

In Chapter two, we utilized optical pump terahertz probe (OPTP) spectroscopy to study the charge carrier recombination dynamics, electron-phonon interactions, and carrier transport mechanisms in formamidinium lead bromide nanocrystal films. Thus, we utilized OPTP to determine the fate of these 3D perovskites in photovoltaic and LED applications.

In Chapter three, we utilized optical Kerr effect (OKE) spectroscopy and DFT calculations to unravel the mechanism of unique optical phenomena in lower dimensional perovskites called exciton self-trapping (STE). We explored pyridinium lead bromide single crystals, which showed the STE emission at RT, and found a significant contribution of the cation dynamics in this unique emissive process, in addition to the lead halide sublattice. Our experimental results are fully supported by DFT calculations.

In Chapters four, five, and Appendix A1, we explored the nonlinear optical responses from a variety of LD lead halide perovskites by cation and halide engineering. Due to dimensionality reduction, a highly enhanced THG output was obtained upon excitation by IR pulses. In chapter 4, we studied pyridinium lead iodide single crystals, and a THG response tunable over a broad wavelength range was obtained. Modulating the polarizability by cation engineering helped us achieve significantly enhanced THG output from diisopropylammonium lead iodide single crystals, as discussed in Chapter 5. Upon varying the composition of the halide ions in pyridinium lead mixed halide single crystals, an efficient wavelength tunable THG response was observed, as discussed in Appendix 1 of this thesis. All these LD perovskite materials explored for NLO properties showed a very high optical stability (Laser-Induced Damage Threshold) under intense laser excitation. Thus, these materials are ideal for potential nonlinear applications.

The optoelectronic properties are temperature-dependent, so to further understand the mechanism of STE formation, we performed temperature-dependent PL measurements to understand the thermal evolution of the STE emission in 1D pyridinium lead iodide single crystals. We found that dynamic disorder and anharmonicity explain the complex PL emission behavior over the temperature range of 5 to 300 K. Additionally, we observed that a change in

the crystal structure at lower temperatures complicates the evolution of STE emission, as elaborately discussed in Appendix 2 of this thesis.

1.8 References

1. Höök, M.; Tang, X., Depletion of Fossil Fuels and Anthropogenic Climate Change, a Review. *Energy Policy* **2013**, *52*, 797-809.

2. Soeder, D. J., Fracking and the Environment: A Scientific Assessment of the Environmental Risks from Hydraulic Fracturing and Fossil Fuels. Fracking and the Environment, **2021**, pp 155-185.

3. Miles, R. W., Photovoltaic Solar Cells: Choice of Materials and Production Methods. *Vacuum* **2006**, *80*, 1090-1097.

4. Thekaekara, M. P.; Kruger, R.; Duncan, C. H., Solar Irradiance Measurements from a Research Aircraft. *Appl. Opt.* **1969**, *8*, 1713-1732.

5. Avrutin, V.; Izyumskaya, N.; Morkoç, H., Semiconductor Solar Cells: Recent Progress in Terrestrial Applications. *Superlattices Microstruct.* **2011**, *49*, 337-364.

6. Office, S. E. T. Solar Photovoltaic Cell Basics.

7. Miyasaka, T.; Jena, A. K., Research Background and Recent Progress of Perovskite Photovoltaics. *Perovskite Photovoltaics and Optoelectronics*, **2022**, pp 1-60.

8. Kojima, A.; Teshima, K.; Shirai, Y.; Miyasaka, T., Organometal Halide Perovskites as Visible-Light Sensitizers for Photovoltaic Cells. *J. Amer. Chem. Soc.* **2009**, *131*, 6050-6051.

9. Lee, M. M.; Teuscher, J.; Miyasaka, T.; Murakami, T. N.; Snaith, H. J., Efficient Hybrid Solar Cells Based on Meso-Superstructured Organometal Halide Perovskites. *Science* **2012**, *338*, 643-647.

10. Etgar, L.; Gao, P.; Xue, Z.; Peng, Q.; Chandiran, A. K.; Liu, B.; Nazeeruddin, M. K.; Grätzel, M., Mesoscopic $CH_3NH_3PbI_3/TiO_2$ Heterojunction Solar Cells. *J. Amer. Chem. Soc.* **2012**, *134*, 17396-17399.

11. Swarnkar, A.; Chulliyil, R.; Ravi, V. K.; Irfanullah, M.; Chowdhury, A.; Nag, A., Colloidal $CsPbBr_3$ Perovskite Nanocrystals: Luminescence Beyond Traditional Quantum Dots. *Angew. Chem. Int. Ed.* **2015**, *54*, 15424-15428.

12. Protesescu, L.; Yakunin, S.; Bodnarchuk, M. I.; Krieg, F.; Caputo, R.; Hendon, C. H.; Yang, R. X.; Walsh, A.; Kovalenko, M. V., Nanocrystals of Cesium Lead Halide Perovskites ($CsPbX_3$, X = Cl, Br, and I): Novel Optoelectronic Materials Showing Bright Emission with Wide Color Gamut. *Nano Lett.* **2015**, *15*, 3692-3696.

13. Cao, D. H.; Stoumpos, C. C.; Farha, O. K.; Hupp, J. T.; Kanatzidis, M. G., 2d Homologous Perovskites as Light-Absorbing Materials for Solar Cell Applications. *J. Amer. Chem. Soc.* **2015**, *137*, 7843-7850.

14. Yettapu, G. R.; Talukdar, D.; Sarkar, S.; Swarnkar, A.; Nag, A.; Ghosh, P.; Mandal, P., Terahertz Conductivity within Colloidal $CsPbBr_3$ Perovskite Nanocrystals: Remarkably High Carrier Mobilities and Large Diffusion Lengths. *Nano Lett.* **2016**, *16*, 4838-4848.

15. Sarkar, S.; Ravi, V. K.; Banerjee, S.; Yettapu, G. R.; Markad, G. B.; Nag, A.; Mandal, P., Terahertz Spectroscopic Probe of Hot Electron and Hole Transfer from Colloidal $CsPbBr_3$ Perovskite Nanocrystals. *Nano Let.* **2017**, *17*, 5402-5407.

16. Kovalenko, M. V.; Protesescu, L.; Bodnarchuk, M. I., Properties and Potential Optoelectronic Applications of Lead Halide Perovskite Nanocrystals. *Science* **2017**, *358*, 745.

17. Akkerman, Q. A.; Rainò, G.; Kovalenko, M. V.; Manna, L., Genesis, Challenges and Opportunities for Colloidal Lead Halide Perovskite Nanocrystals. *Nat. Mater.* **2018**, *17*, 394-405.

18. Dey, A., et al., State of the Art and Prospects for Halide Perovskite Nanocrystals. *ACS Nano* **2021**, *15*, 10775-10981.

19. Kim, M., et al., Conformal Quantum Dot–SnO_2 Layers as Electron Transporters for Efficient Perovskite Solar Cells. *Science* **2022**, *375*, 302-306.

20. NREL's "Best Research-Cell Efficiencies" Chart, https://www.nrel.gov/pv/cell-efficiency.html.

21. Deumel, S., et al., High-Sensitivity High-Resolution X-Ray Imaging with Soft-Sintered Metal Halide Perovskites. *Nat. Electron.* **2021**, *4*, 681-688.

22. Zhou, Y.; Chen, J.; Bakr, O. M.; Mohammed, O. F., Metal Halide Perovskites for X-Ray Imaging Scintillators and Detectors. *ACS Energy Lett.* **2021**, *6*, 739-768.

23. Romano, V.; Agresti, A.; Verduci, R.; D'Angelo, G., Advances in Perovskites for Photovoltaic Applications in Space. *ACS Energy Lett.* **2022**, *7*, 2490-2514.

24. Ho-Baillie, A. W. Y.; Sullivan, H. G. J.; Bannerman, T. A.; Talathi, H. P.; Bing, J.; Tang, S.; Xu, A.; Bhattacharyya, D.; Cairns, I. H.; McKenzie, D. R., Deployment Opportunities for Space Photovoltaics and the Prospects for Perovskite Solar Cells. *Adv. Mater. Technol.* **2022**, *7*, 2101059.

25. Brandt, R. E., et al., Searching for "Defect-Tolerant" Photovoltaic Materials: Combined Theoretical and Experimental Screening. *Chem. Mater.* **2017**, *29*, 4667-4674.

26. Castellan, G. W., Physical Chemistry, *Addison-Wesley Pub. Co: Reading,* **1971**.

27. Gaponenko, S. V., Optical Properties of Semiconductor Nanocrystals, *Cambridge University Press: Cambridge,* **1998**.

28. Wang, L.; McCleese, C.; Kovalsky, A.; Zhao, Y.; Burda, C., Femtosecond Time-Resolved Transient Absorption Spectroscopy of $CH_3NH_3PbI_3$ Perovskite Films: Evidence for Passivation Effect of Pbi2. *J. Amer. Chem. Soc.* **2014**, *136*, 12205-12208.

29. Chang, Q.; Bao, D.; Chen, B.; Hu, H.; Chen, X.; Sun, H.; Lam, Y. M.; Zhu, J.-X.; Zhao, D.; Chia, E. E. M., Tracking Carrier and Exciton Dynamics in Mixed-Cation Lead Mixed-Halide Perovskite Thin Films. *Commun. Phys.* **2022**, *5*, 187.

30. Guse, J. A.; Soufiani, A. M.; Jiang, L.; Kim, J.; Cheng, Y.-B.; Schmidt, T. W.; Ho-Baillie, A.; McCamey, D. R., Spectral Dependence of Direct and Trap-Mediated Recombination Processes in Lead Halide Perovskites Using Time Resolved Microwave Conductivity. *Phys. Chem. Chem. Phys.* **2016**, *18*, 12043-12049.

31. Yao, F.; Lin, Q., Charge Carrier Dynamics of Organic Cation-Treated Perovskites Probed with Time-Resolved Microwave Conductivity. *ACS Photon.* **2022**, *9*, 3165-3171.

32. Rehman, W.; Milot, R. L.; Eperon, G. E.; Wehrenfennig, C.; Boland, J. L.; Snaith, H. J.; Johnston, M. B.; Herz, L. M., Charge-Carrier Dynamics and Mobilities in Formamidinium Lead Mixed-Halide Perovskites. *Adv. Mater.* **2015**, *27*, 7938-7944.

33. Milot, R. L.; Eperon, G. E.; Snaith, H. J.; Johnston, M. B.; Herz, L. M., Temperature-Dependent Charge-Carrier Dynamics in $CH_3NH_3PbI_3$ Perovskite Thin Films. *Adv. Func. Mater.* **2015**, *25*, 6218-6227.

34. Johnston, M. B.; Herz, L. M., Hybrid Perovskites for Photovoltaics: Charge-Carrier Recombination, Diffusion, and Radiative Efficiencies. *Acc. Chem Res.* **2016**, *49*, 146-154.

35. Bretschneider, S. A.; Ivanov, I.; Wang, H. I.; Miyata, K.; Zhu, X.; Bonn, M., Quantifying Polaron Formation and Charge Carrier Cooling in Lead-Iodide Perovskites. *Adv. Mater.* **2018**, *30*, 1707312.

36. Zhao, D.; Chia, E. E. M., Free Carrier, Exciton, and Phonon Dynamics in Lead-Halide Perovskites Studied with Ultrafast Terahertz Spectroscopy. *Adv. Opt. Mater.* **2020**, *8*, 1900783.

37. Beard, M. C.; Turner, G. M.; Schmuttenmaer, C. A., Terahertz Spectroscopy. *J. Phys. Chem. B* **2002**, *106*, 7146-7159.

38. Schmuttenmaer, C. A., Exploring Dynamics in the Far-Infrared with Terahertz Spectroscopy. *Chem. Rev.* **2004**, *104*, 1759-1780.

39. Spies, J. A.; Neu, J.; Tayvah, U. T.; Capobianco, M. D.; Pattengale, B.; Ostresh, S.; Schmuttenmaer, C. A., Terahertz Spectroscopy of Emerging Materials. *J. Phys. Chem. C* **2020**, *124*, 22335-22346.

40. Goldschmidt, V. M., Die Gesetze Der Krystallochemie. *Naturwissenschaften* **1926**, *14*, 477-485.

41. Liu, X.; Hong, R.; Tian, C., Tolerance Factor and the Stability Discussion of ABO_3-Type Ilmenite. *J. Mater. Sci.: Mater. Electron.* **2009**, *20*, 323-327.

42. Saparov, B.; Mitzi, D. B., Organic–Inorganic Perovskites: Structural Versatility for Functional Materials Design. *Chem. Rev.* **2016**, *116*, 4558-4596.

43. Katan, C.; Mercier, N.; Even, J., Quantum and Dielectric Confinement Effects in Lower-Dimensional Hybrid Perovskite Semiconductors. *Chem. Rev.* **2019**, *119*, 3140-3192.

44. Sheikh, T.; Maqbool, S.; Mandal, P.; Nag, A., Introducing Intermolecular Cation-Π Interactions for Water-Stable Low Dimensional Hybrid Lead Halide Perovskites. *Angew. Chem. Int. Ed.* **2021**, *60*, 18265-18271.

45. Saouma, F. O.; Stoumpos, C. C.; Wong, J.; Kanatzidis, M. G.; Jang, J. I., Selective Enhancement of Optical Nonlinearity in Two-Dimensional Organic-Inorganic Lead Iodide Perovskites. *Nat. Commun.* **2017**, *8*, 742.

46. Abdelwahab, I.; Grinblat, G.; Leng, K.; Li, Y.; Chi, X.; Rusydi, A.; Maier, S. A.; Loh, K. P., Highly Enhanced Third-Harmonic Generation in 2D Perovskites at Excitonic Resonances. *ACS Nano* **2018**, *12*, 644-650.

47. Maqbool, S.; Sheikh, T.; Thekkayil, Z.; Deswal, S.; Boomishankar, R.; Nag, A.; Mandal, P., Third Harmonic Upconversion and Self-Trapped Excitonic Emission in 1D Pyridinium Lead Iodide. *J. Phys. Chem. C* **2021**, *125*, 22674-22683.

48. Dohner, E. R.; Jaffe, A.; Bradshaw, L. R.; Karunadasa, H. I., Intrinsic White-Light Emission from Layered Hybrid Perovskites. *J. Amer. Chem. Soc.* **2014**, *136*, 13154-13157.

49. Gan, L.; He, H.; Li, S.; Li, J.; Ye, Z., Distinctive Excitonic Recombination in Solution-Processed Layered Organic–Inorganic Hybrid Two-Dimensional Perovskites. *J.Mater. Chem. C* **2016**, *4*, 10198-10204.

50. Krishnamurthy, S.; Naphade, R.; Mir, W. J.; Gosavi, S.; Chakraborty, S.; Vaidhyanathan, R.; Ogale, S., Molecular and Self-Trapped Excitonic Contributions to the Broadband Luminescence in Diamine-Based Low-Dimensional Hybrid Perovskite Systems. *Adv. Opt. Mater.* **2018**, *6*, 1800751.

51. Yangui, A.; Roccanova, R.; Wu, Y.; Du, M.-H.; Saparov, B., Highly Efficient Broad-Band Luminescence Involving Organic and Inorganic Molecules in a Zero-Dimensional Hybrid Lead Chloride. *J. Phys. Chem. C* **2019**, *123*, 22470-22477.

52. Li, S.; Luo, J.; Liu, J.; Tang, J., Self-Trapped Excitons in All-Inorganic Halide Perovskites: Fundamentals, Status, and Potential Applications. *J. Phys. Chem. Lett.* **2019**, *10*, 1999-2007.

53. DeCrescent, R. A.; Du, X.; Kennard, R. M.; Venkatesan, N. R.; Dahlman, C. J.; Chabinyc, M. L.; Schuller, J. A., Even-Parity Self-Trapped Excitons Lead to Magnetic Dipole Radiation in Two-Dimensional Lead Halide Perovskites. *ACS Nano* **2020**, *14*, 8958-8968.

54. Li, J.; Wang, H.; Li, D., Self-Trapped Excitons in Two-Dimensional Perovskites. *Front. of Optoelectron.* **2020**, *13*, 225-234.

55. Dohner, E. R.; Hoke, E. T.; Karunadasa, H. I., Self-Assembly of Broadband White-Light Emitters. *J. Amer. Chem. Soc.* **2014**, *136*, 1718-1721.

56. Smith, M. D.; Karunadasa, H. I., White-Light Emission from Layered Halide Perovskites. *Acc. Chem. Res.* **2018**, *51*, 619-627.

57. Liang, M., et al., Free Carriers Versus Self-Trapped Excitons at Different Facets of Ruddlesden–Popper Two-Dimensional Lead Halide Perovskite Single Crystals. *J. Phys. Chem. Lett.* **2021**, *12*, 4965-4971.

58. Miyata, K.; Meggiolaro, D.; Trinh, M. T.; Joshi, P. P.; Mosconi, E.; Jones, S. C.; De Angelis, F.; Zhu, X. Y., Large Polarons in Lead Halide Perovskites. *Sci. Adv.*, **2021**, *3*, e1701217.

59. Knox, R. S., Introduction to Exciton Physics. Collective Excitations in Solid*s*, Di Bartolo, B., *Ed. Springer US: Boston, MA*, **1983**; pp 183-245.

60. Maehrlein, S. F., et al., Decoding Ultrafast Polarization Responses in Lead Halide Perovskites by the Two-Dimensional Optical Kerr Effect. *Proc. Natl. Acad. Sci.* **2021**, *118*, e2022268118.

61. Yakunin, S.; Protesescu, L.; Krieg, F.; Bodnarchuk, M. I.; Nedelcu, G.; Humer, M.; De Luca, G.; Fiebig, M.; Heiss, W.; Kovalenko, M. V., Low-Threshold Amplified Spontaneous Emission and Lasing from Colloidal Nanocrystals of Caesium Lead Halide Perovskites. *Nat. Commun.* **2015**, *6*, 8056.

62. Yuan, C.; Li, X.; Semin, S.; Feng, Y.; Rasing, T.; Xu, J., Chiral Lead Halide Perovskite Nanowires for Second-Order Nonlinear Optics. *Nano Lett.* **2018**, *18*, 5411-5417.

63. Boyd, R. W., *Nonlinear Optics*, 2020.

Chapter 2

Ultrafast Charge Carrier Dynamics in Formamidinium Lead Bromide Nanocrystal Film: Time-resolved Terahertz Spectroscopic Study

Chapter 2

Ultrafast Charge Carrier Dynamics in Formamidinium Lead Bromide Nanocrystal Film: Time-resolved Terahertz Spectroscopic Study

Abstract

Lead halide perovskites are in the limelight due to their excellent semiconductor properties, making them ideal for photovoltaic and optoelectronic applications. The emergence of perovskites as a sought-after semiconductor owes to their unique electronic band structure, inherent defect tolerance, and easy processibility. This has led to perovskites being blessed with amazing excited state properties. Exploration of these excited state properties will help to further their progress as idealistic materials for photovoltaics. We used ultrafast optical pump terahertz probe (OPTP) spectroscopy to explore the excited state dynamics in $FAPbBr_3$ nanocrystals (NC) thin films, including charge carrier recombination, carrier-phonon interactions, and other semiconducting properties. Photoinduced lattice fluctuations seem to predominantly affect the carrier transport and recombination mechanisms and hence the carrier mobilities and diffusion lengths. We observe that the backscattering due to photoinduced lattice fluctuations is one of the dominant scattering mechanisms prevalent in $FAPbBr_3$ NC thin films. Phonon modes due to the organic cation formamidinium (FA), visualized in the THz-TDS study, provide additional pathways for photoinduced lattice fluctuations by introducing dynamic disorder into the perovskite lattice. Altogether, long-lived charge carriers, moderate mobility, and diffusion length are observed in $FAPbBr_3$ NC thin films, which are clearly explained by additional backscattering due to photo-induced lattice fluctuations. Moreover, a clear difference in the nature of the generated excited states was observed at different photoexcitations.

Graphical Abstract

Ultrafast Charge Carrier Dynamics in Formamidinium Lead Bromide Nanocrystal Film: Time-resolved Terahertz Spectroscopic Study
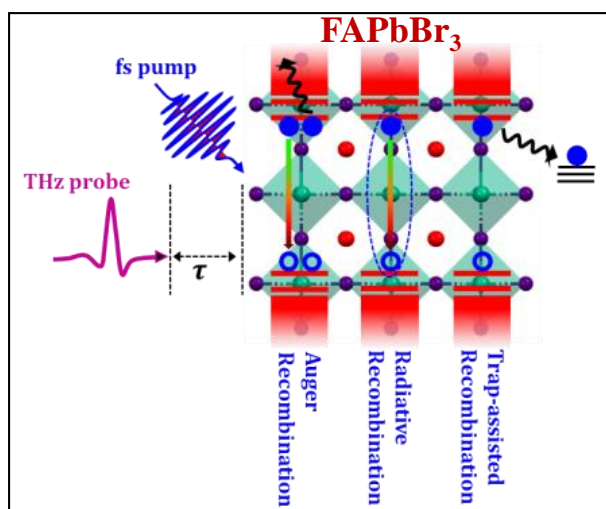
2.1 Introduction

Halide perovskites are a class of materials with generic formula ABX_3, with A being a monovalent cation (methyl ammonium (MA; $CH_3NH_4^+$), formamidinium (FA; $(CH_3)_2NH_2^+$), Cs^+), B being a divalent metal cation (Pb^{2+}, Sn^{2+}), and X is a halide ion.[1-2] These perovskites have emerged as an extremely important class of semiconductor materials, with properties aimed at a futuristic revolution in solar light harvesting, lasing, and light-emitting diodes (LEDs).[3-13] The possibility of covering the whole visible spectrum via bandgap tuning coupled with remarkably high absorption coefficient makes them ideal candidates for solar cell absorbing layers.[14-17] Easy solution processibility approach of synthesis leads to perovskites with low defect concentration and cost-effective device fabrication.[13] This provides an immense edge over the traditional solar cell materials which require high-temperature synthetic protocols. Exploiting the technology of multi-junction solar cell configuration and solar concentrators, ample amount of solar light which was not absorbed by the champion semiconductor material silicon due to its low absorption coefficient and indirect bandgap can be easily converted into renewable energy. Research centered around the evolution of this class of material on fronts vis-à-vis its ambient stability, defect passivation, and lead toxicity is currently at the forefront. Such directions in research are important to tap the full potential of perovskites in all its variations such as quantum dots, 3D bulk crystalline materials, 2D and 1D perovskites, tin (Sn) based perovskites and double perovskites.

Dressed with remarkable excited-state carrier properties such as long bimolecular recombination lifetimes[9, 18-19], charge carrier protection by polaron formation[20-22], minimal monomolecular trap pathways[23-25], and hot carrier harvesting by multi-exciton formation[26-27], the perovskite materials are truly set to be one of the best trail-blazing energy harvesting materials. This has brought to focus the need to extensively study the excited state properties and the carrier dynamics of perovskites using various spectroscopic techniques such as temperature-dependent photoluminescence[28-29] (PL), time-resolved Raman[30], 2D IR[31-32] (infrared), electronic spectroscopy[33-34], broadband transient absorption[35-36], optical Kerr effect[21, 37] (OKE), etc. A unified understanding of such properties is yet to be reached, but significant progress has been achieved. Steady-state and time-resolved terahertz (THz) spectroscopy have also been exploited extensively to garnish important understanding of the ground and the excited state properties of perovskites.[9-10, 18, 38-42]

Chapter 2

Ultrafast Charge Carrier Dynamics in Formamidinium Lead Bromide Nanocrystal Film:
Time-resolved Terahertz Spectroscopic Study

THz spectroscopy provides a non-invasive window[43], by utilizing low-energy photons, to probe the excited state of these semiconducting perovskites. THz spectroscopy is a rather newly established ultrafast spectroscopic method developed around the start of the 21st century when high-power ultrafast lasers became a reality. THz spectroscopy provides information about the processes occurring in the picosecond timescale with energy in the meV range. 1 THz equals 4 meV in energy, 33.3 cm^{-1} in wavenumber, and 300 µm in wavelength. THz is present in the far-infrared (IR) region of the electromagnetic spectrum between microwave and infrared frequencies. It spans ~0.3-30 THz in frequency range or 9.99-999 cm^{-1} wavenumbers and hence provides access to phenomena that were elusive to electronics (microwave) and optical (IR) spectroscopies. Time-domain terahertz (THz-TDS) spectroscopy provides access to the low-frequency optical phonon modes which are inaccessible in other spectroscopic methods.[43-45] Low energy dynamics are crucial for understanding the fundamental properties and hence the device performance in solar cell devices. Material properties such as photoconductivity, mobility, diffusion length, and phonon-charge carrier coupling interactions can be directly studied using time-resolved terahertz spectroscopy (TRTS), also known as optical pump terahertz probe (OPTP) spectroscopy.[45-46]

The charge carriers interact with low-frequency terahertz radiation and manifest in the dielectric response in the terahertz region of the materials.[46-47] By applying various physical models for fitting the dielectric response function, properties like charge carrier density, carrier mobility, and carrier diffusion lengths can be obtained. Charge carriers and their related properties like mobility, lifetime, etc., define the usefulness and functionalities of semiconductors. 3D lead halide perovskites have low-lying phonon modes and exciton binding energies of the order of terahertz range.[48-49] Thus, by exciting the lead halide perovskite using an optical pump pulse, the dynamics of the generated excitons and the exciton-phonon interactions can be easily probed using THz light as probe pulses.

Upon excitation, the perovskite sample absorbs incident photons, and charge carriers are created which can undergo a myriad of processes.[23] Different probe pulses from the electromagnetic spectrum such as white-light continuum, infra-red, microwave, and terahertz, can be used to study this excited state and to determine the fate of the materials in photovoltaic and LED applications. In this work, we have utilized broadband terahertz pulses to probe the excited state properties in a well-studied 3D lead halide perovskite nanocrystal system, i.e., formamidinium lead bromide (FAPbBr$_3$) nanocrystal thin film. FA-based lead halide

Chapter 2

Ultrafast Charge Carrier Dynamics in Formamidinium Lead Bromide Nanocrystal Film: Time-resolved Terahertz Spectroscopic Study

perovskites have exhibited promising photovoltaic properties with enhanced stability towards chemical degradation.[50-52] In the excited state systems, time-resolved terahertz spectroscopy (TRTS) can be used to explore the ultrafast charge carrier dynamics, recombination mechanisms, semiconducting properties, nature of charge carriers, and carrier-phonon interactions.[45] We utilized TRTS to explore the excited state properties of $FAPbBr_3$ NC thin film. This allows us to determine the fate of this material as an efficient photovoltaic and optoelectronic material. We observed that the $FAPbBr_3$ NC thin films, due to their dynamic disorder and flexible crystalline nature of the lattice, have both benefits and disadvantages. We observed a longer lifetime of charge carriers due to localization, but the mobility and diffusion lengths are compromised and are only moderate in value.

2.2 Experimental Section

2.2.1 Chemicals

Lead acetate ($Pb(ac)_2$, Sigma-Aldrich, 99.99%), formamidinium acetate (FA-ac, Sigma-Aldrich), octadecene (ODE, Sigma-Aldrich), oleic acid (OA, Sigma-Aldrich), oleylamine (OLA, Sigma-Aldrich), ethanol (Rankem), HBr (48% aqueous solution, Sigma-Aldrich), diethyl ether (Rankem), Toluene (99.5%), Sigma-Aldrich), hexane (anhydrous, Sigma-Aldrich), methyl acetate (anhydrous, Sigma-Aldrich)

2.2.2 Synthesis and isolation of FAPbBr₃ nanocrystals

$FAPbBr_3$ nanocrystals were synthesized by modifying the method adopted by Protesescu et.al.[53]

2.2.2.1 Preparation of oleyl ammonium bromide (OAMBr)

In a 250 mL two-neck round bottom flask 100 mL ethanol and 12.5 mL of OLA were combined and stirred vigorously. The mixture was placed in an ice-water bath, and 8.56 mL of HBr was added dropwise to yield a final OLA: HBr molar ratio of 1:2. This reaction mixture was left to react overnight under N_2 flow. Next, the solution was dried under vacuum, and the product obtained was recrystallized multiple times with diethyl ether and the white powder of OAMBr was isolated by vacuum drying at 80°C.

2.2.2.2 Synthesis of FAPbBr₃ NCs using a three-precursor method

In a 25 mL three-neck round bottom flask, 0.2 mmol (0.076 g) of $Pb(ac)_2$, 0.75 mmol (0.078 g) of FA-ac, 8 mL of dried ODE, and 2 mL of dried OA were combined and dried under vacuum

Chapter 2

Ultrafast Charge Carrier Dynamics in Formamidinium Lead Bromide Nanocrystal Film: Time-resolved Terahertz Spectroscopic Study

for 30 minutes at 50 °C. The mixture was heated to 120 °C under N_2 flow, followed by injecting a solution of 0.6 mmol (0.21 g) OAMBr in 2 mL of toluene. After 10 s, the reaction was quenched in an ice-water bath.

2.2.2.3 Isolation of colloidal FAPbBr$_3$ NCs[54]

To the crude solution of FaPbBr$_3$, 5 mL of hexane was added and the mixture was centrifuged at 4000 rpm for 5 mins to separate the orange-colored bulk formed. To the supernatant (colloidal FAPbBr$_3$), thrice amount of methyl acetate was added and centrifuged at 7500 rpm for 1.5 minutes. The precipitated NCs were dispersed in hexane, while the supernatant was discarded. The above steps were repeated two more times till a homogenously sized NC solution was obtained.

2.2.3 Characterization

The UV-visible absorption spectrum was recorded by using a Perkin Elmer, Lambda-45 UV-Visible spectrometer. Steady-state photoluminescence (PL) of the NCs was measured by FLS 980 (Edinburgh Instruments). Powder X-ray diffraction (PXRD) data were recorded on a Bruker D8 Advance x-ray diffractometer using Cu Kα radiation (1.54 Å). Transmission electron microscopy (TEM) studies were carried out using a JEOL JEM 2100F field emission transmission electron microscope at 200 kV. The sample preparation for TEM was done by putting a drop of the colloidal solution of NCs in hexane on the carbon-coated copper grids. Scanning electron microscopy (SEM) imaging was performed on Zeiss Ultra Plus SEM instrument.

2.2.4 Terahertz time-domain spectroscopy (THz-TDS)

THz-TDS experiments were performed on FAPbBr$_3$ NC thin films on a home-built setup. Ultrafast femtosecond pulses obtained from the Ti-Sapphire amplifier system (Spitfire, Spectra Physics: 800 nm central wavelength, 45 fs pulse duration, 1 kHz repetition rate, 4 W output power) were split into 1:1 ratio for the pump and probe beams and the probe part was then divided into 92:8 ratio by a pellicle beam splitter for the generation and detection of THz pulses, respectively. THz pulses were generated from the laser-induced air plasma. The 800 nm fundamental pulses pass through a beta barium borate (BBO) crystal thereby generating second harmonic 400 nm light. Fundamental light, together with the second harmonic light was focused tightly into the nitrogen gas to generate air plasma, emitting radiation with a broad range of the electromagnetic spectrum. A parabolic mirror collimates the generated

Chapter 2

Ultrafast Charge Carrier Dynamics in Formamidinium Lead Bromide Nanocrystal Film: Time-resolved Terahertz Spectroscopic Study

electromagnetic spectrum and using a low-resistivity silicon filter, THz light was selectively filtered out and focused onto the sample using another parabolic mirror. The transmitted THz light was collected and collimated using another pair of paraboloidal mirrors and directed into the detection path. The detection laser beam (gate beam) passing through a delay stage was used to detect the THz waveform. The 800 nm gate beam is focused between two electrodes having a 1.5 KV AC electric field acting as a local oscillator. The second harmonic of the gate beam is induced by the THz field by the Terahertz field-induced second harmonic (TFISH) generation mechanism.[55] The second harmonic of the gate beam is filtered out using a pair of dichroic mirrors and a notch filter, and subsequently detected by a photomultiplier tube (PMT). The PMT output is then sent to the current pre-amplifier and detected using Lock-in amplifiers. The intensity of the second-harmonic signal is proportional to the THz electric field. We map out the entire THz waveform by varying the delay between the THz beam and the gate beam. All THz experiments were performed in a nitrogen-purged atmosphere at room temperature.

2.2.5 Optical pump terahertz probe spectroscopy (OPTP)

The OPTP setup is driven by the same amplifier system used for THz-TDS. The THz generation and detection geometries are the same as described above. 50% of the total amplifier output is directed to an optical parametric amplifier (OPA, TOPAS C, Light Conversion) which generates pump light between 280-2600 nm. 480 and 517 nm excitation pulses utilized for OPTP experiments were obtained from the OPA and directed onto the sample through a hole drilled in the parabolic mirror that focuses THz light onto the same. The pump pulses were modulated by a chopper set at one-third of the amplifier frequency. A lens was used to focus the pump light onto the sample. The beam diameter of the pump pulse was maintained at three times than that of the THz probe pulses for a uniform probing of the photoexcited sample in our OPTP measurements. After photo-excitation of the sample, the pump pulses were blocked by a beam blocker which is transparent to the broadband THz pulses. Thus, the THz probe pulses transmitted through the photoexcited sample were filtered to remove the reminiscent pump light. The experiments were performed on a few millimeters sized, uniformly excited samples, and the response recorded is averaged over the probed volume. Hence, the sample properties encoded contain effects from grain boundaries and voids separating the NCs. Schematic 2.1 shows a simplistic depiction of the OPTP setup.

Chapter 2

Ultrafast Charge Carrier Dynamics in Formamidinium Lead Bromide Nanocrystal Film:
Time-resolved Terahertz Spectroscopic Study
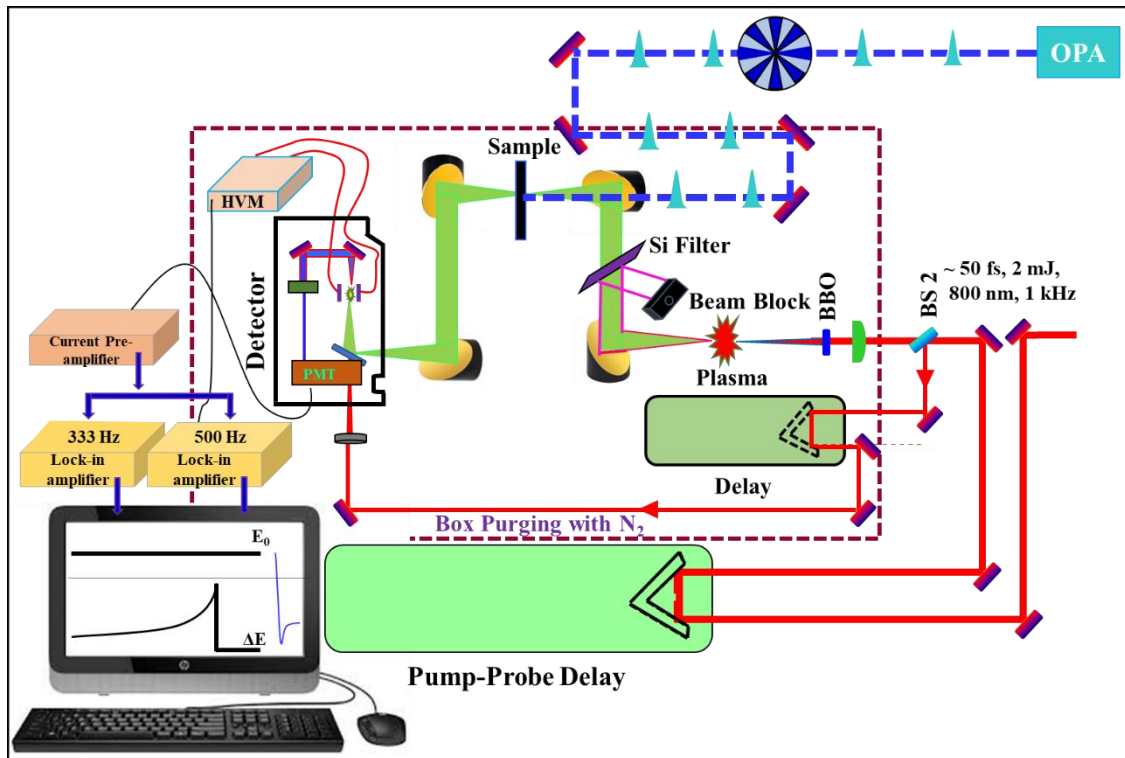
Schematic 2.1: Schematic of an optical pump THz probe setup. Optical pump pulses excite the sample across the bandgap. After a delay time τ, ps-THz pulses monitor the evolution of the sample.

2.3 General THz setup and THz-TDS and TRTS analysis

Generation and detection of THz pulses are achieved by utilizing ultrashort laser pulses with pulse widths of ~10-100 fs. The ps-THz pulses generated are mapped by fs pulses of near-IR gating beam. A generic steady-state THz spectroscopic setup involves two main components: generation and detection of THz waves. For time-resolved THz studies, in addition to TDS setup, a visible optical pump source (variable wavelength) from OPA is used to take the sample to the excited state. THz probe pulses interact with charge carriers in the excited state to reveal the charge carrier dynamics.

Various techniques have been explored for THz generation: a) THz emitters such as photoconductive antennas[56] (PCA) or non-centrosymmetric media such as crystals undergoing optical rectification[57] (OR) and b) Air plasma sources[58]. Air plasma-based THz generation has been further explored by using the DC-bias method and the second harmonic bias method.[59] The generation of THz by air plasma has added advantages as it is not limited by the damage threshold of the generation media of PCAs or OR crystals, and the THz bandwidth is not

Chapter 2

Ultrafast Charge Carrier Dynamics in Formamidinium Lead Bromide Nanocrystal Film:
Time-resolved Terahertz Spectroscopic Study

truncated by optical phonon mode absorption. THz pulses even up to ~75 THz have been achieved using air plasma.[60] Relativistic laser plasma sources provide high energy milli-joule THz pulses, but very high intensity (TW-PW) laser sources are required for its realization.[61]

For the coherent detection of THz pulses, conventional techniques such as PCA[62] and free space electro-optic (EO) sampling[63], as well as air-biased THz detection[55] and spectral-domain interferometry[64] (SDI) have been explored. Air-biased coherent detection, also called as air-breakdown coherent detection (THz-ABCD), is described by a four-wave mixing model and is utilized for the detection of intense THz radiation. The THz pulses carrying the information about the sample interact with fs near-IR (NIR) gating beam (ω) in the presence of a local oscillator to generate a weak plasma. A second harmonic (2ω) of the gate beam is directed into the photomultiplier tube by an assembly of dichroic mirrors and a lens. The second harmonic is generated by the external bias field and is called a THz field-induced second harmonic (TFISH). A spatial and temporal overlap of THz and gate pulses is essential for THz detection.[55] Water vapors present in the atmosphere have strong absorption in THz regime, and so the experimental setups are continuously purged with N_2 or dry air.

The THz electric field is mapped directly in time, which upon Fourier transformation, is spectrally resolved into both amplitude and phase components as shown in equation 1. This provides an added advantage in contrast to other spectroscopic techniques, which carry only the intensity information. The absorption coefficient, of the sample, is calculated from the amplitude, while refractive indices and complex dielectric constant are obtained from the phase information, as described in equations 2 to 5. Finally, complex permittivity can be evaluated from the analysis of the THz-TDS spectra.

$$\frac{E_{ref}(t)}{E_{sample}(t)} \xrightarrow{FFT} \frac{E_{ref}(\omega)}{E_{sample}(\omega)} e^{i(\varphi_{ref}-\varphi_{sample})} \qquad (1)$$

$$Absorption\ coefficient: \alpha = -\frac{1}{d} ln\left(\frac{E_{ref}(\omega)}{E_{sample}(\omega)}\right)^2 \qquad (2)$$

$$Extinction\ coefficient: k = \frac{\lambda\alpha}{4\pi} = \frac{c\alpha}{2\omega} \qquad (3)$$

$$Refractive\ index: n = 1 + \frac{c}{2\pi\omega d}\left(\varphi_{sample} - \varphi_{ref}\right) \qquad (4)$$

$$Absorbance: A = \alpha * d \qquad (5)$$

Chapter 2

*Ultrafast Charge Carrier Dynamics in Formamidinium Lead Bromide Nanocrystal Film:
Time-resolved Terahertz Spectroscopic Study*

The OPTP experiments can essentially be conducted in two ways. Following the photoexcitation by a pump pulse, the change in the entire THz waveform is mapped in a step-wise manner at several fixed pump-probe delay times (t_p). This is referred to as a frequency-resolved TRTS study or probe scan. Another approach is to fix the gating delay at the peak of the THz waveform and then scan the entire pump-probe delay (t_p) line. Thus, the frequency-averaged THz study, also known as the pump scan, provides information about the pump-induced change in the THz peak amplitude. A frequency-averaged sample response is obtained over the entire available temporal window. By scanning the delay between the optical pump and THz probe pulses, change in peak THz transmission, $\frac{-\Delta E}{E_0}$, is obtained, which is proportional to the THz frequency-averaged peak photoconductivity. Further details of the analysis of frequency-averaged dynamics are provided at adequate places in the chapter.

As the THz light is sensitive to moving charges, the frequency-resolved THz spectra show typical signatures of charge carriers. The type of charge carriers determines the nature of the response to the THz probe. To evaluate the transport properties of the semiconductors, the spectra are fit to an appropriate conductivity model. Upon photoexcitation, when free carriers are generated, a suitable fit to Drude model[65] is observed in which case photoconductivity is given by equation 6:

$$\widehat{\sigma}(\omega) = \frac{\varepsilon_0 \omega_p^2 \tau}{1\text{-}i\omega\tau} = \frac{\sigma_{DC}}{1\text{-}i\omega\tau} \qquad (6)$$

where ω_p is the plasma frequency and τ is the scattering time.

If the charge carriers suffer localization and backscattering due to defects or grain boundaries, Drude-Smith model[66] is utilized for fitting the spectra given by equation 7:

$$\widehat{\sigma}(\omega) = \frac{\varepsilon_0 \omega_p^2 \tau}{1\text{-}i\omega\tau} \left[1 + \sum_{n=1}^{\infty} \frac{c_n}{(1\text{-}i\omega\tau)^n} \right] \qquad (7)$$

where c_n is the velocity constant and ranges from 0 to -1. c_n is a parameter related to the backscattering probability of the nth scattering event. $c_n = 0$ represents the Drude-like behavior i.e., free carriers, while $-1 < c_n < 0$ represents localized carriers and $c_n = -1$ implies full backscattering.

Chapter 2

***Ultrafast Charge Carrier Dynamics in Formamidinium Lead Bromide Nanocrystal Film:
Time-resolved Terahertz Spectroscopic Study***

If there are any resonance features present in the conductivity spectra, then the Lorentz model becomes appropriate.[66] The following expression (equation 8) represents the conductivity derived from solving the damped harmonic oscillator:

$$\hat{\sigma}(\omega) = \frac{\varepsilon_0 \omega_p^2 \tau \omega}{\omega - i\tau(\omega^2 - \omega_0^2)} \qquad (8)$$

where ω_0 is the oscillator resonance frequency and $1/\tau$ $(= \gamma)$ is the linewidth of the resonance.

Due to the versatile nature of charge carriers in semiconductors, usually, a superposition of conductivity models is used to adequately explain the behavior of charge carriers.[9-10, 67] For example, if the free carriers interact with the phonon modes, a Drude-Lorentz model or Drude-Smith-Lorentz model is applied. Elaborate discussion and analysis have been provided at adequate places later in the chapter.

2.4 Results and Discussion

Highly crystalline cubic FAPbBr$_3$ NCs were synthesized by hot injection method following a previously reported procedure.[53] The obtained NCs showed a significantly uniform size distribution as shown by the TEM image (Figure 2.1a). The NCs exhibit cubic morphology with average edge dimensions of ~8 nm. The as-synthesized NCs were spin-coated to produce a thin film of NCs onto high-density polyethylene (HDPE) substrate, ideal for broadband time-resolved terahertz experiments. The cubic crystal structure and crystallinity were retained in the NC thin film, confirmed by the powder X-ray diffraction (PXRD) pattern as depicted in Figure 2.1b. The FAPbBr$_3$ NC thin film shows an excitonic feature at ~487 nm and an absorption edge at ~530 nm as shown by the blue trace in Figure 2.1c. Upon excitation with a 405 nm laser, intense PL emission centered at ~517 nm with an FWHM of ~23 nm was observed (red trace in Figure 2.1c). The PL peak position is consistent with the onset of the absorbance spectrum of FAPbBr$_3$ NC thin film, suggesting that the PL arises mainly due to band-edge emission. The time-resolved (TR) PL profile recorded at 517 nm of FAPbBr$_3$ NC film decays with an average lifetime of ~15 nanoseconds (ns) as shown in Figure 2.1d. The TRPL data were fitted using a triexponential decay function, and lifetimes of 1.6 ns (29%), 5.6 ns (59%), and 15.8 ns (12%) were obtained. The three decays probably include the effect of recombination due to shallow trap states and other non-radiative processes in addition to band to band radiative recombination. A 405 nm laser was used as the excitation source for measuring TRPL.

Chapter 2

Ultrafast Charge Carrier Dynamics in Formamidinium Lead Bromide Nanocrystal Film:
Time-resolved Terahertz Spectroscopic Study
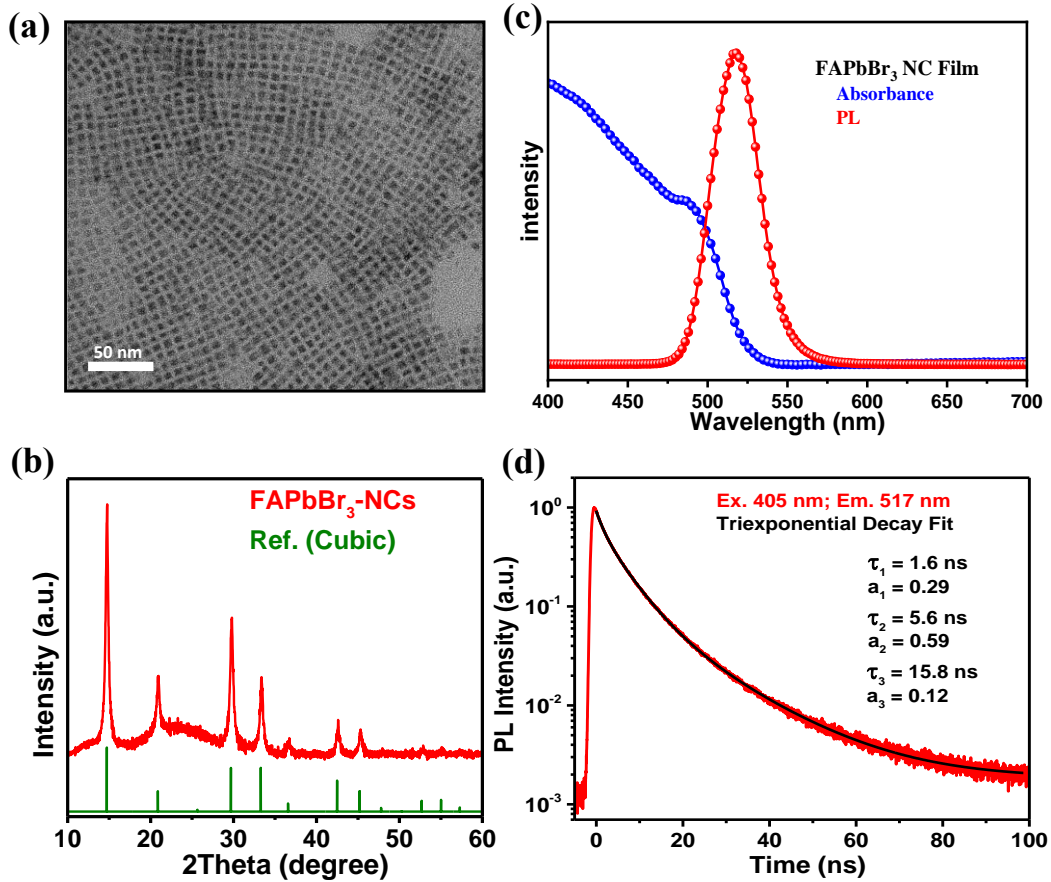
Figure 2.1. Structural and optical characterization of FAPbBr₃ NCs utilized for TRTS measurements. (a) TEM image of FAPbBr₃ nanocrystals revealing a significantly uniform size distribution. (b) powder XRD pattern of FAPbBr₃ NC film compared to a cubic reference depicting crystallinity and cubic crystal structure of the spin-coated FAPbBr₃ NC film. (c) UV-visible absorption spectrum (blue) and photoluminescence spectrum (red) of FAPbBr₃ NC film. (d) Time-resolved PL spectra of FAPbBr₃ NC film for 517 nm emission, after excitation with a 405 nm laser source. The data were fitted using a triexponential decay, giving lifetimes of 1.6 ns (29%), 5.6 ns (59%) and 15.8 ns (12%).

2.4.1 Before photoexcitation: Phonon modes and optical constants from THz-TDS

For THz-TDS and TRTS experiments, thin films of the FAPbBr₃ NCs were fabricated on HDPE substrate. The NCs were spin-cast on HDPE substrate at 1000 RPM for 20 sec followed by 2000 RPM for 5 sec. The thickness of the as-cast FAPbBr₃ NCs film is ~ 1.7 µm as shown by the cross-sectional SEM image in Figure 2.2a.

Ultrafast Charge Carrier Dynamics in Formamidinium Lead Bromide Nanocrystal Film:
Time-resolved Terahertz Spectroscopic Study
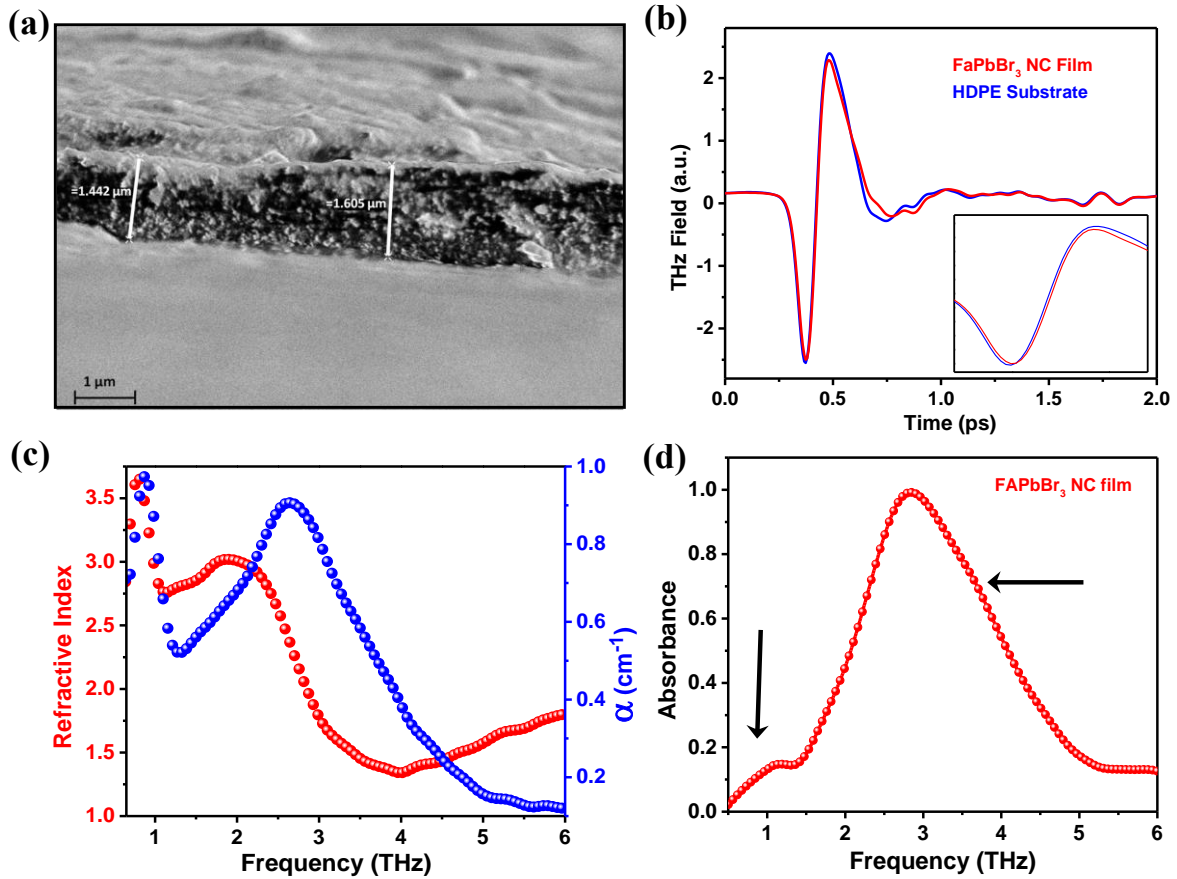
Figure 2.2. (a) SEM image of as cast FAPbBr$_3$ NC film on HDPE substrate used for THz experiments. (b) THz-TDS waveforms transmitted through HDPE substrate (blue) and FAPbBr$_3$ NC film (red); the inset shows the zoomed-in portion of the THz signal. (c) Frequency-dependent refractive index (red) and absorption coefficient α (blue) over a broad (6 THz) range. (d) Normalized THz-TDS absorption spectrum of FAPbBr$_3$ NC film.

In THz-TDS of the non-photoexcited sample, the THz light interacts with the ground state IR-active phonon modes of the FAPbBr$_3$ NC film.[45] The THz electric field undergoes a change in amplitude and phase due to the phonon mode absorption and dispersion in the film, as shown in Figure 2.2b (the inset shows the zoomed-in portion of the THz signal). Fourier transformation of the THz electric field transmitted through the HDPE substrate (reference) and the FAPbBr$_3$ NC thin film (sample) leads to the evaluation of optical constants such as absorption coefficient and refractive index as presented in Figure 2.2c. The decreased dimensionality and high surface-to-volume ratio of these perovskite NCs significantly affect the crystal lattice and its vibrational phonon features.[68] The real refractive index varies between 1.6 and 3.5 in the frequency range from 0.5 to 6 THz. Frequency-dependent effective real

Chapter 2

Ultrafast Charge Carrier Dynamics in Formamidinium Lead Bromide Nanocrystal Film:
Time-resolved Terahertz Spectroscopic Study

dielectric function varies between 13 and 3.5, while the imaginary dielectric function ranges from 0-9 over the given frequency range. As can be clearly seen from Figures 2.2c and 2.2d of Chapter 2, at a frequency of ~2.8 THz, the refractive index decreases dramatically from ~3 to 1.25 (Figure 2.2c) because of the THz absorption peak at the same frequency depicted in Figure 2.2d. Whenever there is a resonance (absorption) at a particular frequency, the refractive index changes drastically. Figure 2.2d shows the broadband THz absorption spectrum of FAPbBr$_3$ NC thin film depicting the associated optical phonon modes. The broadness of THz absorption features in NCs has been attributed to the shorter phonon lifetimes resulting from confinement effects and increased surface scattering.[69] A strong IR-active absorption feature at 2.8 THz (92.4 cm^{-1}) is observed, which has been previously assigned to antisymmetric stretching of apical and equatorial Pb-Br bonds and Br-Pb-Br bending modes.[9] A weaker absorption feature at ~1 THz (33 cm^{-1}) is observed originating due to Pb-Br sublattice distortion as predicted by earlier reports.[70-71] Additionally, a broad shoulder, in THz absorption spectrum at ~3.7 THz (122 cm^{-1}) due to FA cation motions was observed. This assignment of 3.7 THz to FA cation motions was previously done by an earlier theoretical report.[72]

The phonon modes are mostly responsible for carrier-phonon interactions, and the presence of phonons due to both Pb-Br framework and the FA cation suggests that FA cation will also affect the charge-carrier dynamics. Upon comparison with the THz absorption spectrum of 11 nm CsPbBr$_3$ NC solution with 3.4 THz peak, a red-shift in the THz absorption peak is observed. There are two possible reasons for this shift. Firstly, the redshift may be due to the larger FA cation, which slightly expands the lattice, thereby reducing the vibrational frequencies. Secondly, the deposition of NCs on HDPE substrate might lead to Ostwald ripening of NCs resulting in larger-sized NCs compared to the colloidal solution.[68] Absence of the 3.7 THz feature in the THz absorption spectrum of CsPbBr$_3$ NC solution implies that the organic cation FA introduces phonon mode distribution which can affect the charge-carrier dynamics, recombination mechanisms, and the carrier-phonon coupling processes. Thus, the organic cation can modify the carrier recombination and transport properties due to polarization effects. Comparison with earlier reports of the THz absorption spectrum of FAPbI$_3$ reveals a significant blue shift in the peak THz feature, which can be explained due to Pb-Br bond being stronger than the Pb-I bond.

Chapter 2

Ultrafast Charge Carrier Dynamics in Formamidinium Lead Bromide Nanocrystal Film:
***Time-resolved Terahertz Spectroscopic Study***

2.4.2 Mechanism of charge carrier recombination

In semiconductors, upon creation of charge carriers such as electrons, holes, excitons, hot electrons, hot holes, etc., predominantly three recombination processes occur.[23] A monomolecular trap-assisted recombination is observed when carriers get trapped in trap states. This process is pump fluence independent and determined by the crystallinity of the material and inherent defects. Charge carriers mostly undergo bimolecular radiative recombination and show photoluminescence. This process is fluence dependent and governs the use of semiconductors in photovoltaic applications such as LEDs. At very high fluence leading to large charge carrier density, third-order Auger recombination becomes active. This process occurs by two carriers recombining, and the energy is transferred to a third carrier, which loses this energy via non-radiative phonon emission. This Auger process is detrimental to photovoltaic and other optoelectronic applications; however, it is not active under ambient conditions.

Compared to bulk semiconductors, NCs show a higher charge-carrier recombination rate. The multi-order recombination mechanisms in FAPbBr$_3$ NC thin film were explored using TRTS, to understand the excited state properties and to derive the material's semiconducting properties. Using THz pulses as the probe in time-resolved THz spectroscopy provides a measure of complex photoconductivity in a contactless manner. Hence, the carrier dynamics of NCs can be explored explicitly without the requirement of probes requiring physical contact. Additionally, the higher time resolutions also offer an added advantage.

2.4.3 Interaction of charge carriers with the THz probe light

In TRTS experiments, THz radiation interacts with the generated free charge carriers and the excitons by resonant and non-resonant interactions, respectively.[23] In semiconductors with considerable exciton binding energies, i.e., greater than thermal energy at room temperature (~26 meV), excitons are created upon optical transition. THz radiation, due to its low energy, is unable to promote the excitons to higher energy levels. Rather changes in the polarizability of excitons take place, which is manifested in the form of AC dielectric function.[46-47] In the case of the generation of free charge carriers, a momentum transfer, leading to acceleration, occurs due to the transfer of THz photon energies which is manifested by an increase in conductivity. Mainly free charge carriers, rather than excitons, contribute to the THz

Chapter 2

Ultrafast Charge Carrier Dynamics in Formamidinium Lead Bromide Nanocrystal Film: Time-resolved Terahertz Spectroscopic Study

conductivity, which leads to the decrease in the THz transmission in the photo-excited state.[45-46] It is also important to note that THz radiation does not differentiate between charge carriers.[45]

2.4.4 After photoexcitation: carrier dynamics from TRTS

After photoexcitation with a pump pulse, a variety of charge carriers are generated. These charge carriers undergo processes such as recombination as explained in the previous section or charge extraction to the corresponding extraction layers such as electron or hole-transporting layers. Additionally, these charge carriers also undergo coupling interactions with the phonon modes present in the system.[23] The recombination dynamics were studied by tracing the time evolution of the peak of the THz waveform transmitted through $FAPbBr_3$ NC films that were photoexcited by 45 fs pulses of 480 and 517 nm wavelengths at various fluences.

2.4.4.1 Frequency averaged dynamics or pump scan analysis

Because of the low exciton binding energy of perovskites, free charge carriers are created upon excitation, which interact with THz light.[18, 23] Figure 2.3a shows the schematic of the charge-carrier excitation by 480 and 517 nm optical pump pulses. Upon photo-excitation with 480 nm pump pulses, excess energy is provided to the created charge carriers. These charge carriers subsequently undergo recombination processes. THz pulses probe these recombination processes as the mobile charge carriers absorb low-energy THz light.[45] The photo-induced change in terahertz transmission ($-\Delta E/E_0$) at a particular delay is proportional to the complex photoconductivity of the material. The decrease in photoconductivity with increasing pump-probe delay is primarily because of the carrier recombination processes, and is dependent upon the charge carrier density and hence the excitation fluence. At 480 nm excitation, the photoinduced change in THz transmission has a strong dependence on pump fluence both in terms of maximum THz transmission and nature of their temporal evolution, as indicated by Figure 2.3b. With an increase in fluence, photoconductivity decays faster with the emergence of additional recombination channels. A significant photoconductivity exists at 1500 ps (1.5 ns). The decay profile suggests three active recombination pathways, i.e., monomolecular recombination, bimolecular recombination, and third-order recombination. When 517 nm pulses are incident, no or minimum excess energy is provided to carriers, and hence the THz transients suggest predominantly two decay channels, as suggested by the decay profiles in Figure 2.3c. The THz transients are almost fluence independent except for the lowest fluence transients. Interestingly, at the lowest fluence, a slow rise component after photo excitation is

Chapter 2

Ultrafast Charge Carrier Dynamics in Formamidinium Lead Bromide Nanocrystal Film:
Time-resolved Terahertz Spectroscopic Study

observed as shown in Figure 2.3d. We assume this growth feature to be due to carriers getting trapped in shallow trap states, which get thermally reactivated and undergo bimolecular recombination. At higher fluences, most trap-states gets saturated and hence this growth feature is not observed.
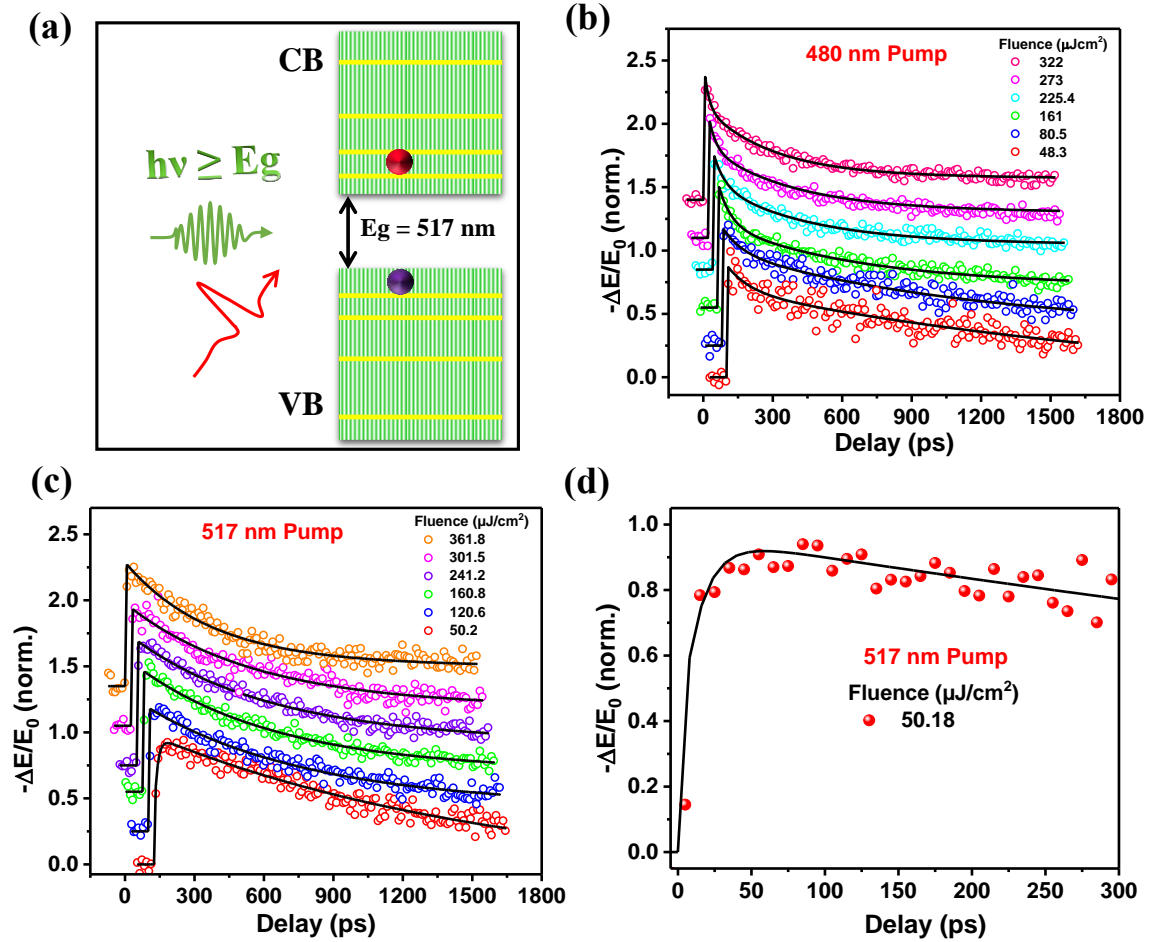
Figure 2.3. (a) Schematic of charge carrier creation upon absorption of ultrafast optical pump pulses followed by the interaction with the THz probe pulses. Fluence-dependent frequency averaged THz transmission transients as a function of pump-probe delay for FAPbBr$_3$ NC thin film upon photoexcitation with (b) 480 nm pump pulses leading to generation of charge carriers with excess energy of 185 meV, and (c) 517 nm optical pump pulses providing energy equal to the bandgap of the sample (normalized and offset along y-axis). (d) THz transient of FAPbBr$_3$ NC film at 517 nm photoexcitation and ~50 µJ/cm^2 fluence depicting a rise feature immediately after photoexcitation and the subsequent recombination of charge carriers. The symbols represent the experimental data points while the lines represent the fitted traces as discussed in the description. All the THz transients are normalized and off-set for visual clarity.

Chapter 2

Ultrafast Charge Carrier Dynamics in Formamidinium Lead Bromide Nanocrystal Film:
Time-resolved Terahertz Spectroscopic Study

By performing OPTP experiments on FAPbBr$_3$ NC thin film using THz frequency pulses as probe at different fluences, we collected the changes in differential THz transmission ($\frac{-\Delta E}{E_0}$) with time. The differential transmission is directly proportional to the charge carrier population as represented in equation 9:[39]

$$Cx(t) = n(t) \qquad (9)$$

Here, $x(t)$ is the differential transmission as a function of time, $n(t)$ is carrier density as a function of time, and C is the proportionality constant. This linear proportionality need not hold for high fluences, due to the occurrence of non-linear effects.

If we consider that the carrier density at peak photoexcitation to be n_0, and the differential transmission at peak photoexcitation to be x_0, we get the value of C as given in equation 10:

$$C = \frac{n_0}{x_0} \qquad (10)$$

A charge carrier in the material can undertake three different types of recombination pathways:[18]

- **Monomolecular recombination (trap-assisted recombination):** This process uses exactly one charge carrier. The rate of decay of charge carriers due to this process can be given by equation 11:

$$\frac{dn}{dt} = -k_1 n \qquad (11)$$

  Here, n represents the density of charge carriers, and k_1 represents the rate constant for the monomolecular recombination.

- **Bimolecular recombination:** In the process of bimolecular recombination, there is the involvement of two charge carriers. In this process, there is recombination between an electron and a hole, and it is mostly a radiative process. The rate of decay of charge carriers due to this process can be given by equation 12:

$$\frac{dn}{dt} = -k_2 n^2 \qquad (12)$$

  Here, k_2 represents the rate constant for the bimolecular recombination.

- **Auger recombination (trimolecular recombination):** In this process, three charge carriers are involved. This process consists of the recombination of an electron and a hole, followed by energy and momentum transfer to a third charge carrier (another

Chapter 2

***Ultrafast Charge Carrier Dynamics in Formamidinium Lead Bromide Nanocrystal Film:
Time-resolved Terahertz Spectroscopic Study***

electron or hole). The rate of decay of charge carriers due to this process can be given by equation 13:

$$\frac{dn}{dt} = -k_3 n^3 \qquad (13)$$

Here, k_3 represents the rate constant for the Auger recombination

Combining these 3 expressions, we get the combined rate for the reduction in charge carrier density for the sample, as given by equation 14:

$$\frac{dn}{dt} = -k_1 n - k_2 n^2 - k_3 n^3 \qquad (14)$$

Converting this equation in terms of x will give us equation 15:

$$\frac{dx}{dt} = -a_1 x - a_2 x^2 - a_3 x^3 \qquad (15)$$

Here, $a_1 = k_1$, $a_2 = Ck_2$, and $a_3 = C^2 k_3$

By globally fitting this differential equation to the time-resolved THz transients using Python to find a_1, a_2, and a_3 (allowing all three to vary), we obtained the values of k_1, k_2, and k_3, the rate constants for the three corresponding processes. The THz transmission transients carry information about the evolution of charge-carrier density over time following photoexcitation. As presented in figure 2.4, a good fit to this equation representing multi-order recombination processes is observed. The obtained rate constants are presented in Table 2.1. Upon comparing FA-based nanocrystal film with polycrystalline film, we observe faster trap-assisted recombination in NC film (*k_1* is larger). This is due to surface-activated trap states present in NCs due to dangling bonds. *k_2* shows dependence upon the nature of the cation with FA based system having a slower (10^{-9}) rate constant compared to Cs based (10^{-7}), with *k_2* being three orders of magnitude higher in FA. Thus, we can say that the organic cation stabilizes the charge carriers in the excited state compared to the Cs-based system. *k_3* shows dependence on the morphology of the system, i.e., whether it is bulk or a nano-crystalline film. *k_3* is significantly faster in the nano-crystalline film due to confined dimensions, and this leads to a faster higher-order recombination process. From the peak terahertz transients, we calculated the peak photoconductivity and the effective mobility by normalizing the photoconductivity with the charge carrier density.

Ultrafast Charge Carrier Dynamics in Formamidinium Lead Bromide Nanocrystal Film:
Time-resolved Terahertz Spectroscopic Study

Table 2.1. Comparison of recombination rate constants in different perovskite systems.

λ_{Pump} (nm)	System	k_1 (s^{-1})	k_2 (cm^{3}s^{-1})	k_3 (cm^{6}s^{-1})	Reference
480	FAPbBr$_3$ (NC film)	3.7 x 10^7	2.1 x 10^{-9}	5.5 x 10^{-27}	This work
517	FAPbBr$_3$ (NC film)	1.4 x 10^8	1.5 x 10^{-9}	7 x 10^{-28}	This work
400	FAPbBr$_3$ (thin film)	4.7 x 10^4	1.1 x 10^{-9}	1.5 x 10^{-28}	[39]
405	MAPbI$_3$ (thin film)	1.5 x 10^7	0.6 x 10^{-10}	1.6 x 10^{-28}	[40]
480	CsPbBr$_3$ (NC sol)	0.9 x 10^9	9.1x 10^{-7}	7 x 10^{-23}	[9]
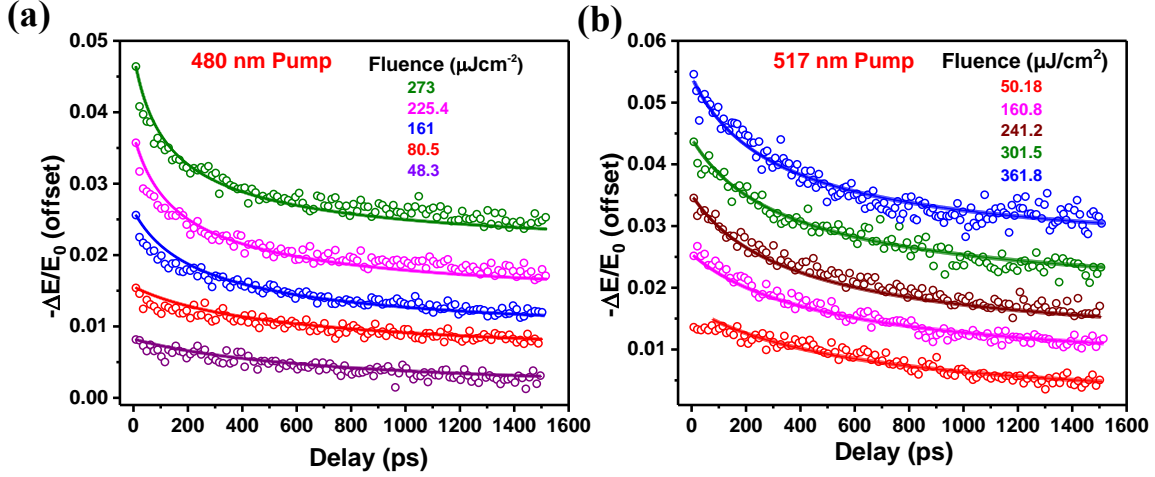
Figure 2.4. (a) THz photoconductivity transients of FAPbBr$_3$ NC film at varying fluences and excitation wavelengths of (a) 480 nm and (b) 517 nm. Symbols represent the data points and the solid lines are the fit to the kinetic equation fitted globally across all fluences.

2.4.4.2 Semiconductor properties: effective carrier mobility and diffusion length from frequency averaged TRTS

Carrier mobility and diffusion length are important figures of merit for the use of any material in optoelectronic device architectures. TRTS provides a contactless probe to obtain these parameters from the time-resolved terahertz transmission transients. The change in terahertz transmission at a particular delay is proportional to the complex photoconductivity and hence the charge carrier density (n).[9] From the peak THz transients, peak conductivity ($\Delta\sigma$) can be calculated using the following equation 16:[67]

$$\Delta\sigma(t_p) = \frac{\varepsilon_0 c}{d}(n_a + n_b)\frac{-\Delta E}{E_0} \qquad (16)$$

where ε_0 is the permittivity of free space, c is the speed of light, Δd is the thickness of the photoexcited film and n_a, n_b are the refractive indices of the media on either side of the film; $n_a = 1$ for air, and $n_b = 1.56$ for HDPE substrate. Here we assume that d << λ. The obtained

Chapter 2

Ultrafast Charge Carrier Dynamics in Formamidinium Lead Bromide Nanocrystal Film:
Time-resolved Terahertz Spectroscopic Study

peak photoconductivity ranges between 27 to 100 S/m for 480 nm, and between 36 to 94 S/cm for 517 nm excitation.

From the peak THz photo-conductivities, initial carrier mobilities are calculated by using the relation (equation 17): [9]

$$\mu = \Delta\sigma/qN_0 \qquad (17)$$

where q is the elementary charge and N_0 is the total carrier density. The initial charge density is related to the density of absorbed photons, N_{ph} by equation 18:

$$N_0 = \varphi . \ 2{*}N_{Ph} \qquad (18)$$

where φ is the photon to free carrier conversion ratio. Assuming that every photon creates 1 electron-hole pair, φ takes a value of 1. N_{ph} depends on the incident photon flux (F_l), optical density (OD), and penetration depth of the pump light (δ) as given by equation 19.

$$N_{Ph} = (F_l(1-10^{-OD_\lambda}))/\delta . \ h\nu \qquad (19)$$

$1-10^{-OD_\lambda}$ accounts for the fraction of the pump light absorbed by the thin film, $h\nu$ is the energy of single photon. The estimated charge carrier density ranges between 6×10^{17} to 4×10^{18} cm^{-3} for 480 nm, and between 1.1×10^{17} to 8×10^{17} cm^{-3} for 517 nm excitation.

The estimated initial mobility varies between 2.8 to 1.6 cm^{2}V^{-1}s^{-1} at 480 nm and 15 to 9 cm^{2}V^{-1}s^{-1} at 517 nm excitation with increase in fluence. The effective mobility at 480 nm excitation wavelength is smaller compared to 517 nm, due to significantly more scattering processes being activated because of the excess energy provided to the charge carriers. These values are slightly larger than the mobility reported for the bulk polycrystalline FAPbBr$_3$ films (14 cm^{2}V^{-1}s^{-1}).[39]

Charge carrier diffusion lengths provide a measure of the average distance covered by the photoexcited charge carriers before undergoing any recombination or scattering event. Diffusion lengths are calculated from the obtained mobilities, charge-carrier density, and the charge-carrier recombination constants from global kinetic fitting, by using the following relation in equation 20:[39]

$$L_D = \sqrt{(\mu k_B T/(k_1 + k_2 n + k_3 n^2)q)} \qquad (20)$$

where μ is mobility, k_B is the Boltzmann constant, T is temperature, k_1, k_2 and k_3 are the charge carrier recombination constants and q is the charge of the fundamental particle.

Chapter 2

Ultrafast Charge Carrier Dynamics in Formamidinium Lead Bromide Nanocrystal Film: Time-resolved Terahertz Spectroscopic Study

The obtained diffusion lengths for the as-cast FAPbBr$_3$ NC film varies between ~0.3 to 0.23 and 0.7 to 0.5 µm with increasing charge carrier densities at 480 and 517 nm pump excitations, respectively. The effective mobility and the diffusion length are limited by increasing scattering processes at 480 nm excitation. Diffusion length decreases significantly as Auger recombination (via k_3) becomes stronger. Diffusion length presents the cumulative effect of normalization of the effective mobility by the charge carrier recombination processes. A smaller diffusion length depicts reduced mobility and higher recombination rates. The calculated semiconductor properties such as effective mobility and diffusion length are comparable to polycrystalline bulk film[39] due to long-range disorder and grain boundaries present in the as-cast untreated film.

Thus, from the analysis of THz transients, semiconductor properties such as photoconductivity, mobility, and diffusion lengths can be obtained in nanocrystalline samples, where electrical contacts cannot be established. The mobility and diffusion length are comparable to bulk polycrystalline films, indicating that nanocrystal size is comparable to or higher than the exciton Bohr radius. At 480 nm excitation, due to excess energy, scattering processes are enhanced, and hence the effective mobility further decreases compared to 517 nm excitation.

2.4.4.3 Frequency resolved dynamics or probe scan analysis

Frequency dependence of THz photoconductivity reveals information about various processes affecting the charge carrier motion such as random scattering events, localization effects, or photoinduced lattice fluctuations.[45] Frequency-resolved THz spectra were obtained at different pump-probe delay times after photoexcitation to understand the nature of the charge transport in FAPbBr$_3$ NC film. Photoexcitation at 480 nm was utilized to visualize the effect of excess energy compared to no excess energy on the charge carrier transport at 517 nm. With charge carriers having excess energy available at 480 nm excitation, scattering effects can predominantly come into effect. Frequency-resolved THz conductivity spectra at both excitation wavelengths were recorded from 1 ps upto 1.5 ns after photoexcitation. Photoexcitation with high energy pulses introduces lattice fluctuations in crystals and hence can affect the charge-carrier photoconductivity. This would be reflected clearly upon comparing the frequency-resolved photoconductivity spectra with the THz absorption spectrum without photoexcitation (Figure 2.5a).

Ultrafast Charge Carrier Dynamics in Formamidinium Lead Bromide Nanocrystal Film:
Time-resolved Terahertz Spectroscopic Study
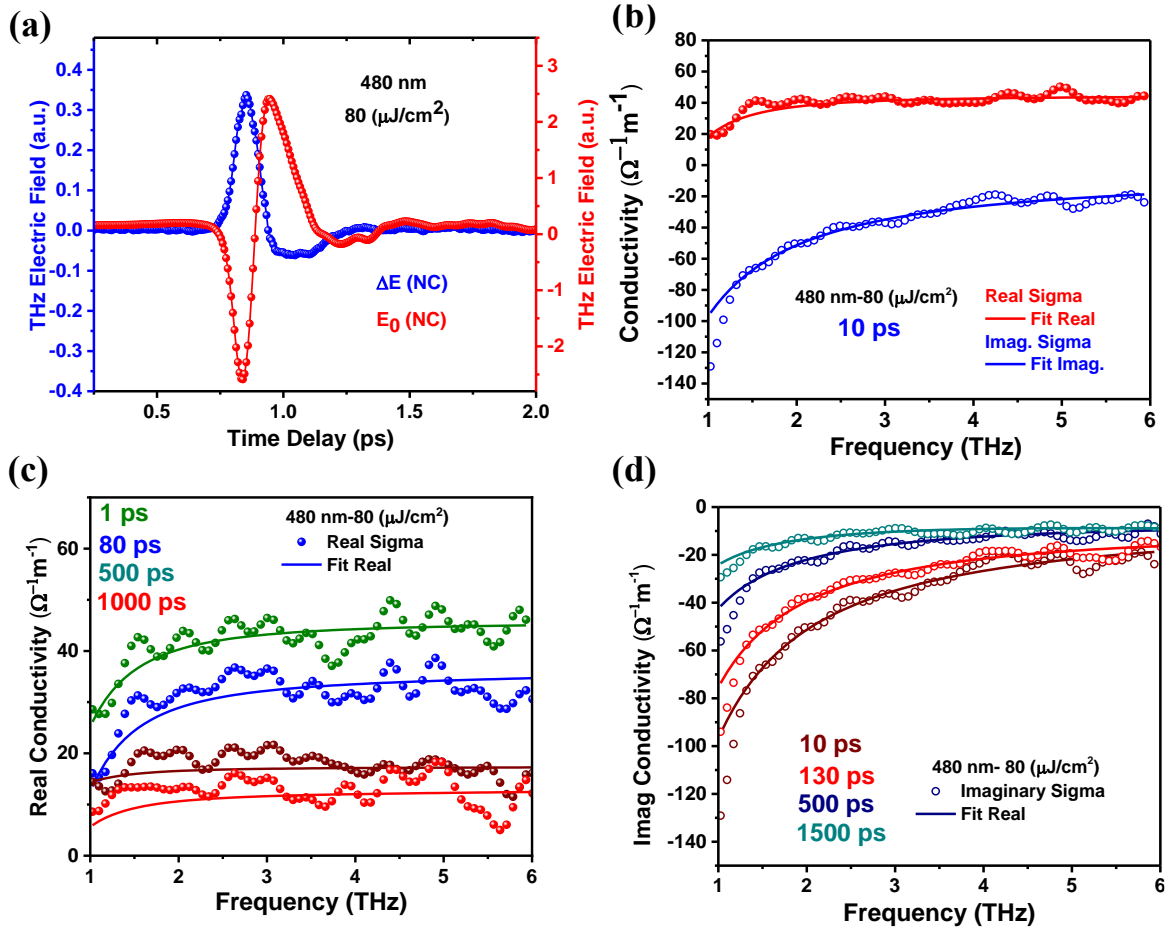
Figure 2.5. (a) THz waveforms in TRTS measurements at 480 nm pump wavelength and 80 µJcm^{-2} fluence. E_0 represents the pump-off THz signal transmitted through the FAPbBr$_3$ NC film. ΔE represents the pump-induced changes of the transmitted THz electric field. (b) Real (red symbols) and imaginary (blue symbols) conductivity spectra at 480 nm excitation, 80 µJcm^{-2} fluence, 10 ps after photo-excitation. Solid lines depict the fits to the Drude-Smith-Anderson model as discussed in the main text. Representative plots of (c) real and (d) imaginary conductivity spectra at 480 nm excitation, 80 µJcm^{-2} fluence, at various time delays after photoexcitation, respectively. Symbols represent data points while the solid lines represent the fits to Drude-Smith-Anderson (DSA) model.

Figure 2.5a represents the THz waveforms of the excited and non-excited FAPbBr$_3$ NC film at 480 nm excitation and 80 µJcm^{-2} fluence wherein E_0 represents the pump-off THz signal and ΔE represents the pump-induced changes of transmitted THz electric field. Figure 2.5b shows the photoinduced change in complex conductivity ($\Delta\sigma$) obtained from photoinduced change in THz transmission ($-\Delta E/E_0$) at 480 nm excitation and 80 µJcm^{-2} fluence. If the IR active phonon modes interact with the THz probe light, the THz beams undergo a change in amplitude due to

Chapter 2

Ultrafast Charge Carrier Dynamics in Formamidinium Lead Bromide Nanocrystal Film: Time-resolved Terahertz Spectroscopic Study

photoexcitation. Additionally, charge carriers also interact with the THz electric field as described in section 2.4.3.

As depicted in Figure 2.5b and Figure 2.5c, the real part of complex photoconductivity spectra has no significant change over a broad THz frequency range (1 to 6 THz), remaining almost constant, and decreases in the magnitude as a function of time after photoexcitation. The imaginary part of complex photoconductivity is negative and not close to zero as often seen for a Drude conductivity response (Figure 2.5d).[9] The non-Drude spectral behavior indicates that in addition to the free charge carriers, there are further processes that affect the photoconductivity spectra. The excitonic contribution can also be ruled out as the reported exciton binding energy (21.9 meV) of $FAPbBr_3$ NCs is lesser than the thermal energy available at room temperature. Thus, free-charge carriers are expected to be the majority carriers. Mechanisms such as carrier scattering from grain boundaries and crystal defects, and localization mechanisms seem to be in action as understood from the negative imaginary $\Delta\sigma$ at all time delays after photoexcitation as shown in Figure 2.5d. Interestingly, the phonon modes present in the THz absorption spectrum (Figure 2.2d) are not present in the frequency-resolved THz conductivity spectra. Hence the carrier-phonon coupling is not directly evident, as otherwise observed in other perovskite systems.[18] A complex photoconductivity behavior was observed, which is not explained by simple conductivity models such as Drude, Drude-Smith or Lorentz models that represent the photoconductivity evolution of free carriers undergoing random scattering events or resonances with phonon modes. Thus, a separate model (Drude-Smith-Anderson model) which takes into account the localization events was incorporated, which depicted the behavior of the complex conductivity spectral responses reasonably well.

The conductivity spectra are fitted to Drude-Smith-Anderson (DSA) model given by equation 21:

$$\Delta\sigma(\nu) = \frac{\sigma_0}{1\text{-}i2\pi\nu\tau}\left(1 + \frac{c_1}{1\text{-}i2\pi\nu\tau}\right) - \frac{\sigma_0 c}{1\text{-}i2\pi\nu\tau_1} \qquad (21)$$

where σ_0 is the Drude conductivity at zero frequency, c_1 is the expectation value of $\cos\theta$ (where θ is the scattering angle) ranging between 0 (free carriers) to -1 (100% backscattering), τ is the Drude scattering time, c is the effective fraction of localized carriers ranging between 0 and 1, and τ_1 is the effective Anderson backscattering time. σ_0 is given by equation 22:

$$\sigma_0 = \frac{Nq^2\tau}{m^*} = \varepsilon_0\omega_p^2\tau \qquad (22)$$

Chapter 2

Ultrafast Charge Carrier Dynamics in Formamidinium Lead Bromide Nanocrystal Film:
Time-resolved Terahertz Spectroscopic Study

where N is the charge density, q is the charge of the electron, $m*$ is the effective mass of the charge carrier, ε_0 is the permittivity of free space, and ω_p is the plasma frequency. Parameters c and τ_1 are related to the Anderson model and are given by the following expressions in equation 23:

$$c = \phi\phi_b \text{ and } \tau_1 = \phi_b\tau_b; \phi_b = \frac{\tau_d}{\tau_d+\tau_b}, \quad (23)$$

ϕ is the fraction of localized charge carriers ranging between 0 to 1, τ_b is the Anderson backscattering time ($\tau_b \gg \tau$), and τ_d is the dephasing time.
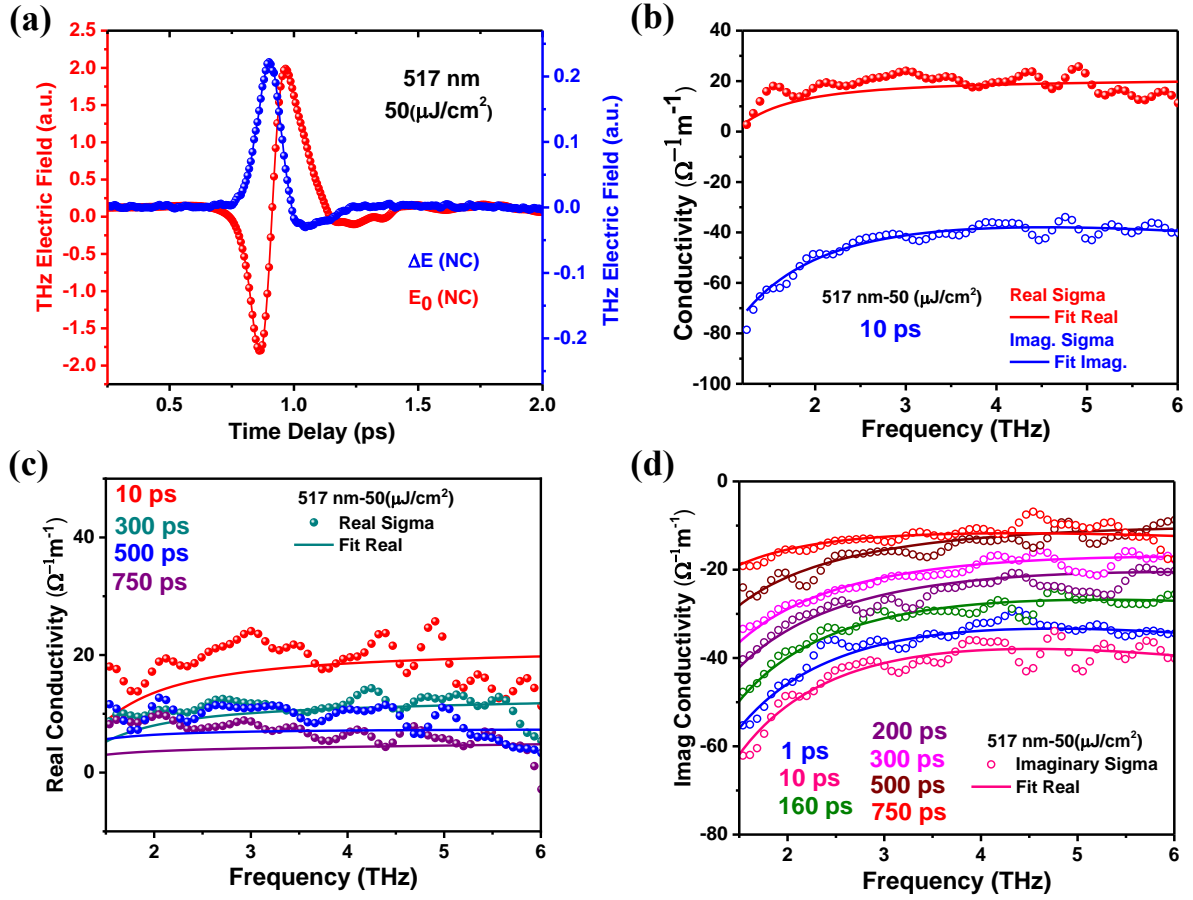
Figure 2.6. (a) THz waveforms in TRTS measurements at 517 nm pump wavelength and 50 µJcm^{-2} fluence. E_0 represents the pump-off THz signal transmitted through the FAPbBr$_3$ NC film. ΔE represents the pump-induced changes of the transmitted THz electric field. (b) Real (red symbols) and imaginary (blue symbols) conductivity spectra at 517 nm excitation, 50 µJcm^{-2} fluence, 10 ps after photo-excitation. Solid lines depict the fits to the Drude-Smith-Anderson model as discussed in the main text. Representative plots of (c) real and (d) imaginary conductivity spectra at 480 nm excitation, 50 µJcm^{-2} fluence, at various time delays after photoexcitation, respectively. Symbols represent data points while the solid lines represent the fits to the Drude-Smith-Anderson model.

Chapter 2

Ultrafast Charge Carrier Dynamics in Formamidinium Lead Bromide Nanocrystal Film: Time-resolved Terahertz Spectroscopic Study

The first part of Equation 21 represents the Drude-Smith model which accounts for carrier transport affected by the disorders or back-scattering due to grain boundaries.[73] In most cases, only the first backscattering is significant and the higher-order scattering events can be neglected, which is why only first-order Smith correction is considered. Photoinduced lattice fluctuations in the perovskite film induce electrostatic potentials which can cause backscattering after many scattering events which is also known as Anderson backscattering, with Anderson backscattering time(τ_1) being much greater than Drude scattering time(τ).[74] This induces localized electronic states near the band edges.[75] The localized states are created by the electron wavefunctions destructively interfering with themselves after each scattering event which creates wave functions that decay exponentially over the lattice. Both real and imaginary spectra were simultaneously fit to the DSA model over the broad THz frequency range. A good match of the fitted curves to our experimental photoconductivity spectra was obtained. Thus, photoinduced THz conductivity spectra exhibit clear localization effects at 480 nm excitation, thereby creating carriers with excess energy of ~185 meV.

Similar photoconductivity behavior was observed upon photoexcitation of FAPbBr$_3$ NC film with 517 nm wavelength at 50 µJcm^{-2} fluence as depicted in Figure 2.6. Figure 2.6a depicts the typical THz waveforms in TRTS measurements at 517 nm pump wavelength and 50 µJcm^{-2} fluence where E$_0$ represents the pump-off THz signal transmitted through the FAPbBr$_3$ NC film and ΔE represents the pump-induced changes of transmitted THz electric field. As seen in Figure 2.6b, compared to Figure 2.5b, the magnitude of both real and imaginary parts of photoconductivity are decreased while the temporal evolution of the spectral response is similar. But even after 1.5 ns, conductivity does not reach zero as was also observed in the frequency averaged THz transients in Figure 2.4. We do not observe any phonon features in the complex THz conductivity spectra upon excitation with 517 nm as well.

Upon normalizing the complex conductivity spectra with the charge carrier density by using the equation $\varphi\mu \cong \Delta\sigma/qn$, frequency-dependent mobility plots were obtained as shown in Figure 2.7. Upon comparing the frequency-dependent mobility plots at 480 nm excitation and 80 µJcm^{-2} fluence at 10, 160, and 300 ps after photoexcitation as shown in Figure 2.7a, a decrease in the real part of spectra is observed while the imaginary part shows a complex behavior. The low-frequency part decreases with increasing time delay while the high-frequency part remains almost constant. For 517 nm excitation and 50 µJcm^{-2} fluence at 10, 160, and 300 ps after photoexcitation, opposite behavior is observed in both real and imaginary

Chapter 2

Ultrafast Charge Carrier Dynamics in Formamidinium Lead Bromide Nanocrystal Film:
Time-resolved Terahertz Spectroscopic Study

photoconductivity spectra as depicted in Figure 2.7b. Almost no change in the real part of the mobility spectra is observed while the imaginary part undergoes a steady decrease with time after photoexcitation. This difference might be arising due to different natures of charge carriers being created at these two different excitation wavelengths. At 480 nm, the free carriers might be present predominantly while at 517 nm, carriers with columbic interaction might be prevalent.
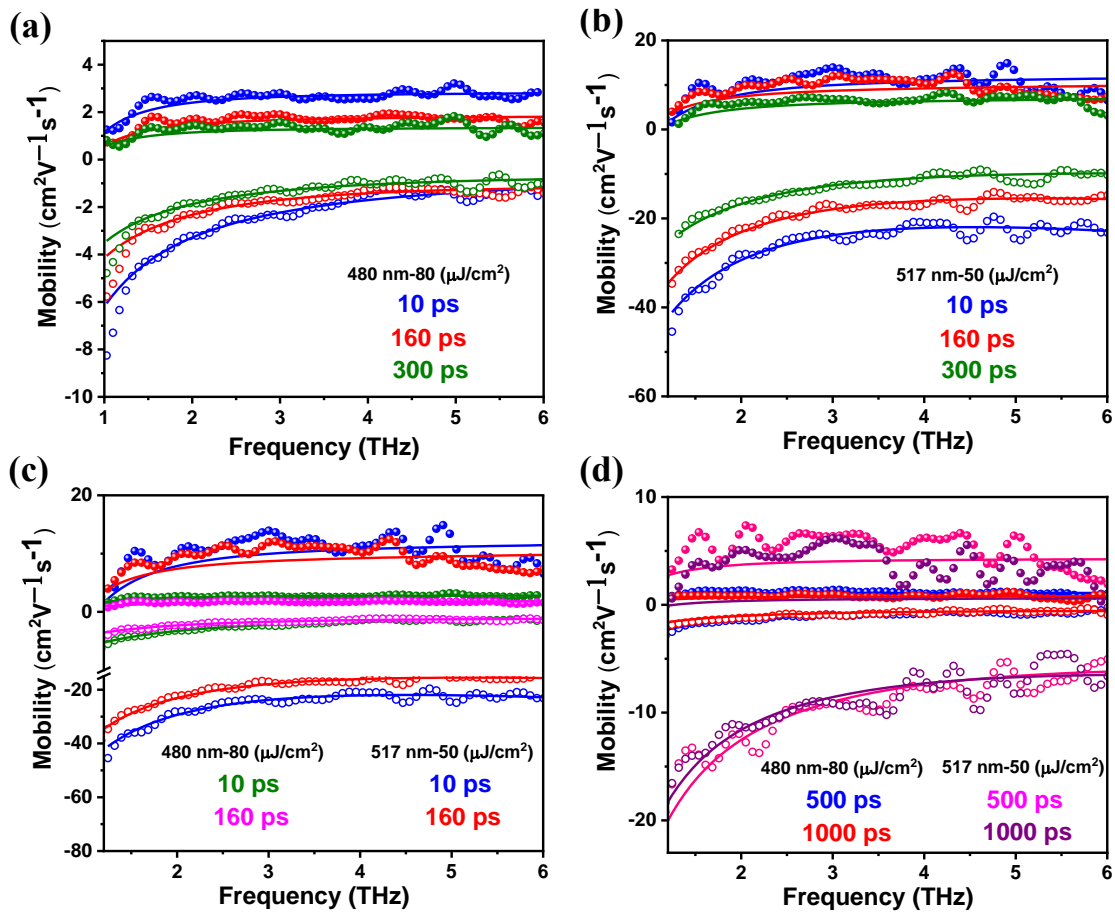
Figure 2.7. Mobility plots of the FAPbBr$_3$ NC thin film at (a) 480 nm excitation and 80 µJcm^{-2} fluence at 10, 160, and 300 ps after photoexcitation. (b) 517 nm excitation and 50 µJcm^{-2} fluence at 10, 160 and 300 ps after photoexcitation. (c) Comparison of mobility plots at 480 and 517 nm excitation at 10 and 160 ps. (d) Comparison of mobility plots at 480 and 517 nm excitation at 500 and 1000 ps. Filled circles represent the real mobilities while hollow circles depict imaginary mobilities in all the above plots.

Figure 2.7c compares the mobility spectra for 480 and 517 nm excitation at the pump-probe delay of 10 and 160 ps, a clear decrease in the mobility is observed with mobility values

Chapter 2

Ultrafast Charge Carrier Dynamics in Formamidinium Lead Bromide Nanocrystal Film:
Time-resolved Terahertz Spectroscopic Study

significantly lower at 480 nm (~ 2 cm^{2}V^{-1}s^{-1}) as compared to 517 nm (~ 20 cm^{2}V^{-1}s^{-1}). We expect this decrease to be due to increased scattering processes with charge carriers having excess energy at 480 nm. This is also reflected in the decreased Drude scattering time at 480 nm as compared to 517 nm excitation, as given in Table 2.2 and Table 2.3. Similarly, the Anderson localization time (τ_1) and effective fraction of localized carriers (c) are also almost doubled at 517 nm compared to 480 nm excitation at 10 ps. Effective mobility obtained from the frequency-averaged THz transients also show a similar trend at 480 and 517 nm pump wavelengths. At 500 ps after photoexcitation, the real and imaginary spectra do not undergo any visible changes in magnitude as is evident in Figure 2.7d. Interestingly, at both 480 and 517 nm, the mobility values do not decrease to zero; rather, a constant value is reached which is retained until 1500 ps. The same is also observed in the frequency-averaged transients shown in Figure 2.4. This indicates a long lifetime of charge carriers, which is outside our experimental window, and also the presence of minimal mid-gap trap states. The presence of Anderson localization in a system suggests a coexistence of band-like and hopping transport in the system. Anderson localization also drastically decreases diffusion length in the system, as was also observed for FAPbBr$_3$ NC thin film discussed in section 2.4.4.2.

Table 2.2. Drude-Smith-Anderson model fitting parameters for different time delays after photoexcitation by 480 nm pump pulses at 80 µJcm^{-2} fluence.

Time delay (ps)	σ_0	τ (fs)	c_1	c	τ_1 (ps)
1	344	0.1	-0.87	1	0.63
3	331	0.1	-0.85	1	0.56
10	446	0.1	-0.9	0.56	0.58
40	422	0.3	-0.91	1	0.82
80	393	0.4	-0.91	0.97	0.73
130	443	0.2	-0.94	0.98	0.78
160	318	0.7	-0.91	0.73	0.51
300	285	0.4	-0.93	0.87	0.73
500	745	0.1	-0.97	0.79	2.22
1000	554	0.1	-0.98	1	2.45
1500	1316	0.1	-0.99	0.65	5.71

Chapter 2

Ultrafast Charge Carrier Dynamics in Formamidinium Lead Bromide Nanocrystal Film:
Time-resolved Terahertz Spectroscopic Study

Mobility for a system with localized states is given by equation 24:[76]

$$\mu = \mu_0 \frac{\tau_{free}}{\tau_{trapped}} \qquad (24)$$

Here, μ is the effective mobility, μ_0 is the mobility without localization, τ_{free} is the time spent by the charge carriers in free states while $\tau_{trapped}$ is the time spent by the charge carriers in localized states.[77] As carriers spend more time in trapped states than in free states, Anderson localization reduces the mobility of charge carriers in the system. This accounts for the discrepancy of observed effective mobility values obtained here for $FAPbBr_3$ NC thin film and the earlier reports.

Table 2.3. Drude-Smith-Anderson model fitting parameters for different time delays after photoexcitation by 517 nm pump pulses at 50 μJcm^{-2} fluence.

Time delay ps	σ_0	τ (fs)	c_1	c	τ_1 (ps)
1	876	0.7	-0.98	0.27	0.49
3	1377	0.4	-0.98	0.17	0.49
10	2491	0.3	-0.99	0.11	0.58
40	1081	0.5	-0.98	0.30	0.61
80	933	0.7	-0.98	0.24	0.512
130	921	0.6	-0.98	0.29	0.68
160	636	0.7	-0.97	0.5	0.74
200	580	0.5	-0.97	0.34	0.49
300	301	0.8	-0.96	0.64	0.6
400	1670	0.1	-1	0.34	2.08
500	1044	0.1	-1	0.41	1.69
750	1593	0.1	-1	0.68	6.08
1000	823	0.1	-1	1	2.15
1250	3523	0.1	-1	1	22.90
1500	3411	0.1	-1	0.54	10.62

The correlations between different DSA model parameters are complex. We have used Spearman Rank Correlation Coefficient to quantify the observed trends in the probe scan data by considering parameters for time-delays between 10 to 300 ps. The spearman rank correlation coefficient is given in equation 25 as:[78]

Chapter 2

Ultrafast Charge Carrier Dynamics in Formamidinium Lead Bromide Nanocrystal Film:
Time-resolved Terahertz Spectroscopic Study

$$\rho = 1 - \frac{6 \sum_{i=1}^{n} d_i^2}{n(n^2-1)} \qquad (25)$$

Here, ρ is the spearman rank correlation coefficient, d_i is the difference between the ranks of the ith x and y values and n is the total number of x and y values. The values of ρ always lie between -1 and 1 (with positive values meaning a positive correlation, and negative values implying a negative correlation). Generally, the following convention is used while interpreting the values of ρ:

Grading Standards	Correlation degree
$\rho = 0$	No correlation
$0 < |\rho| \leq 0.19$	Very weak correlation
$0.20 \leq |\rho| \leq 0.39$	Weak correlation
$0.40 \leq |\rho| \leq 0.59$	Moderate correlation
$0.60 \leq |\rho| \leq 0.79$	Strong correlation
$0.80 \leq |\rho| \leq 1.00$	Very strong correlation
$|\rho| = 1$	Monotonic correlation

The correlations obtained using the Spearman Rank Correlation Coefficients are presented in Table 2.4 and Table 2.5 for 480 nm and 517 nm, respectively.

Table 2.4: Correlation coefficients between parameters of DSA model for 480 nm excitation.

480 nm	time	σ_0	τ	c_1	c	τ_1
time		-0.82857	0.6	-0.71429	-0.25714	-0.14286
σ_0	-0.82857		-0.82857	0.37143	0.25714	0.31429
τ	0.6	-0.82857		-0.2	-0.31429	-0.37143
c_1	-0.71429	0.37143	-0.2		-0.25714	-0.48571
c	-0.25714	0.25714	-0.31429	-0.25714		0.94286
τ_1	-0.14286	0.31429	-0.37143	-0.48571	0.94286	

Table 2.5: Correlation coefficients between parameters of DSA model for 517 nm excitation.

517 nm	time	σ_0	τ	c_1	c	τ_1
time		-1	0.67857	0.82143	0.85714	0.28571
σ_0	-1		-0.67857	-0.82143	-0.85714	-0.28571
τ	0.67857	-0.67857		0.60714	0.53571	0.17857
c_1	0.82143	-0.82143	0.60714		0.96429	0.32143
c	0.85714	-0.85714	0.53571	0.96429		0.5
τ_1	0.28571	-0.28571	0.17857	0.32143	0.5	

Chapter 2

Ultrafast Charge Carrier Dynamics in Formamidinium Lead Bromide Nanocrystal Film:
Time-resolved Terahertz Spectroscopic Study

2.4.4.5 Mechanistic understanding from correlation parameters

For clear visualization, correlation plots were drawn to understand the correlation effects as given in Figures 2.8a and 2.8b. At both photoexcitations, a very strong negative correlation is seen between delay time and σ_0, which means that σ_0 decreases with time in both cases. The reason for this decrease is due to the gradual reduction in carrier density over time due to various recombination processes. Additionally, σ_0 shows a strong negative correlation with τ. As the number of carriers decreases, the scattering events decrease, and hence an increase in scattering time with increasing delay. Combining these two correlations, we also conclude that τ (Drude scattering time) should show a strong positive correlation with pump-probe delay (time), which means that τ increases with time in both cases, as evident from the correlation values presented in Tables 2.4 and 2.5. This is also reflected in the real photoconductivity spectra becoming more curved at longer delays (500 ps and above) as compared to almost a straight line at earlier delay times.

For 480 nm excitation, c_1 shows a strong negative correlation with time as seen in Figure 2.8.a. In contrast, for 517 nm excitation, c_1 shows a very strong positive correlation with time as seen in Figure 2.8.b. This means that amount of Smith backscattering increases with time for 480 nm excitation (as c_1 = -1 means the highest Smith backscattering while c_1 = 0 means no backscattering), while it decreases with time for 517 nm excitation. This behavior of charge carriers may be explained as follows. For 480 nm excitation, the charge carriers after colliding among themselves and equilibrating, suffer more backscattering processes as they emerge out of a multi-body collision situation. On the contrary, for 517 nm excitation, charge carriers are created at the band-edge and might have significant electrostatic interactions among themselves. Thus, as the charge carriers recombine over time, the scattering events with the grain boundaries and defects also decrease.

Upon 480 nm photoexcitation, there is a very strong positive correlation between τ_1 and c, while in 517 nm, there is a moderate positive correlation between τ_1 and c. This means that as the amount of Anderson localization increases, the Anderson backscattering time also increases. This observation points towards the depth of the localization potential well. At 480 nm photoexcitation, the carriers get deeply trapped in the localization potential well, thereby increasing the backscattering time, while at 517 nm photoexcitation, the depth of the localization potential well seems moderate.

Ultrafast Charge Carrier Dynamics in Formamidinium Lead Bromide Nanocrystal Film:
Time-resolved Terahertz Spectroscopic Study

Upon 517 nm photoexcitation, there is a strong positive correlation between c_1 and c implying that the backscattering due to Anderson localization decreases with an increase in Drude-Smith backscattering, and vice-versa. This observation is understandable, as when the carriers get localized due to the photoinduced lattice fluctuations, the probability of their backscattering from the grain boundaries decreases significantly. Additionally, at 517 nm photoexcitation, a moderate positive correlation was seen between τ and c_1 which translates into an increase in the Drude scattering time with an increase in Smith backscattering. A very weak correlation between c and c_1 was observed at 480 nm photoexcitation. We suppose this behavior can arise if the backscattering and localization processes are decoupled at 480 nm photoexcitation. The localized carriers have a different fate as compared to the backscattered carriers. These observations clearly indicate to a difference in the nature of excited states created at different photoexcitations.
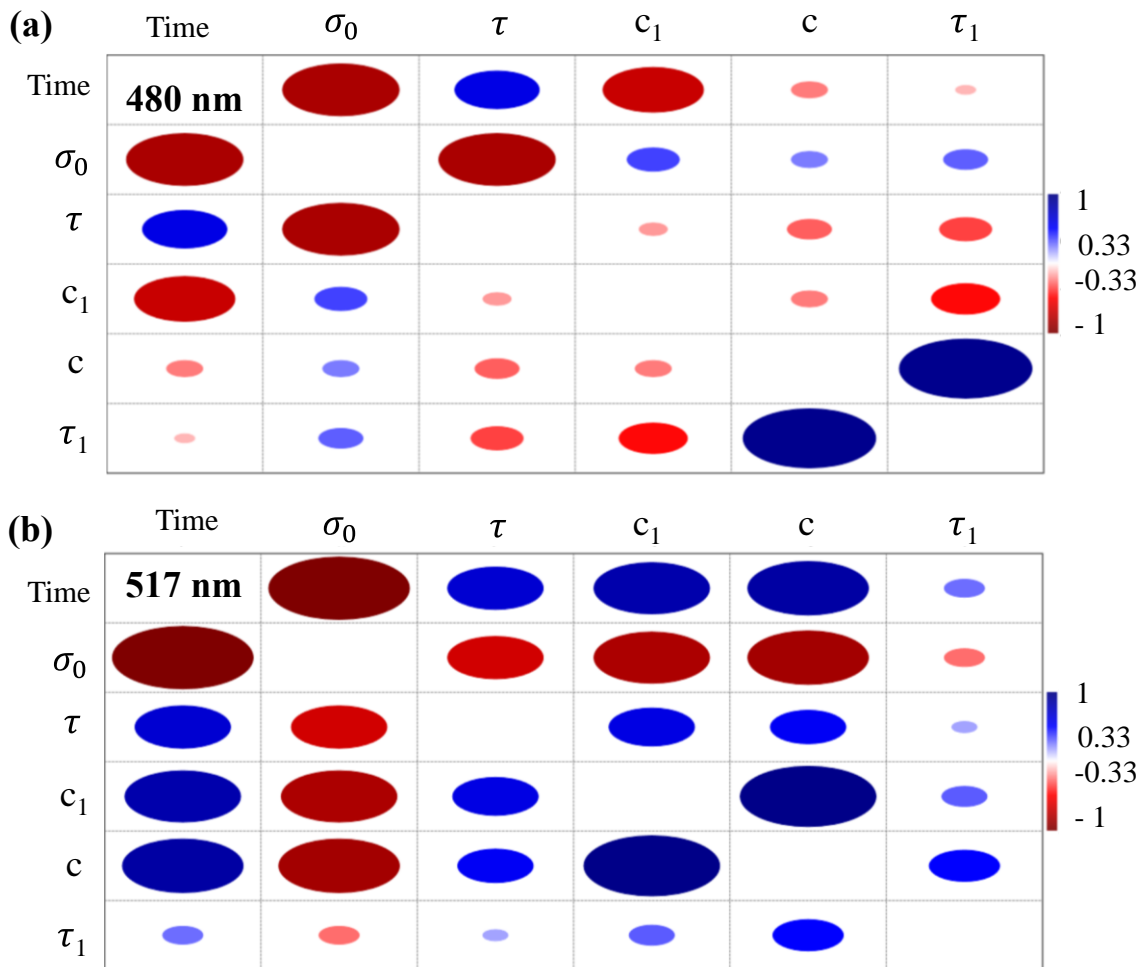
Figure 2.8: The correlation plot between the parameters of DSA model fitted to photoconductivity spectra at (a) 480 nm and (b) 517 nm excitations.

Chapter 2

***Ultrafast Charge Carrier Dynamics in Formamidinium Lead Bromide Nanocrystal Film:
Time-resolved Terahertz Spectroscopic Study***

At 517 nm photoexcitation, there is a very strong positive correlation between delay time and c. This means that at band edge excitation, the amount of Anderson backscattering increases with time. This indicates that rather than undergoing recombination processes after photogeneration immediately, the carriers are trapped in the photoinduced lattice fluctuations and get stabilized in the excited state. This explains a rather long-lived carrier lifetime as also observed from the global kinetic fitting of frequency-averaged THz transients discussed earlier. This behavior is evident probably because of the dynamic nature of the formamidinium cation present in the void of the lattice, in addition to the fluctuations of the lead halide framework.

2.5 Conclusion

In conclusion, we have performed TRTS experiment on $FAPbBr_3$ NC thin films by photoexcitation at 480 nm and 517 nm to understand the carrier dynamics, recombination mechanisms, and determine the carrier transport properties. We used the Drude-Smith-Anderson model to model the behavior of carrier transport and carrier lattice interactions. We unravel the mechanism for decreased carrier mobility at 480 nm photoexcitation. A slower rate of bimolecular recombination as compared to an all-inorganic counterpart is ascribed to the dynamic motion of formamidinium cation temporarily stabilizing the charge carriers in the excited state. The signature of cation motion that can couple with carrier generation and recombination thereby creating long-lived charge carriers was detected in the steady state THz absorption spectrum. In addition to the backscattering events from the grain boundaries and defects, photoinduced lattice fluctuations also act as a significant source of backscattering events. These backscattering processes are expected to slow down the recombination processes as evident from our observations. Conversely, these backscattering processes introduced by grain boundaries, defects, and photoinduced lattice fluctuations also decrease the mobilities to moderate values and limit the diffusion length to sub-micrometer levels. Additionally, from our detailed global analysis, we predict the different nature of excited states created at different photoexcitation wavelengths. Thus, understanding the interaction of charge carriers with not only the barriers and defects but also the changes in the lattice vibrations introduced due to photoexcitation will guide us into the material engineering of more efficient photovoltaic perovskites.

Chapter 2

Ultrafast Charge Carrier Dynamics in Formamidinium Lead Bromide Nanocrystal Film:
Time-resolved Terahertz Spectroscopic Study

2.6 References

1. Weidman, M. C.; Goodman, A. J.; Tisdale, W. A., Colloidal Halide Perovskite Nanoplatelets: An Exciting New Class of Semiconductor Nanomaterials. *Chem. Mater.* **2017**, *29*, 5019-5030.

2. Eperon, G. E.; Ginger, D. S., B-Site Metal Cation Exchange in Halide Perovskites. *ACS Energy Lett.* **2017**, *2*, 1190-1196.

3. Kojima, A.; Teshima, K.; Shirai, Y.; Miyasaka, T., Organometal Halide Perovskites as Visible-Light Sensitizers for Photovoltaic Cells. *J. Am. Chem. Soc.* **2009**, *131*, 6050-6051.

4. Lee, M. M.; Teuscher, J.; Miyasaka, T.; Murakami, T. N.; Snaith, H. J., Efficient Hybrid Solar Cells Based on Meso-Superstructured Organometal Halide Perovskites. *Science* **2012**, *338*, 643-647.

5. Etgar, L.; Gao, P.; Xue, Z.; Peng, Q.; Chandiran, A. K.; Liu, B.; Nazeeruddin, M. K.; Grätzel, M., Mesoscopic CH_3NH_3PbI/TiO_2 Heterojunction Solar Cells. *J. Am. Chem. Soc.* **2012**, *134*, 17396-17399.

6. Swarnkar, A.; Chulliyil, R.; Ravi, V. K.; Irfanullah, M.; Chowdhury, A.; Nag, A., Colloidal $CsPbBr_3$ Perovskite Nanocrystals: Luminescence Beyond Traditional Quantum Dots. *Angew. Chem. Int. Ed.* **2015**, *54*, 15424-15428.

7. Protesescu, L.; Yakunin, S.; Bodnarchuk, M. I.; Krieg, F.; Caputo, R.; Hendon, C. H.; Yang, R. X.; Walsh, A.; Kovalenko, M. V., Nanocrystals of Cesium Lead Halide Perovskites ($CsPbX_3$, X = Cl, Br, and I): Novel Optoelectronic Materials Showing Bright Emission with Wide Color Gamut. *Nano Lett.* **2015**, *15*, 3692-3696.

8. Cao, D. H.; Stoumpos, C. C.; Farha, O. K.; Hupp, J. T.; Kanatzidis, M. G., 2D Homologous Perovskites as Light-Absorbing Materials for Solar Cell Applications. *J. Am. Chem. Soc.* **2015**, *137*, 7843-7850.

9. Yettapu, G. R.; Talukdar, D.; Sarkar, S.; Swarnkar, A.; Nag, A.; Ghosh, P.; Mandal, P., Terahertz Conductivity within Colloidal $CsPbBr_3$ Perovskite Nanocrystals: Remarkably High Carrier Mobilities and Large Diffusion Lengths. *Nano Lett.* **2016**, *16*, 4838-4848.

10. Sarkar, S.; Ravi, V. K.; Banerjee, S.; Yettapu, G. R.; Markad, G. B.; Nag, A.; Mandal, P., Terahertz Spectroscopic Probe of Hot Electron and Hole Transfer from Colloidal $CsPbBr_3$ Perovskite Nanocrystals. *Nano Lett.* **2017**, *17*, 5402-5407.

11. Kovalenko, M. V.; Protesescu, L.; Bodnarchuk, M. I., Properties and Potential Optoelectronic Applications of Lead Halide Perovskite Nanocrystals. *Science* **2017**, *358*, 745.

Chapter 2

Ultrafast Charge Carrier Dynamics in Formamidinium Lead Bromide Nanocrystal Film:
Time-resolved Terahertz Spectroscopic Study

12. Akkerman, Q. A.; Rainò, G.; Kovalenko, M. V.; Manna, L., Genesis, Challenges and Opportunities for Colloidal Lead Halide Perovskite Nanocrystals. *Nat. Mater.* **2018**, *17*, 394-405.

13. Dey, A., et al., State of the Art and Prospects for Halide Perovskite Nanocrystals. *ACS Nano* **2021**, *15*, 10775-10981.

14. Green, M. A.; Ho-Baillie, A.; Snaith, H. J., The Emergence of Perovskite Solar Cells. *Nat. Photon.* **2014**, *8*, 506-514.

15. Gao, P.; Grätzel, M.; Nazeeruddin, M. K., Organohalide Lead Perovskites for Photovoltaic Applications. *Energy Environ. Sci.* **2014**, *7*, 2448-2463.

16. Grätzel, M., The Light and Shade of Perovskite Solar Cells. *Nat. Mater.* **2014**, *13*, 838-842.

17. Yusoff, A. R. b. M.; Nazeeruddin, M. K., Organohalide Lead Perovskites for Photovoltaic Applications. *J. Phys. Chem. Lett.* **2016**, *7*, 851-866.

18. Johnston, M. B.; Herz, L. M., Hybrid Perovskites for Photovoltaics: Charge-Carrier Recombination, Diffusion, and Radiative Efficiencies. *Acc. Chem. Res.* **2016**, *49*, 146-154.

19. deQuilettes, D. W.; Frohna, K.; Emin, D.; Kirchartz, T.; Bulovic, V.; Ginger, D. S.; Stranks, S. D., Charge-Carrier Recombination in Halide Perovskites. *Chem. Rev.* **2019**, *119*, 11007-11019.

20. Zhu, X. Y.; Podzorov, V., Charge Carriers in Hybrid Organic-Inorganic Lead Halide Perovskites Might Be Protected as Large Polarons. *J. Phys. Chem. Lett.* **2015**, *6*, 4758-4761.

21. Miyata, K.; Meggiolaro, D.; Trinh, M. T.; Joshi, P. P.; Mosconi, E.; Jones, S. C.; De Angelis, F.; Zhu, X. Y., Large Polarons in Lead Halide Perovskites. *Sci. Adv.* **2017,** *3*, e1701217.

22. Ghosh, D.; Welch, E.; Neukirch, A. J.; Zakhidov, A.; Tretiak, S., Polarons in Halide Perovskites: A Perspective. *J. Phys. Chem. Lett.* **2020**, *11*, 3271-3286.

23. Herz, L. M., Charge-Carrier Dynamics in Organic-Inorganic Metal Halide Perovskites. *Annu. Rev. Phys. Chem.* **2016**, *67*, 65-89.

24. Brenner, T. M.; Egger, D. A.; Kronik, L.; Hodes, G.; Cahen, D., Hybrid Organic—Inorganic Perovskites: Low-Cost Semiconductors with Intriguing Charge-Transport Properties. *Nat. Rev. Mater.* **2016**, *1*, 15007.

25. Chen, Y.; Yi, H. T.; Wu, X.; Haroldson, R.; Gartstein, Y. N.; Rodionov, Y. I.; Tikhonov, K. S.; Zakhidov, A.; Zhu, X. Y.; Podzorov, V., Extended Carrier Lifetimes and Diffusion in

Chapter 2

***Ultrafast Charge Carrier Dynamics in Formamidinium Lead Bromide Nanocrystal Film:
Time-resolved Terahertz Spectroscopic Study***

Hybrid Perovskites Revealed by Hall Effect and Photoconductivity Measurements. *Nat. Commun.* **2016**, *7*, 12253.

26. Yu, B.; Zhang, C.; Chen, L.; Qin, Z.; Huang, X.; Wang, X.; Xiao, M., Ultrafast Dynamics of Photoexcited Carriers in Perovskite Semiconductor Nanocrystals. **2020**, *10*, 1943-1965.

27. Gao, W.; Ding, J.; Bai, Z.; Qi, Y.; Wang, Y.; Lv, Z., Multiple Excitons Dynamics of Lead Halide Perovskite. *nanophotonics,* **2021**, *10*, 3945-3955.

28. Kao, T. S.; Chou, Y.-H.; Chou, C.-H.; Chen, F.-C.; Lu, T.-C., Lasing Behaviors Upon Phase Transition in Solution-Processed Perovskite Thin Films. *Appl. Phys. Lett.* **2014**, *105*, 231108.

29. Shao, Z.; You, S.; Guo, X.; Xiao, J.; Liu, J.; Song, F.; Xie, H.; Sun, J.; Huang, H., Temperature-Dependent Photoluminescence of Co-Evaporated MaPbI$_3$ Ultrathin Films. *Results Phys.* **2022**, *34*, 105326.

30. Park, M.; Neukirch, A. J.; Reyes-Lillo, S. E.; Lai, M.; Ellis, S. R.; Dietze, D.; Neaton, J. B.; Yang, P.; Tretiak, S.; Mathies, R. A., Excited-State Vibrational Dynamics toward the Polaron in Methylammonium Lead Iodide Perovskite. *Nat. Commun.* **2018**, *9*, 2525.

31. Nishida, J.; Breen, J. P.; Lindquist, K. P.; Umeyama, D.; Karunadasa, H. I.; Fayer, M. D., Dynamically Disordered Lattice in a Layered Pb-I-Scn Perovskite Thin Film Probed by Two-Dimensional Infrared Spectroscopy. *J. Am. Chem. Soc.* **2018**, *140*, 9882-9890.

32. Xing, X.; Li, J.; Breen, J. P.; Nishida, J.; Karunadasa, H. I.; Fayer, M. D., Probing Lattice Dynamics in Two-Dimensional Inorganic Pseudohalide Perovskites with Ultrafast Infrared Spectroscopy. *J. Phys. Chem. C* **2022**, *126*, 10145-10158.

33. Richter, J. M.; Branchi, F.; Valduga de Almeida Camargo, F.; Zhao, B.; Friend, R. H.; Cerullo, G.; Deschler, F., Ultrafast Carrier Thermalization in Lead Iodide Perovskite Probed with Two-Dimensional Electronic Spectroscopy. *Nat. Commun.* **2017**, *8*, 376.

34. Nguyen, X. T.; Winte, K.; Timmer, D.; Rakita, Y.; Cahen, D.; Lorke, M.; Jahnke, F.; Lienau, C.; De Sio, A. In Ultrafast Two-Dimensional Electronic Spectroscopy Reveals Phonon-Driven Exciton Rabi Oscillations in Halide Perovskites, The International Conference on Ultrafast Phenomena (UP) 2022, Montreal, Quebec, 2022/07/18; Légaré, F. T. T. B. J. B. T.; Dudovich, N., Eds. Optica Publishing Group: Montreal, Quebec, 2022; p Th3A.3.

35. Wang, L.; McCleese, C.; Kovalsky, A.; Zhao, Y.; Burda, C., Femtosecond Time-Resolved Transient Absorption Spectroscopy of CH$_3$NH$_3$PbI$_3$ Perovskite Films: Evidence for Passivation Effect of PbI$_2$. *J. Am. Chem. Soc.* **2014**, *136*, 12205-12208.

Chapter 2

Ultrafast Charge Carrier Dynamics in Formamidinium Lead Bromide Nanocrystal Film:
Time-resolved Terahertz Spectroscopic Study

36. Chang, Q.; Bao, D.; Chen, B.; Hu, H.; Chen, X.; Sun, H.; Lam, Y. M.; Zhu, J.-X.; Zhao, D.; Chia, E. E. M., Tracking Carrier and Exciton Dynamics in Mixed-Cation Lead Mixed-Halide Perovskite Thin Films. *Commun. Phys.* **2022**, *5*, 187.

37. Maehrlein, S. F., et al., Decoding Ultrafast Polarization Responses in Lead Halide Perovskites by the Two-Dimensional Optical Kerr Effect. *Proc. Natl. Acad. Sci.* **2021**, *118*, e2022268118.

38. Wehrenfennig, C.; Eperon, G. E.; Johnston, M. B.; Snaith, H. J.; Herz, L. M., High Charge Carrier Mobilities and Lifetimes in Organolead Trihalide Perovskites. *Adv. Mater.* **2014**, *26*, 1584-1589.

39. Rehman, W.; Milot, R. L.; Eperon, G. E.; Wehrenfennig, C.; Boland, J. L.; Snaith, H. J.; Johnston, M. B.; Herz, L. M., Charge-Carrier Dynamics and Mobilities in Formamidinium Lead Mixed-Halide Perovskites. *Adv. Mater.* **2015**, *27*, 7938-7944.

40. Milot, R. L.; Eperon, G. E.; Snaith, H. J.; Johnston, M. B.; Herz, L. M., Temperature-Dependent Charge-Carrier Dynamics in $CH_3NH_3PbI_3$ Perovskite Thin Films. *Adv. Funct. Mater.* **2015**, *25*, 6218-6227.

41. Bretschneider, S. A.; Ivanov, I.; Wang, H. I.; Miyata, K.; Zhu, X.; Bonn, M., Quantifying Polaron Formation and Charge Carrier Cooling in Lead-Iodide Perovskites. *Adv. Mater.* **2018**, *30*, 1707312.

42. Zhao, D.; Chia, E. E. M., Free Carrier, Exciton, and Phonon Dynamics in Lead-Halide Perovskites Studied with Ultrafast Terahertz Spectroscopy. *Adv. Opt. Mater.* **2020**, *8*, 1900783.

43. Beard, M. C.; Turner, G. M.; Schmuttenmaer, C. A., Terahertz Spectroscopy. *J. Phys. Chem. B* **2002**, *106*, 7146-7159.

44. Neu, J.; Schmuttenmaer, C. A., Tutorial: An Introduction to Terahertz Time Domain Spectroscopy (Thz-Tds). *J. Appl. Phys.* **2018**, *124*, 231101.

45. Spies, J. A.; Neu, J.; Tayvah, U. T.; Capobianco, M. D.; Pattengale, B.; Ostresh, S.; Schmuttenmaer, C. A., Terahertz Spectroscopy of Emerging Materials. *J. Phys. Chem. C* **2020**, *124*, 22335-22346.

46. Schmuttenmaer, C. A., Exploring Dynamics in the Far-Infrared with Terahertz Spectroscopy. *Chem. Rev.* **2004**, *104*, 1759-1780.

47. Ulbricht, R.; Hendry, E.; Shan, J.; Heinz, T. F.; Bonn, M., Carrier Dynamics in Semiconductors Studied with Time-Resolved Terahertz Spectroscopy. *Rev. Mod. Phys.* **2011**, *83*, 543-586.

Chapter 2

Ultrafast Charge Carrier Dynamics in Formamidinium Lead Bromide Nanocrystal Film:
Time-resolved Terahertz Spectroscopic Study

48. Leguy, A. M. A., et al., Dynamic Disorder, Phonon Lifetimes, and the Assignment of Modes to the Vibrational Spectra of Methylammonium Lead Halide Perovskites. *Phys. Chem. Chem. Phys.* **2016**, *18*, 27051-27066.

49. Sendner, M., et al., Optical Phonons in Methylammonium Lead Halide Perovskites and Implications for Charge Transport. *Mater. Horiz.* **2016**, *3*, 613-620.

50. Hanusch, F. C., et al., Efficient Planar Heterojunction Perovskite Solar Cells Based on Formamidinium Lead Bromide. *J. Phys. Chem. Lett.* **2014**, *5*, 2791-2795.

51. Arora, N.; Dar, M. I.; Abdi-Jalebi, M.; Giordano, F.; Pellet, N.; Jacopin, G.; Friend, R. H.; Zakeeruddin, S. M.; Grätzel, M., Intrinsic and Extrinsic Stability of Formamidinium Lead Bromide Perovskite Solar Cells Yielding High Photovoltage. *Nano Lett.* **2016**, *16*, 7155-7162.

52. Perumal, A., et al., High Brightness Formamidinium Lead Bromide Perovskite Nanocrystal Light Emitting Devices. *Sci. Rep.* **2016**, *6*, 36733.

53. Protesescu, L.; Yakunin, S.; Bodnarchuk, M. I.; Bertolotti, F.; Masciocchi, N.; Guagliardi, A.; Kovalenko, M. V., Monodisperse Formamidinium Lead Bromide Nanocrystals with Bright and Stable Green Photoluminescence. *J. Am. Chem. Soc.* **2016**, *138*, 14202-14205.

54. Swarnkar, A.; Marshall, A. R.; Sanehira, E. M.; Chernomordik, B. D.; Moore, D. T.; Christians, J. A.; Chakrabarti, T.; Luther, J. M., Quantum Dot-Induced Phase Stabilization of A-CsPbI$_3$ Perovskite for High-Efficiency Photovoltaics. *Science* **2016**, *354*, 92-95.

55. Dai, J.; Xie, X.; Zhang, X. C., Detection of Broadband Terahertz Waves with a Laser-Induced Plasma in Gases. *Phys. Rev. Lett.* **2006**, *97*, 103903.

56. Matsuura, S.; Tani, M.; Sakai, K., Generation of Coherent Terahertz Radiation by Photomixing in Dipole Photoconductive Antennas. *Appl. Phys. Lett.* **1997**, *70*, 559-561.

57. Zhang, X. C.; Hu, B. B.; Darrow, J. T.; Auston, D. H., Generation of Femtosecond Electromagnetic Pulses from Semiconductor Surfaces. *Appl. Phys. Lett.* **1990**, *56*, 1011-1013.

58. Cook, D. J.; Hochstrasser, R. M., Intense Terahertz Pulses by Four-Wave Rectification in Air. *Opt. Lett.* **2000**, *25*, 1210-1212.

59. Hafez, H. A.; Chai, X.; Ibrahim, A.; Mondal, S.; Férachou, D.; Ropagnol, X.; Ozaki, T., Intense Terahertz Radiation and Their Applications. *J. Opt.* **2016**, *18*, 093004.

60. Kim, K. Y.; Taylor, A. J.; Glownia, J. H.; Rodriguez, G., Coherent Control of Terahertz Supercontinuum Generation in Ultrafast Laser-Gas Interactions. *Nature Photonics* **2008**, *2*, 605-609.

Chapter 2

Ultrafast Charge Carrier Dynamics in Formamidinium Lead Bromide Nanocrystal Film:
Time-resolved Terahertz Spectroscopic Study

61. Vicario, C.; Ovchinnikov, A. V.; Ashitkov, S. I.; Agranat, M. B.; Fortov, V. E.; Hauri, C. P., Generation of 0.9-Mj Thz Pulses in Dstms Pumped by a Cr:Mg$_2$SiO$_4$ Laser. *Opt. Lett.* **2014**, *39*, 6632-6635.

62. DeFonzo, A. P.; Lutz, C. R., Optoelectronic Transmission and Reception of Ultrashort Electrical Pulses. *Appl. Phys. Lett.* **1987**, *51*, 212-214.

63. Wu, Q.; Zhang, X. C., Free-Space Electro-Optic Sampling of Terahertz Beams. *Appl. Phys. Lett.* **1995**, *67*, 3523-3525.

64. Johnson, J. L.; Dorney, T. D.; Mittleman, D. M., Interferometric Imaging with Terahertz Pulses. *IEEE J Sel Top Quantum Electron.* **2001**, *7*, 592-599.

65. Ashcroft N. W and N. D Mermin. Solid State Physics. *Saunders College,* **1976**.

66. Smith, N. V., Classical Generalization of the Drude Formula for the Optical Conductivity. *Phys. Rev. B* **2001**, *64*, 155106.

67. Nienhuys, H.-K.; Sundström, V., Influence of Plasmons on Terahertz Conductivity Measurements. *Appl. Phys. Lett.* **2005**, *87*, 012101.

68. Gaponenko, S. V., Optical Properties of Semiconductor Nanocrystals; *Cambridge University Press: Cambridge,* **1998.**

69. Motti, S. G.; Krieg, F.; Ramadan, A. J.; Patel, J. B.; Snaith, H. J.; Kovalenko, M. V.; Johnston, M. B.; Herz, L. M., CsPbBr$_3$ Nanocrystal Films: Deviations from Bulk Vibrational and Optoelectronic Properties. *Adv. Funct. Mater.* **2020**, *30*, 1909904.

70. Monahan, D. M.; Guo, L.; Lin, J.; Dou, L.; Yang, P.; Fleming, G. R., Room-Temperature Coherent Optical Phonon in 2D Electronic Spectra of CH$_3$NH$_3$PbI$_3$ Perovskite as a Possible Cooling Bottleneck. *J. Phys. Chem. Lett.* **2017**, *8*, 3211-3215.

71. Maeng, I., et al., Significant Thz Absorption in CH$_3$NH$_2$ Molecular Defect-Incorporated Organic-Inorganic Hybrid Perovskite Thin Film. *Sci. Rep.* **2019**, *9*, 5811.

72. He, J.; Fang, W.-H.; Long, R., Unravelling the Effects of a-Site Cations on Nonradiative Electron–Hole Recombination in Lead Bromide Perovskites: Time-Domain Ab Initio Analysis. *J. Phys. Chem. Lett.* **2018**, *9*, 4834-4840.

73. La-o-vorakiat, C., et al., Elucidating the Role of Disorder and Free-Carrier Recombination Kinetics in CH$_3$NH$_3$PbI$_3$ Perovskite Films. *Nat. Commun.* **2015**, *6*, 7903.

74. Wang, M.; Gao, Y.; Wang, K.; Liu, J.; De Wolf, S.; Laquai, F., Photo-Induced Enhancement of Lattice Fluctuations in Metal-Halide Perovskites. *Nat. Commun.* **2022**, *13*, 1019.

Chapter 2

Ultrafast Charge Carrier Dynamics in Formamidinium Lead Bromide Nanocrystal Film: Time-resolved Terahertz Spectroscopic Study

75. Mott, N., The Mobility Edge since 1967. *J. Solid State Phys.* **1987**, *20*, 3075.

76. Www.Coursera.Org/Lecture/Plastic-Electronics/Localisation-by-Disorder-Fkwc6.

77. Yaffe, O., et al., Local Polar Fluctuations in Lead Halide Perovskite Crystals. *Phys. Rev. Lett.* **2017**, *118*, 136001.

78. Lehman, A., Jmp for Basic Univariate and Multivariate Statistics: A Step-by-Step Guide; *SAS Press,* **2005**.

Chapter 3

Direct Probing of the Origins of Exciton Self-trapping in 1D Perovskite

Chapter 3

Direct Probing of the Origins of Exciton Self-trapping in 1D Perovskite

Abstract

Lead halide perovskites showed amazing diversity in photophysical properties over the past decade of intense research efforts. The possibility of dimensional diversity, by varying the organic cations, has broadened the applications of perovskites to a much larger domain. Reducing the dimensionality modifies the band structure, and hence the absorptive and emissive properties are also modified. Interesting broad and red-shifted PL emission is observed in most of the lower dimensional perovskites. This unique PL emission is suitable for white light LEDs and has been assigned to exciton self-trapping. We utilized optical Kerr effect (OKE) spectroscopy to unravel the fundamental understanding of exciton self-trapping in 1D pyridinium lead bromide single crystals. In OKE experiments, by performing the pre-resonant and non-resonant excitations, we decipher the composition of phonon modes involved in exciton self-trapping. A red-shift in spectral density plot of the excited state, with respect to the ground state, reveal the phonon modes which get affected due to exciton self-trapping. We unravel a strong role played by cation phonon modes in addition to the phonon modes of lead-bromide sublattice in exciton self-trapping. DFT calculations provide a strong support to our experimental findings and the role of cation in the exciton self-trapping. It also reveals that the CBM is predominantly composed of orbitals of pyridinium cations, and hence will most probably affect the optical properties.

Graphical Abstract
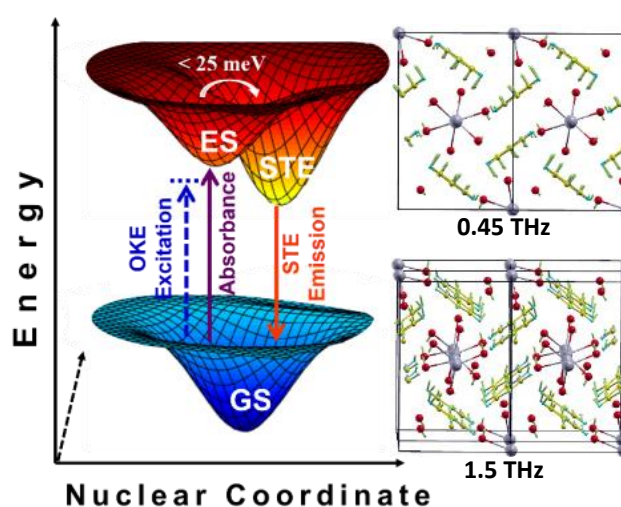
3.1 Introduction

Lead halide perovskites (LHPs) have now been established as excellent materials for photovoltaic and other optoelectronic applications because of their inherent defect tolerance, bandgap tunability, narrow emission bandwidth, and long-lived carriers with high mobilities.[1-9] Tunability of halide ions and organic cations offers versatile chemical compositions, thereby, allowing band structure engineering and bandgap tuning.[10-16] Due to this versatility, LHPs exist with–huge dimensional diversity, ranging from three-dimensional (3D) to zero-dimensional (0D) systems.[17-19] The decreased dimensionality induces a strong exciton/carrier-phonon coupling in two-dimensional (2D), one-dimensional (1D), and 0D perovskites.[20-21] This strong interaction between the excitons and the lattice vibrations of the perovskite crystal often leads to the exciton self-trapping[22] evidenced by unusual optical properties, such as highly stokes shifted photoluminescence (PL) and broadband white light emission.[19, 23] A majority of the lower dimensional systems reported show a strong self-trapped emission (STE) either at room temperature or at lower temperatures.[24] Though the organic cations play a deciding role in inducing the dimensionality and the band structure modulations, the effect of cation motions on exciton self-trapping has not been dealt in detail.

The exciton self-trapping, where a polarizable carrier, exciton, is trapped in lattice distortions, is closely related to the process of polaron formation, wherein a charge carrier is coupled with the long-range lattice distortions/deformations.[22] A previous model has related STE formation in LHPs to the electron being transferred to a Pb_2^{4+} dimer domain reducing it to a transient Pb_2^{3+} dimer, while the hole gets stabilized onto the Br_2^{2-} dimer yielding a transient Br_2^{1-} entity.[22] The vibrionic coupling of the wave function of the polarizable exciton would be very strong with that of the polarizable Raman active modes of the whole perovskite lattice. A technique that would experimentally trace these Raman-active modes over a large frequency range (few GHz to 100's of THz) would be immensely adequate.[25] Time-resolved, optically-heterodyned, optical Kerr effect spectroscopy (OKE)[26] serves as an appropriate technique to approach the understanding of this phenomenon of exciton self-trapping.

In this work, we have utilized a combination of ultrafast spectroscopy and density functional theory (DFT) based calculations to probe the origin of STE in pyridinium lead bromide ($PyPbBr_3$), a face-shared 1D perovskite system that exhibits a highly stokes shifted broad emission at room temperature. We note that the electronic properties of this material are distinct from other halide perovskites. In $PyPbBr_3$, the conduction band is localized on the cation and

the valence band is localized on the lead halide octahedra, whereas, in the usually studied halide perovskites, both the valence and the conduction bands are localized on the lead-halide octahedra. We utilized OKE to probe the origin of the exciton self-trapping. OKE spectroscopy directly traces the polarizable Raman active phonons. We observe a prominent change in the Raman active phonon modes of the perovskite lattice in the non-resonant and pre-resonant excitations. The Raman active phonon modes undergo a red shift due to strong coupling with excitons, resulting in the exciton self-trapping. These modes were theoretically assigned to soft phonon modes where the liberational motions of the cations are coupled with the vibration of the lead-halide octahedral chain. The DFT calculations show that these modes couple strongly with the conduction and valence bands. Our study suggests that these strongly coupled soft phonon modes can induce lattice distortions, thereby self-trapping the excitons in lower dimensional 1D hybrid lead halide perovskites.

3.2 Experimental Section

3.2.1 Chemicals

Lead oxide (Sigma Aldrich, 99.9%), pyridinium bromide (Sigma Aldrich, 99.9%), hydrobromic acid (Sigma Aldrich, 48% w/w in H_2O, 99.9%), hypophosphorous acid (Avra, 50% w/w H_2O), acetone (Rankem, 99.5%).

3.2.2 Synthesis of 1D PyPbBr$_3$ single crystals

PyPbBr$_3$ crystals were synthesized following a previously reported method.[27] 10 mmol (2232 mg) of PbO were dissolved in a mixture of 48% w/w aqueous HBr solution (15 mL) and 50% aqueous H_3PO_2 (1.7 mL) by heating to 110 ˚C under constant stirring for 10 mins. A transparent colorless solution was obtained. To this solution, 10 mmol pyridinium bromide was added while heating was continued until the solution became clear. At this moment, the stirring was stopped and the solution was allowed to cool down to room temperature naturally. While cooling white needle-shaped crystals started to crystalize. The obtained crystals were filtered, rinsed with acetone, and dried under reduced pressure.

3.2.3 Characterization

Single crystal X-ray diffraction (SCXRD) data were recorded on a Bruker Smart Apex Duo diffractometer at 100 K and 296 K using Mo Kα radiation (λ = 0.71073 Å). The frames were integrated with the Bruker SAINT Software package using a narrow-frame algorithm. The

structures were solved by direct method and refined by full-matrix least-squares on F2 using the SHELXTL software package. The PbI$_4$ framework was refined anisotropically without any constraint on Pb and Br atoms.

Powder X-ray Diffraction (PXRD) data were recorded on Bruker D8 Advance X-ray diffractometer using Cu Kα radiation (1.54 Å). Scanning electron microscopy (SEM) images were recorded on Zeiss Ultra Plus FESEM instrument. The powdered sample was taken for thermogravimetric analysis (TGA) by utilizing Perkin Elmer STA 6000. The sample was heated at the rate of 10 ˚C per minute under an inert atmosphere from 30 to 800 ˚C. Fourier transform infrared spectroscopy (FTIR) study of powdered sample was recorded with KBr disc using NICOLET 6700 FTIR spectrometer. Raman spectrum was obtained from the powdered sample using a 632.8 nm laser from Horiba Jobin Yvon.

The optical diffuse-reflectance spectrum of the powdered sample with BaSO$_4$ as a 100% reflectance reference was obtained using a Shimadzu UV-3600 plus UV-VIS-NIR double-beam, double monochromator spectrophotometer. Absorbance was calculated from the reflectance spectrum using the Kubelka-Munk transformation.[28] Steady-state Photoluminescence (PL) measurements were performed on FLS 980 (Edinburgh Instruments). Time-correlated single photon counting (TCSPC) set-up from Horiba Jobin Yvon was exploited for the PL decay dynamics measurement using a 370 nm picosecond diode laser as the excitation source. The decay signals were obtained at a magic angle using an MCP-PMT (Hamamatsu, Japan) detector and analyzed by IBH DAS6 analysis software.

3.2.4 Time-resolved optically heterodyned optical Kerr effect spectroscopy (OKE)

OKE, also known as femtosecond-Raman induced Kerr effect spectroscopy (fs-RIKES),[29] is a third-order, four-wave mixing (FWM) technique that probes the Raman-active modes in a condensed phase system over a wide frequency range, (GHz to 100's of THz) covering a variety of reorientational, intermolecular and intramolecular nuclear motions. The signal obtained has a very high signal-to-noise (S/N) ratio allowing a detailed analysis of the spectra. In OKE spectroscopy, a linearly polarized pump pulse induces a transient birefringence or anisotropy in a condensed phase medium. A delayed probe pulse, spatially overlapping with the pump on the sample, with a different polarization compared to that of the pump pulse reads out the temporal evolution of this transient anisotropy/polarizability. The probe pulse becomes elliptically polarized upon interaction with the sample. A Wollaston prism splits the orthogonal

components of this elliptically polarized probe and these components are detected by an auto-balanced detector.

The OKE signal is obtained as a function of the time delay between the pump and the probe pulses, thereby, measuring the relaxation of the material birefringence in real-time. The large spectral width of several hundreds of wave numbers is obtained by using ultra-short pulses. This technique has been extensively used for the study of structural and reorientational dynamics in condensed phases like simple liquids and complex liquids,[26] solvents and ionic liquids,[29] liquid crystals,[30] plastic crystals,[31] biomolecules like proteins,[32] peptides,[33] enzymes,[34] DNA,[35-36] etc. In molecular liquids, generally, four types of responses are observed in the OKE transients: 1) an instantaneous electronic response, 2) an ultrafast response (< 200 fs) caused by polarization anisotropy due to liberations and/or frustrated rotations, 3) an intermediate response (400-600 fs) due to the anisotropy induced by the molecular reorientational motions, and 4) a slow response (>1 ps) due to the molecules with permanent anisotropic polarizability undergoing diffusive reorientations.[26]

We performed the time-resolved OKE spectroscopic studies on a home-built two-color pump-probe spectrometer as shown in Figure 3.1.[37] The pump and probe beams were obtained from a regenerative amplifier (Spitfire Pro XP, Spectra Physics) with 35 fs (full width half maximum, FWHM) wide pulses having wavelength centered at 800 nm and 1 kHz repetition rate. An ultrafast oscillator (35 fs, 800 nm, Tsunami, Spectra Physics) pumped by 533 nm continuous wave diode laser (Millennia Prime, Spectra Physics), served as the seed laser for the regenerative amplifier. The output beam of about 2 mJ energy was split into two, using a beam splitter. Using a type-I β-Barium Borate (BBO) crystal of 100 µm thickness, pump pulses of 400 nm wavelength were generated. The 800 nm pulses from the source laser served as a probe. Because of the requirement of lower energy for OKE experiment neutral density (ND) filters with variable optical density (OD) were placed in both pump and probe paths. Two half-wave plates were used to maintain the polarization of the pump beam at 45° with respect to probe polarization. The pump beam was modulated by passing it through an optical chopper. A plano-convex lens of 500 mm focal length was used to focus the pump beam onto the crystal. The 800 nm probe beam was passed through a 300 mm variable delay stage (PI-M413) and then focused tightly, using a plano-convex lens with focal length 100 mm, onto the sample to probe the photo-induced change in the polarizability. For optimum results, we utilized a co-linear geometry for the pre-resonant OKE experiment by placing a dichroic mirror at an angle

of 45˚to the pump beam and the probe beam was allowed along a normal incidence. After interacting with the sample, the pump beam was directed to a beam blocker using a dichroic mirror while the modified probe beam carrying the information about sample dynamics transmitted through it. A notch filter was also used to avoid the pump beam reaching the detector. The probe beam was then allowed to pass through a quarter wave-plate, thereby inducing polarization ellipticity. A Wollaston prism split the probe beam into two, with a 2:1 (reference: sample) intensity ratio for auto-balanced detection. The slight changes in the probe beam polarization due to change in the sample birefringence was detected using an auto-balanced photodetector (Nirvana 2007, Newport). The signal output from the detector was fed into a lock-in amplifier (SR830, Stanford Research Systems) locked to the pump pulse chopping frequency. This lock-in signal was recorded as a function of the time delay between the pump and probe beams. The laser pulse cross-correlation in this OKE setup measured with a 3 mm calcium fluoride crystal placed at the sample position was ~70 fs for pre-resonant condition and non-resonant condition. The step size for high time resolution transients is 1 µm.
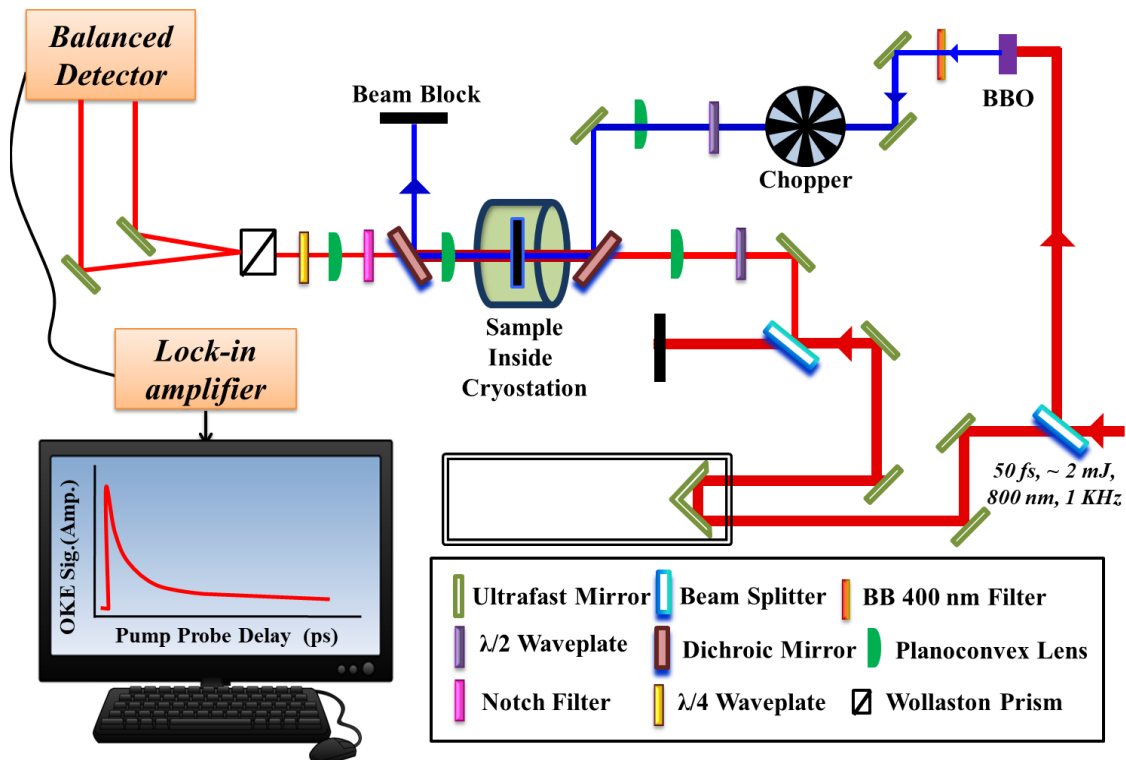

Figure 3.1: Schematic of the OKE spectroscopy setup.

In OKE, a linearly polarized pump beam creates transient anisotropy in a condensed phase medium and a probe beam with a different polarization traces the relaxation of the induced birefringence. The frequency range approachable by OKE spectroscopy includes motions pertaining to cations, lead halide octahedra, and even ion migrations present in the perovskites.[38] OKE provides a holistic window to fundamentally understand and approach the process of exciton self-trapping in the lower dimensional perovskites. OKE experiment was performed to probe the ground state Raman-active modes by non-resonant excitation and the transient virtual state by pre-resonant excitation.[39]

3.2.5 Computational details

First principles plane-wave based density functional theory (DFT) based calculations were done using the Quantum Espresso software. Electron-ion interactions were described using ultrasoft pseudopotentials. The presence of Pb, which is a heavy element, makes spin-orbit interactions important (SOI) in these systems. Hence, to correctly take into account the SOI, we have solved relativistic Kohn-Sham equations self consistently using relativistic ultrasoft pseudopotentials. The electron-electron exchange and correlation energy were described using the Perdew-Burke-Ernzerhof parametrization of the generalized gradient approximation. Brillouin zone integrations were done using a 4×8×8 Monkhorst-Pack k-point grid. The wavefunctions and the charge density were expanded in a plane wave basis with kinetic energy cut-offs of 60 and 600 Ry respectively. The Br ions being highly polarizable, van der Waals interactions are important for these systems. Since conventional DFT functionals do not include van der Waals interaction, to incorporate these effects we have used semi-empirical Grimme's correction. The phonons at the zone center and the dielectric constants have been calculated using density functional perturbation theory.

In order to identify the coupling of the phonon modes that couple with the states near the band edges, we have computed the electron-phonon self-energy for the phonons at the Γ-point of the Brillouin zone. The electron-phonon self-energy for the nth state at the kth k-point of the Brillouin zone ($\sum_{nk}$) is given by:

$$\sum_{nk} = \sum_{qv,m} w_q \left| g_{qv,m}^{SE}(k,q) \right|^2 \left[\frac{n_{qv} + 1 \text{-} f_{mk+q}}{\varepsilon_{nk}\text{-}\varepsilon_{mk+q}\text{-}\hbar\omega_{qv}\text{-}i\delta} + \frac{n_{qv} + f_{mk+q}}{\varepsilon_{nk}\text{-}\varepsilon_{mk+q} + \hbar\omega_{qv}\text{-}i\delta} \right] \qquad (1)$$

where $g_{qv,m}^{SE}(k, q) = \left(\frac{\hbar}{2m_0\omega_{qv}}\right)^{1/2} \langle\psi_{mk+q}|\partial_{qv}V|\psi_{nk}\rangle$. w_q is the weight associated with phonon wavevector q in the BZ, ψ_{nk} and ε_{nk} represents the electronic wavefunction and energy eigenvalue respectively of the nth band at the kth point of the BZ. $\partial_{qv}V$ is the derivative of the self-consistent potential associated with a phonon wavevector q, branch index v, and frequency ω_{qv}. f and n denote the electronic and vibrational states at a given temperature T and are given by the Fermi-Dirac and Bose-Einstein distribution respectively. For our case, since we are computing only for the phonons at the BZ center, the summation over q in the right-hand side of the above equation is not considered. The electron-phonon interactions were computed with the EPW code. The electron-phonon matrix element was first computed with the above-mentioned coarse k-point grid for the electrons. These are then interpolated to a denser $8\times16\times16$ k-mesh. We have used a 0.025 eV Gaussian smearing for the δ-function in the above equation.

3.3 Results and Discussion

3.3.1 Synthesis and crystal structure

PyPbBr$_3$ single crystals were synthesized by dissolving 10 mmol (2232 mg) of lead oxide in a mixture of 15 mL of hydrobromic acid (48% w/w) and 1.7 mL of hypo-phosphorous acid (50%) by heating to 110 ˚C. A transparent solution was obtained, to which 10 mmol of pyridinium bromide was added. The heating was stopped once the pyridinium bromide completely dissolved and the solution was allowed to cool to room temperature naturally. Needle-shaped colorless crystals of PyPbBr$_3$ precipitated out during the cooling process. Figures 3.2a and 3.2b show the as-grown crystal under ambient light and UV illumination. Figure 3.2c shows the scanning electron microscopy (SEM) image of these needle-shaped crystals having a hexagonal crystal habit (see the inset of Figure 3.2c). SCXRD data was recorded at 100 K. PyPbBr$_3$ has an orthorhombic crystal structure and space group *pna2$_1$* at both temperatures. Figure 3.2d left panel shows the crystal structure of PyPbBr$_3$ at 100 K. The lattice parameters are $a = 14.0017(18)$ Å, $b = 9.1813(11)$ Å, $c = 7.7759(10)$ Å and $\alpha = \beta = \gamma = 90$˚ (see Table 3.1 for detailed crystal structure data). The crystal structure consists of a face-shared lead bromide octahedral network, forming a one-dimensional (1D) structure. The monovalent aromatic pyridinium cations encompass the infinite [PbBr$_3$]$^-$ chains. The bulky pyridinium cation is too big to fit in the cub-octahedral voids of the regular corner-shared 3D [PbBr$_6$]$^{4-}$ network. This leads to the deviation from the usual corner shared polymeric [PbBr$_6$]$^{4-}$ network.[40] The layered

two-dimensional architecture formed by corner/edge sharing of lead bromide octahedra, is not observed as well.[41] This is because the cation is a secondary amine and the nitrogen atom is present in a highly planar and rigid aromatic ring. This results in the formation of a highly distorted face-shared linear 1D-perovskitoid structure, with a large extent of out-of-plane Pb-Br-Pb bending, that accommodates the bulky cation.
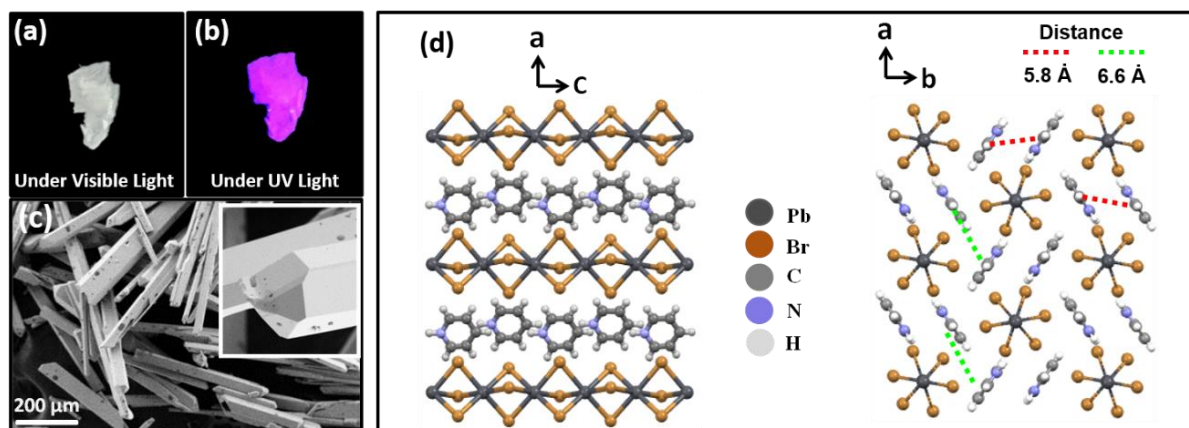

Figure 3.2: (a) and (b) show as grown crystal under visible light and UV illumination. (c) SEM images of the $PyPbBr_3$ single crystals showing needle-shaped morphology. The inset contains a magnified view of a crystal showing a hexagonal crystal habit. (d) Crystal structure of $PyPbBr_3$ showing 1D network of lead bromide octahedra. Non-covalent interactions between the adjacent pyridinium cations lead to a pseudo-2D structure of the crystal.

Interestingly, the aromatic pyridinium cations show strong non-covalent interactions among themselves and orient in an ordered fashion.[42] Figure 3.2d right panel shows the arrangement of pyridinium cations between polymeric lead bromide octahedral networks.

The powder X-ray diffraction (PXRD) pattern of the $PyPbBr_3$ clearly matches with the simulated PXRD pattern obtained from SC-XRD as shown in Figure 3.3a, suggesting the phase purity of the sample.

The presence of an asymmetric aromatic cation in $PyPbBr_3$ reduces the lattice symmetry from orthorhombic *Pnma* to *Pna2₁*. This is indicated but not explained elaborately in a previous report.[45] The distortion in the electron cloud, because of one additional electron (of nitrogen atom) compared to a symmetric benzene ring induces asymmetry into the system leading to a measurable induced electric polarization. A considerable ferroelectric response is obtained in

a PyPbBr$_3$ pellet, as shown in Figure 3.3b. The polarization value of 0.01 µC/cm^2 is comparable to that of other organic inorganic lead halide perovskites.[46]

Table 3.1: Crystal data and structure refinement of PyPbBr$_3$ at 100 K.

|	
Empirical formula	C$_5$H$_6$Br$_3$NPb
Formula weight	527.03
Temperature	100(2) K
Wavelength	0.71073 Å
Crystal system	Orthorhombic
Space group	*P*na2$_1$
Unit cell dimensions	a = 14.0017(18) Å
	b = 9.1813(11) Å
	c = 7.7759(10) Å
	α = β = γ = 90°
Volume	999.6(2) Å3
Z	4
Density (calculated)	3.502 Mg/m^3
Absorption coefficient	28.803 mm-1
F(000)	920
Crystal size	0.04 x 0.03 x 0.02 mm3
Theta range for data collection	4.440 to 25.023°.
	-16 ≤ h ≤ 16,
	-10 ≤ k ≤ 10,
Index ranges	-9 ≤ l ≤ 9
Reflections collected	21039
Independent reflections	1748 [R(int) = 0.0493]
Completeness to theta = 25.023°	99.40%
Absorption correction	Semi-empirical from equivalents
Max. and min. transmission	0.7457 and 0.3731
Refinement method	Full-matrix least-squares on F2
Data / restraints / parameters	1748 / 73 / 56
Goodness-of-fit on F2	1.223
Final R indices [I > 2sigma(I)]	R1 = 0.0364, wR2 = 0.0865
R indices (all data)	R1 = 0.0457, wR2 = 0.0914
Absolute structure parameter	0.50(10)
Largest diff. peak and hole	2.293 and -3.414 e.Å^{-3}
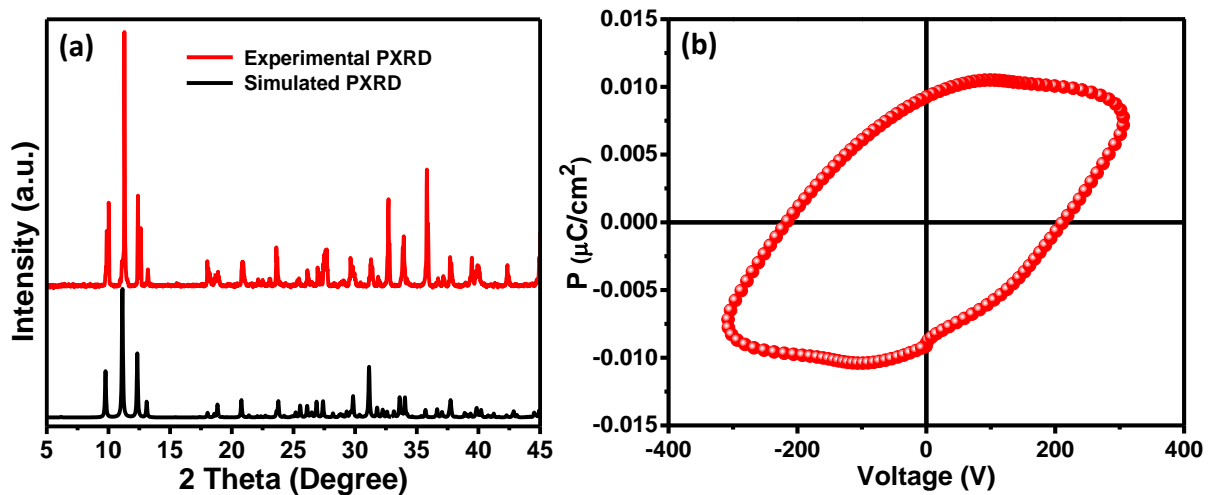
Figure 3.3: (a) Experimental and the simulated PXRD patterns of $PyPbBr_3$. The simulated PXRD pattern is obtained from the SCXRD data. (b) Electric polarization of the $PyPbBr_3$ pellet.

We have performed DFT-based calculations for bulk $PyPbBr_3$ and Figure 3.4 shows the computed structure of bulk $PyPbBr_3$. Our computed values of the lattice parameters (a = 13.78 Å, b = 9.01 Å and c = 7.81 Å) are slightly underestimated compared to those measured experimentally (a = 14.00 Å, b = 9.18 Å and c = 7.76 Å). This results in about 2.77% underestimation of the unit cell volume. The distance between the Pb atoms in two consecutive octahedron is about 3.90 Å, which is in reasonably good agreement with the experimentally measured distance of about 3.88 Å. The Pb-Br octahedra are distorted with Pb-Br bond lengths varying between 2.94 to 3.09 Å, with an exception of one Pb-Br bond where the bond length is about 3.24 Å. The corresponding experimental value for this Pb-Br bond is 3.12 Å. In the pyridinium cation, the computed C-C (C-N) bond lengths are about 1.38 Å (1.35 Å) and are in reasonable agreement with the experimental value of 1.39 Å (1.39 Å). Our computed values of the C-H and N-H bond lengths of 1.08 and 1.03 Å are slightly overestimated compared to the corresponding experimental values of 0.95 and 0.88 Å respectively. It is to be noted that the N and H atoms of the pyridinium ion have a H-bond-like interaction with the Br ion of the Pb-Br octahedral that has the longest Pb-Br bond length. The H-Br distance is about 2.62 Å, the N-Br distance is about 3.44 Å and the N-H-Br bond angle is about 136.2°. Our results are in reasonably good agreement with the experimental values.
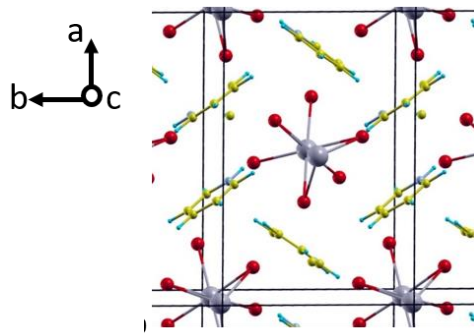
Figure 3.4: The computed crystal structure of PyPbBr$_3$.

3.3.2 Optical properties

The absorption spectrum of PyPbBr$_3$ single crystals (Figure 3.5a), exhibits a strong excitonic feature at 340 nm (~3.65 eV). Interestingly, at room temperature, the photoluminescence (PL) spectrum, shown in Figure 3.5b, does not feature any prominent band-edge excitonic emission. Instead, we observe a highly stokes-shifted broad emission with a peak at ~607 nm (2.04 eV) and a full width at half maximum (FWHM) of 135 nm (0.4 eV) (Figure 3.5b). PL excitation profile, given in Figure 3.5a, confirms that the emission corresponds to the bandgap excitation. The PL spectrum was recorded till 660 nm only, to prevent saturation of the detector from second-order scattering from the excitation source. Figure 3.5c shows the time-resolved PL decay profile having a lifetime of ~5.4 ns similar to other lower dimensional materials.[47]

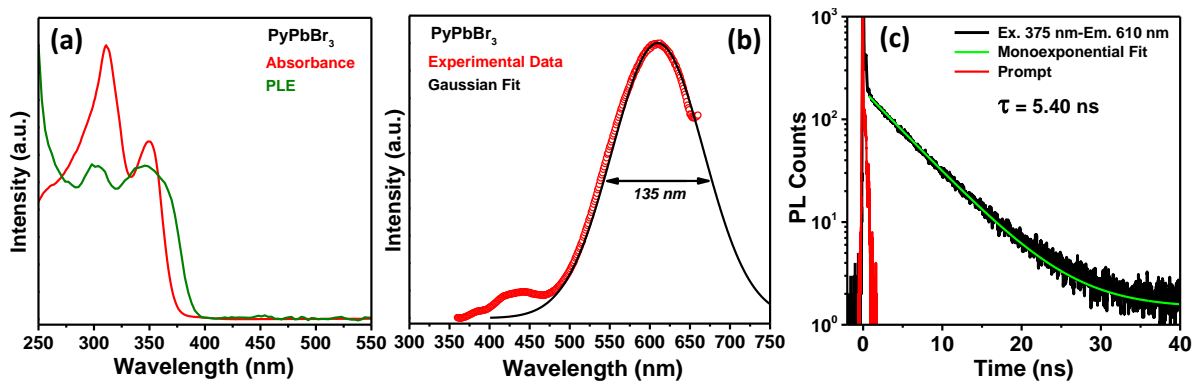
Figure 3.5: (a) Absorbance and PL excitation spectra of PyPbBr$_3$ single crystals. The absorbance spectrum has been obtained from the reflectance data by using Kubelka-Munk transformation.[28] (b) PL spectrum of PyPbBr$_3$ single crystals. The spectrum is fitted to a Gaussian function to account for the FWHM of the PL emission spectrum. (c) PL decay dynamics of PyPbBr$_3$ single crystals.

Electronic structure and density of states (DOS) computed using DFT-based calculations provide valuable information for these excitations. Figure 3.6a shows the phonon density of states (black curve) and the contributions from Pb (in red), Br (in green), and Py (in blue) ions. Figure 3.6b shows the band structure and DOS for bulk $PyPbBr_3$. We observe that the material has an indirect band gap of 2.28 eV with the valence band maximum lying at the Γ-point of the Brillouin zone (BZ) and the conduction band minimum is at the T-point of the BZ. The direct band gap at the Γ-point is about 2.44 eV while that at the T-point is about 2.49 eV. Compared to other Br-based hybrid halide perovskites, the valence band of $PyPbBr_3$ is narrow with a width of about 0.50 eV. However, similar to the other compounds, the valence band has contributions primarily from Br-4p and Pb-6s states. This is also evident from the plot of the wave function corresponding to the VBM (Figure 3.6c). In contrast to the other 3 and 2-dimensional hybrid halide perovskites, we find that in $PyPbBr_3$ the conduction band is localized on the pyridinium cation as evident from DOS in Figure 3.6b and the plot of the wavefunction of the CBM in Figure 3.6d. The conduction band is narrower with a bandwidth of about 0.20 eV. This suggests that the low energy excitations in this system correspond to charge transfer excitations where electrons from the 1-dimensional Pb-Br octahedra are transferred to the pyridinium ions. Therefore, unlike the 2D halide perovskites where the electron and the hole that forms the exciton are confined within the Pb-Br octahedral, in $PyPbBr_3$ the electron will be on the cation while the hole will be on the 1D octahedron.

While the narrow bandwidths of the conduction and valence bands suggest a larger exciton binding energy, the fact that the exciton is not confined within the Pb-Br octahedra implies an exciton binding energy smaller than that observed in 2D perovskites. Using the effective masses of electrons and holes and the dielectric constant, we have computed the exciton binding energy (E_b) and the Bohr exciton radius (a_B) within the static and high-frequency limit. We find that $E_b^\infty = 129$ meV while $E_b^S = 6.88$ meV. The corresponding exciton Bohr radii are 14.26 Å and 61.78 Å respectively (details in next section).

According to the effective mass theory, the Bohr exciton radius (a_0) is given by:

$$a_0 = \frac{\varepsilon a_0^H}{\mu} \qquad (2)$$

and the exciton binding energy (E_b) is given by:

$$E_b = 13.6 \frac{\mu}{\varepsilon^2} \qquad (3)$$

In the above equations, ε and a_0^H are the dielectric constant and the radius of the H atom respectively. μ is the exciton's reduced mass and is given by $\frac{1}{\mu} = \frac{1}{m_e^*} + \frac{1}{m_h^*}$, m_e^* and m_h^* are the electron and hole effective masses, respectively. These are calculated along the [100], [001], and [010] directions and are determined by fitting the band structure (within $k_B T$ of band edges) at the valence band maximum (VBM) and the conduction band minimum (CBM). In the expression for μ, we have used the average value of the effective masses for electrons and holes. These average values are computed using the following equation:

$$\frac{1}{m^*} = \frac{1}{3}\left(\frac{1}{m_{100}^*} + \frac{1}{m_{010}^*} + \frac{1}{m_{001}^*}\right) \qquad (4)$$
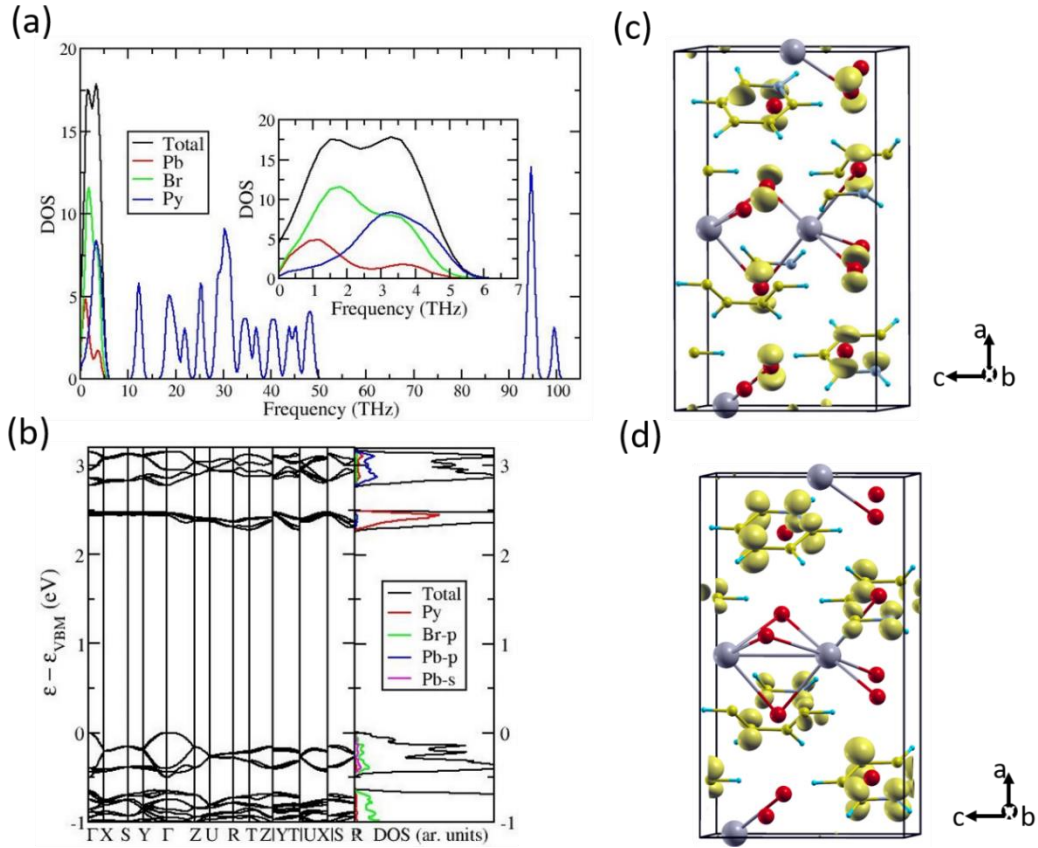
Figure 3.6: (a) The phonon density of states (black curve). Also shown are the contributions from Pb (in red), Br (in green) and Py (in blue) ions. (b) The band structure (left panel) and the electronic density of states (right panel) and the contributions from different atomic orbitals. (c) and (d) are the isosurfaces of the wavefunctions corresponding to the valence band maxima at the Γ-point of the Brillouin zone and the conduction band minima at the T-point of the BZ, respectively. In this and the remaining figures of the manuscript red, brown, yellow, blue and turquoise spheres represent Br, Pb, C, N and H atoms respectively.

3.3.3 Calculation of exciton binding energy and Bohr exciton radius

The exact value of the exciton Bohr radius and binding energies depends on the dielectric constant that shows a large variation with frequency and temperature. Hence, we have given only upper and lower estimates of these quantities, listed in table 3.2 and 3.3, by computing the high frequency (ε_∞) and static (ε_s) limit of the dielectric constant. We obtained $\varepsilon_\infty = 3.91$ and $\varepsilon_s = 16.92$.

Table 3.2: Effective masses of electrons and holes along the three high symmetry directions and their average values.

Direction	m_e^*	m_h^*
[100]	0.69	0.11
[010]	1.16	0.25
[001]	1.47	1.52
Average	0.45	0.21

Table 3.3: Bohr exciton radius and exciton effective mass in the high frequency and static limit of the dielectric constant.

Property	High-frequency limit	Static limit
Bohr exciton radius (Å)	14.26	61.78
Exciton binding energy (meV)	129.00	6.88

At room temperature broad, highly Stokes shifted PL emission is atypical of 3D lead halide perovskites. 2D layered perovskites also show this characteristic PL emission with only certain cations, at room temperature or at lower temperatures.[48-49] However, most of the 1D perovskites show a broad and highly stokes shifted PL emission at room temperature[22, 24, 49-51] Normally, a narrow and slightly red-shifted excitonic emission is observed due to radiative recombination of strongly bound free excitons.[52] In lower dimensional perovskites, in addition to the free excitonic emission, a peculiar white light (WL) emission is observed which has been assigned to self-trapped excitonic (STE) emission.[53-54] Self-trapped excitons are generated when the free excitons (FE), created on photo-excitation, couple strongly with the collective polarizable motions of the lattice and get stabilized.[22] Thus the free excitons get self-trapped intrinsically, in the distortions of the lattice. The radiative recombination of this energetically stabilized self-trapped exciton leads to a highly Stokes-shifted emission.[22] The broadening of the STE

emission is due to the distortion of self-trapped states with respect to the ground state. This is described by Huang- Rhys Parameter, S.[22] There can be multiple self-trapped excitonic states with different trapping energies.[22]. An average lifetime of 5.4 ns (shown in Figure 3.3c) from the PL decay dynamics also suggests towards the excitonic emission (self-trapped) rather than a defect emission.

The difference between available thermal energy and the stabilization energy of self-trapping would govern the nature of emission, i.e., whether it will be FE emission, STE emission, or a broad WL emission. It is observed that at a particular temperature if the thermal energy available is greater than the stabilization energy of STE, a free excitonic emission is obtained. Rather when the stabilization energy of STE is greater than the available thermal energy, a strong STE emission would be obtained. White light is emitted when the thermal energy available and the stabilization energy of STE are comparable. The emission obtained in this case is a combination of free excitonic emission and self-trapped excitonic emission.[55] The exciton binding energy in 1D perovskitoids is expected to be more than that of the 2D layered perovskites due to enhanced quantum and dielectric confinement. [21, 56]

At room temperature, $PyPbBr_3$ single crystals show negligible band-edge emission as compared to STE emission. This indicates that STE is highly stabilized by highly polarizable phonon modes such that the available thermal energy is not sufficient for de-trapping. The enhanced stabilization of STE could most probably be due to the presence of this highly planar, aromatic cation in addition to the distortions of the lead halide network. To probe this, we utilized OKE spectroscopy to study these polarizable phonon modes leading to STE formation. OKE spectroscopy detects the Raman active phonon modes with which the exciton coupling can take place. By performing OKE at non-resonant and pre-resonant states, we can detect the changes in the phonon mode distributions due to STE formation. Moreover, DFT calculations were performed to visualize these phonon modes and to calculate the carrier-phonon coupling strengths.

3.3.4 Pre-resonant and non-resonant OKE spectroscopic studies

The OKE experiments were performed in pre-resonant condition, by excitation with 400 nm laser pulses, and in non-resonant condition by excitation with 800 nm laser pulses.[38] Laser pulses centered around 800 nm at a polarization angle 45° to that of pump pulses were utilized as probe pulses. On the resonant excitation, the excitons created undergo coupling with the polarizable modes in the excited state leading to exciton self-trapping. Due to the non-

availability of pump pulses below 400 nm (experimental limitation), a resonant excitation was not possible. PyPbBr$_3$ crystals start absorbing from 380 nm and excitation by pump pulses of 400 nm creates a transient virtual state very close to the conduction band minimum (CBM) and hence leads to a pre-resonant excitation (Figure 3.7). By creating the virtual state close to the CBM we intend to probe the contribution from the stationary state close to the excited state polarizable modes. By performing a non-resonant excitation experiment, we trace the Raman modes in the ground electronic state.
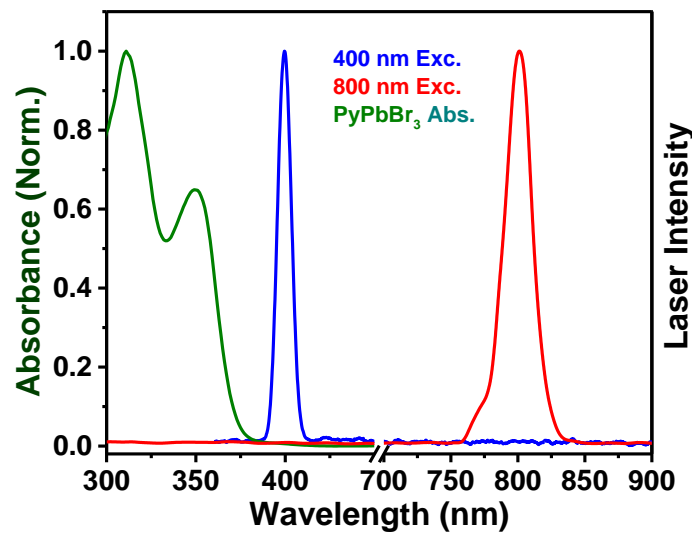

Figure 3.7: Comparison of the absorbance spectrum (olive) of PyPbBr$_3$ single crystals and the excitation laser pulse for pre-resonant (blue) and non-resonant (red) excitation wavelengths.

Figure 3.8 shows the OKE transients. At t = 0 ps, there is a high OKE amplitude due to the hyper-polarizability response of electrons, followed by the nuclear response from the sample. The nuclear response consists of ultrafast motions from the intra- and intermolecular vibrations, followed by the intermediate reorientational motions and the slow diffusional motions. The OKE transients appear quite similar to that of the molecular liquids rather than the usual solid crystals.[57-58] The OKE transients of solids usually show characteristic and prominent oscillatory features representing the intra- and intermolecular vibrations at discrete frequencies in the frequency domain.[59] The liquid-like behavior of OKE transients, lasting for hundreds of picoseconds, implies the structural flexibility, strong anharmonicity, and dynamic disorder in this 1D system. The strong anharmonicity and dynamic disorder lead to the detection of predominantly overdamped phonon modes as seen from the phonon mode analysis of the spectral density. It is apparent from the OKE transients, the dynamic organization of liquid-

like molecular dipoles suggesting the presence of preformed local ferroelectric domains, leading to the ferroelectric behavior as discussed in Figure 3.3b.[60] Figure 3.8a shows the normalized OKE responses of PyPbBr$_3$ crystals at room temperature under pre-resonant and non-resonant excitations. Both the OKE transients show a similar temporal profile. For both the pump wavelengths, after instantaneous electronic hyper-polarizability relaxation, the nuclear response follows. The nuclear response consists of an ultrafast relaxation till a few hundred fs due to collective intra and intermolecular Raman-active modes being coherently excited by the pump pulses, an intermediate response lasting for few ps caused by reorientational motions, and a slow response till few hundreds of ps because of diffusive motions of polarizable molecules and ions. For the intramolecular and intermolecular modes to appear in OKE transients, they must be Raman active and have some degree of anisotropic polarizability.[61] The inset of Figure 3.8a compares the instrument response function (IRF) to that of sample response at non-resonant excitation (blue) and pre-resonant excitation (red) in the first 2 ps after excitation. The nuclear response upon pre-resonant excitation is relatively slow, in the first few hundreds of femtoseconds, compared to the nuclear response at non-resonant excitation. The normalized amplitude of OKE transients also reveals increased contribution from the intermediate time response as well as slow temporal response upon the pre-resonant condition as compared to the non-resonant excitation. These subtle differences in the OKE transients reveal the probing of the contributions of several polarizable modes to different potential surfaces, i.e., the ground state and the excited state potential energy surfaces. Figure 3.8b shows the OKE transients fitted to the Gaussian convoluted triexponential function given as equation 1 (represented by black short dashes).[6]

$$y = G(t\text{-}t_0) \otimes \sum_i a_i \exp\left[-(t\text{-}t_0)/\tau_i\right] \qquad (5)$$

where $G(t\text{-}t_0)$ is a Gaussian function centered at t_0 with full width at half maximum (FWHM) of ~85 fs which represents the instrument response function of the OKE experiment, and a_i is the coefficient of the ith time component with τ_i time constant.

In figure 3.8b, blue curves represent the residual plots obtained by the subtraction of the fit curves from the OKE time transients. The complex oscillations present in the residual OKE transients correspond to different lattice vibrations that couple to the pumped/excited state(s) of the PyPbBr$_3$ system. The time components and the corresponding amplitudes of the fitted OKE transients are presented in Table 3.4.
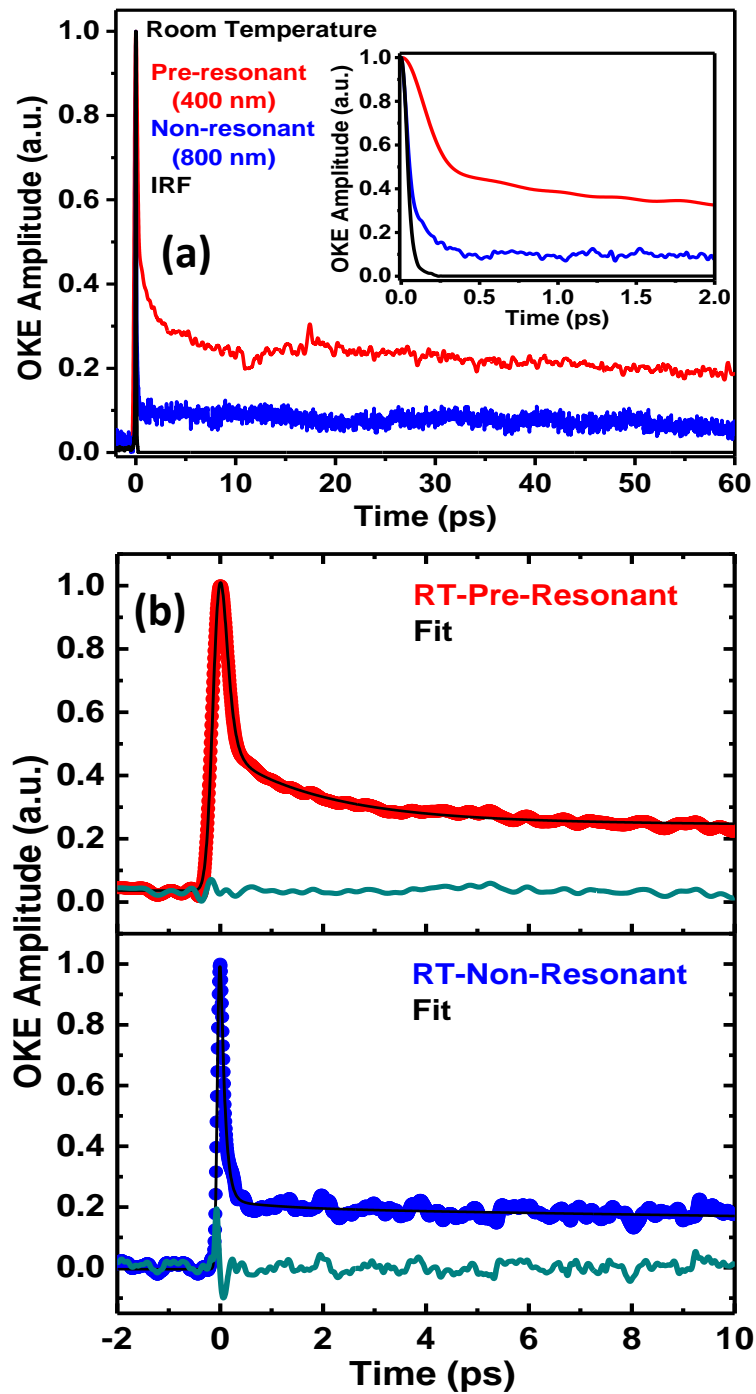
Figure 3.8: (a) OKE time transients of PyPbBr$_3$ single crystals obtained at room temperature under pre-resonant (400 nm) and non-resonant (800 nm) pump excitation. Inset shows the ultrafast nuclear response of the single crystals immediately after the electronic hyper-polarizability response. (b) Comparison of the fitted transients and the residual profiles under pre-resonant (400 nm) and non-resonant (800 nm) pump excitation, to check for underlying oscillations representing the vibrational signatures associated with self-trapping of excitons.

Table 3.4: Time constants (t_i) and their corresponding contributions (a_i), obtained from the fitting of the experimentally obtained OKE transients to the Gaussian convoluted multi-exponential fit functions.

Temperature	a_1	t_1 (ps)	a_2	t_2 (ps)	a_3	t_3 (ps)
RT (400 nm)	0.89	0.084	0.08	0.704	0.02	438.24
RT (800 nm)	0.87	0.083	0.02	1.09	0.11	71.73

3.3.5 Analysis of OKE data

Separation of the electronic response from the nuclear response in the OKE transients of the sample is done by following the procedure developed by Dale McMorrow and Lotshaw.[62] The heterodyne detected IRF and the OKE transients are Fourier transformed into frequency domain spectra. A deconvolution procedure of frequency domain sample spectrum with respect to the IRF is performed to obtain the OKE spectral density (OKE-SD) which is formally equivalent to the Bose-Einstein corrected Raman spectral density.[63] This procedure corrects the effects of the finite laser pulse duration, thereby producing a signal independent of the instrument fluctuations. The OKE signal, $S(t)$, obtained by heterodyne detection is a convolution of the cross-correlation of the pump-probe pulse at the sample position, $G^{(2)}(t)$, and the depolarized Raman material response function, $R_{xyxy}^{(3)}(t)$.[26, 62] If both the pulses coming from the same source are almost transform limited, $G^{(2)}(t)$ is measurable exactly as the second harmonic generation cross-correlation between pump and probe pulses, and is measurable in the experimental setup.

$$S(t) \propto \int G^{(2)}(t) \otimes R_{xyxy}^{(3)}(t) \qquad (6)$$

Using the convolution theorem, the material response function, $R_{xyxy}^{(3)}(t)$, can be recovered by following the Fourier transform relationship:

$$F\left[G^{(2)}(t) \otimes R_{xyxy}^{(3)}(t)\right] = F\left[G^{(2)}(t)\right] \times F\left[R_{xyxy}^{(3)}(t)\right] = F[S(t)] \qquad (7)$$

Here F indicates a forward complex Fourier transform.

$$F\left[R_{xyxy}^{(3)}(t)\right] = \frac{F[S(t)]}{F[G^{(2)}(t)]} = D(\omega) \qquad (8)$$

$D(\omega)$ represents the sample dynamics recovered in the frequency domain, undistorted by the convolution with the finite pulse width of the laser. This sample response contains contributions from the nuclear dynamics, $r(t)$, as well as the instantaneous electronic response, $\sigma(t)$ from the sample.

$$S(t) = \sigma(t) + r(t) \qquad (9)$$

$\sigma(t)$ being the electronic component is real, and hence does not contribute to the imaginary part of $D(\omega)$, $Im[D(\omega)]$. $Im[D(\omega)]$, known as the Raman spectral density, contains all the information about the structural dynamics of a particular system. The electronic response, $\sigma(t)$, represents the magnitude of the electronic hyperpolarizability of the system. The nuclear response function, $r(t)$ in the time domain, is obtained from the inverse Fourier transform F^{-1} as follows:

$$r(t) = 2F^{-1}\{Im[D(\omega)]\}\varphi(t\text{-}t_0) \qquad (10)$$

$\varphi(t)$ being the Heaviside step function, assigned a value of unity.

Figure 3.9a shows the Raman spectral density of the PyPbBr$_3$ single crystals upon pre-resonant and non-resonant excitation by 400 nm and 800 nm laser pulses, respectively. Upon excitation by pump pulses, the Raman active modes are traced over a broad frequency range, from ~ 3 GHz to ~ 50 THz, probed by 800 nm pulses. The spectral density spreads over a frequency range that includes the collective correlated motions and the frustrated rotational motions of the aromatic cation, the collective vibrations of the PbBr$_3$ 1D cage, and the intramolecular motions of the pyridinium cation. Ion diffusion/migrations take place in the microsecond to nanosecond timescales, librations and restricted rotational processes take place in picosecond time scale and the intramolecular and intermolecular vibrations take place with time periods of tens to hundreds of femtoseconds.[64] Figure 3.9b shows a comparison of the ground-state linear Raman response and the Raman response of the non-resonant OKE signal. The ground state Raman mode frequencies match perfectly with those of non-resonant OKE signal, suggesting that indeed we probe the ground state vibrational modes by non-resonant excitation. Minor shifts in frequency might be because OKE spectroscopy is sensitive to the collective orientational correlation function while the linear Raman spectrum represents the single-molecule orientational correlation function.[57] Thus, our study clearly establishes that the STE formation is an excited state phenomenon with potential energy surfaces very different than the ground state.
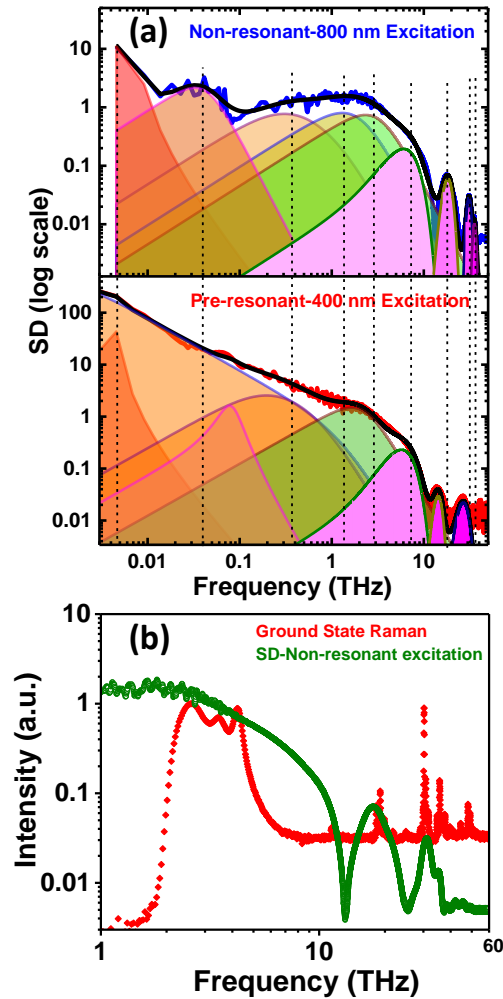
Figure 3.9: (a) Raman spectral density (SD) responses representing the nuclear motions of the $PyPbBr_3$ system upon pre-resonant (400 nm) and non-resonant (800 nm) pump excitation. A shift of vibrational modes is observed due to the vibrionic coupling of these to the transient carriers. (b) Comparison of the ground state Raman spectrum and the non-resonant excitation of $PyPbBr_3$.

To understand the vibrational mode compositions of the accessed frequencies, by non-resonant and pre-resonant excitations, a detailed line shape analysis was performed. From the appearance of the spectral density plots, we observe a considerable change in the line shapes for the pre-resonant and non-resonant excitation. The line shape analysis of the Raman spectral lines has been done by fitting the observed spectral density to the sum of multiple Anti-symmetrized Gaussian functions (ASG), the Lorentzian function, and the Brownian oscillators. Lorentz function has been used to fit the lowest region of the accessed frequency range. The time period of this frequency range is so large that it is beyond the scope of our instrument and hence the nature of such motions is not very clear and hence it was fixed around the frequency

range 0.001-0.008 THz. Brownian oscillators were used to fit the middle frequency range from tens of GHz to few THz. This frequency region mostly corresponds to the intermolecular motions of the aromatic cations and the inorganic lattice as a whole. Anti-symmetrized Gaussian functions were utilized to fit the higher frequency side of the spectral density plot (for frequency range above 5 THz to over 35 THz). This region corresponds to the intramolecular motions of the pyridinium cation. The choice of the type and number of fitting functions is variable for the systems with a broad spectral density plot.

3.3.6 Details of line shape analysis of SD plots

The Lorentz (LO) function is represented by the equation:[29]

$$I_{LO}(\omega) = A_L/\{(\omega-\omega_L)^2 + \triangle\,\omega_L^2\} \qquad (11)$$

where A_L, ω_L, and $\triangle\,\omega_L$ are the amplitude, characteristic frequency, and width of the Lorentz operator, respectively.

The Brownian oscillator (BO) function is represented by:[65]

$$I_{BO}(\omega) = \sum_i \left(\frac{A_{BO,j}\gamma_{BO,j}\omega}{(\omega_{BO,i}^2-\omega^2)^2+\gamma_{BO,i}^2\omega^2} \right) \qquad (12)$$

where $A_{BO,j}$, $\gamma_{BO,j}$, and $\omega_{BO,i}$ are the amplitude, damping parameter, and characteristic frequency, respectively, of the ith Brownian oscillator.

The Anti-symmetrized Gaussian (ASG) function is represented by:[66]

$$I_G(\omega) = A_G[\exp\{-2(\omega-\omega_G)^2/\triangle\,\omega_G^2\}-\exp\{-2(\omega+\omega_G)^2/\triangle\,\omega_G^2\}] \qquad (13)$$

where A_G, ω_G, and $\triangle\,\omega_G$ are the amplitude, characteristic frequency, and width of the ASG function, respectively. Because of the complexity of the spectral line shape, multiple fitting functions need to be summed to obtain a desirable fit.

The details of the fit for the low, middle, and high-frequency range of the non-resonant OKE spectrum at room temperature is given in Tables 3.5 and 3.6. For the intermediate frequency range, we obtain three peaks, namely, B1, B2, B3, and B4 centered at 0.042, 0.64, 1.90 and 3.18 THz. Similarly, for the high-frequency range the spectra can be fit to four Gaussian functions namely G1, G2, G3 and G4 centered at 6.00, 18.20, 31.00 and 35.50 THz, respectively.

Table 3.5: Room temperature pre-resonant and non-resonant fitting parameters of the spectral density in the lower and middle frequency range. (A is amplitude; L and B are the central frequencies (THz); d is width parameters (THz) in the corresponding functions).

	Lorentz function	Brownian oscillators			
	L1	B1	B2	B3	B4
RT- 800 nm	AL1 = 0.001	AB1 = 1.29	AB2 = 132	AB3 = 997.3	AB4 = 2400
	L1 = 0.006	B1 = 0.042	B2 = 0.64	B3 = 1.9	B4 = 3.18
	dL1 = 0.0001	dB1 = 0.06	dB2 = 1.54	dB3 = 3.16	dB4 = 4.77
RT- 400 nm	AL1 = 0.001	AB1 = 242.5	AB2 = 1.6	AB3 = 170.1	AB4 = 2246
	L1 = 0.004	B1 = 0.035	B2 = 0.081	B3 = 0.4	B4 = 2.2
	dL1 = 0.001	dB1= 1.25	dB2 = 0.05	dB3=0.95	dB4 = 3.18

Table 3.6: Room temperature pre-resonant and non-resonant fitting parameters of the spectral density in the higher frequency range. (AG is amplitude; G is the central frequency (THz); dG is width parameter (THz) in the corresponding functions).

	Anti-symmetrized Gaussian oscillators			
	G1	G2	G3	G4
RT- 800 nm	AG1= 0.2	AG2 = 0.06	AG3 = 0.03	AG4 = 0.01
	G1 = 6	G2 = 18.2	G3 = 31	G4 = 35.5
	dG1 = 3.2	dG2 = 2.8	dG3 = 2.3	dG4 = 2
RT- 400 nm	AG1 = 0.23	AG2 = 0.03	AG3 = 0.02	
	G1 = 5.7	G2 = 14.3	G3 = 27	
	dG1 = 2.7	dG2 = 1.9	dG3 = 4.7	

In order to understand the nature of the vibrational modes corresponding to the peaks in the non-resonant excitation (Figure 3.6a), we have computed the phonon density of states (computed only at the Γ-point of the BZ). In PyPbBr$_3$ the frequencies extend to about 100 THz (Figure 3.6a). To understand the contributions to each mode from the lead-bromide octahedra and the pyridinium cation, we have also computed the phonon density of states projected onto the Pb, Br and pyridinium cation. Our calculations show that in all the modes below 5 THz there is a coupling between the vibrations of the lead halide octahedron and the motion of the cation. While for the low-frequency region ($< \sim$ 2 THz) the vibrational modes are dominated primarily by the motions of the Pb-Br octahedra, those lying between 2 and 5 THz have significant contributions from the motions of the pyridinium cation and the Br ions. Based on

our calculations, we assign the peaks centered at B2 = 0.64 THz, B3 = 1.9 THz, and B4 = 3.18 THz to the coupled vibrational modes of the cation and the lead bromide octahedral. From the displacement patterns corresponding to these modes (shown in Tables 3.7 and 3.8), we note for most of these modes the cation undergoes a liberational motion coupled with the vibration of the lead octahedral chain. However, for B3 = 1.9 THz, we note that the phonon mode is also associated with the rotational motion of the 1D lead bromide octahedral chain coupled with the cationic liberational motion. The intramolecular modes of lead bromide lattice motions and the collective cation motions are overdamped with $\gamma \gg \omega$ (see Table 3.5 and 3.6). The high-frequency G2 = 18.2 THz, G3 = 31 THz and G4 = 35.5 THz in the non-resonant excitation spectra (Figure 3.9a) correspond to the intramolecular vibrational modes of the pyridinium cation as is evident from the displacement patterns shown in Tables 3.7 and 3.8. These intramolecular vibrational modes G2, G3, and G4 are underdamped with damping factor γ much less than the central frequency ω ($\gamma \ll \omega$, see Tables 3.5 and 3.6).

In addition to these modes, the fit to the experimental spectrum yield two more modes, namely, an extremely soft mode in the lower end of the intermediate frequency range (B1=0.042 THz) and the second one in the high-frequency range (G1=6 THz). While B1, like the other modes in that frequency range, is also over-damped, G1, unlike the other high-frequency modes is critically damped ($\omega = 2\gamma$). However, we do not observe similar modes in our calculations. The low-frequency B1 mode may arise from anharmonic effects that are not considered in our calculations.

Upon pre-resonant excitation, the transient excited state/virtual state vibrational modes undergo a red-shift in frequencies. This shift is most probably due to the coupling of these modes to the generated excitons, upon photo-irradiation. The transient state of PyPbBr$_3$ formed by pre-resonant excitation may have coupling interactions leading to a decrease in bond strengths and hence a red shift of frequencies. Because the process of STE formation occurs in the excited state, the interacting phonon modes become weaker in bond strengths and there is a decrease in force constants, hence a red-shift in frequency. A dramatic shift is observed in the intramolecular modes corresponding to the pyridinium cation. The central frequencies shift to G1 = 5.7 THz, G2 = 14.3 THz and G3 = 27 THz. The G4 upon red-shifting merges with the G3 and cannot be resolved separately. This leads to an increase in the dampening factor of G3 (Table 3.6). Here also intramolecular vibrational modes G2, and G3 are underdamped with damping factor γ much less than the central frequency ω ($\gamma \ll \omega$, see Table 3.6) while G1

remains critically damped ($\omega = 2\gamma$). The intermolecular vibrational modes of the lead bromide lattice are red-shifted in frequency spectra as well, being centered at B2 = 0.081 THz, B3 = 0.40 THz, and B4 = 2.2 THz. The inter-molecular collective cation motion, due to non-covalent interactions between pyridinium cations, centered at B1 = 0.035 THz also redshifts in frequency. The intermolecular modes remain overdamped with $\gamma \gg \omega$. The overall intensity of SD Raman plots also changes considerably in the lower frequency GHz region below 100 GHz. This frequency region, mostly representing the halide migration and cation diffusive reorientations, shows about a ten-fold enhanced Raman intensity. This increased intensity may be possibly due to higher dipole moment being developed by 400 nm laser pulses and hence a higher rate of dipole-induced diffusion of ions as compared to excitation by 800 nm laser pulses. This may be because of the enhanced polarizability contributed by the excited stationary state (the excitonic state).

Table 3.7: Anisotropic displacement parameters ($Å^2 x\ 10^3$) for PyPbBr$_3$.

The anisotropic displacement factor exponent takes the form: $-2p^2[\ h^2a^{*2}U11 + ... + 2\ h\ k\ a^*\ b^*\ U12]$

	U11	U22	U33	U23	U13	U12
Pb(1)	13(1)	12(1)	9(1)	0(1)	0(1)	1(1)
Br(1)	11(1)	17(1)	46(1)	-1(3)	-1(3)	2(1)
Br(2)	16(1)	14(1)	58(2)	-5(2)	4(3)	-5(1)
Br(3)	12(1)	10(1)	148(3)	11(4)	-1(5)	1(1)
N(1)	42(12)	26(8)	29(7)	9(7)	3(9)	10(9)
C(2)	22(5)	20(4)	25(5)	5(6)	1(7)	-3(4)
C(3)	22(5)	20(4)	25(5)	5(6)	1(7)	-3(4)
C(4)	22(5)	20(4)	25(5)	5(6)	1(7)	-3(4)
C(5)	22(5)	20(4)	25(5)	5(6)	1(7)	-3(4)
C(6)	22(5)	20(4)	25(5)	5(6)	1(7)	-3(4)

Table 3.8: Hydrogen coordinates (x 104) and isotropic displacement parameters (Å^2x 103) for PyPbBr$_3$.

	x	y	z	U(eq)
H(1)	4247	8601	5059	39
H(2)	4346	8421	8012	27
H(3)	3560	10165	9687	27
H(4)	2698	12038	8360	27
H(5)	2623	12166	5358	27
H(6)	3409	10421	3682	27

3.3.7 Carrier-phonon coupling

The creation of STEs is usually associated with lattice deformability and electron-phonon coupling (EPC). The STEs are associated with distortions in the lattice in the excited state. However, in literature, their formation is studied through the study of the formation of self-trapped electrons and holes that are localized at specific lattice sites by their own distortion field. Moreover, in most cases, these distortions are quite random and are based on the fact that in normal lead halides there is the formation of dimers, etc. In this work, we use a novel approach. Since EPC plays an important role, we have computed the imaginary part of the mode-resolved electron-phonon self-energy for the valence and conduction band. The phonon modes that strongly couple with the electronic state will have a larger contribution to the imaginary part of the electron-phonon self-energy. We use this information to identify the relevant phonon mode. The eigenvector corresponding to this phonon mode provides us the direction of the distortion to be applied to the lattice to observe the trapping of electrons and holes. The phonon-resolved (showing only the dominant contributions) imaginary part of the self-energy is shown in Figure 3.10a and 3.10b for the valence and conduction bands, respectively. For both cases, we find that the modes which involve coupled motions of the lead-halide octahedral and the pyridinium cation couple strongly with the electronic states in the valence and conduction band. At the band edges, i.e VBM at Γ-point and CBM at T-point, the electronic states show the strongest coupling with the phonon mode having a frequency of 1.03 THz. The displacement pattern corresponding to this mode is shown in Table 3.9.
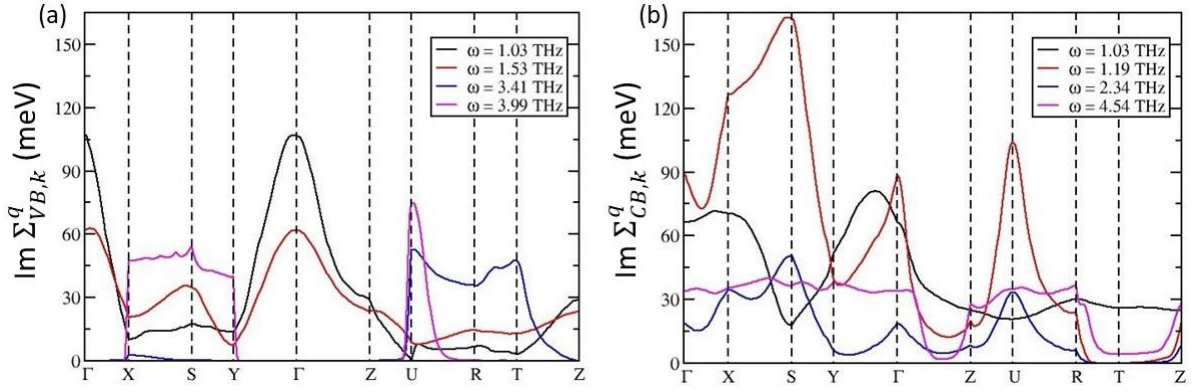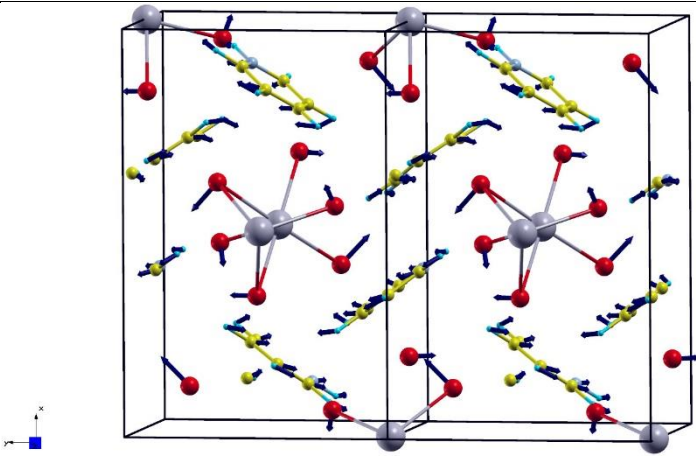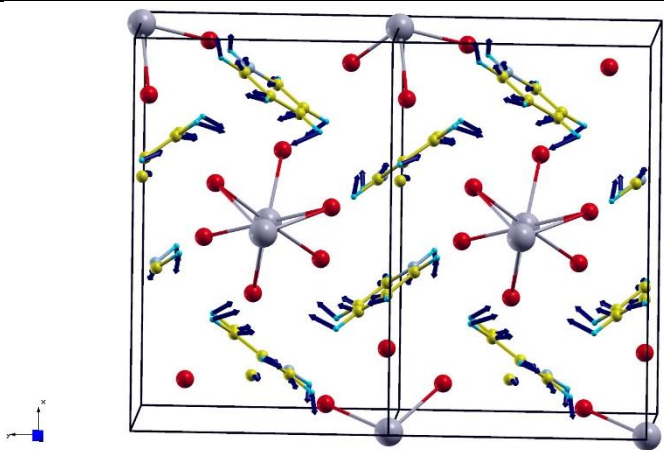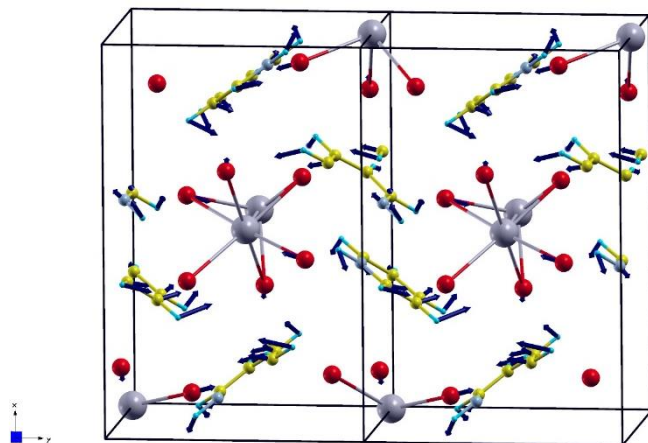
Figure 3.10: Phonon resolved imaginary part of the electron-phonon self-energy ($\Sigma_{n,k}^{q}$) for the highest energy valence band (a) and lowest energy conduction band (b).

Table 3.9: Representative displacement patterns corresponding to the vibrational modes.

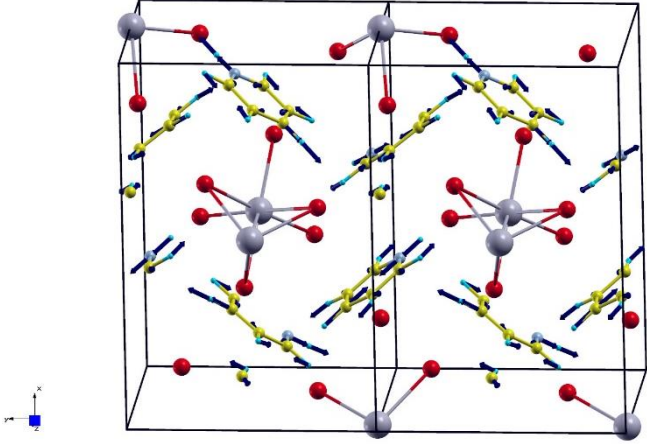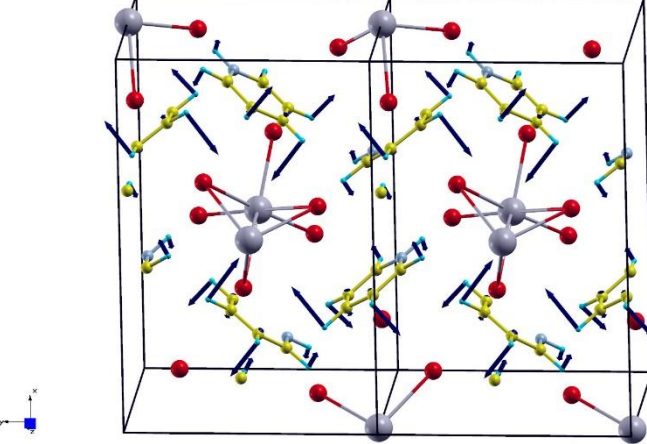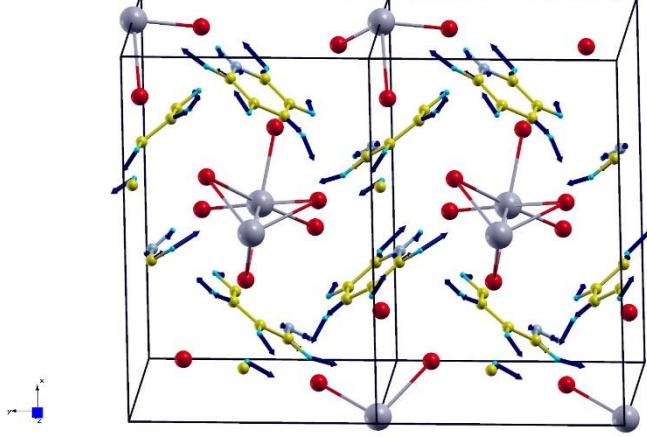| Experimental frequency (THz)	Computed frequency (THz)	Displacement patterns
0.64	0.72	
	0.82	

1.9	1.85	
3.18	2.84	
	3.42	

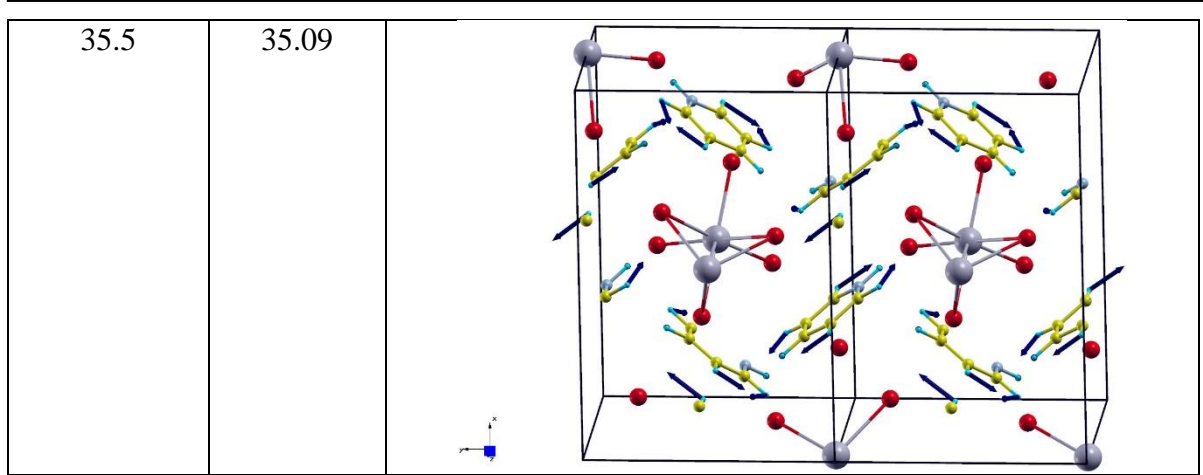|		
18.2	18.19	
31	30.23	
	30.65	

35.5	35.09	

Table 3.10: Change in energy (ΔE) with respect to the undistorted structure, Pb-Pb distance d_{Pb-Pb}, band gap (E_g), and positions of VBM and CBM in the BZ as a function of deformation (δ) along the eigenvector corresponding to mode with ω =1.03 THz.

Displacement (δ)(Å)	ΔE (eV)	d_{Pb-Pb} (Å)	E_g (eV)	Position of VBM	Position of CBM
0.0	0.00	3.91	2.29	G	T
0.5	0.123	3.87	2.23	G	T
1.0	0.547	3.84	2.14	G->Z	T->R
1.5	1.264	3.80	2.02	G->Z	R
2.0	2.291	3.76	1.89	G->Z*	R
2.5	3.662	3.73	1.67	S->R*	R
3.0	5.432	3.69	1.42	R	S->R*

This tells us that the self-trapping of electrons and holes will be associated with lattice deformation along the eigenvector corresponding to this mode. Based on this result, we induced lattice deformation by displacing the atoms in the unit cell along the eigenvector and observed the evolution of the band gap, the positions of VBM and CBM and the corresponding wavefunctions (Table 3.10). We note that as the deformation increases, not only do the positions of the VBM and CBM increase but also the band gap is reduced. Further, this

deformation is also associated with the shortening of the Pb-Pb distance. The evolution of the wavefunction corresponding to the VBM and CBM as the lattice is deformed is shown in Figure 3.11. We find that a slight displacement (in the multidimensional configurational space) of about 0.5 Å results in the localization of the CBM. In contrast with the undistorted case where the CBM is delocalized on all the pyridinium cations, at $\delta = 0.5$ Å the CBM is localized only on two of the pyridinium cations. A similar situation prevails for the wavefunction corresponding to the CBM for larger amount of lattice deformation. In contrast, we observe that it is quite difficult to localize the hole (wavefunction corresponding to VBM). The hole begins to localize when $\delta = 2.0$ Å and is completely localized on a few Br ions of the Pb-Br octahedral for $\delta = 3.0$ Å. Our results suggest that while the self-trapping of electrons in this system is easy, the self-trapping of holes is relatively difficult.
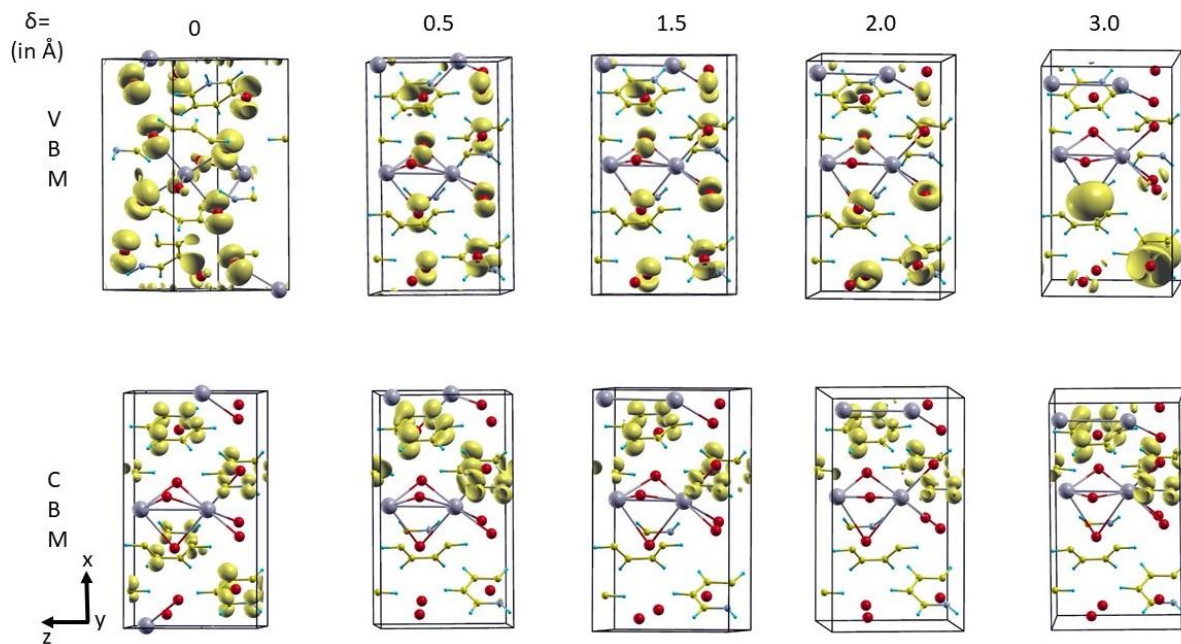

Figure 3.11: Evolution of the wavefunction at the VBM (top panel) and CBM (bottom panel) as a function of lattice distortion.

3.4 Conclusion

In conclusion, we have synthesized a perovskite system with highly planar asymmetric aromatic Pyridinium cation, which formed a face shared 1D-perovskite lattice. The photoluminescence emission from this 1D system was highly red-shifted from its band gap excitation due to the formation of self-trapped excitons. We utilized the ultrafast spectroscopic technique, OKE spectroscopy, to directly probe the origin of the self-trapped exciton formation

in the time domain. Upon Fourier analysis, we obtain Raman spectral density plots composed of all the polarizable vibrational modes in non-resonant and pre-resonant conditions to unravel the modes undergoing vibrionic coupling with the excitons. We observed a red shift in the phonon mode frequencies in the excited state as compared to the ground state. The composition of these phonon modes was revealed by DFT calculations. DFT calculations reveal that CBM is predominantly composed of pyridinium orbitals and hence this A-site cation will affect the optical properties of the system. We observe that the strong contributions from the cation motions together with the lattice motions couple with the generated excitons to form the self-trapped excitonic states in the 1D-perovskite systems. Thus, the role of A-site cation is not merely restricted to dimensionality modification, rather it strongly affects the optoelectronic properties in pyridinium lead bromide single crystals.

3.5 References

1. Xing, G.; Mathews, N.; Sun, S.; Lim, S. S.; Lam, Y. M.; Grätzel, M.; Mhaisalkar, S.; Sum, T. C., Long-Range Balanced Electron- and Hole-Transport Lengths in Organic-Inorganic $CH_3NH_3PbI_3$. *Science* **2013**, *342*, 344-347.

2. Walsh, A.; Scanlon, D. O.; Chen, S.; Gong, X. G.; Wei, S.-H., Self-Regulation Mechanism for Charged Point Defects in Hybrid Halide Perovskites. *Angew. Chem. Int. Ed.* **2015**, *54*, 1791-1794.

3. Dong, Q.; Fang, Y.; Shao, Y.; Mulligan, P.; Qiu, J.; Cao, L.; Huang, J., Electron-Hole Diffusion Lengths >175 µm in Solution-Grown $CH_3NH_3PbI_3$ Single Crystals. *Science* **2015**, *347*, 967-970.

4. Stoumpos, C. C.; Kanatzidis, M. G., The Renaissance of Halide Perovskites and Their Evolution as Emerging Semiconductors. *Acc. Chem. Res.* **2015**, *48*, 2791-2802.

5. Shi, D., et al., Low Trap-State Density and Long Carrier Diffusion in Organolead Trihalide Perovskite Single Crystals. *Science* **2015**, *347*, 519.

6. Yettapu, G. R.; Talukdar, D.; Sarkar, S.; Swarnkar, A.; Nag, A.; Ghosh, P.; Mandal, P., Terahertz Conductivity within Colloidal $CsPbBr_3$ Perovskite Nanocrystals: Remarkably High Carrier Mobilities and Large Diffusion Lengths. *Nano Lett.* **2016**, *16*, 4838-4848.

7. Chen, Y.; Yi, H. T.; Wu, X.; Haroldson, R.; Gartstein, Y. N.; Rodionov, Y. I.; Tikhonov, K. S.; Zakhidov, A.; Zhu, X. Y.; Podzorov, V., Extended Carrier Lifetimes and Diffusion in Hybrid Perovskites Revealed by Hall Effect and Photoconductivity Measurements. *Nat. Commun.* **2016**, *7*, 12253.

8. Zhang, W.; Eperon, G. E.; Snaith, H. J., Metal Halide Perovskites for Energy Applications. *Nat. Energy* **2016**, *1*, 16048.

9. Xu, F.; Zhang, T.; Li, G.; Zhao, Y., Mixed Cation Hybrid Lead Halide Perovskites with Enhanced Performance and Stability. *J. Mater. Chem. A* **2017**, *5*, 11450-11461.

10. Sadhanala, A., et al., Blue-Green Color Tunable Solution Processable Organolead Chloride–Bromide Mixed Halide Perovskites for Optoelectronic Applications. *Nano Lett.* **2015**, *15*, 6095-6101.

11. Fu, Y.; Zhu, H.; Stoumpos, C. C.; Ding, Q.; Wang, J.; Kanatzidis, M. G.; Zhu, X.; Jin, S., Broad Wavelength Tunable Robust Lasing from Single-Crystal Nanowires of Cesium Lead Halide Perovskites ($CsPbX_3$, X = Cl, Br, I). *ACS Nano* **2016**, *10*, 7963-7972.

12. Sutton, R. J., et al., Bandgap-Tunable Cesium Lead Halide Perovskites with High Thermal Stability for Efficient Solar Cells. *Adv. Energy Mater.* **2016**, *6*, 1502458.

13. Freppon, D. J.; Men, L.; Burkhow, S. J.; Petrich, J. W.; Vela, J.; Smith, E. A., Photophysical Properties of Wavelength-Tunable Methylammonium Lead Halide Perovskite Nanocrystals. *J Mater. Chem. C* **2017**, *5*, 118-126.

14. Rehman, W.; McMeekin, D. P.; Patel, J. B.; Milot, R. L.; Johnston, M. B.; Snaith, H. J.; Herz, L. M., Photovoltaic Mixed-Cation Lead Mixed-Halide Perovskites: Links between Crystallinity, Photo-Stability and Electronic Properties. *Energy Environ. Sci.* **2017**, *10*, 361-369.

15. Rosales, B. A.; Hanrahan, M. P.; Boote, B. W.; Rossini, A. J.; Smith, E. A.; Vela, J., Lead Halide Perovskites: Challenges and Opportunities in Advanced Synthesis and Spectroscopy. *ACS Energy Lett.* **2017**, *2*, 906-914.

16. Binyamin, T.; Pedesseau, L.; Remennik, S.; Sawahreh, A.; Even, J.; Etgar, L., Fully Inorganic Mixed Cation Lead Halide Perovskite Nanoparticles: A Study at the Atomic Level. *Chem. Mater.* **2020**, *32*, 1467-1474.

17. Jana, A.; Ba, Q.; Kim, K. S., Compositional and Dimensional Control of 2D and Quasi-2D Lead Halide Perovskites in Water. *Adv. Funct. Mater.* **2019**, *29*, 1900966.

18. Zheng, K.; Pullerits, T., Two Dimensions Are Better for Perovskites. *J. Phys. Chem. Lett.* **2019**, *10*, 5881-5885.

19. Sheikh, T.; Maqbool, S.; Mandal, P.; Nag, A., Introducing Intermolecular Cation-Π Interactions for Water-Stable Low Dimensional Hybrid Lead Halide Perovskites. *Angew. Chem. Int. Ed.* **2021**, *60*, 18265-18271.

20. Mitzi, D. B., Templating and Structural Engineering in Organic–Inorganic Perovskites. *J. Chem. Soc., Dalton Trans.* **2001**, 1-12.

21. Katan, C.; Mercier, N.; Even, J., Quantum and Dielectric Confinement Effects in Lower-Dimensional Hybrid Perovskite Semiconductors. *Chem. Rev.* **2019**, *119*, 3140-3192.

22. Smith, M. D.; Karunadasa, H. I., White-Light Emission from Layered Halide Perovskites. *Acc. Chem. Res.* **2018**, *51*, 619-627.

23. Maqbool, S.; Sheikh, T.; Thekkayil, Z.; Deswal, S.; Boomishankar, R.; Nag, A.; Mandal, P., Third Harmonic Upconversion and Self-Trapped Excitonic Emission in 1D Pyridinium Lead Iodide. *J. Phys. Chem. C* **2021**, *125*, 22674-22683.

24. Yuan, Z., et al., One-Dimensional Organic Lead Halide Perovskites with Efficient Bluish White-Light Emission. *Nat. Commun.* **2017**, *8*, 14051.

25. Righini, R., Ultrafast Optical Kerr Effect in Liquids and Solids. *Science* **1993**, *262*, 1386.

26. McMorrow, D.; Lotshaw, W. T.; Kenney-Wallace, G. A., Femtosecond Optical Kerr Studies on the Origin of the Nonlinear Responses in Simple Liquids. *IEEE J. Quantum Electron.* **1988**, *24*, 443-454.

27. Stoumpos, C. C.; Cao, D. H.; Clark, D. J.; Young, J.; Rondinelli, J. M.; Jang, J. I.; Hupp, J. T.; Kanatzidis, M. G., Ruddlesden–Popper Hybrid Lead Iodide Perovskite 2D Homologous Semiconductors. *Chem. Mater.* **2016**, *28*, 2852-2867.

28. Eickhoff, T.; Grosse, P.; Theiss, W., Diffuse Reflectance Spectroscopy of Powders. *Vib. Spectrosc.* **1990**, *1*, 229-233.

29. Kakinuma, S.; Shirota, H., Femtosecond Raman-Induced Kerr Effect Study of Temperature-Dependent Intermolecular Dynamics in Pyrrolidinium-Based Ionic Liquids: Effects of Anion Species. *J. Phys. Chem. B* **2019**, *123*, 1307-1323.

30. Li, J.; Fruchey, K.; Fayer, M. D., Dynamics of a Discotic Liquid Crystal in the Isotropic Phase. *J. Chem. Phys.* **2006**, *125*, 194901.

31. Torre, R.; Sánta, I.; Righini, R., Pre-Transitional Effects in the Liquid-Plastic Phase Transition of P-Terphenyl. *Chem. Phys. Lett.* **1993**, *212*, 90-95.

32. Turton, D. A.; Senn, H. M.; Harwood, T.; Lapthorn, A. J.; Ellis, E. M.; Wynne, K., Terahertz Underdamped Vibrational Motion Governs Protein-Ligand Binding in Solution. *Nat. Commun.* **2014**, *5*, 3999.

33. Giraud, G.; Karolin, J.; Wynne, K., Low-Frequency Modes of Peptides and Globular Proteins in Solution Observed by Ultrafast Ohd-Rikes Spectroscopy. *Biophys. J.* **2003**, *85*, 1903-1913.

34. Giraud, G.; Wynne, K., Time-Resolved Optical Kerr-Effect Spectroscopy of Low-Frequency Dynamics in Di-L-Alanine, Poly-L-Alanine, and Lysozyme in Solution. *J. Am. Chem. Soc.* **2002**, *124*, 12110-12111.

35. González-Jiménez, M.; Ramakrishnan, G.; Harwood, T.; Lapthorn, A. J.; Kelly, S. M.; Ellis, E. M.; Wynne, K., Observation of Coherent Delocalized Phonon-Like Modes in DNA under Physiological Conditions. *Nat. Commun.* **2016**, *7*, 11799.

36. Hithell, G.; González-Jiménez, M.; Greetham, G. M.; Donaldson, P. M.; Towrie, M.; Parker, A. W.; Burley, G. A.; Wynne, K.; Hunt, N. T., Ultrafast 2D-IR and Optical Kerr Effect Spectroscopy Reveal the Impact of Duplex Melting on the Structural Dynamics of DNA. *Phys. Chem. Chem. Phys.* **2017**, *19*, 10333-10342.

37. Taschin, A.; Bartolini, P.; Eramo, R.; Righini, R.; Torre, R., Optical Kerr Effect of Liquid and Supercooled Water: The Experimental and Data Analysis Perspective. *J. Chem. Phys.* **2014**, *141*, 084507.

38. Miyata, K.; Meggiolaro, D.; Trinh, M. T.; Joshi, P. P.; Mosconi, E.; Jones, S. C.; De Angelis, F.; Zhu, X.-Y., Large Polarons in Lead Halide Perovskites. *Sci. Adv.* **2017**, *3*, e1701217.

39. Miyata, K.; Atallah, T. L.; Zhu, X.-Y., Lead Halide Perovskites: Crystal-Liquid Duality, Phonon Glass Electron Crystals, and Large Polaron Formation. *Sci. Adv.* **2017**, *3*, e1701469.

40. Zhang, W.-F.; Pan, H.-M.; Ma, Y.-Y.; Li, D.-Y.; Jing, Z., One-Dimensional Corner-Sharing Perovskites: Syntheses, Structural Evolutions and Tunable Photoluminescence Properties. *J. Mol. Struct.* **2022**, *1253*, 132221.

41. Ma, Y.-Y.; Pan, H.-M.; Li, D.-Y.; Liu, Y.-H.; Lu, T.; Lei, X.-W.; Jing, Z., Two-Dimensional Hybrid Halide Perovskites Composed of Mixed Corner- and Edge-Shared Octahedron as Broadband Yellow-Light Emissions. *Inorg. Chem. Commun.* **2022**, *139*, 109411.

42. Nicholas, A. D.; Garman, L. C.; Albano, N.; Cahill, C. L., Insight on Noncovalent Interactions and Orbital Constructs in Low-Dimensional Antimony Halide Perovskites. *Phys. Chem. Chem. Phys.* **2022**, *24*, 15305-15320.

43. Mitzi, D. B.; Dimitrakopoulos, C. D.; Kosbar, L. L., Structurally Tailored Organic−Inorganic Perovskites: Optical Properties and Solution-Processed Channel Materials for Thin-Film Transistors. *Chem. Mater.* **2001**, *13*, 3728-3740.

44. Park, I.-H., et al., Highly Stable Two-Dimensional Tin(II) Iodide Hybrid Organic–Inorganic Perovskite Based on Stilbene Derivative. *Adv. Funct. Mater.* **2019**, *29*, 1904810.

45. Selivanov, N. I.; Murashkina, A. A.; Kevorkyants, R.; Emeline, A. V.; Bahnemann, D. W., Pyridinium Lead Tribromide and Pyridinium Lead Triiodide: Quasi-One-Dimensional Perovskites with an Optically Active Aromatic π-System. *Dalton Trans.* **2018**, *47*, 16313-16319.

46. Liao, W.-Q.; Zhang, Y.; Hu, C.-L.; Mao, J.-G.; Ye, H.-Y.; Li, P.-F.; Huang, S. D.; Xiong, R.-G., A Lead-Halide Perovskite Molecular Ferroelectric Semiconductor. *Nat. Commun.* **2015**, *6*, 7338.

47. Laxmi; Kabra, D., Origin of Contrasting Emission Spectrum of Bromide Versus Iodide Layered Perovskite Semiconductors. *J. Phys. Chem. Lett.* **2022**, *13*, 2737-2743.

48. Dohner, E. R.; Jaffe, A.; Bradshaw, L. R.; Karunadasa, H. I., Intrinsic White-Light Emission from Layered Hybrid Perovskites. *J. Am. Chem. Soc.* **2014**, *136*, 13154-13157.

49. Mao, L.; Guo, P.; Kepenekian, M.; Hadar, I.; Katan, C.; Even, J.; Schaller, R. D.; Stoumpos, C. C.; Kanatzidis, M. G., Structural Diversity in White-Light-Emitting Hybrid Lead Bromide Perovskites. *J. Am. Chem. Soc.* **2018**, *140*, 13078-13088.

50. Zhou, C.; Tian, Y.; Khabou, O.; Worku, M.; Zhou, Y.; Hurley, J.; Lin, H.; Ma, B., Manganese-Doped One-Dimensional Organic Lead Bromide Perovskites with Bright White Emissions. *ACS Appl. Mater. Interfaces* **2017**, *9*, 40446-40451.

51. Wu, G., et al., A One-Dimensional Organic Lead Chloride Hybrid with Excitation-Dependent Broadband Emissions. *ACS Energy Lett.* **2018**, *3*, 1443-1449.

52. Akkerman, Q. A.; Rainò, G.; Kovalenko, M. V.; Manna, L., Genesis, Challenges and Opportunities for Colloidal Lead Halide Perovskite Nanocrystals. *Nat. Mater.* **2018**, *17*, 394-405.

53. Benin, B. M.; Dirin, D. N.; Morad, V.; Wörle, M.; Yakunin, S.; Rainò, G.; Nazarenko, O.; Fischer, M.; Infante, I.; Kovalenko, M. V., Highly Emissive Self-Trapped Excitons in Fully Inorganic Zero-Dimensional Tin Halides. *Angew. Chem. Int. Ed.* **2018**, *57*, 11329-11333.

54. Pan, F.; Li, J.; Ma, X.; Nie, Y.; Liu, B.; Ye, H., Free and Self-Trapped Exciton Emission in Perovskite $CsPbBr_3$ Microcrystals. *RSC Adv.* **2022**, *12*, 1035-1042.

55. Gautier, R.; Paris, M.; Massuyeau, F., Exciton Self-Trapping in Hybrid Lead Halides: Role of Halogen. *J. Am. Chem. Soc.* **2019**, *141*, 12619-12623.

56. Chakraborty, R.; Nag, A., Correlation of Dielectric Confinement and Excitonic Binding Energy in 2D Layered Hybrid Perovskites Using Temperature Dependent Photoluminescence. *J. Phys. Chem. C* **2020**, *124*, 16177-16185.

57. Loughnane, B. J.; Scodinu, A.; Fourkas, J. T., Temperature-Dependent Optical Kerr Effect Spectroscopy of Aromatic Liquids. *J. Phys. Chem. B* **2006**, *110*, 5708-5720.

58. Turton, D. A.; Wynne, K., Universal Nonexponential Relaxation: Complex Dynamics in Simple Liquids. *J. Chem. Phys.* **2009**, *131*, 201101.

59. Königsmann, F.; Fushitani, M.; Owschimikow, N.; Anderson, D. T.; Schwentner, N., Femtosecond Pump-Probe 2d Optical Kerr Effect Spectroscopy of Molecular Hydrogen Crystals. *Chem. Phys. Lett.* **2008**, *458*, 303-307.

60. Zhu, H.; Miyata, K.; Fu, Y.; Wang, J.; Joshi, P. P.; Niesner, D.; Williams, K. W.; Jin, S.; Zhu, X.-Y., Screening in Crystalline Liquids Protects Energetic Carriers in Hybrid Perovskites. *Science* **2016**, *353*, 1409-1413.

61. Zhong, Q.; Fourkas, J. T., Optical Kerr Effect Spectroscopy of Simple Liquids. *J. Phys. Chem. B* **2008**, *112*, 15529-15539.

62. McMorrow, D., Separation of Nuclear and Electronic Contributions to Femtosecond Four-Wave Mixing Data. *Opt. Commun.* **1991**, *86*, 236-244.

63. Smith, N. A.; Meech, S. R., Optically-Heterodyne-Detected Optical Kerr Effect (OHD-OKE): Applications in Condensed Phase Dynamics. *Int. Rev. Phys. Chem.* **2002**, *21*, 75-100.

64. Herz, L. M., How Lattice Dynamics Moderate the Electronic Properties of Metal-Halide Perovskites. *J. Phys. Chem. Lett.* **2018**, *9*, 6853-6863.

65. Shirota, H., Comparison of Low-Frequency Spectra between Aromatic and Nonaromatic Cation Based Ionic Liquids Using Femtosecond Raman-Induced Kerr Effect Spectroscopy. *ChemPhysChem* **2012**, *13*, 1638-1648.

66. Smith, N. A.; Lin, S.; Meech, S. R.; Shirota, H.; Yoshihara, K., Ultrafast Dynamics of Liquid Anilines Studied by the Optical Kerr Effect. *J. Phys. Chem. A* **1997**, *101*, 9578-9586.

Chapter 4

# Third Harmonic Up-Conversion in Lower Dimensional 1D Pyridinium Lead Iodide Perovskite

The work presented in this chapter has been published in the Journal of Physical Chemistry C with the following details:

Maqbool, S.; Sheikh, T.; Thekkayil, Z.; Deswal, S.; Boomishankar, R.; Nag, A.; Mandal, P.; Third Harmonic Up-conversion and Self-Trapped Excitonic Emission in 1D Pyridinium Lead Iodide*. J. Phys. Chem. C* **2021**, *125, 41, 22674–22683*.

Chapter 4
Third Harmonic Up-Conversion in Lower Dimensional 1D Pyridinium Lead Iodide Perovskite

Abstract

Hybrid lead halide perovskites have emerged as an important class of optoelectronic materials. A creative choice of 'A' site organic cations produces hybrid perovskites with reduced dimensionality and intriguing light-matter interactions. Nonlinear optical effects are expected to be stronger in one-dimensional (1D) lead halides compared to their 2D or 3D analogues due to greater quantum and dielectric confinements. We performed an extensive probe of the third harmonic generation (THG) properties in 1D pyridinium lead iodide single crystals for the first time. An efficient THG with a high laser-induced damage threshold is the highlight of this system. THG is selectively enhanced for excitation at optical communication wavelength (1.5 microns) corresponding to bandgap resonance.

Graphical Abstract
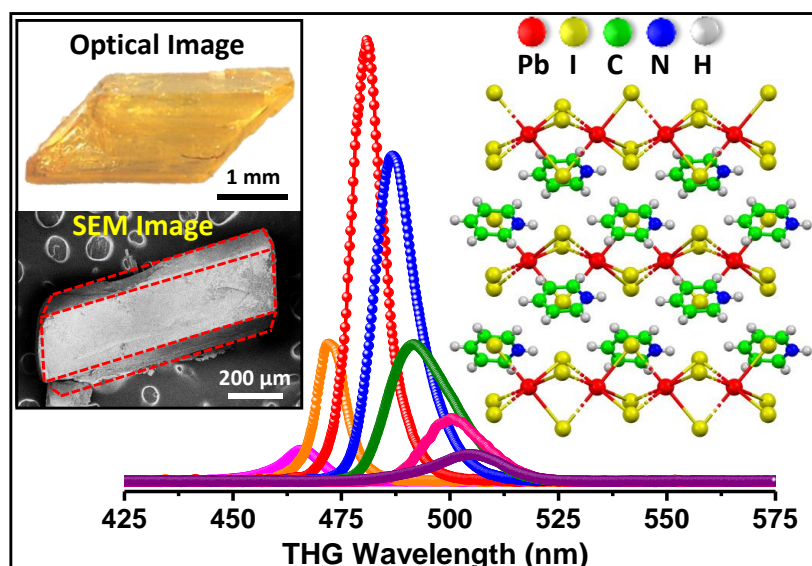
4.1 Introduction

Lead halide perovskites (LHPs) showcase semiconductor and carrier transport properties ideal for next-generation photovoltaics.[1-7] They also exhibit excellent response in the linear[8-10] and nonlinear optical (NLO)[11-17] regimes. Due to the substantial quantum and dielectric confinement, the lower-dimensional (LD) perovskitoids[18] show strong excitonic effects and interesting linear optical properties.[2, 19-23] Similarly, the NLO properties of these LD lead halides are highly enhanced compared to the 3D perovskites.[12, 14-15, 17] In this chapter, we demonstrate a highly enhanced NLO response in the form of third-harmonic generation (THG) in face-shared one-dimensional (1D) pyridinium lead iodide (PyPbI$_3$) single-crystals.

Nonlinear optics are essential for photon energy conversion, light manipulation, and detection in photonics and other optical technologies.[24-25] Therefore, materials with high NLO coefficients are of explicit importance. Second-order NLO processes like second harmonic generation (SHG) have been studied extensively due to their application in frequency doubling.[26-30] The third-order nonlinear susceptibility $\chi^{(3)}$ of a material determines important nonlinear properties such as two-photon absorption, Optical Kerr Effect (OKE), THG, saturable absorption, etc. THG is one of the most convenient processes to study the third order NLO characteristics of a material and has essential applications in laser frequency up-conversion. The commercial materials currently used for frequency tripling involve a 2-step process, employing SHG, followed by sum-frequency generation (SFG).[31] Hence, there is a broad scope for developing materials with efficient THG for a single-step frequency tripling. Two-dimensional (2D) perovskitoids, because of their strong quantum and dielectric confinement, show highly enhanced THG response at the excitonic resonance compared to their 3D counterparts.[14] Further enhancement in the THG response is expected in 1D perovskitoids due to stronger quantum and dielectric confinement. However, as per our knowledge, there was no report of THG in 1D lead halides until a very recent report by us.[32] Herein, we demonstrate a highly enhanced THG in PyPbI$_3$ single crystals. This is the first comprehensive report of THG from any 1D-perovskitoid system to the best of our knowledge. PyPbI$_3$ single crystals show highly selective enhancement in THG for the band-edge excitations with a remarkably high laser-induced damage threshold (LIDT). The selectively enhanced THG with high LIDT makes PyPbI$_3$ and similar 1D perovskitoids potential candidates for energy up-conversion and photo-detection for next-generation photonic devices in the crucial frequency range of IR communication.

4.2 Experimental Section

4.2.1 Chemicals

Hydroiodic acid (HI, Sigma Aldrich, 57% w/w in H_2O, 99.9%), lead oxide (Sigma Aldrich, 99.9%), pyridinium bromide (Sigma Aldrich, 99.9%), hypophosphorous acid (H_3PO_2, Avra, 50% w/w H_2O), acetone (Rankem, 99.5%).

4.2.2 Synthesis of 1D pyridinium lead iodide ($PyPbI_3$) single crystals

Single crystals of pyridinium lead iodide were synthesized by following a previously reported method.[33] 10 mmol (2232 mg) of PbO was dissolved in a mixture of 57% w/w aqueous HI solution (15 mL) and 50% aqueous H_3PO_2 (1.7 mL) by heating to 100 ˚C under constant magnetic stirring for 10 minutes. A transparent yellow solution was obtained. To this solution, 10 mmol of pyridinium iodide (synthesized by treating pyridinium bromide with an excess of HI) was added while heating was continued until the solution became clear. The solution was allowed to cool down to room temperature naturally. While cooling, bright yellow needle-shaped crystals started to crystalize. The obtained crystals were filtered, rinsed with acetone, and dried under reduced pressure.

4.2.3 Characterization

Single-crystal X-ray diffraction (SCXRD) data were recorded on a Bruker Smart Apex Duo diffractometer at 100 K using Mo Kα radiation (λ = 0.71073 Å). The frames were integrated with the Bruker SAINT Software package using a narrow-frame algorithm. The structures were solved by direct method and refined by full-matrix least-squares on F2 using the SHELXTL software. All the atoms were refined anisotropically.

Powder X-ray Diffraction (PXRD) data were recorded on Bruker D8 Advance X-ray diffractometer using Cu Kα radiation (1.54 Å). Scanning Electron Microscopy (SEM) images were recorded on the Zeiss Ultra Plus FESEM instrument.

4.2.4 Third harmonic generation (THG)

The THG experiments were conducted using a 250-2600 nm wavelength tunable TOPAS-C Optical Parametric Amplifier (OPA, Light Conversion) powered by a regenerative Spitfire Pro XP amplifier (Spectra-Physics) generating pulses of 45 fs (FWHM), with 800 nm central wavelength at 1 kHz repetition rate. The amplifier was seeded by Tsunami Oscillator (Spectra-Physics). The experiments were performed in the wavelength range of 1200-1600 nm. An 850

nm long-pass filter was used to ensure the purity of the pump beam. A variable density N.D. filter was used for power-dependent measurements. The beam was focused using a 200 mm plano-convex lens, and the sample was kept at a distance of 135 mm from the lens. The sample was kept away from the focus so that it is not damaged during the experiment and to ensure enough spot size for the interaction of the sample and the pump beam to provide a good signal strength. The sample was placed on a threaded cage rotation mount (THORLABS CRM1/M) so that it could be rotated accordingly to orient the crystallographic planes for maximum interaction with the pump optical field to get maximum output. The output signal was collimated using a 25 mm plano-convex lens, and a 750 nm short-pass filter was used to eliminate any signal contribution from the pump beam. The signal was coupled to a 400 μm optical fiber and recorded using a miniature spectrometer (USB4000, Ocean Optics). The obtained signal in arbitrary units (counts) was converted to intensity units ($\mu W/cm^2$) with the spectrometer calibration data obtained using Ocean Optics Radiometric Calibration Lamp. Figure 4.1 provides the schematic details of the THG setup used.
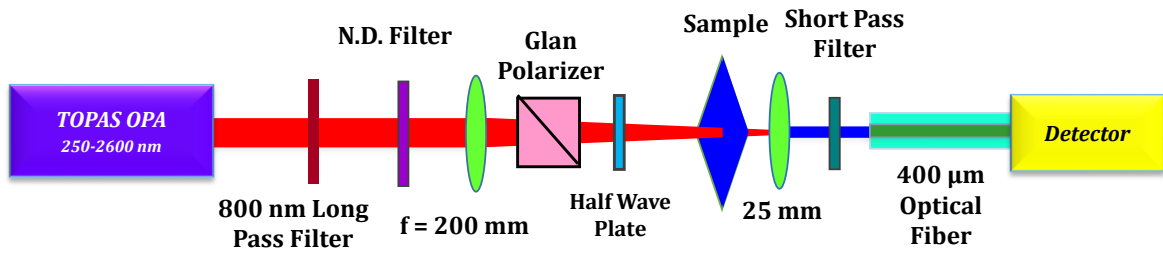

Figure 4.1: Schematic of the THG Setup.

The power of the input beam was measured using Newport 818-UV Optical Power meter connected to a Newport 842-PE Optical Power/Energy Meter. The beam radius was determined by the knife-edge method and fitting the data using the equation:[34]

$$f(s) = \frac{1}{1+\exp\left((-1.5954086)s+(-7.3638857 \times 10^{-2})s^3+(6.4121343 \times 10^{-4})s^5\right)} \qquad (1)$$

where f(s) is the power output and $s = \frac{\sqrt{2}(x-x_0)}{w}$, x being the knife-edge position, x_0 the center of the beam where the intensity is maximum, and w being the beam radius where the intensity reduces to $1/e$. After fitting, the radius was obtained to be w = 300 x 10^{-6}m.

4.3 Results and Discussion

4.3.1 Synthesis and characterization of PyPbI₃ single crystals

$PyPbI_3$ single-crystals were synthesized by dissolving lead oxide and pyridinium iodide in excess of hydroiodic acid at 100 °C, followed by a temperature-controlled cooling process of crystallization. We obtained bright yellow crystals of a few mm in length. The crystal structure (Figure 4.2) consists of face-shared 1D lead iodide octahedral network along the '*c*' crystallographic direction with pyridinium (*Py*) cations surrounding the 1D lead iodide chains. The $PyPbI_3$ has an orthorhombic lattice with the *P*nma space group. The lattice parameters are $a = 14.9$ Å, $b = 8.07$ Å, $c = 9.58$ Å, and $\alpha = \beta = \gamma = 90°$. Complete crystal structure data are provided in Table 4.1. The left panel of Figure 4.2 shows the crystal structure in the '*ab*' plane, revealing the arrangement of *Py* cations around the 1D chains. Six *Py* cations surround the 1D lead iodide chains, forming a core-shell quantum wire structure. The right panel of Figure 4.2 delineates the face-shared network of lead iodide octahedra along the '*c*' crystallographic direction. The *Py* cations are arranged in specific orientations around the lead iodide octahedral chains indicating the presence of favorable non-covalent interactions among the cations.
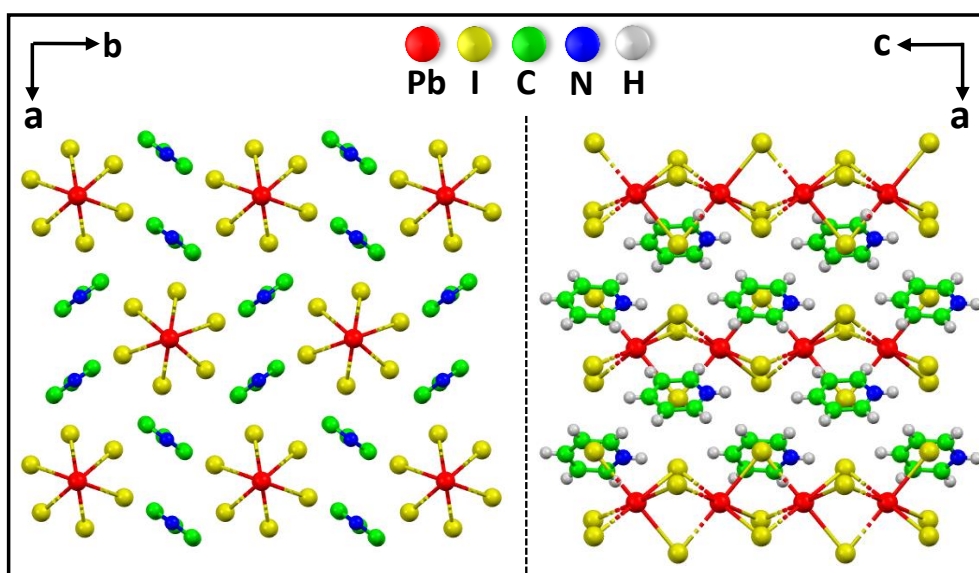

Figure 4.2: Crystal structure of PyPbI₃. The left and right panels show the crystal structure viewed along the '*ab*' and '*ac*' planes, respectively. A 1D array of face-shared lead iodide octahedra surrounded by the *Py* cations is observed along the '*c*' crystallographic direction.

Table 4.1: Crystal structure and data refinement parameters of PyPbI$_3$ single crystals at 100 K and 300 K:

PyPbI$_3$	100(2) K		300(2) K	
Empirical formula	C$_5$H$_5$I$_3$NPb		C$_5$H$_5$I$_3$NPb	
Formula weight	666.99		666.99	
Wavelength	0.71073 Å		0.71073 Å	
Crystal system	Orthorhombic		Orthorhombic	
Space group	*P* n m a		*P* n m a	
Unit cell dimensions	a = 14.9008(3) Å	α = 90°	a = 14.968(5) Å	α = 90°
	b = 8.0698(17) Å	β = 90°	b = 8.102(3) Å	β = 90°
	c = 9.5844(2) Å	γ = 90°	c = 9.901(4) Å	γ = 90°
Volume	1152.0(48) Å^3		1200.7(8) Å^3	
Z	4		4	
Density (calculated)	3.844 Mg/m^3		3.690 Mg/m^3	
Absorption coefficient	22.570 mm^{-1}		21.711 mm^{-1}	
F(000)	1132		1132	
Theta range for all data collection	4.253 to 25.027°.		4.116 to 28.267°.	
Index range	-19 ≤ h ≤ 19,		-19 ≤ h ≤ 19,	
	-10 ≤ k ≤ 10,		-10 ≤ k ≤ 10,	
	-13 ≤ l ≤ 12		-13 ≤ l ≤ 12	
Reflections collected	28133		16860	
Independent reflections	1095 [R(int) = 0.0486]		1582 [R(int) = 0.1765]	
Completeness of independent reflections	99.50%		99.50%	
Absorption correction	Multi-scan		Multi-scan	
Max. and min. transmission	0.7457 and 0.5022		0.7457 and 0.4331	
Refinement method	Full-matrix least-squares on F^2		Full-matrix least-squares on F^2	
Data / restraints / parameters	1095 / 1 / 43		1582 / 1 / 44	
Goodness-of-fit on F2	1.214		0.988	
Final R indices [I>2sigma(I)]	R1 = 0.0671, wR2 = 0.0614		R1 = 0.0520, wR2 = 0.1078	
R indices (all data)	R1 = 0.0302, wR2 = 0.0629		R1 = 0.1302, wR2 = 0.1400	
Largest diff. peak and hole	0.995 and -2.236 e.Å^{-3}		1.628 and -1.289 e.Å^{-3}	

The experimental powder X-ray diffraction (PXRD) pattern of the $PyPbI_3$ single crystals corroborates well with the single crystal XRD (SCXRD), confirming the phase purity (see Figure 4.3a). The crystal structure of $PyPbI_3$ is in accordance with an earlier report.[35] Figure 4.3b shows the optical microscopic image of a $PyPbI_3$ single-crystal. The scanning electron microscopic (SEM) image of a micro-crystal reveals a multi-faceted crystal habit, as depicted in Figure 4.3c.
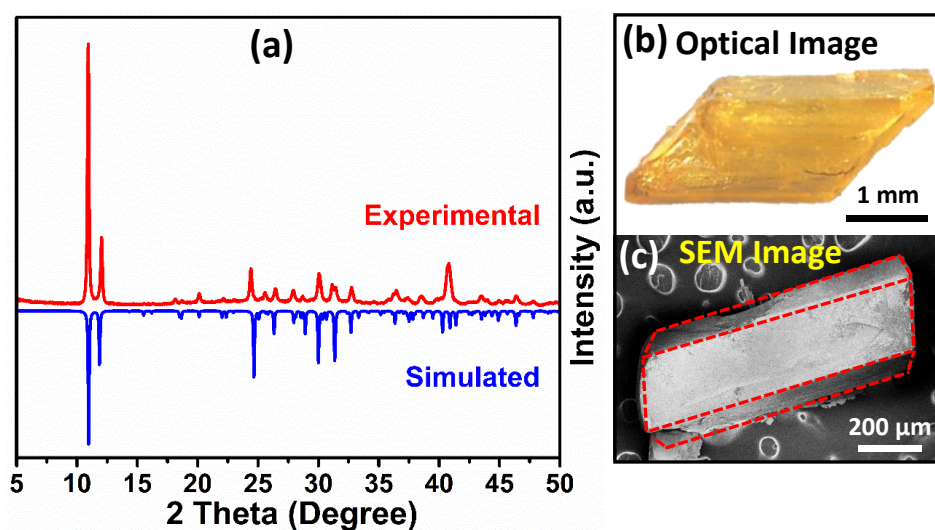

Figure 4.3: (a) Experimental and simulated PXRD patterns of $PyPbI_3$ crystals. The simulated PXRD pattern is obtained from SCXRD data. (b) Optical image of a $PyPbI_3$ crystal under an optical microscope. (c) SEM image of $PyPbI_3$ crystal showing a multi-faceted crystal habit.

4.3.2 Optical properties of PyPbI₃ single crystals

Figure 4.4 shows the UV-visible absorption of $PyPbI_3$ single crystals. A strong absorption with the first excitonic peak at 435 nm and a sharp absorption edge at ~475 nm is observed. The high bandgap of $PyPbI_3$ is due to the strong quantum confinement arising from the reduced dimension and the face-shared nature of the lead iodide octahedral network. The higher energy feature ~350 nm could probably be due to higher excitonic transitions.
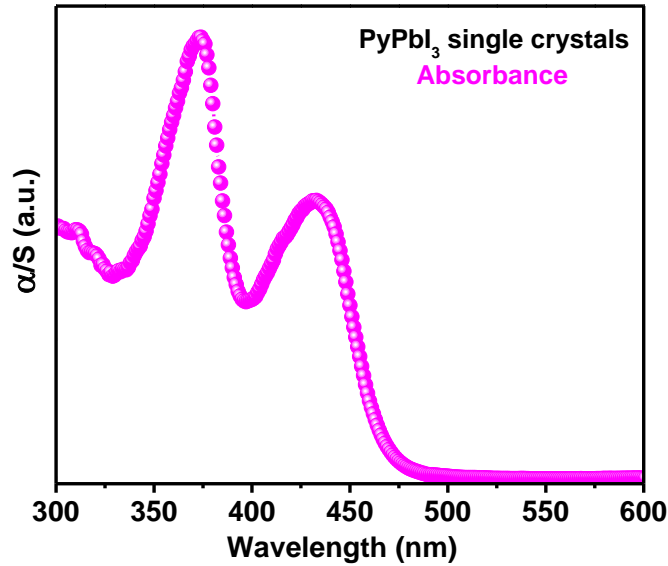
Figure 4.4. UV-Visible absorption spectrum of PyPbI₃ single crystals. Diffuse reflectance measurements converted using Kubelka-Munk transformation gave rise to the absorption spectrum.

4.3.3 Third harmonic generation (THG) from PyPbI₃ single crystals

Lower dimensional lead halides show enhanced NLO properties.[12] A strong THG is observed in 2D layered lead halides due to the quantum and dielectric confinement.[14] The 1D lead halides, with stronger quantum and dielectric confinement, are expected to exhibit further enhancement in their THG response. [14] So, we measured the THG response of PyPbI₃ single-crystals at varied excitation wavelengths ranging from 1200 to 1600 nm, including the important IR communication wavelength. Figure 4.5a shows the THG response in 1D PyPbI₃ single-crystals upon nonlinear interaction with excitation wavelengths from 1400 to 1600 nm, having an average power of 4 mW at RT. We used a femtosecond (~45 fs) OPA as the excitation light source for the THG measurements (details in section 4.2.4). Interestingly, a dramatic enhancement in the THG response is observed as the pump wavelength approaches the bandgap resonance due to highly enhanced light-matter interaction.[38] The variation in the THG intensity with changing pump wavelength is shown in Figure 4.5b (blue spectrum). The maximum THG is obtained at $\lambda/3 = 480$ nm, i.e., corresponding to the pump wavelength of 1440 nm. The THG response peaks at the band edge due to the local enhancement of the incident field.[38] Upon further decrease in the pump wavelength, the THG intensity drops drastically. The THG peak intensity drops by nearly 25 times at the pump wavelength of 1380 nm, and almost a negligible THG signal is obtained below 1370 nm. This decrease is probably

105

due to the intense self-absorption of the THG wave by the sample above the resonance. Surprisingly, we did not observe any THG enhancement at the excitonic absorption wavelength ($\lambda/3 = 435$ nm, $\lambda = 1305$ nm) unlike other perovskites.[14]
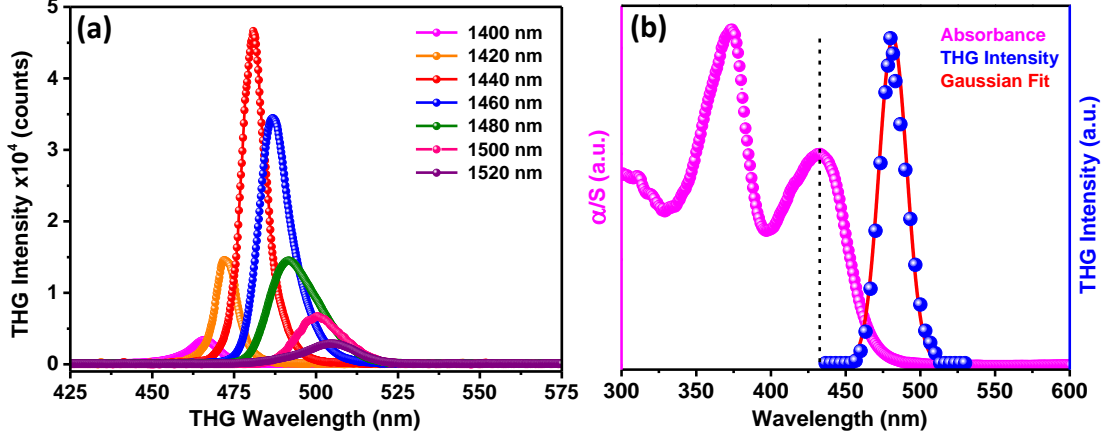

Figure 4.5. Nonlinear optical response from PyPbI$_3$ crystals. (a) THG profiles of PyPbI$_3$ by tuning the pump wavelength. (b) THG intensity (blue spheres) at different excitation wavelengths and the absorbance spectrum (magenta) of PyPbI$_3$. The Red line shows the Gaussian fitting of wavelength-dependent THG response.

4.3.4 Third-order NLO susceptibility ($\chi^{(3)}$)

The third-order NLO susceptibility $\chi^{(3)}$ determines the efficiency of a third-order nonlinear process. We have determined the $\chi^{(3)}$ of the PyPbI$_3$ single crystal using a relative method based on the nonlinear Maxwell's equation. We used 2D Butyl ammonium lead iodide (BA)$_2$PbI$_4$ single crystal as a reference. The solution of nonlinear Maxwell's equation (equation 2) relates the THG intensity ($I_{3\omega}$) with the third-order NLO susceptibility at the pump wavelength ($\chi^{(3)}$) and the pump intensity (I_ω):[39]

$$I_{3\omega} = \frac{9\omega^2}{16|\tilde{n}_{3\omega}||\tilde{n}_\omega|^3\varepsilon_0^2 c^4} I_\omega^3 |\chi^{(3)}|^2 \left(\frac{e^{-2\alpha t} - 2\cos(\Delta kt)e^{-\alpha t} + 1}{\alpha^2 + \Delta k^2}\right) e^{-2\alpha t}$$

$$\chi^{(3)} = \frac{\sqrt{I_{3\omega}}}{3\omega} \frac{4\varepsilon_0 c^2}{(I_\omega)^{\frac{3}{2}}} \left(|\tilde{n}_{3\omega}|^{\frac{1}{2}}|\tilde{n}_\omega|^{\frac{3}{2}}\right) \left(\frac{e^{-2\alpha t} - 2\cos(\Delta kt)e^{-\alpha t} + 1}{\alpha^2 + \Delta k^2}\right)^{\frac{-1}{2}} e^{\alpha t} \qquad (2)$$

where ω is the pump frequency, ε_0 is the dielectric constant of free space, c is the speed of light, $\tilde{n}_\omega$ and $\tilde{n}_{3\omega}$ are the complex refractive indices at the pump and THG frequencies

respectively, α is the absorption coefficient of the material at the THG frequency, and Δk is the phase mismatch between the pump and third harmonic waves.

In the non-phase-matching condition with minimum absorption effects, the $\chi^{(3)}$ of two materials excited under similar conditions can be compared using the THG intensities:[40]

$$\chi_S^{(3)} = \chi_R^{(3)} \left[\frac{I_S(3\omega)}{I_R(3\omega)}\right]^{1/2} \qquad (3)$$

where $\chi_S^{(3)}$ and $\chi_R^{(3)}$ are the third order NLO susceptibilities of the sample and the reference, $I_S(3\omega)$ and $I_R(3\omega)$ are the THG intensities of the sample and reference, respectively. We used 2D butylammonium lead iodide $(BA)_2PbI_4$ single-crystals as a reference to determine the $\chi^{(3)}$ of $PyPbI_3$ single-crystals, for which a strong THG response is reported.[14] The comparison of THG response of $(BA)_2PbI_4$ and $PyPbI_3$ is given in Figure 4.6. For $(BA)_2PbI_4$ at a pump wavelength of 1500 nm, $\chi_R^{(3)} = 3.5 \times 10^{-18}$ m^2V^{-2}.[14] Using the $\chi^{(3)}$ value of $(BA)_2PbI_4$ at 1500 nm in equation 5, the $\chi^{(3)}$ of $PyPbI_3$ at 1500 nm comes out to be 0.78×10^{-18} m^2V^{-2}.

$PyPbI_3$ shows the maximum THG response at 1440 nm. To calculate the $\chi^{(3)}$ of $PyPbI_3$ at 1440 nm, we need to incorporate the frequency dependence as well. Referring back to Equation 4, we get:

$$\chi_{\omega_1}^{(3)} = \chi_{\omega_2}^{(3)} \left(\frac{3\omega_2}{3\omega_1}\right) \left[\frac{I(3\omega_1)}{I(3\omega_2)}\right]^{1/2} \qquad (4)$$

where $\chi_{\omega_1}^{(3)}$ and $\chi_{\omega_2}^{(3)}$ are the third order NLO susceptibilities at pump frequencies ω_1 and ω_2, and $I(3\omega_1)$ and $I(3\omega_2)$ being the respective THG intensities. We obtain the maximum $\chi^{(3)}$ value for $PyPbI_3$ at 1440 nm to be 1.96×10^{-18} m^2V^{-2} which is comparable to the 2D perovskites (see Table 4.2 for comparison). The THG response of $PyPbI_3$ and $(BA)_2PbI_4$ were recorded at 1440 nm and 1500 nm at 4 mW power. We observe that the THG response of $PyPbI_3$, although being less than that of $(BA)_2PbI_4$, is within the same order of magnitude. It is worth noting that the highest $\chi^{(3)}$ has been obtained for the nanosheets of layered perovskitoid $((BA)_2(MA)PbI_4$ (MA = methylammonium)) embedded in the h-BN matrix. Whereas the $\chi^{(3)}$ value in the present case has been obtained for the $PyPbI_3$ single crystals without any encapsulation, which is quite remarkable.
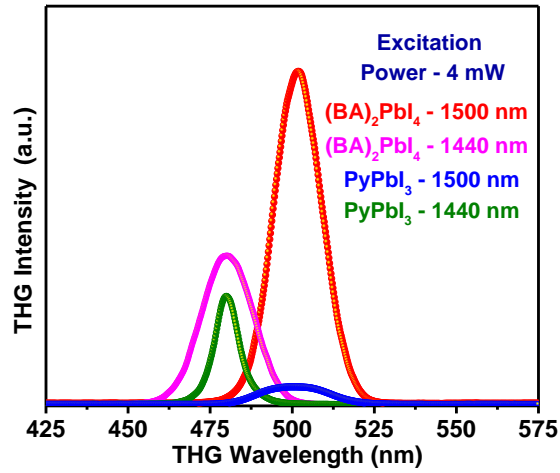
Figure 4.6: Comparison of THG response intensity of $(BA)_2PbI_4$ (n = 1) and $PyPbI_3$ single crystals at excitation wavelengths 1440 nm and 1500 nm at 4 mW power. At 1440 nm, the THG response of $PyPbI_3$ single-crystals becomes comparable to $(BA)_2PbI_4$ (n = 1) single-crystals.

4.3.5 Laser induced damage threshold (LIDT)

To analyze the exact nature of the THG response in $PyPbI_3$ single-crystals and evaluate the LIDT, we recorded the power-dependent THG response at the resonant condition (λ_{pump} = 1440 nm), where the maximum response is observed. Figure 4.7a shows the THG spectra, corresponding to the 1440 nm excitation, at increasing pump powers. Upon increasing the pump power from 0.8 mW to ~8 mW, the THG power increases from ~0.016 nW to ~2.64 nW (Figure 4.7b). The THG intensity shows a cubic dependence on the pump power till ~4.2 mW, indicating that the response is from THG. The pump intensity at which the THG response deviates from cubic behavior determines the LIDT of the sample.[41] This deviation occurs due to saturation effects such as local heating, lattice relaxations, etc., which lead to a decrease in THG efficiency.[14] Therefore, the peak intensity corresponding to 4.2 mW is the LIDT of the sample which is determined as follows:

$$\text{Peak intensity} = \frac{\text{Energy per pulse}}{(\text{Pulse width}) \times (\text{effective spot area})} \quad (5)$$

$$\text{Energy per pulse} = \frac{\text{Average power}}{\text{Repetition Rate}}$$

$$\therefore \text{Peak intensity} = \frac{\text{Average power}}{(\text{Repetition rate}) \times (\text{Pulse width}) \times (\text{effective spot area})} \quad (6)$$

For our setup, Repetition Rate = 1000 Hz, Pulse width 10^{-6} m, and Average power = 4.2×10^{-3} W.

Therefore,

$$\text{LIDT} = \text{Peak intensity} = \frac{4.2 \times 10^{-3} \text{ W}}{(1000 \text{ Hz}) \times (45 \times 10^{-15} \text{ s}) \times (\pi \times (300 \times 10^{-6} \text{ m})^2)}$$

$$= 33 \times 10^{13} \text{ W/m}^2$$

$$= 33 \times 10^9 \text{ W/cm}^2$$

$$= 33 \text{ GW/cm}^2$$

Materials with high LIDT and THG efficiency are desired for potential applications. The LIDT for $PyPbI_3$ single-crystals comes out to be ~33 GW/cm^2, which is nearly threefold larger than the benchmark 2D lead halides.[14] The LIDT values of some benchmark materials have been provided in Table 4.2. Notably, the $PyPbI_3$ single crystals show very high LIDT even without any encapsulation.
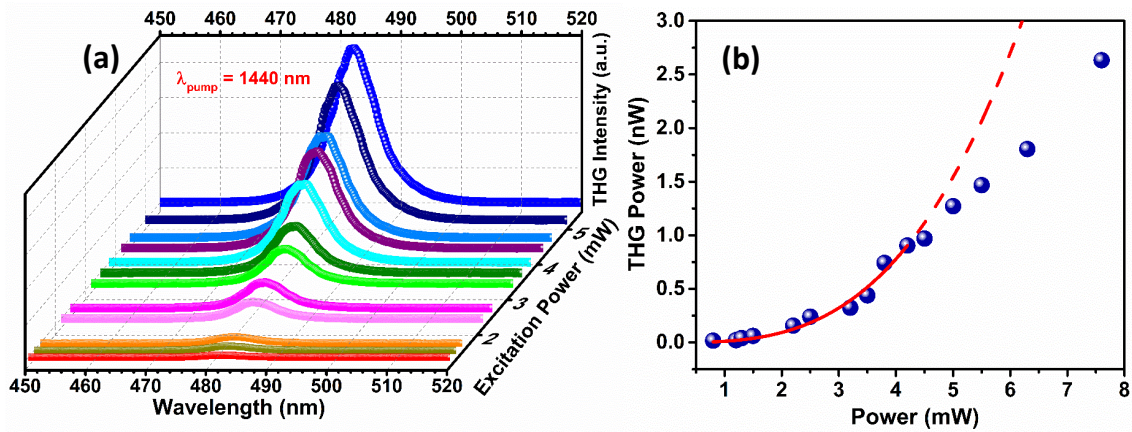

Figure 4.7: (a) Excitation power-dependent THG spectra at pump wavelength 1440 nm. (b) Cubic fitting of the power-dependent THG response. Deviation from cubic behavior represents LIDT.

Table 4.2. Comparison of $\chi^{(3)}$ and LIDT values for the present work and previous literature.

Compound	λ (nm)	$\chi^{(3)}$ (m^2V^{-2})	LIDT ($GW\ cm^{-2}$)	Reference
$PyPbI_3$	1440	1.96×10^{-18}	33	This work
$(C_4H_9NH_3)_2PbBr_4$ (encapsulated)	1210	4.7×10^{-18}		[14]
$(C_4H_9NH_3)_2PbI_4$	1500	3.5×10^{-18}		[14]
$(C_4H_9NH_3)_2(CH_3NH_3)Pb_2I_4$	1675	11.2×10^{-18}	11*	[14]
$(C_4H_9NH_3)_2(CH_3NH_3)_2Pb_3I_{10}$	1800	5.1×10^{-18}		[14]
$FAPbBr_3$ NCs in SiO_2 matrix	1560	1.5×10^{-19}	35#	[42]
Au-Si hybrid nano-antenna	1320	6.9×10^{-17}	3	[43]
Black Phosphorus flakes	1557	1.4×10^{-18}		[39]
$AgGa(IO_3)_4$	1500	7.7×10^{-22}	1.04*	[41]
$Ag_3In(IO_3)_6$	1500	1.1×10^{-21}	0.82*	[41]

* The values are obtained by calculations done using parameters provided in respective papers.

The reported LIDT value was 50 while using the FWHM radius. The value presented here was obtained by converting to 1/e radius.

4.4 Conclusion

We demonstrated an efficient THG in a wide spectral range in 1D face-shared $PyPbI_3$ single crystals. The THG response is highly enhanced at the bandgap excitation compared to the 3D perovskites due to strong quantum and dielectric confinement. $PyPbI_3$ exhibits a large third-order nonlinear susceptibility $\chi^{(3)}$, comparable to the 2D layered perovskites, and a high LIDT, an essential requirement for high-power NLO applications. Thus, 1D $PyPbI_3$ single crystals can efficiently serve as IR visualizing equipment in practically important optical communication wavelength (~1.5 µm), efficient up-converters for lasing, laser modulators, and photo-detection. Further, bandgap engineering using halide exchange would make these 1D lead halides ($PyPbX_aY_{3-a}$, X, Y = Cl, Br, I) and similar systems available for THG over a variable wavelength range in the UV and near-UV regime. The selective enhancement of THG at the bandgap resonance can be further exploited to understand the excited states of such systems.

4.5 References

1. Kojima, A.; Teshima, K.; Shirai, Y.; Miyasaka, T., Organometal Halide Perovskites as Visible-Light Sensitizers for Photovoltaic Cells. *J. Am. Chem. Soc.* **2009**, *131*, 6050-6051.

2. Cao, D. H.; Stoumpos, C. C.; Farha, O. K.; Hupp, J. T.; Kanatzidis, M. G., 2D Homologous Perovskites as Light-Absorbing Materials for Solar Cell Applications. *J. Am. Chem. Soc.* **2015**, *137*, 7843-7850.

3. Yettapu, G. R.; Talukdar, D.; Sarkar, S.; Swarnkar, A.; Nag, A.; Ghosh, P.; Mandal, P., Terahertz Conductivity within Colloidal $CsPbBr_3$ Perovskite Nanocrystals: Remarkably High Carrier Mobilities and Large Diffusion Lengths. *Nano Lett.* **2016**, *16*, 4838-4848.

4. Sarkar, S.; Ravi, V. K.; Banerjee, S.; Yettapu, G. R.; Markad, G. B.; Nag, A.; Mandal, P., Terahertz Spectroscopic Probe of Hot Electron and Hole Transfer from Colloidal $CsPbBr_3$ Perovskite Nanocrystals. *Nano Lett.* **2017**, *17*, 5402-5407.

5. Akkerman, Q. A.; Rainò, G.; Kovalenko, M. V.; Manna, L., Genesis, Challenges and Opportunities for Colloidal Lead Halide Perovskite Nanocrystals. *Nat. Mater.* **2018**, *17*, 394-405.

6. Jena, A. K.; Kulkarni, A.; Miyasaka, T., Halide Perovskite Photovoltaics: Background, Status, and Future Prospects. *Chem. Rev.* **2019**, *119*, 3036-3103.

7. Fu, Y.; Zhu, H.; Chen, J.; Hautzinger, M. P.; Zhu, X. Y.; Jin, S., Metal Halide Perovskite Nanostructures for Optoelectronic Applications and the Study of Physical Properties. *Nat. Rev. Mater.* **2019**, *4*, 169-188.

8. Protesescu, L.; Yakunin, S.; Bodnarchuk, M. I.; Krieg, F.; Caputo, R.; Hendon, C. H.; Yang, R. X.; Walsh, A.; Kovalenko, M. V., Nanocrystals of Cesium Lead Halide Perovskites ($CsPbX_3$, X = Cl, Br, and I): Novel Optoelectronic Materials Showing Bright Emission with Wide Color Gamut. *Nano Lett.* **2015**, *15*, 3692-3696.

9. Swarnkar, A.; Chulliyil, R.; Ravi, V. K.; Irfanullah, M.; Chowdhury, A.; Nag, A., Colloidal $CsPbBr_3$ Perovskite Nanocrystals: Luminescence Beyond Traditional Quantum Dots. *Angew. Chem. Int. Ed.* **2015**, *54*, 15424-15428.

10. Manser, J. S.; Christians, J. A.; Kamat, P. V., Intriguing Optoelectronic Properties of Metal Halide Perovskites. *Chem. Rev.* **2016**, *116*, 12956-13008.

11. Walters, G.; Sutherland, B. R.; Hoogland, S.; Shi, D.; Comin, R.; Sellan, D. P.; Bakr, O. M.; Sargent, E. H., Two-Photon Absorption in Organometallic Bromide Perovskites. *ACS Nano* **2015**, *9*, 9340-9346.

12. Saouma, F. O.; Stoumpos, C. C.; Wong, J.; Kanatzidis, M. G.; Jang, J. I., Selective Enhancement of Optical Nonlinearity in Two-Dimensional Organic-Inorganic Lead Iodide Perovskites. *Nat. Commun.* **2017**, *8*, 742.

13. Ferrando, A.; Martínez Pastor, J. P.; Suárez, I., Toward Metal Halide Perovskite Nonlinear Photonics. *J. Phys. Chem. Lett.* **2018**, *9*, 5612-5623.

14. Abdelwahab, I.; Grinblat, G.; Leng, K.; Li, Y.; Chi, X.; Rusydi, A.; Maier, S. A.; Loh, K. P., Highly Enhanced Third-Harmonic Generation in 2D Perovskites at Excitonic Resonances. *ACS Nano* **2018**, *12*, 644-650.

15. Wang, J., et al., Giant Nonlinear Optical Response in 2D Perovskite Heterostructures. *Adv. Opt. Mater.* **2019**, *7*, 1900398.

16. Xu, J.; Li, X.; Xiong, J.; Yuan, C.; Semin, S.; Rasing, T.; Bu, X.-H., Halide Perovskites for Nonlinear Optics. *Adv. Mater.* **2020**, *32*, 1806736.

17. Liang, W.-Y.; Liu, F.; Lu, Y.-J.; Popović, J.; Djurišić, A.; Ahn, H., High Optical Nonlinearity in Low-Dimensional Halide Perovskite Polycrystalline Films. *Opt. Express* **2020**, *28*, 24919-24927.

18. Akkerman, Q. A.; Manna, L., What Defines a Halide Perovskite? *ACS Energy Lett.* **2020**, *5*, 604-610.

19. Tsai, H., et al., High-Efficiency Two-Dimensional Ruddlesden–Popper Perovskite Solar Cells. *Nature* **2016**, *536*, 312-316.

20. Saparov, B.; Mitzi, D. B., Organic–Inorganic Perovskites: Structural Versatility for Functional Materials Design. *Chem. Rev.* **2016**, *116*, 4558-4596.

21. Mao, L.; Ke, W.; Pedesseau, L.; Wu, Y.; Katan, C.; Even, J.; Wasielewski, M. R.; Stoumpos, C. C.; Kanatzidis, M. G., Hybrid Dion–Jacobson 2D Lead Iodide Perovskites. *J. Am. Chem. Soc.* **2018**, *140*, 3775-3783.

22. Katan, C.; Mercier, N.; Even, J., Quantum and Dielectric Confinement Effects in Lower-Dimensional Hybrid Perovskite Semiconductors. *Chem. Rev.* **2019**, *119*, 3140-3192.

23. Sheikh, T.; Nawale, V.; Pathoor, N.; Phadnis, C.; Chowdhury, A.; Nag, A., Molecular Intercalation and Electronic Two Dimensionality in Layered Hybrid Perovskites. *Angew. Chem. Int. Ed.* **2020**, *59*, 11653-11659.

24. Garmire, E., Nonlinear Optics in Daily Life. *Opt. Express* **2013**, *21*, 30532-30544.

25. Boyd, R., *Nonlinear Optics*, 4th ed.; *Elsivier*, **2020**, p 634.

26. Simon, H. J.; Mitchell, D. E.; Watson, J. G., Optical Second-Harmonic Generation with Surface Plasmons in Silver Films. *Phys. Rev. Lett.* **1974**, *33*, 1531-1534.

27. Byer, R. L.; Choy, M. M.; Herbst, R. L.; Chemla, D. S.; Feigelson, R. S., Second Harmonic Generation and Infrared Mixing in AgGaSe$_2$. *Appl. Phys. Lett.* **1974**, *24*, 65-68.

28. Prusseit-Elffroth, W.; Schwabl, F., Second Harmonic Light Scattering in Paraelectric Perovskites. *Appl. Phys. A* **1990**, *51*, 361-368.

29. Yu, Z.-G., Estimation of the Rashba Strength from Second Harmonic Generation in 2D and 3D Hybrid Organic–Inorganic Perovskites. *J. Phys. Chem. C* **2018**, *122*, 29607-29612.

30. Wei, W.-J., et al., Regulating Second-Harmonic Generation by Van Der Waals Interactions in Two-Dimensional Lead Halide Perovskite Nanosheets. *J. Am. Chem. Soc.* **2019**, *141*, 9134-9139.

31. Bi, Y.; Feng, Y.; Gong, H.; Zhang, H.; Xu, Z., High-Average Power THG of a Diode-Pumped Nd:Yag Laser at 355 nm Generated by LiB$_3$O$_5$ Crystal. *Chin. Opt. Lett.* **2003**, *1*, 91-92.

32. Sheikh, T.; Maqbool, S.; Mandal, P.; Nag, A., Introducing Intermolecular Cation-Π Interactions for Water-Stable Low Dimensional Hybrid Lead Halide Perovskites. *Angew. Chem. Int. Ed.* **2021**, *60,* 18265-18271.

33. Stoumpos, C. C.; Cao, D. H.; Clark, D. J.; Young, J.; Rondinelli, J. M.; Jang, J. I.; Hupp, J. T.; Kanatzidis, M. G., Ruddlesden–Popper Hybrid Lead Iodide Perovskite 2D Homologous Semiconductors. *Chem. Mater.* **2016**, *28*, 2852-2867.

34. de Araújo, M. A.; Silva, R.; de Lima, E.; Pereira, D. P.; de Oliveira, P. C., Measurement of Gaussian Laser Beam Radius Using the Knife-Edge Technique: Improvement on Data Analysis. *Appl. Opt.* **2009**, *48*, 393-396.

35. Selivanov, N. I.; Murashkina, A. A.; Kevorkyants, R.; Emeline, A. V.; Bahnemann, D. W., Pyridinium Lead Tribromide and Pyridinium Lead Triiodide: Quasi-One-Dimensional Perovskites with an Optically Active Aromatic Π-System. *Dalton Trans.* **2018**, *47*, 16313-16319.

36. Kamminga, M. E.; de Wijs, G. A.; Havenith, R. W. A.; Blake, G. R.; Palstra, T. T. M., The Role of Connectivity on Electronic Properties of Lead Iodide Perovskite-Derived Compounds. *Inorg. Chem.* **2017**, *56*, 8408-8414.

37. Gapontsev, V. P.; Tyrtyshnyy, V. A.; Vershinin, O. I.; Davydov, B. L.; Oulianov, D. A., Third Harmonic Frequency Generation by Type-I Critically Phase-Matched LiB$_3$O$_5$ Crystal by Means of Optically Active Quartz Crystal. *Opt. Express* **2013**, *21*, 3715-3720.

38. Markowicz, P. P.; Tiryaki, H.; Pudavar, H.; Prasad, P. N.; Lepeshkin, N. N.; Boyd, R. W., Dramatic Enhancement of Third-Harmonic Generation in Three-Dimensional Photonic Crystals. *Phys. Rev. Lett.* **2004**, *92*, 083903.

39. Youngblood, N.; Peng, R.; Nemilentsau, A.; Low, T.; Li, M., Layer-Tunable Third-Harmonic Generation in Multilayer Black Phosphorus. *ACS Photonics* **2017**, *4*, 8-14.

40. Haynes, A. S.; Banerjee, A.; Saouma, F. O.; Otieno, C. O.; Jang, J. I.; Kanatzidis, M. G., Phase Transition, Conformational Exchange, and Nonlinear Optical Third Harmonic Generation of $ACsP_2Se_8$ (A = K, Rb, Cs). *Chem. Mater.* **2016**, *28*, 2374-2383.

41. Park, G.; Byun, H. R.; Jang, J. I.; Ok, K. M., Dimensionality–Band Gap–Third-Harmonic Generation Property Relationship in Novel Main-Group Metal Iodates. *Chem. Mater.* **2020**, *32*, 3621-3630.

42. Rubino, A.; Huq, T.; Dranczewski, J.; Lozano, G.; Calvo, M. E.; Vezzoli, S.; Míguez, H.; Sapienza, R., Efficient Third Harmonic Generation from $FAPbBr_3$ Perovskite Nanocrystals. *J. Mater. Chem. C* **2020**, *8*, 15990-15995.

43. Shibanuma, T.; Grinblat, G.; Albella, P.; Maier, S. A., Efficient Third Harmonic Generation from Metal–Dielectric Hybrid Nanoantennas. *Nano Lett.* **2017**, *17*, 2647-2651.
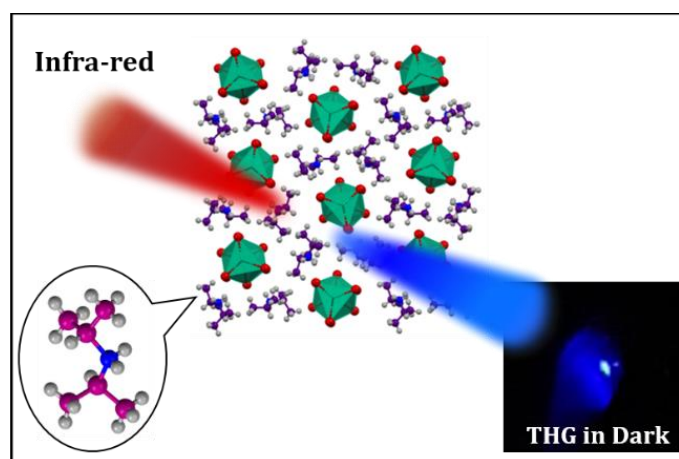
Chapter 5

1D Diisopropylammonium Lead Iodide Perovskite Shows Exceptional Optical Stability and Third-Order Nonlinearity

The work presented in this chapter has been published in the Advanced Optical Materials with the following details:

Maqbool, S.; Thekkayil, Z.; Mandal, P.; 1D Diisopropylammonium Lead Iodide Perovskite Shows Exceptional Optical Stability and Third-Order Nonlinearity**.** *Adv. Opt. Mater. just aaccepted*.

1D Diisopropylammonium Lead Iodide Perovskite Shows Exceptional Optical Stability and Third-Order Nonlinearity

Abstract

Lower dimensional lead halide perovskites show wide structural and compositional diversity. Multiple functionalities can thus be introduced in this class of materials for diverse linear and nonlinear optical applications. Nonlinear optical (NLO) processes are highly dependent on material polarizability, crystal symmetry, and material processibility. The flexibility of choice of organic cations in lead halide perovskites provides an opportunity for enhanced NLO responses by enhancing the system polarizability. We used highly polarizable diisopropylammonium [$((CH_3)_2CH)_2NH_2^+$] as 'A' site cation to synthesize 1D lead iodide perovskite single crystals, which show highly efficient resonance-enhanced third-harmonic generation (THG) with amazing optical stability and high polarization ratio due to enhanced bulk polarization. The THG efficiency ($\chi^{(3)} \sim 4 \times 10^{-18}$ m^2V^{-2}) and laser-induced damage threshold (LIDT, 144 GW/cm^2) are an order of magnitude higher than the reported perovskites explored as THG materials. The stability of these single crystals in ambient temperature and humidity for an extended period adds to their potential for commercial application in the near future.

Graphical Abstract

1D Diisopropylammonium Lead Iodide Perovskite Shows Exceptional Optical Stability and Third-Order Nonlinearity

5.1 Introduction

Nonlinear optics (NLO) presents an efficient way for photon energy up-conversion.[1] Lower frequency light can easily be up-converted to a higher frequency by NLO processes like second harmonic generation (SHG), third-harmonic generation (THG), sum-frequency generation (SFG), etc.[2] Crystals with significant nonlinear susceptibility coefficients are crucial for the generation of ultrafast laser pulses in the ultraviolet to infrared range, from the robust laser sources emitting only a few discrete wavelengths. Third harmonic generation is the simplest way to triple the photon energy in a single step without worrying about tedious phase-matching conditions otherwise required in a two-step process of SHG followed by SFG.[3] The third-order nonlinear susceptibility, $\chi^{(3)}$, which is an important parameter for governing processes such as two-photon absorption, saturable absorption, and the optical Kerr effect, is also obtained from THG. Though all the materials are expected to show THG due to no symmetry constraints, the $\chi^{(3)}$ values need to be significant for efficient THG. Efficient THG materials find applications in frequency transformation, optical rectification, communications, bioimaging, etc.[4-5] Though there are a handful of efficient SHG materials commercially available, a highly efficient THG material has not yet been realized due to higher-order nonlinear processes being intrinsically weaker.[6] Thus, a vast field of material design and synthesis remains to be explored for efficient THG. In this work, we synthesized a one-dimensional (1D) perovskite system, diisopropylammonium lead iodide (DipaPbI$_3$), for efficient THG and high optical stability.

Hybrid lead halide perovskites,[7-8] in addition to their marvellous optoelectronic and photovoltaic properties,[9-11] have shown promises in NLO applications[12-13]. The polarizability anisotropy of lead halide perovskites affect not only the charge carrier recombinations and the transport properties[14], but also make them conducive for energy manipulation and frequency conversion.[15-16] There are numerous reports of lead halide perovskites showing SHG,[17] THG,[18] and multi-photon absorption owing to their excellent properties, such as larger absorption coefficients.[19] Lower-dimensional hybrid lead halide perovskites, due to quantum and dielectric confinement, show further enhancement in their NLO properties.[20-22] Due to strong excitonic resonance[23] and intrinsic crystal-liquid duality,[15] they are also promising THG candidates.[18] Unlike 3D perovskites, lower-dimensional perovskites show huge structural and compositional flexibility.[24-26] A variety of organic A-site cations can be explored for imparting properties for multitude of desired applications.[27-29] Especially organic cations with high polarizability can be used to achieve enhanced NLO responses by enhancing the bulk

polarizability of the perovskite systems, since the NLO response is directly dependent on the polarizability of the material. Xiong and co-workers reported that the bromide salt of diisopropylamine shows high spontaneous polarization of 23 μC/cm^2, which is close to a benchmark ferroelectric material, Barium Titanate (BTO).[30] Incorporating this diisopropylammonium ion as an A-site for synthesizing a lower-dimensional perovskite system should provide an opportunity for generating strong NLO effects in the organic lead halide systems with similar structural characteristics. This motivated us to utilize this organic cation, diisopropylammonium $(((CH_3)_2CH)_2NH_2^+$, Dipa),[30] to synthesize 1D DipaPbI$_3$ perovskite, which shows a highly efficient THG and significantly high optical stability. Resonance-enhanced THG efficiency and laser-induced damage threshold (LIDT) of this highly crystalline system are orders of magnitude higher than the reported perovskites explored for THG output. Thus, DipaPbI$_3$ crystals can be used as potential high-power energy up-convertors in a wide wavelength range.

5.2 Experimental Section

5.2.1 Chemicals

Hydroiodic acid (HI, Sigma Aldrich, 57% w/w in H$_2$O, 99.9%), Lead oxide (Sigma Aldrich, 99.9%), diisopropylamine (Dipa, Avra, 98%), hypophosphorous acid (H$_3$PO$_2$, Avra, 50% w/w H$_2$O), acetone (Rankem, 99.5%). All chemicals were used with no further purification.

5.2.2 Synthesis of 1D diisopropylammonium lead iodide (DipaPbI$_3$) single crystals

In 10 mL of HI solution, 10 mmol of lead oxide was added. 1 mL of H$_3$PO$_2$ acid was also added to the same. The mixture was heated under constant stirring, up to 100 °C till a clear yellow solution was obtained. To this solution, 10 mmol of diisopropylamine solution was carefully added. Upon proper mixing, heating was stopped and the solution was allowed to cool under controlled conditions. Large yellow crystals of few cm length appeared in the solution after few days.

5.2.3 Characterization

We collected the single-crystal X-ray diffraction (SCXRD) data using a Bruker Smart Apex Duo diffractometer at 100 K using Mo Kα radiation (λ = 0.71073 Å). Bruker SAINT Software package using a narrow-frame algorithm integrated the frames. The structures were solved by direct method and refined by full-matrix least-squares on F2 using the SHELXTL software

package. All the atoms were refined anisotropically. Powder X-ray Diffraction (PXRD) data were recorded on Bruker D8 Advance X-ray diffractometer using Cu Kα radiation (1.54 Å). Optical Diffuse-reflectance data of the powdered sample with $BaSO_4$ as a 100% reflectance reference was obtained using a Shimadzu UV-3600 plus UV-VIS-NIR double-beam, double monochromator spectrophotometer. The absorption spectrum was calculated from the reflectance spectrum using Kubelka-Munk transformation.

5.2.4 Third harmonic generation

We used ultrashort (~45 fs) pulses generated from an optical parametric amplifier (OPA, TOPAS-C, Light Conversion) powered by 1.5 mJ beam of ~35 fs pulses (800 nm, 1 kHz) coming from a regenerative amplifier (Spitfire Pro XP, Spectra-Physics) as the excitation source for our THG experiments. Excitation wavelengths ranging from 1200 to 1700 nm were used for the THG experiments. We used a variable optical density neutral density filter to control the excitation power. Fundamental laser pulses of appropriate energy were focused onto the sample with a planoconvex lens having a focal length of 200 mm. The THG output from the sample (in transmission geometry) was collimated by a planoconvex lens (25 mm focal length). We used a 750 nm short-pass filter to block the fundamental beam. The collimated THG beam was directed into the optical fiber coupled with a miniature spectrometer (USB4000, Ocean Optics). We used an assembly of a glan-polarizer (Thorlabs) and a half-wave plate to vary the polarization angle of the incident pump light with respect to the crystal axis. See Chapter 4 section 4.2.4 for more details.

5.3 Results and Discussion

5.3.1 Synthesis, characterization and optical properties of DipaPbI₃ single crystals

We synthesized $DipaPbI_3$ single crystals by the acid-precipitation method (experimental section). Figure 5.1 shows the crystal structure of $DipaPbI_3$, obtained from single-crystal X-ray diffraction (SCXRD) recorded at 100 K. $DipaPbI_3$ belongs to the monoclinic crystal system with the P21/c space group. The lattice parameters are $a = 7.99$ Å, $b = 19.49$ Å, $c = 19.38$ Å, and $\alpha = \gamma = 90°$, $\beta = 96.1°$. The adjacent lead iodide octahedra are connected via face-sharing, giving rise to a 1D lead iodide network which is surrounded by Dipa cations. Refer to Table 5.1 for detailed structural characterization. The experimental powder XRD pattern corroborates well with the simulated XRD pattern (Figure 5.2), establishing the phase-purity of the sample.
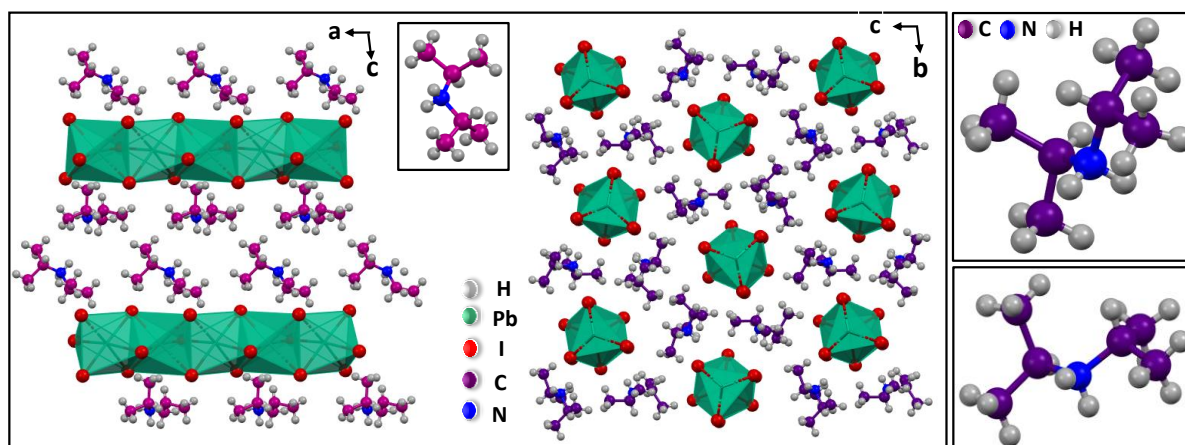
1D Diisopropylammonium Lead Iodide Perovskite Shows Exceptional Optical Stability and Third-Order Nonlinearity

Figure 5.1: Crystal structure of DipaPbI$_3$ single crystals along a-c, and b-c-plane. Inset shows the Dipa cation. Right panel shows the structure of Diisopropylammonium (Dipa) cations within the crystal lattice.
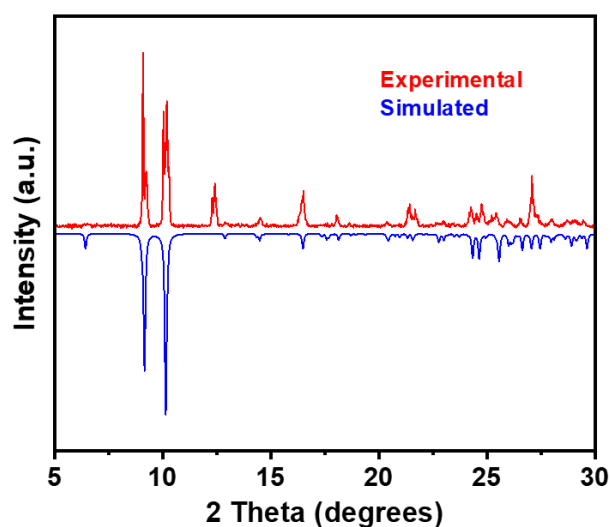

Figure 5.2: Experimental and simulated PXRD patterns of DipaPbI$_3$ crystals. The simulated PXRD pattern is obtained from SCXRD data.

1D Diisopropylammonium Lead Iodide Perovskite Shows Exceptional Optical Stability and Third-Order Nonlinearity

Table 5.1: Crystal structure and data refinement parameters.

Chemical formula	$C_6H_{16}I_3NPb$
Formula weight	690.08 g/mol
Temperature	100(2) K
Wavelength	0.71073 Å
Crystal system	monoclinic
Space group	P21/c
Unit cell dimensions	a = 7.9989(8) Å $\alpha = 90°$
	b = 19.4935(17) Å $\beta = 96.130(3)°$
	c = 19.3876(19) Å $\gamma = 90°$
Volume	3005.8(5) $Å^3$
Z	2
Density (calculated)	3.050 g/cm^3
Absorption coefficient	17.350 mm^{-1}
F(000)	2400
Theta range for data collection	2.97 to 26.37°
Index ranges	$-9 \le h \le 9$, $-24 \le k \le 24$, $-24 \le l \le 24$
Reflections collected	55676
Independent reflections	6098 [R(int) = 0.0652]
Coverage of independent reflections	99.4%
Absorption correction	Numerical Mu Calculated
Max. and min. transmission	0.0920 and 0.0300
Structure solution technique	direct methods
Structure solution program	SHELXT 2014/5 (Sheldrick, 2014)
Refinement method	Full-matrix least-squares on F^2
Refinement program	SHELXL-2018/3 (Sheldrick, 2018)
Function minimized	$\Sigma\ w(F_o^2 - F_c^2)^2$
Data / restraints / parameters	6098 / 0 / 212
Goodness-of-fit on F^2	0.829
Δ/σ_{max}	0.040
Final R indices: 5590 data; $I>2\sigma(I)$	R1 = 0.0302, wR2 = 0.0714
All Data	R1 = 0.0337, wR2 = 0.0736
Weighting scheme	$w=1/[\sigma^2(F_o^2)+(0.0200P)^2+5.0000P]$ where $P=(F_o^2+2F_c^2)/3$
Largest diff. peak and hole	0.256 and -0.350 $eÅ^{-3}$
R.M.S. deviation from mean	0.066 $eÅ^{-3}$

Table 5.2: Comparison of crystal structure parameters of the freshly synthesized $DipaPbI_3$ and the same crystals after six months.

Parameters	Fresh	After Six Months
Crystal system	monoclinic	monoclinic
Space group	$P2_1/c$	$P2_1/c$
Temperature	100 K	100 K
Unit cell dimensions	a = 7.9989(8) Å	a = 8.0039(16) Å
	b = 19.4935(17) Å	b = 19.551(4) Å
	c = 19.3876(19) Å	c = 19.410(4) Å
	$\alpha = \gamma = 90°$; $\beta = 96.130(3)°$	$\alpha = \gamma = 90°$; $\beta = 96.185(5)°$
Volume	3005.8(5) $Å^3$	3019.7(10) $Å^3$

Figure 5.3 shows the UV-Vis absorption spectrum of $DipaPbI_3$ single crystals, with the absorption edge around 470 nm. High-quality, centimeter-sized single crystals were obtained from the recrystallization process, as shown in the inset of Figure 5.3. It is worth mentioning that the $DipaPbI_3$ single crystals remain stable in ambient conditions for months, which is confirmed by their SCXRD (Table 5.2) and simulated powder-XRD data recorded after six months (Figure 5.4).
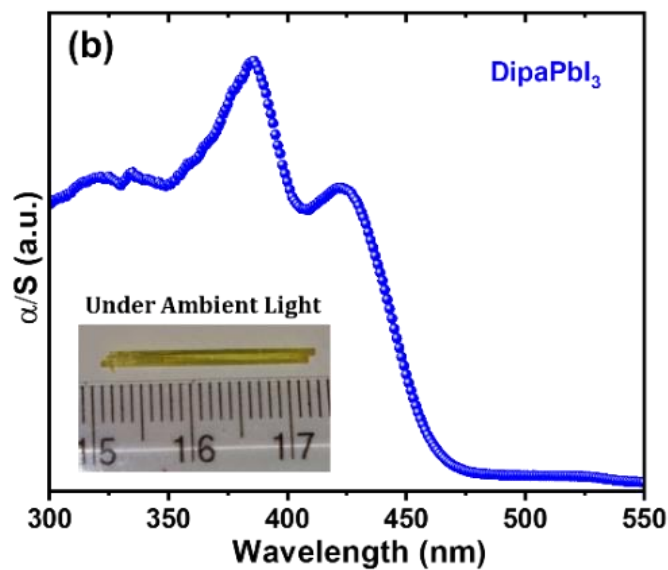
Figure 5.3: Absorption spectrum of $DipaPbI_3$ single crystals obtained from reflectance data by applying Kubulka-Munk transformation. Inset shows the optical image of a centimetre-long $DipaPbI_3$ single crystal under ambient light.
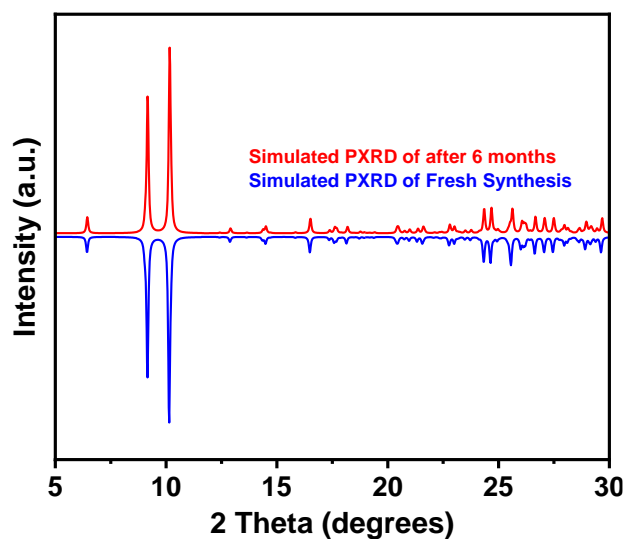
Figure 5.4: Comparison of the simulated PXRD patterns of the freshly synthesised DipaPbI$_3$ and the same crystals after six months. The simulated PXRD patterns are obtained from SCXRD.

Furthermore, these crystals showed thermal stability till ~250 °C, as shown by thermogravimetric analysis (Figure 5.5). The optically transparent window for these lower dimensional perovskites usually extend into the near IR regime. [31] They show strong absorbance only at the optical transitions in the UV-Visible spectrum. Only at very high wavenumbers do the IR absorbances of cations come into play, as seen in 1D halide perovskite with NIR-active heptamethine cations.[31]
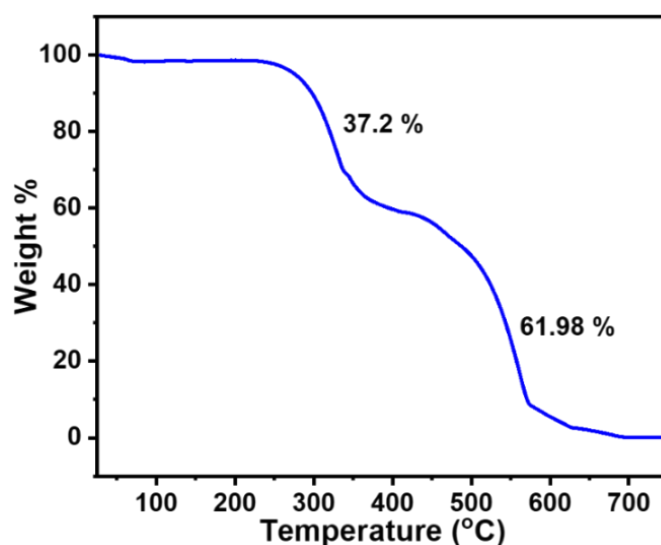
Figure 5.5: Thermogravimetric analysis (TGA) plot of DIPAPbI$_3$ single crystals showing thermal stability till ~250 °C.

5.3.2 Third harmonic generation (THG) from DipaPbI₃ single crystals

Figure 5.6a shows the wavelength-dependent THG response of DipaPbI$_3$ single crystal. The single crystals are pumped with wavelengths ranging between 1200 to 1600 nm at a constant power of 1.7 mW. The THG response increases as the pump wavelength is varied from 1600 nm to 1410 nm. At 1410 nm pump wavelength, the maximum THG response is observed. Interestingly, the frequency tripling of the 1410 nm pump, i.e., ~470 nm THG output, matches exactly with the absorption edge of the DipaPbI$_3$ single crystals (Figure 5.3). This selective enhancement of THG response is due to enhanced light-matter interaction at the resonance condition.[23] Below the 1410 nm pump, the THG intensity decreases sharply, probably due to self-absorption.[23] At the absorption edge (470 nm), minimal self-absorption is expected (see Figure 5.3). The spectral region with significant THG output is free from the absorption effects. The inset of Figure 5.6a shows the optical images of strong THG response at 1410 nm excitation with 1mW pump power, under ambient light and in the dark. Figure 5.6b shows the variation of THG intensity with the incident excitation wavelength. The spectral width (FWHM) of the THG response also varies and is minimum at the excitation wavelength corresponding to the maximum THG output (Figure 5.6b).
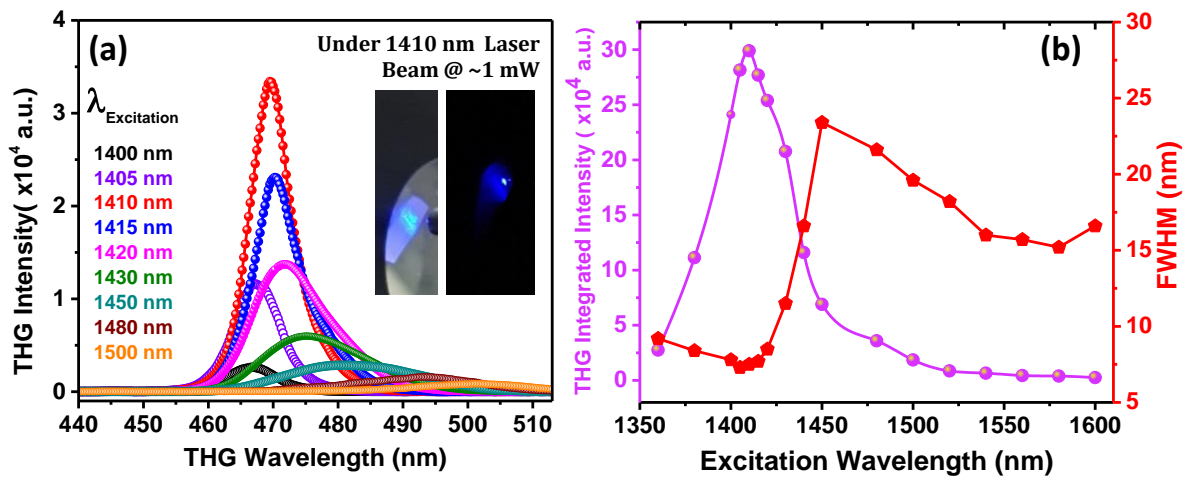

Figure 5.6: (a) Wavelength dependent THG response from DipaPbI$_3$ single crystals at constant excitation power of 1.7 mW. Inset shows the optical images of the THG signal upon excitation with a pump wavelength of 1410 nm and ~1 mW power, under ambient light and in the dark. (b) Wavelength dependent THG intensity (magenta) and FWHM of THG signals (red) of DipaPbI$_3$ single crystals.

1D Diisopropylammonium Lead Iodide Perovskite Shows Exceptional Optical Stability and Third-Order Nonlinearity

5.3.3 Determination of third-order NLO susceptibility ($\chi^{(3)}$)

The efficiency of THG process by nonlinear media is governed by the nonlinear Maxwell's equation which relates the THG intensity ($I_{3\omega}$) with the third-order NLO susceptibility at the pump wavelength $\chi^{(3)}$ and the pump intensity (I_ω) as given in equation 1 and 2:[32]

$$I_{3\omega} = \frac{9\omega^2}{16|\tilde{n}_{3\omega}||\tilde{n}_\omega|^3\varepsilon_0{}^2c^4} I_\omega{}^3 |\chi^{(3)}|^2 \left(\frac{e^{-2\alpha t}-2\cos(\Delta kt)e^{-\alpha t}+1}{\alpha^2+\Delta k^2}\right) e^{-2\alpha t} \quad (1)$$

$$\chi^{(3)} = \frac{\sqrt{I_{3\omega}}}{3\omega}\frac{4\varepsilon_0 c^2}{(I_\omega)^{\frac{3}{2}}}\left(|\tilde{n}_{3\omega}|^{\frac{1}{2}}|\tilde{n}_\omega|^{\frac{3}{2}}\right)\left(\frac{e^{-2\alpha t}-2\cos(\Delta kt)e^{-\alpha t}+1}{\alpha^2+\Delta k^2}\right)^{\frac{-1}{2}} e^{\alpha t} \quad (2)$$

where ω is the pump frequency, ε_0 is the dielectric constant of free space, *c* is the speed of light, $\tilde{n}_\omega$ and $\tilde{n}_{3\omega}$ are the complex refractive indices at the pump and THG frequencies respectively, α is the absorption coefficient of the material at the THG frequency, and Δk is the phase mismatch between the pump and third harmonic waves.

In the non-phase-matching condition, by using the relative method for two materials excited under similar conditions, $\chi^{(3)}$ can be compared using the THG intensities as given in equation 3:[33]

$$\chi_S^{(3)} = \chi_R^{(3)}\left[\frac{I_S(3\omega)}{I_R(3\omega)}\right]^{1/2} \quad (3)$$

where $\chi_S^{(3)}$ and $\chi_R^{(3)}$ are the third order NLO susceptibilities of the sample and the reference, $I_S(3\omega)$ and $I_R(3\omega)$ are the integrated THG intensities of the sample and reference, respectively. Recently reported 1D pyridinium lead iodide (PyPbI$_3$) single-crystals were used as a reference to determine the $\chi^{(3)}$ of DipaPbI$_3$ single-crystals, having a similar bandgap.[34] For PyPbI$_3$ at a pump wavelength of 1440 nm, $\chi_R^{(3)} = 1.96 \times 10^{-18}$ m^{2}V^{-2}.[23] Using the $\chi^{(3)}$ value of PyPbI$_3$ at 1440 nm in equation 3, the $\chi^{(3)}$ of DipaPbI$_3$ at 1440 nm comes out to be 2.05×10^{-18} m^{2}V^{-2}. DipaPbI$_3$ shows the selectively enhanced maximum THG response at 1410 nm. To calculate the $\chi^{(3)}$ of DipaPbI$_3$ at 1410 nm, the frequency dependence was incorporated. Referring back to Equation 2, we obtain $\chi^{(3)}$ of DipaPbI$_3$ at 1410 nm from the following equation:

$$\chi_{\omega_1}^{(3)} = \chi_{\omega_2}^{(3)} \left(\frac{3\omega_2}{3\omega_1}\right) \left[\frac{I(3\omega_1)}{I(3\omega_2)}\right]^{1/2} \qquad (4)$$

where $\chi_{\omega_1}^{(3)}$ and $\chi_{\omega_2}^{(3)}$ are the third-order NLO susceptibilities at pump frequencies ω_1 and ω_2, and $I(3\omega_1)$ and $I(3\omega_2)$ being the respective THG intensities. Figure 5.7 compares the THG responses of PyPbI$_3$ and DipaPbI$_3$ single crystals under same experimental conditions. The maximum $\chi^{(3)}$ value for DipaPbI$_3$ at 1410 nm is 4×10^{-18} m^{2}V^{-2} (refer to Table 5.3). The THG response of PyPbI$_3$ and DipaPbI$_3$ were recorded at 1440 nm and 1410 nm at 1.7 mW power. We observe that the THG response of DipaPbI$_3$, is in the same order of magnitude of 2D butylammonium lead iodide which showed maximum output at 1500 nm, as has been reported previously[23], and 2 times higher than 1D PyPbI$_3$ which showed maximum output at 1440 nm.[34]
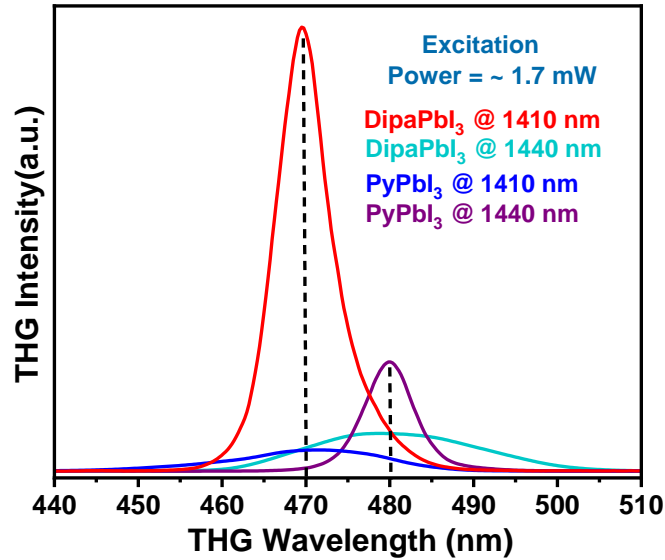

Figure 5.7: Comparison of THG response of DipaPbI$_3$ and PyPbI$_3$ single crystals to evaluate THG efficiency.

To further confirm the $\chi^{(3)}$ value of DipaPbI$_3$ single crystals, butylammonium lead iodide (Bu$_2$PbI$_4$) crystals, with a slightly lower bandgap, were also used as reference.[23] Bu$_2$PbI$_4$ shows peak THG response at 1500 nm excitation wavelength at which the THG response of DipaPbI$_3$ is significantly reduced. Figure 5.8 compares the THG output responses of Bu$_2$PbI$_4$ and DipaPbI$_3$. We obtained a higher $\chi^{(3)} = \sim 1.3 \times 10^{-17}$ m^{2}V^{-2} of DipaPbI$_3$ at 1410 nm using Bu$_2$PbI$_4$ as the reference. Since the linear and nonlinear optical properties of PyPbI$_3$ are closer to DipaPbI$_3$ single crystals the $\chi^{(3)}$ value estimated from PyPbI$_3$ as the reference seems more meaningful. Other commercial THG materials with output in this wavelength range and optical

properties and thickness similar to the DipaPbI$_3$ were not available for relative THG measurements.
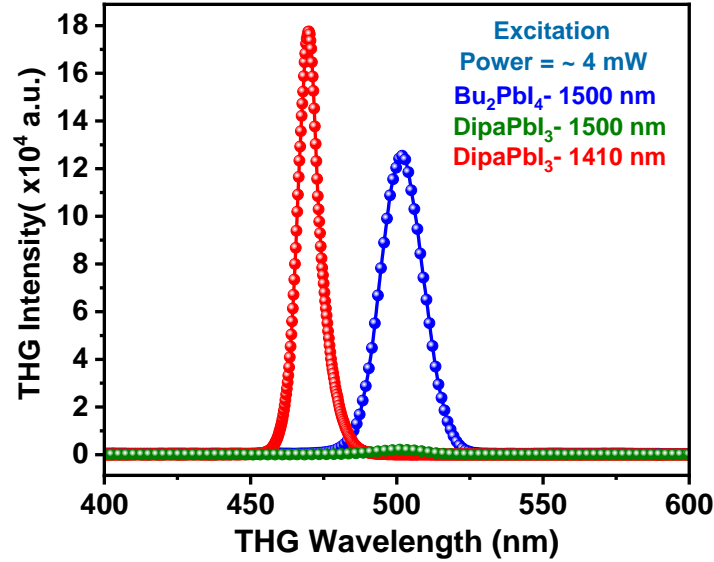

Figure 5.8: Comparison of THG response of Bu$_2$PbI$_4$ and DipaPbI$_3$ single crystals to evaluate THG efficiency at excitation power ~ 4 mW.

Table 5.3: Comparison of χ$^{(3)}$ and LIDT of DipaPbI$_3$ single crystals with lead halide perovskites.

Compound	λ (nm)	χ$^{(3)}$ (m^{2}V^{-2})	Method	LIDT (GWcm^{-2})	Space Group	Reference
DIPAPbI$_3$	**1410**	**4 x 10^{-18}**	**THG**	**144**	**P21/c**	**This work**
PyPbI$_3$	1440	1.96 x 10^{-18}	THG	33	Pnma	[34]
WS$_2$	1500	2.4 x 10^{-19}	THG		R3m	[18]
(C$_4$H$_9$NH$_3$)$_2$PbI$_4$	1500	3.5 x 10^{-18}	THG		Pcab	[23]
(C$_4$H$_9$NH$_3$)$_2$PbBr$_4$ (encapsulated)	1210	4.7 x 10^{-18}	THG		Pcab	[23]
(C$_4$H$_9$NH$_3$)$_2$(CH$_3$NH$_3$)Pb$_2$I$_7$	1675	11.2 x 10^{-18}	THG	11*	Ccmm	[23]
FAPbBr$_3$ NCs in SiO$_2$ matrix	1560	1.5 x 10^{-19}	THG	35		[34-35]
Au-Si hybrid nano-antenna	1320	6.9 x 10^{-17}	THG	3		[36]
Ag$_3$In(IO$_3$)$_6$	1500	1.1 x 10^{-21}	THG	0.82*	P-1	[37]

*The values are obtained by calculations done using parameters provided in respective papers.

As shown in the Table 5.3, Abdelwahab et. al. reported $\chi^{(3)} = 3.5\text{-}11.2 \times 10^{-18}$ m^{2}V^{-2} for 2D RPP single crystals of $(C_4H_9NH_3)_2PbBr_4$ embedded in hBN matrix.[23] Rubino et al. also presented a maximum $\chi^{(3)}$ of $1.46 \pm 0.19 \times 10^{-19}$ m^2 V^{-2} for FAPbBr$_3$ NCs embedded in a layer of porous silicon dioxide (SiO$_2$) nanoparticles. [31] Because of large expected bulk polarizability of the perovskite system containing Dipa cation as reported earlier, the nonlinear optical coeeficient $\chi^{(3)}$ is significantly enhanced as compared to other perovskite systems.[30] Additionally, a probable modification of the band structure might as well introduce a higher non-linear optical response.

5.3.4 Laser induced damage threshold (LIDT)

Along with the efficiency, the optical stability, quantified by LIDT, of an NLO material is of paramount importance. The LIDT implies to the optical stability of a nonlinear material used for NLO processes. The incident pump intensity at which the THG signal response deviates from cubic dependence determines the LIDT of the sample.[37] We determined the LIDT of DipaPbI$_3$ single crystals from excitation power-dependent THG at 1410 nm pump wavelength with a laser spot size of ~150 µm at the sample. Figure 5.9a depicts the incident power-dependent THG intensity variation at 1410 nm. As expected for a THG, we observed a cubic dependence of THG counts on the excitation power till ~4.6 mW as shown in Figure 5.9b. A deviation from the cubic behaviour beyond 4.6 mW is due to depletion of THG intensity because of saturation effects such as local heating.[23] Therefore, the LIDT of DipaPbI$_3$ single crystals is the peak laser intensity corresponding to 4.6 mW of incident laser light at 1410 nm. The data presented in the Figure 5.9b estimates an LIDT value of ~144 GW/cm^2 for DipaPbI$_3$ single crystals, which is an order of magnitude higher than the reported perovskites (refer to Table 5.3). The measured LIDT value depends on many factors, the quality of the crystal being one of the most critical parameters. The slow, controlled crystallization process over a few weeks results into a highly enhanced optical quality of the crystals. In addition, due to the flexible nature of the lattice of lead halide perovskites, their phonon modes can significantly help in heat dissipation processes under laser irradiation. The Dipa cations are connected to the lead iodide octahedra via electrostatic and hydrogen-bonding interactions. Hence, similar to other hybrid perovskite systems,[15, 38-39] Dipa cations are also expected to undergo molecular motions such as rotations, vibrations, and even translation to some extent. We anticipate that these modes play an important role in carrying the heat out of the laser irradiation site and decrease the local temperature. Also, photoinduced halide migration[40, 41-42]

may also be crucial in local heat dissipation. The structural uniqueness probably helps with heat dissipation processes and hence lead to a significantly higher LIDT, which is otherwise a signature of robust oxide perovskites. It is important to note that the mechanism of heat transport in hybrid lead halides under laser irradiation may be different than that in the absence of any strong radiation. The breathability in crystal structure prevents easy physical damage upon excitation with pulses of high energy, thus making them available for high-power nonlinear experiments. However, there is still a possibility of damage in optical crystals below the calculated LIDT value due to the presence of defects or occurrence of surface damage.
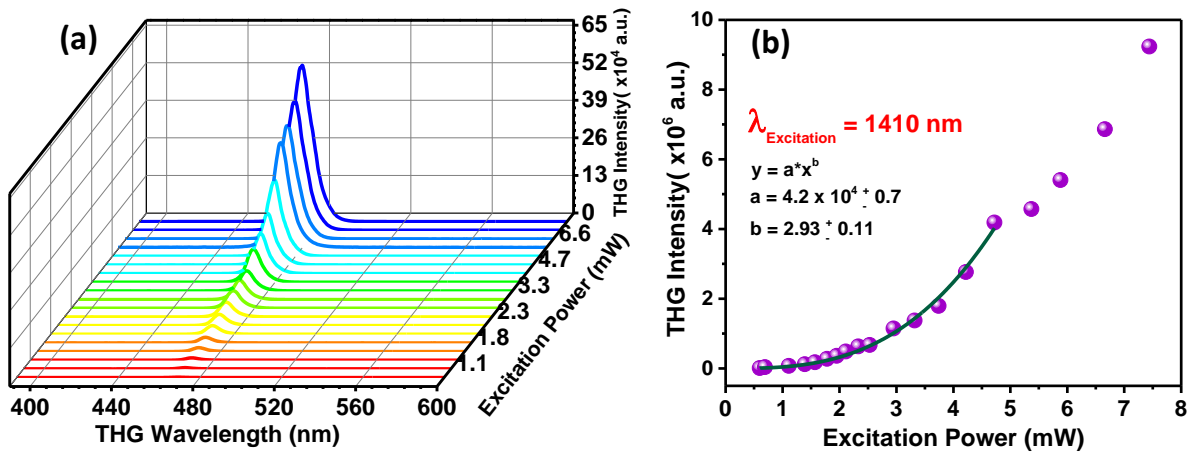
Figure 5.9: Power-dependent THG response of DipaPbI$_3$ single crystals (a) at 1410 nm excitation wavelength and (b) shows a cubic dependence of integrated THG intensity with respect to incident excitation power.

5.3.5 Polarization dependence of THG response

For a third order nonlinear process like third harmonic generation, the nonlinear polarization ($P^{(3)}$) is related to the incident electric field by the following equation:

$$P_i^{(3)} = \varepsilon_0 \sum_{jkl} \chi_{ijkl}^{(3)} E_j E_k E_l$$

where i, j, k, l are the Cartesian indices. $\chi_{ijkl}^{(3)}$ is a polar fourth rank tensor.[43] $\chi_{ijkl}^{(3)}$ is dependent upon the symmetry properties of a crystal, and can be useful to understand the structure-property relationship in case of NLO effects. To understand the correlation between the lattice symmetry and NLO properties of DipaPbI$_3$, we recorded the THG response as a function of the polarization of incident laser light,[18] shown in Figure 5.10. The *a*-axis of DipaPbI$_3$ crystal was

oriented orthogonal to the vertically polarized light, and the polarization of incident light was varied by rotation of the half-wave plate. A four-petal distribution of THG intensity variation is observed (Figure 5.10). The four lobes being nearly equal in intensity and the intensity dropping to near zero at the minimal angles indicates that there is high nonlinearity along both the axes. The crystal lattice interacts differently with the angle of polarization of the incident light, suggesting an anisotropic nature of DipaPbI$_3$ single crystals.[4] This anisotropic nature leads to a highly angular-dependent THG response due to the polarization-dependent third-order nonlinear susceptibility. From the polarization dependent THG response, DipaPbI$_3$ single crystals displayed a significantly large Polarization ratio ρ = 99.3% [$\rho = (I_{max}-I_{min})/(I_{max} + I_{min})$]. The maximum ρ value for chiral perovskites is reported to be ~96.4%, which is considered to be due to high sensitivity of SHG to the crystal symmetry and the orientations of the dipole moments.[44-45] Thus, we conclude that the THG response of DipaPbI$_3$ is even more sensitive to the crystal symmetry.
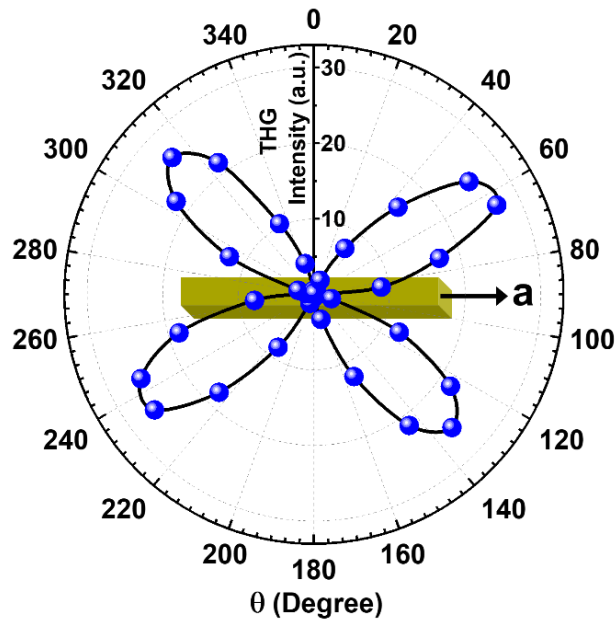

Figure 5.10: Polarization-dependent THG signal of DipaPbI$_3$ single crystals as a function of the polarization of incident laser light at 1410 nm with ~1 mW constant power. θ represents the change in the angle of polarization of the incident light with respect to the vertical axis (lab frame). The blue spheres represent the experimental THG data and the black line is the guide to the eye. The yellow cuboid represents the DipaPbI$_3$ single crystal showing the *a*-axis of the crystal in the experimental configuration.

5.4 Conclusion

In conclusion, 1D DipaPbI$_3$ perovskite single crystals are highly efficient and optically stable THG up-convertors of NIR light beams. These crystals show promising potential for high-energy, nonlinear optical applications such as lasing without any need for encapsulation. The high bulk polarization of the perovskite system containing Dipa organic cation is probably one of the significant factors for the enhanced THG efficiency. Crystal stability in ambient conditions over a long duration provides an additional benefit for real-life applications. The substitution by an asymmetric cation also opens up an avenue for a systemic understanding of the relationship between structural aspects and the NLO properties in perovskites. Bandgap tuning by varying halide ion and choice of other 'B' site cations will enable efficient THG at other desired wavelengths. The use of organic cations with higher polarizability should be further explored. With decreasing dimensionality from 3D to 0D in lead halide perovskites, the electronic band structure changes and the bandgap increases. In lower dimensional systems, the quantum and dielectric confinements are enhanced and these systems show very strong excitonic features. These excitonic states are probably leading to the resonant enhancement of the incident electric field, resulting to the enhancement of non-linear properties such as THG in lower dimensional systems. Hence, we predict that 0D systems will have even more enhanced THG response compared to the 1D systems.

5.5 References

1. Boyd, R., *Nonlinear Optics*, 4th ed.; *Elsivier*, **2020**, p 634.

2. Shen, W.; Chen, J.; Wu, J.; Li, X.; Zeng, H., Nonlinear Optics in Lead Halide Perovskites: Mechanisms and Applications. *ACS Photonics* **2021**, *8*, 113-124.

3. Lee, C.-K.; Zhang, J.-Y.; Huang, J. Y.; Pan, C.-L., Generation of Femtosecond Laser Pulses Tunable from 380 nm to 465 nm via Cascaded Nonlinear Optical Mixing in a Noncollinear Optical Parametric Amplifier with a Type-I Phase Matched BBO Crystal. *Opt. Express* **2003**, *11*, 1702-1708.

4. Yi, G.; Lee, H.; Jiannan, J.; Chun, B. J.; Han, S.; Kim, H.; Kim, Y. W.; Kim, D.; Kim, S.-W.; Kim, Y.-J., Nonlinear Third Harmonic Generation at Crystalline Sapphires. *Opt. Express* **2017**, *25*, 26002-26010.

5. Wang, G.; Mei, S.; Liao, J.; Wang, W.; Tang, Y.; Zhang, Q.; Tang, Z.; Wu, B.; Xing, G., Advances of Nonlinear Photonics in Low-Dimensional Halide Perovskites. *Small* **2021**, *17*, 2100809.

6. Säynätjoki, A., et al., Ultra-Strong Nonlinear Optical Processes and Trigonal Warping in MoS_2 Layers. *Nat. Commun.* **2017**, *8*, 893.

7. Sarkar, S.; Ravi, V. K.; Banerjee, S.; Yettapu, G. R.; Markad, G. B.; Nag, A.; Mandal, P., Terahertz Spectroscopic Probe of Hot Electron and Hole Transfer from Colloidal $CsPbBr_3$ Perovskite Nanocrystals. *Nano Lett.* **2017**, *17*, 5402-5407.

8. Jena, A. K.; Kulkarni, A.; Miyasaka, T., Halide Perovskite Photovoltaics: Background, Status, and Future Prospects. *Chem. Rev.* **2019**, *119*, 3036-3103.

9. Yettapu, G. R.; Talukdar, D.; Sarkar, S.; Swarnkar, A.; Nag, A.; Ghosh, P.; Mandal, P., Terahertz Conductivity within Colloidal $CsPbBr_3$ Perovskite Nanocrystals: Remarkably High Carrier Mobilities and Large Diffusion Lengths. *Nano Lett.* **2016**, *16*, 4838-4848.

10. Akkerman, Q. A.; Rainò, G.; Kovalenko, M. V.; Manna, L., Genesis, Challenges and Opportunities for Colloidal Lead Halide Perovskite Nanocrystals. *Nat. Mater.* **2018**, *17*, 394-405.

11. Nayak, P. K.; Mahesh, S.; Snaith, H. J.; Cahen, D., Photovoltaic Solar Cell Technologies: Analysing the State of the Art. *Nat. Rev. Mater.* **2019**, *4*, 269-285.

12. Xu, J.; Li, X.; Xiong, J.; Yuan, C.; Semin, S.; Rasing, T.; Bu, X.-H., Halide Perovskites for Nonlinear Optics. *Adv. Mater.* **2020**, *32*, 1806736.

13. Han, X.; Ge, F.; Xu, J.; Bu, X.-H., Aggregation-Induced Emission Materials for Nonlinear Optics. *Aggregate* **2021**, *2*, e28.

14. Rivett, J. P. H., et al., Long-Lived Polarization Memory in the Electronic States of Lead-Halide Perovskites from Local Structural Dynamics. *Nat. Commun.* **2018**, *9*, 3531.

15. Miyata, K.; Atallah, T. L.; Zhu, X.-Y., Lead Halide Perovskites: Crystal-Liquid Duality, Phonon Glass Electron Crystals, and Large Polaron Formation. *Sci. Adv.* **2017**, *3*, e1701469.

16. Yaffe, O., et al., Local Polar Fluctuations in Lead Halide Perovskite Crystals. *Phys. Rev. Lett.* **2017**, *118*, 136001.

17. Liao, W.-Q.; Zhang, Y.; Hu, C.-L.; Mao, J.-G.; Ye, H.-Y.; Li, P.-F.; Huang, S. D.; Xiong, R.-G., A Lead-Halide Perovskite Molecular Ferroelectric Semiconductor. *Nat. Commun.* **2015**, *6*, 7338.

18. Yao, L., et al., Strong Second- and Third-Harmonic Generation in 1D Chiral Hybrid Bismuth Halides. *J. Amer. Chem. Soc.* **2021**, *143*, 16095-16104.

19. Gan, Z.; Wen, X.; Chen, W.; Zhou, C.; Yang, S.; Cao, G.; Ghiggino, K. P.; Zhang, H.; Jia, B., The Dominant Energy Transport Pathway in Halide Perovskites: Photon Recycling or Carrier Diffusion? *Adv. Energy Mater.* **2019**, *9*, 1900185.

20. Saouma, F. O.; Stoumpos, C. C.; Wong, J.; Kanatzidis, M. G.; Jang, J. I., Selective Enhancement of Optical Nonlinearity in Two-Dimensional Organic-Inorganic Lead Iodide Perovskites. *Nat. Commun.* **2017**, *8*, 742.

21. Abdelwahab, I.; Dichtl, P.; Grinblat, G.; Leng, K.; Chi, X.; Park, I.-H.; Nielsen, M. P.; Oulton, R. F.; Loh, K. P.; Maier, S. A., Giant and Tunable Optical Nonlinearity in Single-Crystalline 2D Perovskites Due to Excitonic and Plasma Effects. *Adv. Mater.* **2019**, *31*, 1902685.

22. Han, X.; Zheng, Y.; Chai, S.; Chen, S.; Xu, J., 2D Organic-Inorganic Hybrid Perovskite Materials for Nonlinear Optics. *Nanophotonics* **2020**, *9*, 1787-1810.

23. Abdelwahab, I.; Grinblat, G.; Leng, K.; Li, Y.; Chi, X.; Rusydi, A.; Maier, S. A.; Loh, K. P., Highly Enhanced Third-Harmonic Generation in 2D Perovskites at Excitonic Resonances. *ACS Nano* **2018**, *12*, 644-650.

24. Wang, Y.; Zhang, X.; Wang, D.; Li, X.; Meng, J.; You, J.; Yin, Z.; Wu, J., Compositional Engineering of Mixed-Cation Lead Mixed-Halide Perovskites for High-Performance Photodetectors. *ACS Appl. Mater. Interfaces* **2019**, *11*, 28005-28012.

25. Blancon, J.-C.; Even, J.; Stoumpos, C. C.; Kanatzidis, M. G.; Mohite, A. D., Semiconductor Physics of Organic–Inorganic 2D Halide Perovskites. *Nat. Nanotechnol.* **2020**, *15*, 969-985.

26. Li, X., et al., Expanding the Cage of 2D Bromide Perovskites by Large A-Site Cations. *Chem. Mater.* **2022**.

27. Knight, A. J.; Herz, L. M., Preventing Phase Segregation in Mixed-Halide Perovskites: A Perspective. *Energy Environ. Sci.* **2020**, *13*, 2024-2046.

28. Sheikh, T.; Nawale, V.; Pathoor, N.; Phadnis, C.; Chowdhury, A.; Nag, A., Molecular Intercalation and Electronic Two Dimensionality in Layered Hybrid Perovskites. *Angew. Chem. Int. Ed.* **2020**, *59*, 11653-11659.

29. Sheikh, T.; Maqbool, S.; Mandal, P.; Nag, A., Introducing Intermolecular Cation-Π Interactions for Water-Stable Low Dimensional Hybrid Lead Halide Perovskites. *Angew. Chem. Int. Ed.* **2021**, *60*, 18265-18271.

30. Fu, D.-W., et al., Diisopropylammonium Bromide Is a High-Temperature Molecular Ferroelectric Crystal. *Science* **2013**, *339*, 425-428.

31. Véron, A. C.; Linden, A.; Leclaire, N. A.; Roedern, E.; Hu, S.; Ren, W.; Rentsch, D.; Nüesch, F. A., One-Dimensional Organic–Inorganic Hybrid Perovskite Incorporating near-Infrared-Absorbing Cyanine Cations. *J. Phys. Chem. Lett.* **2018**, *9*, 2438-2442.

32. Youngblood, N.; Peng, R.; Nemilentsau, A.; Low, T.; Li, M., Layer-Tunable Third-Harmonic Generation in Multilayer Black Phosphorus. *ACS Photonics* **2017**, *4*, 8-14.

33. Haynes, A. S.; Banerjee, A.; Saouma, F. O.; Otieno, C. O.; Jang, J. I.; Kanatzidis, M. G., Phase Transition, Conformational Exchange, and Nonlinear Optical Third Harmonic Generation of $ACsP_2Se_8$ (A = K, Rb, Cs). *Chem. Mater.* **2016**, *28*, 2374-2383.

34. Maqbool, S.; Sheikh, T.; Thekkayil, Z.; Deswal, S.; Boomishankar, R.; Nag, A.; Mandal, P., Third Harmonic Upconversion and Self-Trapped Excitonic Emission in 1D Pyridinium Lead Iodide. *J. Phys. Chem. C* **2021**, *125*, 22674-22683.

35. Rubino, A.; Huq, T.; Dranczewski, J.; Lozano, G.; Calvo, M. E.; Vezzoli, S.; Míguez, H.; Sapienza, R., Efficient Third Harmonic Generation from $FAPbBr_3$ Perovskite Nanocrystals. *J. Mater. Chem. C* **2020**, *8*, 15990-15995.

36. Shibanuma, T.; Grinblat, G.; Albella, P.; Maier, S. A., Efficient Third Harmonic Generation from Metal–Dielectric Hybrid Nanoantennas. *Nano Lett.* **2017**, *17*, 2647-2651.

37. Park, G.; Byun, H. R.; Jang, J. I.; Ok, K. M., Dimensionality–Band Gap–Third-Harmonic Generation Property Relationship in Novel Main-Group Metal Iodates. *Chem. Mater.* **2020**, *32*, 3621-3630.

38. Bechtel, J. S.; Seshadri, R.; Van der Ven, A., Energy Landscape of Molecular Motion in Cubic Methylammonium Lead Iodide from First-Principles. *J. Phys. Chem. C* **2016**, *120*, 12403-12410.

39. Mattoni, A.; Filippetti, A.; Saba, M. I.; Delugas, P., Methylammonium Rotational Dynamics in Lead Halide Perovskite by Classical Molecular Dynamics: The Role of Temperature. *J. Phys. Chem. C* **2015**, *119*, 17421-17428.

40. Kamat, P. V.; Kuno, M., Halide Ion Migration in Perovskite Nanocrystals and Nanostructures. *Acc. Chem. Res.* **2021**, *54*, 520-531.

41. Kaiser, W.; Mosconi, E.; Alothman, A. A.; Meggiolaro, D.; Gagliardi, A.; De Angelis, F., Halide-Driven Formation of Lead Halide Perovskites: Insight from Ab Initio Molecular Dynamics Simulations. *Mater. Adv.* **2021**, *2*, 3915-3926.

42. Liu, Y.; Ievlev, A. V.; Borodinov, N.; Lorenz, M.; Xiao, K.; Ahmadi, M.; Hu, B.; Kalinin, S. V.; Ovchinnikova, O. S., Direct Observation of Photoinduced Ion Migration in Lead Halide Perovskites. *Adv. Funct. Mater.* **2021**, *31*, 2008777.

43. Fehn, T.; Vogtmann, T.; Hübner, J.; Schwoerer, M., Anisotropy of the Nonlinear Optical Susceptibility X$^{(3)}$ in Polydiacetylene Single Crystals. *Appl. Phys. B* **1994**, *59*, 203-209.

44. Duan, Y., et al., Aggregation Induced Enhancement of Linear and Nonlinear Optical Emission from a Hexaphenylene Derivative. *Adv. Funct. Mater.* **2016**, *26*, 8968-8977.

45. Yuan, C.; Li, X.; Semin, S.; Feng, Y.; Rasing, T.; Xu, J., Chiral Lead Halide Perovskite Nanowires for Second-Order Nonlinear Optics. *Nano Lett.* **2018**, *18*, 5411-5417.

Appendix 1

Interplay of Phase Stability and Polarizability in the Third Harmonic Up Conversion Process in Pyridinium Lead Mixed Halides
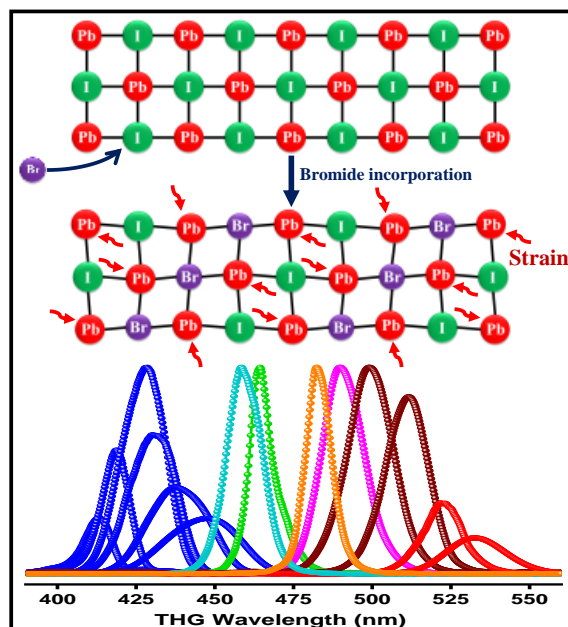
Interplay of Phase Stability and Polarizability in the Third Harmonic Upconversion Process in Pyridimium Lead Mixed Halides

Abstract

Lower dimensional lead halide perovskites have demonstrated highly enhanced nonlinear optical (NLO) properties with near band-edge NLO resonance due to strong quantum and dielectric confinement. Varying the halide composition can tune the bandgap of lead halide perovskites, which can be employed to achieve the wavelength tunability of the NLO response. The halide composition of the 1D pyridinium lead iodide system was varied to establish if the earlier demonstrated highly enhanced third harmonic generation (THG) near the band-edge with remarkable optical stability is retained. We performed extensive THG studies on $PyPbBr_xI_{3-x}$ systems, varying the wavelength, power, and polarization of the IR pump wavelength. We observe an efficient but complex THG response from the systems, affected by the induced lattice strain due to the mixed halide composition. A wide wavelength tunability is achieved for the THG, although the systems deviate from near band-edge resonance behavior. Polarization-dependent studies show a relatively less anisotropic THG response.

Graphical Abstract

*Interplay of Phase Stability and Polarizability in the Third Harmonic Upconversion
Process in Pyridimium Lead Mixed Halides*

A1.1 Introduction

Lead halide perovskites (LHPs) have been in the spotlight of material chemistry and semiconductor research due to their remarkable optoelectronic and photovoltaic performance.[1-7] Convenient solution processibility, choice of suitable organic cations for desirable properties, and bandgap engineering by varying the halide composition make them a suitable choice for a variety of applications.[8] However, unlike conventional semiconductors, lead halide perovskites exhibit a soft and disordered lattice associated with their dual ionic-covalent nature[9], which directly affects their optoelectronic properties.[10-11] As a result, they are quite sensitive to variations in their composition. This is especially true in the case of hybrid LHPs where there is an organic A-site cation. The organic cations give a further soft texture, resulting in a mechanically soft and dynamically disordered lattice, and many studies have indicated liquid-crystal-like properties in the hybrid LHPs.[12-14] Further interesting properties emerge upon dimensionality reduction by employing large and aromatic cations.[2, 15-16] These lower dimensional (LD) perovskites or perovskitoids[17] show strong excitonic effects and interesting linear and nonlinear optical (NLO) properties due to quantum and dielectric confinement.[2, 15-16, 18-24] It has also been established that the excited state properties and dynamics of these LD systems are affected by traps and self-trapped states.[25-29] The flexibility of the components is, in fact, what gives rise to a lot of intriguing properties and observations in the perovskites. Apart from the A-site cations, different compositions of halides and even non-halide/pseudohalide ions have been incorporated into perovskite systems.[11] In this report, we study the effect of varying the halide composition on the nonlinear third harmonic up-conversion process in one-dimensional pyridinium lead halide systems.

Varying halides dramatically impact the optical and electronic properties of perovskites, and mixed halide systems with varying halide compositions have been employed for bandgap engineering in perovskite systems.[30-32] An important aspect of the mixed halide systems is the associated strain induced by the mismatch in the size of the constituting halide ions.[11, 30, 33] This often results in phase instabilities and ion migrations upon external stimuli like applied electric bias, light irradiation, etc.[30, 33-38] This may lead to dynamic structural disorders resulting in trap states, which can affect the performance of the perovskite systems and the devices fabricated devices.[11, 34-35, 38]

Nonlinear optics is important for a variety of applications in photonics and other optical technologies, including light manipulation, lasing, photon energy conversion, and detection.[39-]

Appendix 1

Interplay of Phase Stability and Polarizability in the Third Harmonic Upconversion Process in Pyridimium Lead Mixed Halides

[40] Parametric NLO processes like higher harmonic generation, sum & difference frequency generation, etc., are essential for laser frequency tuning and upconversion. NLO processes are governed by the nonlinear polarization equation:[40]

$$P(E) = \varepsilon_0\left[\chi^{(1)}E + \chi^{(2)}E^2 + \chi^{(3)}E^3 + \cdots\right] \qquad (1)$$

where P(E) is the polarization or the dipole moment induced per unit volume upon the application of an electric field 'E', and $\chi^{(n)}$ refers to the nth-order optical susceptibility of the system. The efficiency of a particular NLO process in a material is dependent on the corresponding nonlinear susceptibility. The NLO processes are dependent on the nonlinear powers of the electric field, and hence they come into play at high light intensities.

Since NLO processes are important for a lot of important applications, materials with high nonlinear coefficients are always of interest. There are two important factors to consider while classifying materials for NLO applications. One is the higher-order NLO susceptibility $\chi^{(n)}$, which determines the efficiency of the NLO response of the system. As evident from equation (1), the susceptibilities are a measure of polarization induced in the system upon applying an electric field. Therefore, materials with high polarizability are expected to show a high $\chi^{(3)}$ and thereby an efficient NLO response.[41] However, this alone cannot guarantee an efficient NLO response. As the system will experience very high electric fields during the NLO processes, it is also important that the material remain stable at high incident light intensities. The stability of a material during an NLO process is determined by its laser-induced damage threshold (LIDT).[42] So, it is important for the materials to have mechanisms to avoid local heating and other undesired saturation effects and maintain structural stability during high-intensity NLO processes.

The LD perovskitoids show enhanced NLO properties upon a suitable choice of organic cations.[19] We have explored a 1D perovskitoid system pyridinium lead iodide (PyPbI$_3$) showing a highly enhanced third harmonic generation (THG) upon near band-edge excitation, and with a remarkably high LIDT, in Chapter 4. Based on this observation, we decided to employ band gap engineering using halide exchange to study the THG response of pyridinium-based perovskitoid systems with mixed bromide-iodide composition. Since these mixed halide systems crystalize as 1D crystal systems with a polarizable aromatic cation and varying halide composition, there are a number of factors that could be expected to come into play in the THG response. Firstly, the bandgap engineering[11, 30-31] will provide a wide wavelength range

Appendix 1

Interplay of Phase Stability and Polarizability in the Third Harmonic Upconversion Process in Pyridimium Lead Mixed Halides

tunability of the efficient third harmonic up-conversion process similar to the pyridinium lead iodide system, as reported in Chapter 4. The efficiency of the THG process is dependent on the nonlinear polarizability of the system[40], and the presence of aromatic cation makes the lattice highly polarizable, along with the strong confinement of charge carriers due to the 1D nature of the system.[41] Secondly, the varying composition of halide ions can give rise to strain in the system, thereby affecting the electronic structure, and can induce trap states.[11, 30, 33-35, 38] The 1D nature of the system, along with the strain induced by the mixed halide composition, can result in an increased density of traps. These traps can provide states for resonant enhancement of THG output.

Herein we report the THG response of pyridinium lead halides with varying halide composition. We observe that a number of factors, including the polarizability and the soft & dynamic nature incorporated by the aromatic cation to the perovskite system, confinement effects in the hybrid 1D system, as well as the strain induced by the halide composition play a role in the THG response of the pyridinium lead halide systems. An interesting observation is that only the iodide system shows a band-edge resonance of the THG response. Multiple factors, including the strain induced due to mixed halide composition in the system, have possibly led to this deviation from the band-edge resonance behavior in the case of mixed halide systems, as we shall discuss in this chapter. However, we observe that even though the band-edge resonance is not observed, we obtain an efficient and wide wavelength range tunability of the third harmonic up-conversion, which was one of our primary motivations for this study. All the systems show a comparable THG efficiency, with the third-order nonlinear susceptibility $\chi^{(3)}$ of the same order of magnitude as that of the pyridinium lead iodide, which we have reported in Chapter 4. It is also interesting that all the mixed halide systems show good optical stability during the THG process. We also studied the polarization dependence of the THG response and observed that the pyridinium lead halide systems show a relatively less anisotropic polarizable response, which might be one of the reasons for the efficient THG response of the system.

A1.2 Experimental Section

A1.2.1 Synthesis

Single crystals of PyPbBr$_3$ and PyPbBr$_x$I$_{3-x}$ mixed halides were synthesized by following a previously reported method.[43] 10 mmol (2232 mg) PbO was dissolved in 15 mL of HI, HBr

Appendix 1

Interplay of Phase Stability and Polarizability in the Third Harmonic Upconversion Process in Pyridimium Lead Mixed Halides

acids (taken in required proportions; see discussion section for details) with 50% aqueous H_3PO_2 (1.7 mL) by heating to 100 °C under constant stirring for 10 min until a clear solution was obtained. To this, 10 mmol of pyridinium bromide was added with continued heating until a clear solution was obtained again. The solution was allowed to cool down to room temperature naturally. Needle-shaped crystals started to crystalize upon cooling. The crystals were filtered, rinsed with acetone, and dried under reduced pressure.

A1.2.2 Characterization

Powder X-ray Diffraction: A Bruker D8 Advance X-ray diffractometer using Cu Kα radiation (1.54 Å) was used to record the Powder X-ray diffraction (PXRD) data.

Scanning Electron Microscopy & Energy Dispersive X-Ray Spectroscopy: A Zeiss Ultra Plus FESEM instrument was used to obtain the Scanning electron microscopy (SEM) images and Energy Dispersive X-Ray (EDAX) spectra.

Optical Diffuse Reflectance Spectrum: A Shimadzu UV-3600 plus UV−VIS−NIR double-beam, double-monochromator spectrophotometer was used to record the optical diffuse reflectance spectrum of the powdered samples with $BaSO_4$ as the reference with 100% reflectance. Kubelka−Munk transformation was used to calculate the absorbance from the reflectance spectrum.

A1.2.3 Third harmonic generation setup

A 250-2600 nm wavelength tunable TOPAS-C Optical Parametric Amplifier (OPA, Light Conversion) was used for the THG experiments, pumped by a regenerative Spitfire Pro XP amplifier (Spectra-Physics) generating pulses of 800 nm central wavelength with 45 fs (FWHM) at 1 kHz repetition rate. The amplifier was seeded by a Tsunami oscillator (Spectra-Physics). The wavelength-dependent experiments were performed in the range of 1200-1600 nm at a constant power of 3 mW. An 850 nm long-pass filter was used to ensure the purity of the pump beam, and a variable density N.D. filter was used for power-dependent measurements at the resonant wavelengths of the respective samples. A half-wave plate was used for the polarization-dependent measurements, and a Glan polarizer was placed before it to provide a perfectly plain polarized beam. The beam was focused using a 250 mm plano-convex lens, and the sample was kept at a 200 mm distance from the lens; the sample was kept away from the focus so that it is not damaged during the measurements and to ensure enough spot size for the interaction of the sample and the pump beam to provide a good signal strength. The sample

Appendix 1

Interplay of Phase Stability and Polarizability in the Third Harmonic Upconversion Process in Pyridimium Lead Mixed Halides

was placed on a threaded cage rotation mount (THORLABS CRM1/M), so that it could be rotated accordingly for the initial optimization for maximum output. A 25 mm plano-convex lens was used to collimate the output signal, and a 750 nm short-pass filter was used to eliminate any signal contribution from the pump beam. The signal was coupled to a 400 μm optical fiber and recorded using a miniature spectrometer (USB4000, Ocean Optics).

The beam radius was determined by the knife-edge method by fitting the transmitted power data using the equation:[44]

$$f(s) = \frac{1}{\exp\left((-1.5954086)s + (-7.3638857 \times 10^{-2})s^3 + (6.4121343 \times 10^{-4})s^5\right)} \tag{2}$$

where f(s) is the power output and $s = \frac{\sqrt{2}(x-x_0)}{w}$, x being the knife-edge position, x_0 the center of the beam, and w being the 1/e radius of the Gaussian beam. After fitting, the radius was obtained to be $w = 218 \times 10^{-6}$m.

A1.3 Results & Discussion

A1.3.1 Synthesis & characterization

PyPbBr$_3$ and PyPbBr$_x$I$_{3-x}$ mixed halides were synthesized by following a previous report (see Experimental Section). The SEM images of the crystals are shown in Figure A1.1. We observed that it is difficult to incorporate bromide ions into the perovskitoid crystal structure for the mixed halides, with a larger quantity of bromide precursor being required. This is evident from the large difference in I:Br precursor ratios used in the synthesis and the I:Br ions being incorporated in the crystal lattice as determined by EDAX analysis of the crystals as presented in Table A1.1. Five mixed halide compositions were synthesized, starting with the I:Br precursor ratios of 1:7, 1:10, 1:20, 1:30, and 1:50. The corresponding chemical compositions of the mixed halides were PyPbBr$_{0.57}$I$_{2.43}$, PyPbBr$_{0.76}$I$_{2.24}$, PyPbBr$_{1.69}$I$_{1.31}$, PyPbBr$_{2.32}$I$_{0.68}$, and PyPbBr$_{2.61}$I$_{0.39}$, as listed in Table A1.1.
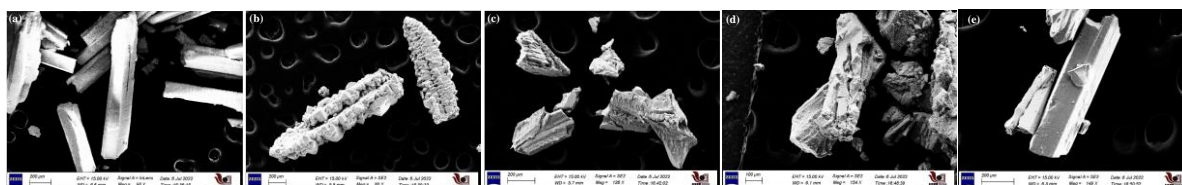
Figure A1.1: SEM images of (a) PyPbBr$_{0.57}$I$_{2.43}$, (b) PyPbBr$_{0.76}$I$_{2.24}$, (c) PyPbBr$_{1.69}$I$_{1.31}$, (d) PyPbBr$_{2.32}$I$_{0.68}$, and (e) PyPbBr$_{2.61}$I$_{0.39}$ single crystals.

Interplay of Phase Stability and Polarizability in the Third Harmonic Upconversion Process in Pyridimium Lead Mixed Halides

Table A1.1: Elemental analysis from EDAX

| HI:HBr Ratio | Element | Atomic % | | | | Average | I:Br Ratio | Fraction of Br | Comp. of Br in X_3 | Formula |
		Scan 1	Scan 2	Scan 3	Scan 4					
1:7	N	19.8	29.16			24.48	1 : 0.24	0.191	0.573	$PyPbBr_{0.57}I_{2.43}$
	Br	1.42	3.79			2.605				
	I	12.67	9.41			11.04				
	Pb	4.85	2.85			3.85				
1:10	N	11.05	8.82			9.935	1 : 0.34	0.254	0.762	$PyPbBr_{0.76}I_{2.24}$
	Br	5.36	4.49			4.925				
	I	14.51	14.36			14.435				
	Pb	6.27	6.03			6.15				
1:20	N	8.79	12.97	4.09		8.6167	1 : 1.30	0.564	1.692	$PyPbBr_{1.69}I_{1.31}$
	Br	10.91	10.7	13.2		11.6033				
	I	8.09	8.6	10.17		8.9533				
	Pb	5.81	6.11	7.57		6.4967				
1:30	N	15.49	8.93	7.65		10.69	1 : 3.34	0.774	2.322	$PyPbBr_{2.32}I_{0.68}$
	Br	14.35	14.8	15.28		14.81				
	I	4.19	4.78	4.33		4.4333				
	Pb	5.26	6.11	5.41		5.5933				
1:50	N	5.19	3.7	8.62	4.22	5.4325	1 : 6.64	0.869	2.607	$PyPbBr_{2.61}I_{0.39}$
	Br	16.75	20.96	20.4	15.97	18.52				
	I	2.37	3.35	3.06	2.38	2.79				
	Pb	5.68	7.53	6.94	5.18	6.3325				

The powder X-ray diffraction patterns of different $PyPbBr_xI_{3-x}$ compositions are shown in Figure A1.2. These PXRD patterns suggest that all these diffraction peaks are not at the same 2θ values, suggesting slightly different structures from the pure bromide (*Pna2₁* chapter 3) and iodide compositions (*Pnma*, chapter 4).

Interplay of Phase Stability and Polarizability in the Third Harmonic Upconversion Process in Pyridimium Lead Mixed Halides
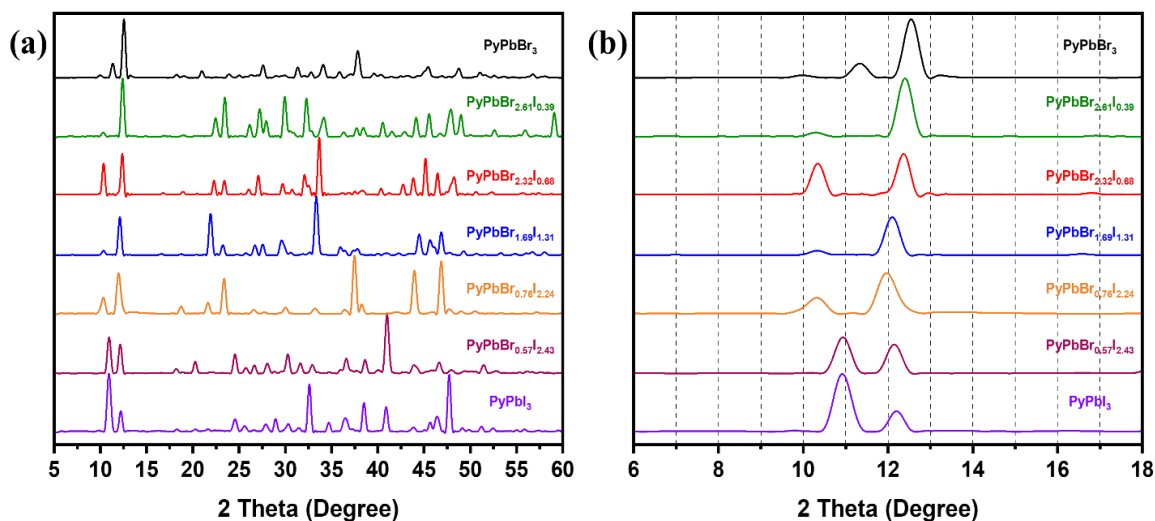

Figure A1.2: (a) PXRD patterns of PyPbBr$_x$I$_{3-x}$ (x= 0, 0.57, 0.76, 1.69, 2.32, 2.61, 3) single crystals. (b) The zoomed-in spectra showing a gradual shift in the position of the diffraction peak at 2θ value of ~12.
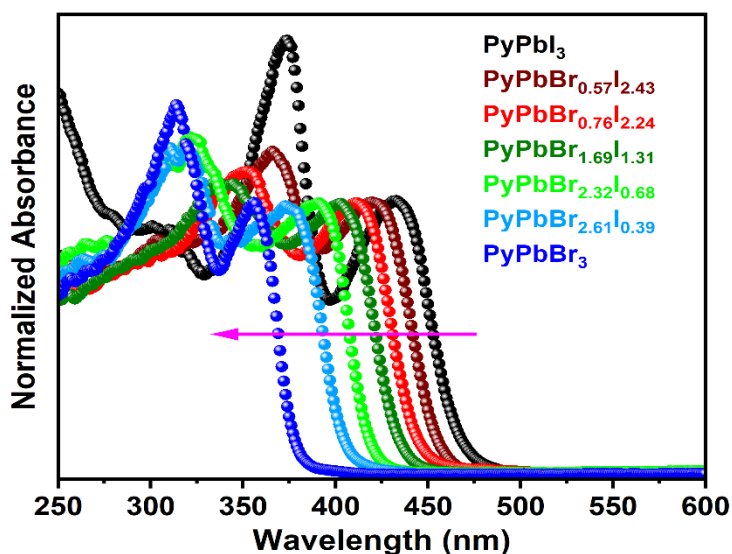

Figure A1.3: UV-Visible absorbance of PyPbBr$_x$I$_{3-x}$ (x= 0, 0.57, 0.76, 1.69, 2.32, 2.61, 3) showing a gradual blue shift of the band edge with an increase in bromide composition. The absorbance data is obtained from the optical diffused reflectance data using the Kubelka-Munk transformation.

Figure A1.3 shows the UV-Vis absorption spectra of the PyPbBr$_x$I$_{3-x}$ crystals (x = 0 to 3). Upon increasing the bromide composition in the PyPbBr$_x$I$_{3-x}$, the band-edge shifts gradually from 480 nm to 380 nm, indicating an increase in the band gap. Unlike PyPbI$_3$ (Chapter 4) and PyPbBr$_3$ (Chapter 3), no photoluminescence (PL) emission was observed from any of the

Appendix 1

Interplay of Phase Stability and Polarizability in the Third Harmonic Upconversion Process in Pyridimium Lead Mixed Halides

mixed halide compositions. This suggests the possibility of trap states in these mixed halide systems, which are known to affect the photo-emissive properties in perovskites. It is evident from the literature that the varied halide composition can induce strain in the crystal system due to the mismatch in the size of the halide ions, which can affect the structure and the electronic properties of the perovskite system.[11, 30-31, 33-35, 38] These strain effects are often triggered by external stimuli like light, and therefore the optical properties of the system are affected by these strain effects. Does the induced strain affect the NLO properties as well? To find the answer, we recorded the NLO responses of the mixed $PyPbBr_xI_{3-x}$, as discussed in the next section.

A1.3.2 Third harmonic generation

In 1D perovskitoid systems with varying halide composition, a number of factors, including quantum & dielectric confinement due to the 1D nature of the system, bandgap tuning, and strain-induced due to the mixed halide composition, can affect the NLO response. Therefore, we studied the THG response of $PyPbBr_xI_{3-x}$ (x = 0 to 3) single crystals over a range of excitation wavelengths (1200-1600 nm).

Figure A1.4 shows the wavelength-dependent THG response of the $PyPbBr_xI_{3-x}$ single crystals. Wavelength tunable THG response was obtained from all the studied systems. All the mixed halide crystals and $PyPbBr_3$ do not show the characteristic resonance of THG at the band edge.[45] This deviation from the band-edge resonance is suspected to be due to the mixed-halide composition-induced strain in the system. As we have discussed earlier, the mixed halide composition can induce strain in the perovskite system due to a mismatch in the size of ions and lead to phase instabilities and undesired phenomena like ion migration, which can alter the electronic structure and induce sub-bandgap trap states. The strain effects are often triggered by external stimuli like light.[30, 33-38]

For a third-order NLO process like THG, very high-intensity light is used as the excitation source (our measurements employed light intensities of the order of GW/cm^2), and so the effect on the NLO response should be more prominent than that on the linear optical properties. It is also interesting to note that the samples with a high ratio of either iodide or bromide, namely $PyPbBr_{0.57}I_{2.43}$ and $PyPbBr_{2.61}I_{0.39}$, show a sudden drop in THG intensity for shorter wavelengths after the resonance, similar to pure halide systems, whereas the other mixed halide systems with similar relative compositions of both iodide and bromide show a more symmetric

Appendix 1

Interplay of Phase Stability and Polarizability in the Third Harmonic Upconversion Process in Pyridimium Lead Mixed Halides

response around the resonant wavelength (Figure A1.4). In the case of PyPbBr$_3$, it is surprising that it too shows an off-band-edge resonance of THG response despite being a monohalide system. However, it is to be noted that the band-edge of PyPbBr$_3$ is around 375 nm, which is towards the UV regime. All our THG measurements were conducted in the open air under ambient temperature and pressure, and it is possible that the near-UV response might be diminished due to absorption and scattering by the gases and vapor present in ambient air.
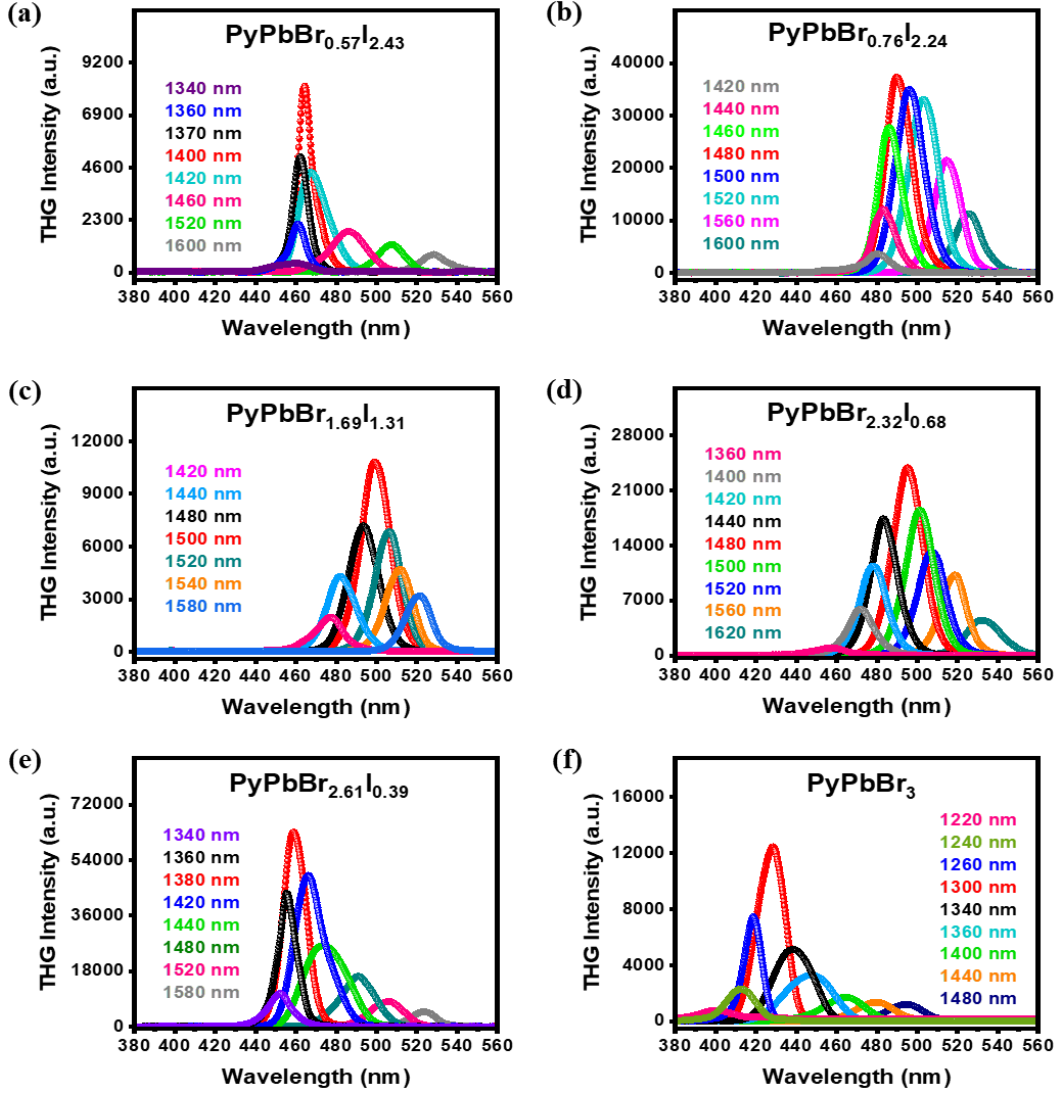
Figure A1.4: Excitation wavelength dependent THG spectra of (a) PyPbBr$_{0.57}$I$_{2.43}$, (b) PyPbBr$_{0.76}$I$_{2.24}$, (c) PyPbBr$_{1.69}$I$_{1.31}$, (d) PyPbBr$_{2.32}$I$_{0.68}$, (e) PyPbBr$_{2.61}$I$_{0.39}$ and (f) PyPbBr$_3$ single crystals at ~3 mW excitation power.

To quantify the THG response, we calculated the third-order nonlinear susceptibility, $\chi^{(3)}$, of the PyPbBr$_3$ and the mixed halide single crystals using a relative method based on the nonlinear

Interplay of Phase Stability and Polarizability in the Third Harmonic Upconversion Process in Pyridimium Lead Mixed Halides

Maxwell's equation by taking $PyPbI_3$ single crystals as a reference system, for which the $\chi^{(3)}$ was determined in Chapter 4. The magnitude of $\chi^{(3)}$ for two materials excited under similar conditions, in the non-phase-matching condition with minimum absorption effects, can be compared using the following equation by using the THG intensities:[46]

$$\chi_S^{(3)} = \chi_R^{(3)} \left[\frac{I_S(3\omega)}{I_R(3\omega)} \right]^{1/2} \qquad (3)$$

where $\chi_S^{(3)}$ and $\chi_R^{(3)}$ are the third order NLO susceptibilities and $I_S(3\omega)$ and $I_R(3\omega)$ are the THG intensities of the sample and the reference, respectively. The comparison of the THG response of $PyPbI_3$ with other samples at 1440 nm is given in Figure A1.5.
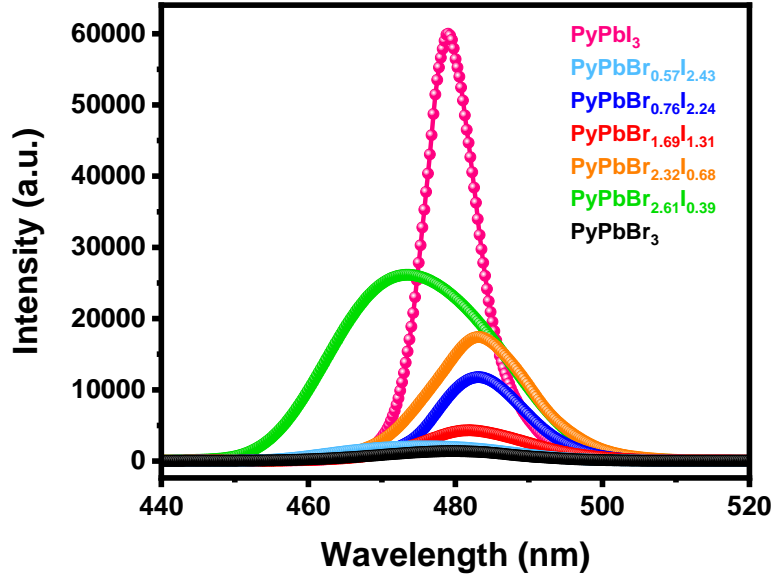
Figure A1.5: Comparison of THG responses of other $PyPbBr_xI_{3-x}$ single-crystals at 1440 nm with that of the reference $PyPbI_3$ single crystals under similar experimental conditions.

To calculate the $\chi^{(3)}$ of the samples at their maximum THG response wavelengths, we need to incorporate the frequency dependence as well, given by:[41]

$$\chi_{\omega_1}^{(3)} = \chi_{\omega_2}^{(3)} \left(\frac{3\omega_2}{3\omega_1} \right) \left[\frac{I(3\omega_1)}{I(3\omega_2)} \right]^{1/2} \qquad (4)$$

where $\chi_{\omega_1}^{(3)}$ and $\chi_{\omega_2}^{(3)}$ are the third-order NLO susceptibilities at pump frequencies ω_1 and ω_2, and $I(3\omega_1)$ and $I(3\omega_2)$ are the respective THG intensities. Figure A1.6 shows the THG response of the samples at the excitation wavelengths where the maximum response is

Interplay of Phase Stability and Polarizability in the Third Harmonic Upconversion Process in Pyridimium Lead Mixed Halides

obtained, compared with that at 1440 nm. The calculated $\chi^{(3)}$ of the samples at their maximum THG response wavelength are tabulated in Table A1.2.
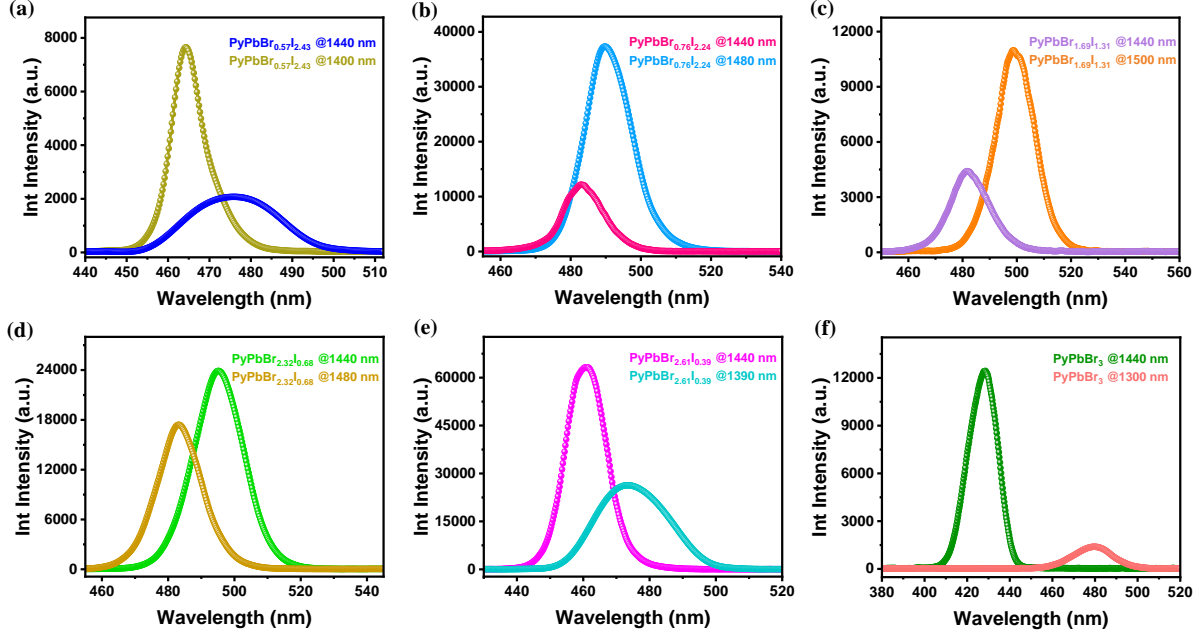

Figure A1.6: Comparison of the THG response at the excitation wavelengths where maximum THG response is obtained as compared to that of 1440 nm excitation for (a) PyPbBr$_{0.57}$I$_{2.43}$, (b) PyPbBr$_{0.76}$I$_{2.24}$, (c) PyPbBr$_{1.69}$I$_{1.31}$, (d) PyPbBr$_{2.32}$I$_{0.68}$, (e) PyPbBr$_{2.61}$I$_{0.39}$ and (f) PyPbBr$_3$ single crystals.

Table A1.2: Calculated $\chi^{(3)}$ and LIDT values of the pyridinium lead halides

Compound	λ (nm)	$\chi^{(3)}$ (m^{2}V^{-2})	LIDT (GW cm^{-2})
PyPbI$_3$	1440	1.96 X 10^{-18}	33
PyPbBr$_{0.57}$I$_{2.43}$	1400	0.80 X 10^{-18}	87.5
PyPbBr$_{0.76}$I$_{2.24}$	1480	2.00 X 10^{-18}	50.6
PyPbBr$_{1.69}$I$_{1.31}$	1500	1.12 X 10^{-18}	107.2
PyPbBr$_{2.32}$I$_{0.68}$	1480	1.69 X 10^{-18}	71.4
PyPbBr$_{2.61}$I$_{0.39}$	1390	2.66 X 10^{-18}	49.4
PyPbBr$_3$	1300	1.32 X 10^{-18}	74.7

Interplay of Phase Stability and Polarizability in the Third Harmonic Upconversion Process in Pyridimium Lead Mixed Halides

An important thing to note is that although the band-edge resonance is not observed in the mixed halides and PyPbBr$_3$, we still achieve an efficient THG over a wide range covering nearly the 400-540 nm range, as shown in Figure A1.7, which was one of our primary motives for this study. We believe that a careful and more detailed approach to tuning the strain effects in mixed halide systems for NLO response can be a potential goal for future studies.
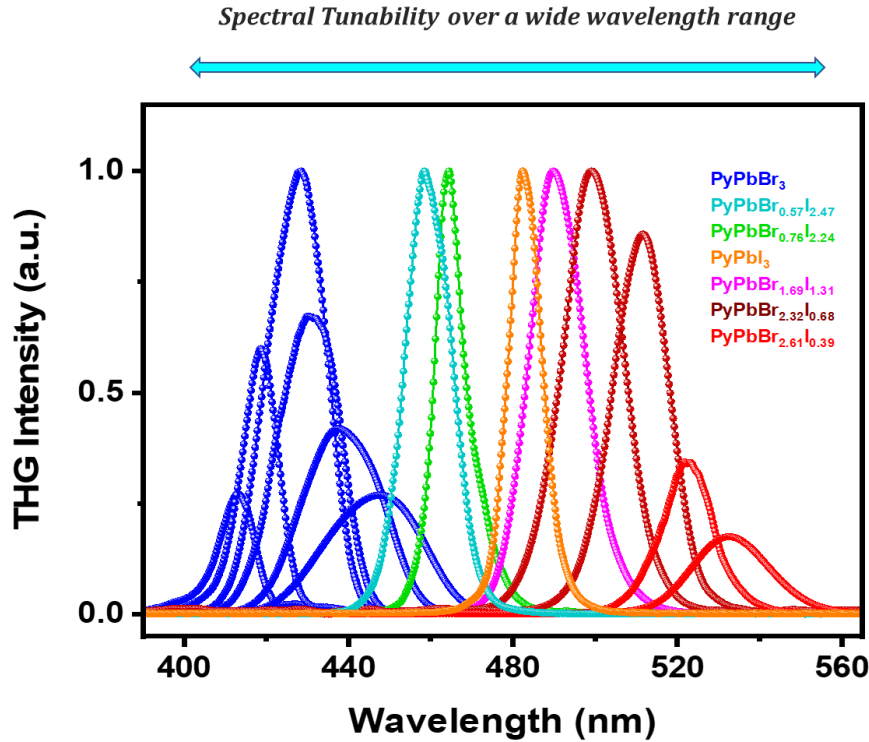
Figure A1.7: Representative spectra showing wide range THG response from PyPbBr$_x$I$_{3-x}$.

A1.3.3 Laser induced damage threshold (LIDT)

Power-dependent measurements were performed at the maximum THG response wavelengths to analyze the exact nature of the THG response and to evaluate the laser-induced damage threshold (LIDT). Figure A1.8 shows the power-dependent THG spectra of PyPbBr$_x$I$_{3-x}$ single crystals. The pump intensity at which the THG response deviates from cubic behavior determines the LIDT of the sample.[47] The power-dependent THG intensity of the samples was plotted against the input power (Figure A1.9), and the LIDTs, or the powers at which the THG response deviated from the cubic behavior, were obtained.

Interplay of Phase Stability and Polarizability in the Third Harmonic Upconversion Process in Pyridimium Lead Mixed Halides
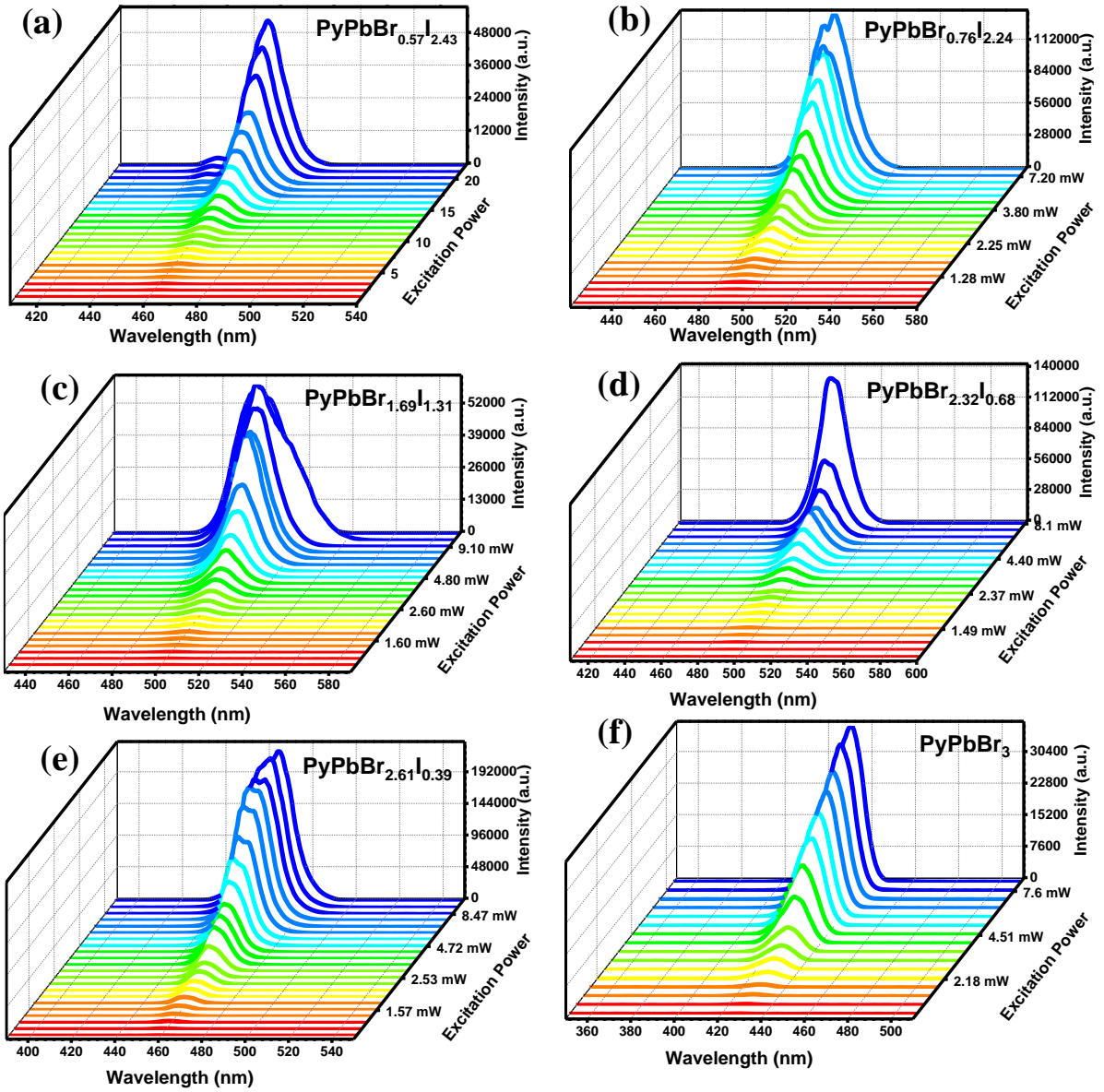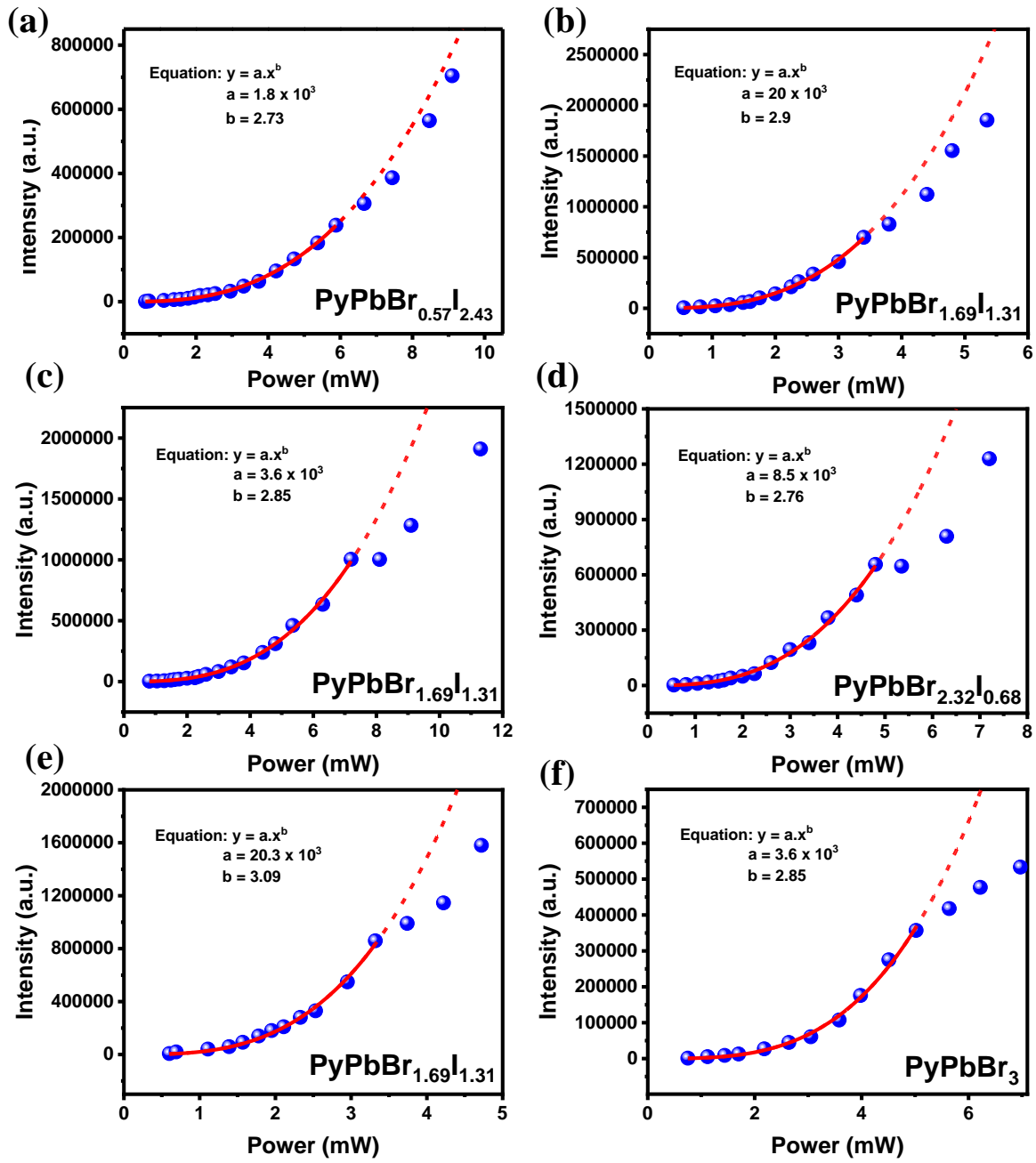

Figure A1.8: Power dependent THG spectra of (a) $PyPbBr_{0.57}I_{2.43}$, (b) $PyPbBr_{0.76}I_{2.24}$, (c) $PyPbBr_{1.69}I_{1.31}$, (d) $PyPbBr_{2.32}I_{0.68}$, (e) $PyPbBr_{2.61}I_{0.39}$ and (f) $PyPbBr_3$ single crystals.

$$LIDT = \text{Peak intensity at the power at which deviation from cubic behaviour occurs}$$

$$= \frac{\text{Average power}}{(\text{Repetition rate}) \times (\text{Pulse width}) \times (\text{effective spot area})} \quad (5)$$

For the setup used, Repetition Rate = 1000 Hz, Pulse width = 45×10^{-15} s, Average power = 3.0×10^{-3} W and beam radius = 218×10^{-6} m. The calculated LIDTs for the samples are tabulated in Table A1.2.

Interplay of Phase Stability and Polarizability in the Third Harmonic Upconversion Process in Pyridimium Lead Mixed Halides

Figure A1.9: Cubic fitting and determination of the LIDT power of (a) $PyPbBr_{0.57}I_{2.43}$, (b) $PyPbBr_{0.76}I_{2.24}$, (c) $PyPbBr_{1.69}I_{1.31}$, (d) $PyPbBr_{2.32}I_{0.68}$, (e) $PyPbBr_{2.61}I_{0.39}$ and (f) $PyPbBr_3$ single crystals.

It is notable that all the samples have a relatively high $\chi^{(3)}$ (of the order of 10^{-18} m^2/V^2), and a high LIDT, thereby making them a suitable choice for high-power nonlinear optical applications in this wavelength range. One possible reason for this might be that the soft nature of the organic lattice within the perovskitoid system, formed by the large aromatic cation, might

Appendix 1

Interplay of Phase Stability and Polarizability in the Third Harmonic Upconversion Process in Pyridimium Lead Mixed Halides

be acting as a dissipation channel for the heating effects caused by the high-intensity light, making the system stable up to sufficiently high intensities.

A1.3.4 Polarization-dependent THG response

To understand the impact of crystal symmetry on the THG response of the system, pump polarization-dependent THG measurements were performed. The intensity of THG was measured against the polarization of the pump light with respect to the vertical plane, which is orthogonal to the c-axis of the crystals. The zero angle was set with the help of a Glan polarizer. Interaction of the pump beam with the $\chi^{(3)}$ tensor yields the THG wave. $\chi^{(3)}$ is a material property, and therefore the structural symmetries of the sample determine the elements of the $\chi^{(3)}$ tensor, according to Neumann's principle.[48] $\chi^{(3)}$, being a fourth rank tensor, consists of $3^4 = 81$ elements. However, many of these elements vanish to zero considering the symmetries present in the material. For the orthorhombic class of crystals, the contracted form of the $\chi^{(3)}$ tensor for THG can be written as:[49]

$$\chi^{(3)} = \begin{bmatrix} \chi_{11} & 0 & 0 & 0 & 0 & \chi_{16} & 0 & \chi_{18} & 0 & 0 \\ 0 & \chi_{22} & 0 & \chi_{24} & 0 & 0 & 0 & 0 & \chi_{29} & 0 \\ 0 & 0 & \chi_{33} & 0 & \chi_{35} & 0 & \chi_{37} & 0 & 0 & 0 \end{bmatrix} \quad (6)$$

where the first subscript refers to the indices 1=x, 2=y and 3=z, and the second subscript refers to combinations of indices:

xxx	*yyy*	*zzz*	*yzz*	*yyz*	*xzz*	*xxz*	*xyy*	*xxy*	*xyz*
1	2	3	4	5	6	7	8	9	0

Considering the pump beam with the frequency 'ω' to be linearly polarized in the x-y plane and the polarization vector making an angle 'θ' with the x-axis, the beam can be expressed as:

$$\vec{E}^\omega = E_x{}^\omega \cos(\theta) + E_y{}^\omega \sin(\theta) \quad (7)$$

Since the polarization of the pump beam is in the x-y plane, the z-containing elements in the $\chi^{(3)}$ tensor can be neglected, and only the four remaining elements χ_{11}, χ_{18}, χ_{22} and χ_{29} contribute to the THG response from the sample along the x-y plane, which can be expressed as:

Appendix 1

Interplay of Phase Stability and Polarizability in the Third Harmonic Upconversion Process in Pyridimium Lead Mixed Halides

$$I_x^{(3\omega)} \propto (\chi_{11} \cos^3 \theta + \chi_{18} \cos \theta \sin^2 \theta)^3 \qquad (8)$$

$$I_y^{(3\omega)} \propto (\chi_{22} \sin^3 \theta + \chi_{29} \sin \theta \cos^2 \theta)^3 \qquad (9)$$

The net THG response will be the resultant of the above two expressions. Figure A1.10 shows the polarization-dependent THG response of $PyPbBr_xI_{3-x}$ single crystals along with the theoretical fits using equations 8 and 9. It is observed that all the samples show a four-lobed THG response. It should be mentioned that the measurements were conducted on a bunch of single crystals with their c-axis in the x-y plane, but the a & b axes of the crystals were randomly oriented, and so it is to be noted that the recorded output will be an averaged response of all the crystals. The average THG anisotropy ratio is defined as the ratio of $I_x^{(3\omega)}/I_y^{(3\omega)}$.[50] We see that the orthogonal lobes are of nearly equal magnitude for all the samples, and the anisotropy ~1. So, the THG response is relatively less anisotropic unlike most materials.[51-53] The THG response from both axes is nearly equal, which might be a reason for the high $\chi^{(3)}$ values of the samples.
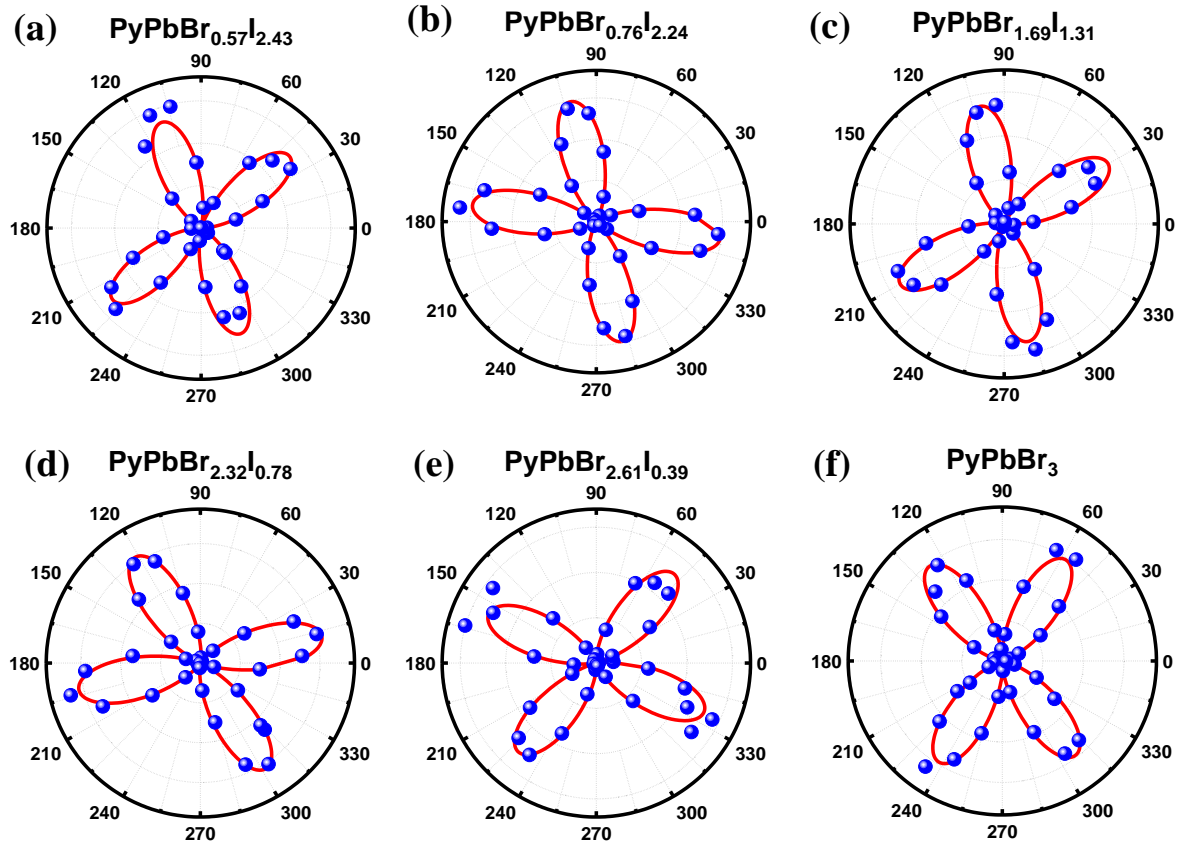

Figure A1.10: Polarization-dependent THG response and theoretical fit of (a) $PyPbBr_{0.57}I_{2.43}$, (b) $PyPbBr_{0.76}I_{2.24}$, (c) $PyPbBr_{1.69}I_{1.31}$, (d) $PyPbBr_{2.32}I_{0.68}$, and (e) $PyPbBr_{2.61}I_{0.39}$ and (f) $PyPbBr_3$ single crystals.

Interplay of Phase Stability and Polarizability in the Third Harmonic Upconversion Process in Pyridimium Lead Mixed Halides

A1.4 Conclusion

We demonstrated the THG response of bandgap-engineered $PyPbBr_xI_{3-x}$ single crystals. A number of factors, including the 1D nature of the perovskitoid system, the polarizability and soft nature of the aromatic cation, and strain induced by the mixed halide composition affect the THG response of the $PyPbBr_xI_{3-x}$ systems. The THG response shows an off-band-edge resonance for the mixed halide systems. However, as a result of strong confinement due to the 1D nature of the system and high bulk polarizability of all the $PyPbBr_xI_{3-x}$ systems, they exhibit a large third-order nonlinear susceptibility $\chi^{(3)}$. They also exhibit a high LIDT, making them suitable candidates for high-power NLO applications. The polarization-dependent THG studies reveal a relatively less anisotropic THG response from the $PyPbBr_xI_{3-x}$ single crystals, which might also be a reason for the high $\chi^{(3)}$ response of the system. Thus, the $PyPbBr_xI_{3-x}$ single crystals can efficiently serve as IR visualizing equipment in practically important optical communication wavelength (~1.5 µm), laser modulators, efficient up-converters for lasing, and photo-detection.

A1.5 References

1. Kojima, A.; Teshima, K.; Shirai, Y.; Miyasaka, T., Organometal Halide Perovskites as Visible-Light Sensitizers for Photovoltaic Cells. *J. Am. Chem. Soc.* **2009**, *131*, 6050-6051.

2. Cao, D. H.; Stoumpos, C. C.; Farha, O. K.; Hupp, J. T.; Kanatzidis, M. G., 2d Homologous Perovskites as Light-Absorbing Materials for Solar Cell Applications. *J. Am. Chem. Soc.* **2015**, *137*, 7843-7850.

3. Yettapu, G. R.; Talukdar, D.; Sarkar, S.; Swarnkar, A.; Nag, A.; Ghosh, P.; Mandal, P., Terahertz Conductivity within Colloidal $CsPbBr_3$ Perovskite Nanocrystals: Remarkably High Carrier Mobilities and Large Diffusion Lengths. *Nano Lett.* **2016**, *16*, 4838-4848.

4. Sarkar, S.; Ravi, V. K.; Banerjee, S.; Yettapu, G. R.; Markad, G. B.; Nag, A.; Mandal, P., Terahertz Spectroscopic Probe of Hot Electron and Hole Transfer from Colloidal $CsPbBr_3$ Perovskite Nanocrystals. *Nano Lett.* **2017**, *17*, 5402-5407.

5. Akkerman, Q. A.; Rainò, G.; Kovalenko, M. V.; Manna, L., Genesis, Challenges and Opportunities for Colloidal Lead Halide Perovskite Nanocrystals. *Nat. Mater.* **2018**, *17*, 394-405.

6. Jena, A. K.; Kulkarni, A.; Miyasaka, T., Halide Perovskite Photovoltaics: Background, Status, and Future Prospects. *Chem. Rev.* **2019**, *119*, 3036-3103.

Appendix 1

Interplay of Phase Stability and Polarizability in the Third Harmonic Upconversion Process in Pyridimium Lead Mixed Halides

7. Fu, Y.; Zhu, H.; Chen, J.; Hautzinger, M. P.; Zhu, X. Y.; Jin, S., Metal Halide Perovskite Nanostructures for Optoelectronic Applications and the Study of Physical Properties. *Nat. Rev. Mater.* **2019**, *4*, 169-188.

8. Chen, J.; Jia, D.; Johansson, E. M. J.; Hagfeldt, A.; Zhang, X., Emerging Perovskite Quantum Dot Solar Cells: Feasible Approaches to Boost Performance. *Energy Environ. Sci.* **2021**, *14*, 224-261.

9. Walsh, A., Principles of Chemical Bonding and Band Gap Engineering in Hybrid Organic–Inorganic Halide Perovskites. *J. Phys. Chem. C* **2015**, *119*, 5755-5760.

10. Protesescu, L.; Yakunin, S.; Bodnarchuk, M. I.; Krieg, F.; Caputo, R.; Hendon, C. H.; Yang, R. X.; Walsh, A.; Kovalenko, M. V., Nanocrystals of Cesium Lead Halide Perovskites ($CsPbX_3$, X = Cl, Br, and I): Novel Optoelectronic Materials Showing Bright Emission with Wide Color Gamut. *Nano Lett.* **2015**, *15*, 3692-3696.

11. Muscarella, L. A.; Ehrler, B., The Influence of Strain on Phase Stability in Mixed-Halide Perovskites. *Joule* **2022**, *6*, 2016-2031.

12. Wang, F.; Fu, Y.; Ziffer, M. E.; Dai, Y.; Maehrlein, S. F.; Zhu, X. Y., Solvated Electrons in Solids-Ferroelectric Large Polarons in Lead Halide Perovskites. *J. Am. Chem. Soc.* **2021**, *143*, 5-16.

13. Wang, M.; Yang, Z.; Zhang, C., Polarized Photoluminescence from Lead Halide Perovskites. *Adv. Opt. Mater.* **2021**, *9*, 2002236.

14. Walsh, A., Atomistic Models of Metal Halide Perovskites. *Matter* **2021**, *4*, 3867-3873.

15. Tsai, H., et al., High-Efficiency Two-Dimensional Ruddlesden–Popper Perovskite Solar Cells. *Nature* **2016**, *536*, 312-316.

16. Mao, L.; Ke, W.; Pedesseau, L.; Wu, Y.; Katan, C.; Even, J.; Wasielewski, M. R.; Stoumpos, C. C.; Kanatzidis, M. G., Hybrid Dion–Jacobson 2D Lead Iodide Perovskites. *J. Am. Chem. Soc.* **2018**, *140*, 3775-3783.

17. Akkerman, Q. A.; Manna, L., What Defines a Halide Perovskite? *ACS Energy Lett.* **2020**, *5*, 604-610.

18. Saparov, B.; Mitzi, D. B., Organic–Inorganic Perovskites: Structural Versatility for Functional Materials Design. *Chem. Rev.* **2016**, *116*, 4558-4596.

19. Saouma, F. O.; Stoumpos, C. C.; Wong, J.; Kanatzidis, M. G.; Jang, J. I., Selective Enhancement of Optical Nonlinearity in Two-Dimensional Organic-Inorganic Lead Iodide Perovskites. *Nat. Commun.* **2017**, *8*, 742.

Appendix 1

Interplay of Phase Stability and Polarizability in the Third Harmonic Upconversion Process in Pyridimium Lead Mixed Halides

20. Abdelwahab, I.; Grinblat, G.; Leng, K.; Li, Y.; Chi, X.; Rusydi, A.; Maier, S. A.; Loh, K. P., Highly Enhanced Third-Harmonic Generation in 2D Perovskites at Excitonic Resonances. *ACS Nano* **2018**, *12*, 644-650.

21. Katan, C.; Mercier, N.; Even, J., Quantum and Dielectric Confinement Effects in Lower-Dimensional Hybrid Perovskite Semiconductors. *Chem. Rev.* **2019**, *119*, 3140-3192.

22. Wang, J., et al., Giant Nonlinear Optical Response in 2D Perovskite Heterostructures. *Adv. Opt. Mater.* **2019**, *7*, 1900398.

23. Liang, W.-Y.; Liu, F.; Lu, Y.-J.; Popović, J.; Djurišić, A.; Ahn, H., High Optical Nonlinearity in Low-Dimensional Halide Perovskite Polycrystalline Films. *Opt. Express* **2020**, *28*, 24919-24927.

24. Sheikh, T.; Nawale, V.; Pathoor, N.; Phadnis, C.; Chowdhury, A.; Nag, A., Molecular Intercalation and Electronic Two Dimensionality in Layered Hybrid Perovskites. *Angew. Chem. Int. Ed.* **2020**, *59*, 11653-11659.

25. Zhang, J.; Yang, X.; Deng, H.; Qiao, K.; Farooq, U.; Ishaq, M.; Yi, F.; Liu, H.; Tang, J.; Song, H., Low-Dimensional Halide Perovskites and Their Advanced Optoelectronic Applications. *Nano-Micro Lett.* **2017**, *9*, 36.

26. Mauck, C. M.; Tisdale, W. A., Excitons in 2D Organic–Inorganic Halide Perovskites. *Trends Chem.* **2019**, *1*, 380-393.

27. Zhou, C.; Lin, H.; He, Q.; Xu, L.; Worku, M.; Chaaban, M.; Lee, S.; Shi, X.; Du, M.-H.; Ma, B., Low Dimensional Metal Halide Perovskites and Hybrids. *Mater. Sci. Eng. R Rep.* **2019**, *137*, 38-65.

28. Blancon, J.-C.; Even, J.; Stoumpos, C. C.; Kanatzidis, M. G.; Mohite, A. D., Semiconductor Physics of Organic–Inorganic 2D Halide Perovskites. *Nat. Nanotechnol.* **2020**, *15*, 969-985.

29. Peng, X.; Yan, C.; Chun, F.; Li, W.; Fu, X.; Yang, W., A Review of Low-Dimensional Metal Halide Perovskites for Blue Light Emitting Diodes. *J. Alloys Compd.* **2021**, *883*, 160727.

30. Srimath Kandada, A. R.; Petrozza, A., Photophysics of Hybrid Lead Halide Perovskites: The Role of Microstructure. *Acc. Chem. Res.* **2016**, *49*, 536-544.

31. Yoon, S. J.; Stamplecoskie, K. G.; Kamat, P. V., How Lead Halide Complex Chemistry Dictates the Composition of Mixed Halide Perovskites. *J. Phys. Chem. Lett.* **2016**, *7*, 1368-1373.

32. Xiao, Z.; Zhao, L.; Tran, N. L.; Lin, Y. L.; Silver, S. H.; Kerner, R. A.; Yao, N.; Kahn, A.; Scholes, G. D.; Rand, B. P., Mixed-Halide Perovskites with Stabilized Bandgaps. *Nano Lett.* **2017**, *17*, 6863-6869.

Appendix 1

Interplay of Phase Stability and Polarizability in the Third Harmonic Upconversion Process in Pyridimium Lead Mixed Halides

33. Zhu, C., et al., Strain Engineering in Perovskite Solar Cells and Its Impacts on Carrier Dynamics. *Nat. Commun.* **2019**, *10*, 815.

34. Chen, P.; Bai, Y.; Lyu, M.; Yun, J.-H.; Hao, M.; Wang, L., Progress and Perspective in Low-Dimensional Metal Halide Perovskites for Optoelectronic Applications. *Sol. RRL* **2018**, *2*, 1700186.

35. Yusoff, A. R. b. M.; Nazeeruddin, M. K., Low-Dimensional Perovskites: From Synthesis to Stability in Perovskite Solar Cells. *Adv. Energy Mater.* **2018**, *8*, 1702073.

36. Futscher, M. H.; Milić, J. V., Mixed Conductivity of Hybrid Halide Perovskites: Emerging Opportunities and Challenges. *Front. Energy Res.* **2021**, *9*.

37. Sakhatskyi, K., et al., Assessing the Drawbacks and Benefits of Ion Migration in Lead Halide Perovskites. *ACS Energy Lett.* **2022**, *7*, 3401-3414.

38. Scheideler, W. J., Editorial: Solutions to Scaling and Reliability of Metal Halide Perovskites: Materials and Manufacturing Innovation at the Inflection Point of Solar Energy. *Front. Energy Res.* **2022**, *10*.

39. Garmire, E., Nonlinear Optics in Daily Life. *Opt. Express* **2013**, *21*, 30532-30544.

40. Boyd, R. W., *Nonlinear Optics*, **2020**.

41. Maqbool, S.; Sheikh, T.; Thekkayil, Z.; Deswal, S.; Boomishankar, R.; Nag, A.; Mandal, P., Third Harmonic Upconversion and Self-Trapped Excitonic Emission in 1D Pyridinium Lead Iodide. *J. Phys. Chem. C* **2021**, *125*, 22674-22683.

42. Youngblood, N.; Peng, R.; Nemilentsau, A.; Low, T.; Li, M., Layer-Tunable Third-Harmonic Generation in Multilayer Black Phosphorus. *ACS Photonics* **2017**, *4*, 8-14.

43. Stoumpos, C. C.; Cao, D. H.; Clark, D. J.; Young, J.; Rondinelli, J. M.; Jang, J. I.; Hupp, J. T.; Kanatzidis, M. G., Ruddlesden–Popper Hybrid Lead Iodide Perovskite 2D Homologous Semiconductors. *Chem. Mater.* **2016**, *28*, 2852-2867.

44. de Araújo, M. A.; Silva, R.; de Lima, E.; Pereira, D. P.; de Oliveira, P. C., Measurement of Gaussian Laser Beam Radius Using the Knife-Edge Technique: Improvement on Data Analysis. *Appl. Opt.* **2009**, *48*, 393-396.

45. Markowicz, P. P.; Tiryaki, H.; Pudavar, H.; Prasad, P. N.; Lepeshkin, N. N.; Boyd, R. W., Dramatic Enhancement of Third-Harmonic Generation in Three-Dimensional Photonic Crystals. *Phys. Rev. Lett.* **2004**, *92*, 083903.

46. Haynes, A. S.; Banerjee, A.; Saouma, F. O.; Otieno, C. O.; Jang, J. I.; Kanatzidis, M. G., Phase Transition, Conformational Exchange, and Nonlinear Optical Third Harmonic Generation of $ACsP_2Se_8$ (A = K, Rb, Cs). *Chem. Mater.* **2016**, *28*, 2374-2383.

Appendix 1

***Interplay of Phase Stability and Polarizability in the Third Harmonic Upconversion
Process in Pyridimium Lead Mixed Halides***

47. Park, G.; Byun, H. R.; Jang, J. I.; Ok, K. M., Dimensionality–Band Gap–Third-Harmonic Generation Property Relationship in Novel Main-Group Metal Iodates. *Chem. Mater.* **2020**, *32*, 3621-3630.

48. Nye, J. F.; Lindsay, R. B., Physical Properties of Crystals: Their Representation by Tensors and Matrices. *Phys. Today* **1957**, *10*, 26-26.

49. Yang, X.-l.; Xie, S.-w., Expression of Third-Order Effective Nonlinear Susceptibility for Third-Harmonic Generation in Crystals. *Appl. Opt.* **1995**, *34*, 6130-6135.

50. Tripathi, R. P. N.; Gao, J.; Yang, X., Anisotropic Optical Responses of Layered Thallium Arsenic Sulfosalt Gillulyite. *Sci. Rep.* **2021**, *11*, 22002.

51. Li, X.; Liu, H.; Ke, C.; Tang, W.; Liu, M.; Huang, F.; Wu, Y.; Wu, Z.; Kang, J., Review of Anisotropic 2D Materials: Controlled Growth, Optical Anisotropy Modulation, and Photonic Applications. *Laser Photonics Rev.* **2021**, *15*, 2100322.

52. Chen, Z.; Zhang, Q.; Zhu, M.; Chen, H.; Wang, X.; Xiao, S.; Loh, K. P.; Eda, G.; Meng, J.; He, J., In-Plane Anisotropic Nonlinear Optical Properties of Two-Dimensional Organic–Inorganic Hybrid Perovskite. *J. Phys. Chem. Lett.* **2021**, *12*, 7010-7018.

53. Chen, Z.; Shi, Z.; Zhang, W.; Li, Z.; Zhou, Z.-K., High Efficiency and Large Optical Anisotropy in the High-Order Nonlinear Processes of 2D Perovskite Nanosheets. *Nanophotonics* **2022**, *11*, 1379-1387.

Appendix 2

Anharmonicity and Dynamic-Disorder Driven Self Trapped Excitonic Emission in Pyridinium Lead Iodide Single Crystals

Anharmonicity and Dynamic-Disorder Driven Self Trapped Excitonic Emission in Pyridinium Lead Iodide Single Crystals

Abstract

Lead halide perovskites (LHPs) have emerged as one of the most important class of materials for potential optoelectronics. Creative choice of 'A' site cation leads to the realization of structures having intriguing properties. LHPs with reduced dimensionality exhibit a strong light-matter interaction due to stronger quantum and dielectric confinements. We have investigated linear optical properties in face-shared one-dimensional pyridinium lead iodide (PyPbI$_3$) single crystals. Strong exciton-phonon interaction results in highly Stokes-shifted self-trapped excitonic emission at the 5-300 K temperature range. An interplay between anharmonicity and dynamic disorder dictates the emission properties, further complicated by an isostructural phase-transition at 170 K.

Graphical Abstract
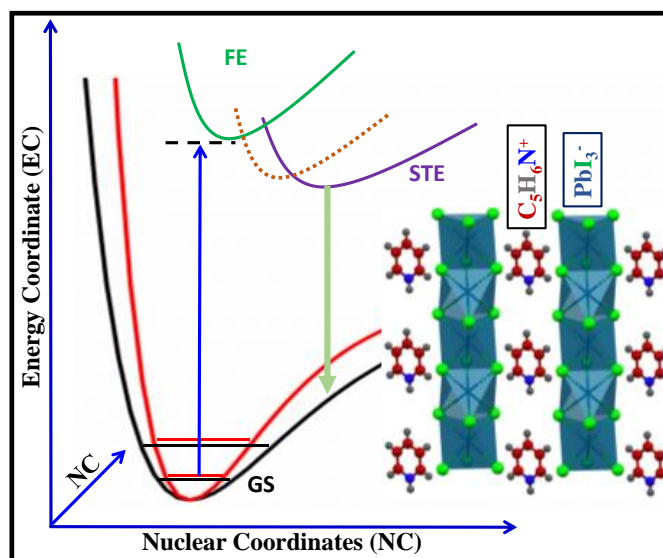
Anharmonicity and Dynamic-Disorder Driven Self Trapped Excitonic Emission in Pyridinium Lead Iodide Single Crystals

A2.1 Introduction

Lead halide perovskites (LHPs), exhibit excellent response in the linear and nonlinear optical (NLO) regime. Due to the strong quantum and dielectric confinement, the lower-dimensional perovskites show strong excitonic effects and hence interesting linear optical properties. Similarly, the NLO properties of these lower dimensional perovskites are highly enhanced compared to the 3D perovskites. Upon bandgap excitation, lower dimensional hybrid LHPs show strong photoluminescence (PL) from excitonic recombination. Moreover, a broad thermally activated emission far from the band edge, due to the phonon energy dispersions in excited state, is also observed in these lower dimensional perovskites. This thermally activated highly stokes shifted PL emission is known as self-trapped excitonic (STE) emission.

The STE formation arises due to the structural distortions, which are characteristics of lower dimensional perovskites due to their structural flexibility. One dimensional (1D) perovskites offer more degrees of freedom and higher crystal structure distortions and hence become even more conducive for STE formation. The exact nature of STE formation is still unclear and various spectroscopic investigations like transient absorption, etc., have been performed in this regard. STE formation has been attributed to strong electron-phonon interactions leading to the formation of transient distortions in photo-excited state. Variable temperature experiments, like low temperature PL, provide an opportunity to access the energy of various phonon modes that could be involved in the STE formation.

Herein we report the STE emission having a microsecond long lifetime from 1D pyridinium lead iodide (PyPbI$_3$) single-crystals. Temperature evolution of the STE emission suggests a strong suppression of the exciton de-trapping upon lowering the temperature till 100 K, below which the exciton trapping itself is suppressed. Furthermore, the exciton trapping states split below 50 K, indicating the coexistence of two types of trapping states.

A2.2 Experimental Section

A2.2.1 Synthesis

Single crystals of PyPbI$_3$ were synthesized by the procedure as explained in Chapter 4.

A2.2.2 Characterization

Single-crystal X-ray diffraction (SCXRD) data were recorded on a Bruker Smart Apex Duo diffractometer at 100 K, 150 K, 200 K, 250 K, and 300 K using Mo Kα radiation (λ = 0.71073

Å). The frames were integrated with the Bruker SAINT Software package using a narrow-frame algorithm. The structures were solved by direct method and refined by full-matrix least-squares on F2 using the SHELXTL software. All the atoms were refined anisotropically.

Optical diffuse-reflectance spectrum of the powdered sample with $BaSO_4$ as a 100% reflectance reference was obtained using a Shimadzu UV-3600 plus UV-VIS-NIR double-beam, double monochromator spectrophotometer. Absorbance was calculated from the reflectance spectrum using Kubelka-Munk transformation.

Temperature-dependent steady-state PL measurements were performed on FLS 980 (Edinburgh Instruments). The sample was loaded on a sapphire substrate, which was mounted on a gold-coated sample holder attached to a closed-cycle helium cryostat (Advanced Research Systems). Lake Shore Cryotronics temperature controller was utilized to achieve the desired temperatures. PL decay dynamics measurements were performed in the same instrument.

Raman spectrum was obtained from the powdered sample using a 632.8 nm laser from Horiba Jobin Yvon.

The dielectric measurements were obtained on the compacted powder sample of $PyPbI_3$ in the form of a circular disc with copper adhesive tapes as the top and the bottom electrodes. The temperature-dependent dielectric permittivity data were recorded on a Solartron Analytical Impedance Analyzer model 1260 coupled with a Dielectric Interface 1296A, which operates with a Janis 129610A cryostat sample holder and a Lakeshore 336 model temperature controller.

Measurements of temperature-dependent specific heat (C_p) were carried out in a physical property measurement system (PPMS), Quantum Design (QD), USA. Single crystals were directly mounted on the specific heat puck using Apiezon N grease for measurements till 200 K. Addenda were measured prior to measurement of specimen crystals so as to subtract the specific heat of sample holder and that of grease used during the measurement.

A2.3 Results and Discussion

$PyPbI_3$ single-crystals were synthesized using the procedure described in Chapter 4. The crystal structure and characterization by X-ray diffraction and SEM imaging are well explained in Chapter 4, section 4.3.1. Table A2.1 presents the crystal X-ray data at 100 K and 300 K temperatures.

Anharmonicity and Dynamic-Disorder Driven Self Trapped Excitonic Emission in Pyridinium Lead Iodide Single Crystals

A2.3.1 Optical properties of PyPbI$_3$ single crystals

Figure A2.1 shows the UV-visible absorption (blue), PL (red), and PL excitation (PLE) spectra of PyPbI$_3$ crystals recorded at room temperature (RT). A strong absorption with the first excitonic peak at 435 nm and a sharp absorption edge at ~475 nm is observed. The high bandgap of PyPbI$_3$ is due to the strong quantum confinement arising from the reduced dimension and the face-shared nature of the lead iodide octahedral network.[1] PyPbI$_3$ single crystals show an orange-red emission under 365 nm UV-light (inset of Figure A2.1). Upon excitation with 405 nm light, a broad emission with a peak at ~634 nm is observed in the PL spectrum (red, Figure A2.1). The PL peak has a full width at half maximum (FWHM) of 147 nm (~470 meV) and is hugely red-shifted by about 199 nm (894 meV) from the absorption peak. The large FWHM and the significant Stokes shift indicate that the emission is not the free excitonic (FE) emission. The PLE spectrum recorded at the PL peak (green, Figure A2.1) confirms that the emission is due to the bandgap excitation of PyPbI$_3$. Such broad and highly Stokes-shifted PL, observed either at RT or at cryogenic temperatures, is typical of the lower dimensional (2D, 1D, and 0D) perovskitoids and is labeled as STE emission.[2]
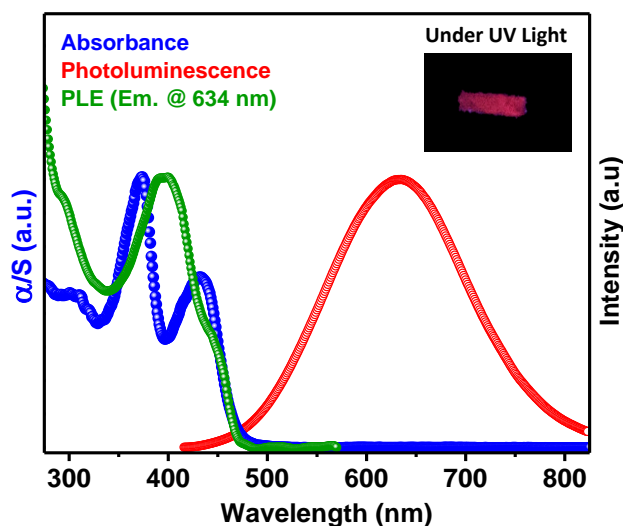
Figure A2.1: UV-Visible absorption spectrum (blue), PL (red), and PL excitation (green) spectra of PyPbI$_3$ single crystals. Diffuse reflectance measurements converted using Kubelka-Munk transformation gave rise to the absorption spectrum. The excitation light of 405 nm is used to record the PL spectrum. The PLE spectrum is recorded at the PL peak of 634 nm. Inset shows the optical image of a PyPbI$_3$ crystal under 365 nm UV light.

Anharmonicity and Dynamic-Disorder Driven Self Trapped Excitonic Emission in Pyridinium Lead Iodide Single Crystals

Table A2.1: Crystal structure and data refinement parameters of PyPbI$_3$ single crystals at 100 K and 300 K:

PyPbI$_3$	100(2) K		300(2) K	
Empirical formula	C$_5$ H$_5$ I$_3$ N Pb		C$_5$ H$_5$ I$_3$ N Pb	
Formula weight	666.99		666.99	
Wavelength	0.71073 Å		0.71073 Å	
Crystal system	Orthorhombic		Orthorhombic	
Space group	*P* n m a		*P* n m a	
Unit cell dimensions	a = 14.9008(3) Å	$\alpha = 90°$	a = 14.968(5) Å	$\alpha = 90°$
	b = 8.0698(17) Å	$\beta = 90°$	b = 8.102(3) Å	$\beta = 90°$
	c = 9.5844(2) Å	$\gamma = 90°$	c = 9.901(4) Å	$\gamma = 90°$
Volume	1152.0(48) Å^3		1200.7(8) Å^3	
Z	4		4	
Density (calculated)	3.844 Mg/m^3		3.690 Mg/m^3	
Absorption coefficient	22.570 mm^{-1}		21.711 mm^{-1}	
F(000)	1132		1132	
Theta range for all data collection	4.253 to 25.027°.		4.116 to 28.267°.	
Index range	-19 ≤ h ≤ 19,		-19 ≤ h ≤ 19,	
	-10 ≤ k ≤ 10,		-10 ≤ k ≤ 10,	
	-13 ≤ l ≤ 12		-13 ≤ l ≤ 12	
Reflections collected	28133		16860	
Independent reflections	1095 [R(int) = 0.0486]		1582 [R(int) = 0.1765]	
Completeness of independent reflections	99.50%		99.50%	
Absorption correction	Multi-scan		Multi-scan	
Max. and min. transmission	0.7457 and 0.5022		0.7457 and 0.4331	
Refinement method	Full-matrix least-squares on F^2		Full-matrix least-squares on F^2	
Data / restraints / parameters	1095 / 1 / 43		1582 / 1 / 44	
Goodness-of-fit on F2	1.214		0.988	
Final R indices [I>2sigma(I)]	R1 = 0.0671, wR2 = 0.0614		R1 = 0.0520, wR2 = 0.1078	
R indices (all data)	R1 = 0.0302, wR2 = 0.0629		R1 = 0.1302, wR2 = 0.1400	
Largest diff. peak and hole	0.995 and -2.236 e.Å^{-3}		1.628 and -1.289 e.Å^{-3}	

Anharmonicity and Dynamic-Disorder Driven Self Trapped Excitonic Emission in Pyridinium Lead Iodide Single Crystals

A2.3.2 Temperature-dependent PL studies of PyPbI₃ single crystals

To understand the origin and the nature of the broad emission in PyPbI$_3$ single crystals, we investigated the temperature-dependent PL in 300 to 5 K range. As shown in Figure A2.2a, a single broad emission feature (STE, ~635 nm) is observed in the temperature range of 300 to 50 K, revealing the presence of a unique emissive state. Interestingly, a second weak emission feature centered at ~480 nm emerges below 50 K (see inset of Figure A2.2a) and is attributed to the FE emission. Therefore, the thermal barrier between the FE and STE states is of the order of 4 meV (40-50 K). Similar results have been observed for other 1D face-shared hybrid metal halide systems, and the higher energy emission peaks observed at low temperatures have been attributed to FE emission.[3-5] The variable temperature PLE spectra of the STE emission (Figure A2.2b) show a clear blue shift in the band edge with decreasing temperature. A significant change is observed in the PLE spectra around 200 K. From 300 K to 200 K, the PLE spectra show a slow rise above the band edge along with a broad peak. Below 200 K, the PLE spectra change entirely and show a sharp ascent along with a stronger excitonic feature.
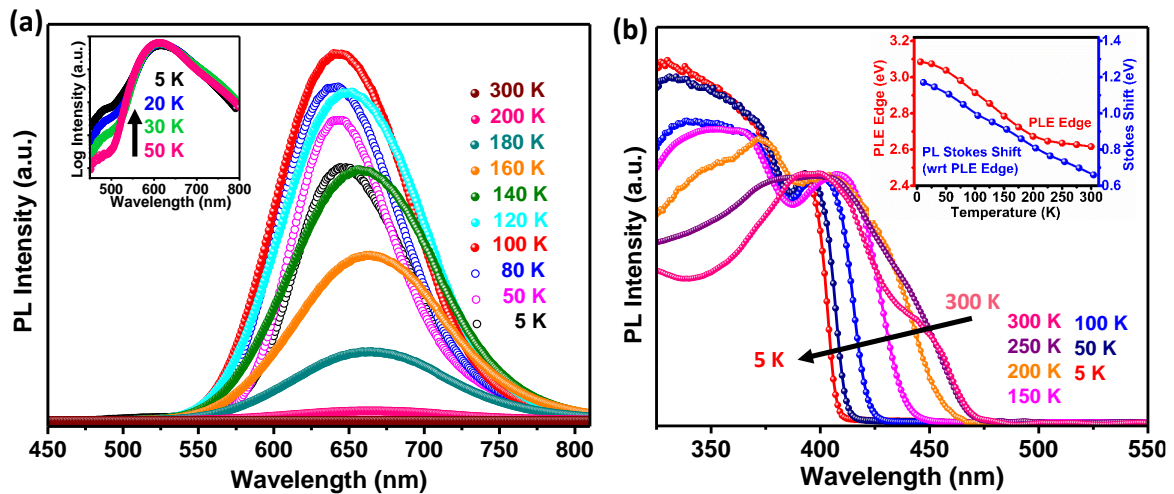
Figure A2.2: (a) Variable temperature PL spectra of PyPbI$_3$ single crystals. Inset shows the PL spectra from 50 to 5 K showing intensity in the log scale. A second emission feature is observed below 50 K. (b) Temperature-dependent PLE spectra of the STE emission in PyPbI$_3$ single-crystals. Inset shows the correlation of PLE edge and PL Stokes shift (w.r.t. PLE edge) with temperature.

Figure A2.3a plots the temperature-dependent PL intensity. Usually, a monotonous increase in PL intensity is expected with lowering temperature due to the quenching of thermally activated non-radiative decay channels. However, here we observe a rather complex trend. The PL

Anharmonicity and Dynamic-Disorder Driven Self Trapped Excitonic Emission in Pyridinium Lead Iodide Single Crystals

intensity grows slowly till 200 K (see inset of Figure A2.3a) with a sharp increase below 200 K. The PL intensity peaks at 100 K, below which it reverses its trend and remains nearly the same below 50 K. The temperature dependence of the PL peak (STE) position and width (FWHM) is equally intriguing (Figure A2.3b). Upon decreasing the temperature from 300 K, the FWHM drops monotonically till 50 K (red data Figure A2.3b). This monotonous decrease in the FWHM is due to the fewer phonons being thermally accessible for coupling. The rate of change in FWHM with temperature changes at ~200 K and ~100 K (indicated in the green shade in Figure A2.3b). A slight increase in FWHM observed below ~50 K may be due to the appearance of the second emission peak at ~480 nm. A more elaborate discussion about the PL spectrum fittings and FWHM trends is presented in below in section A2.2.3.3.
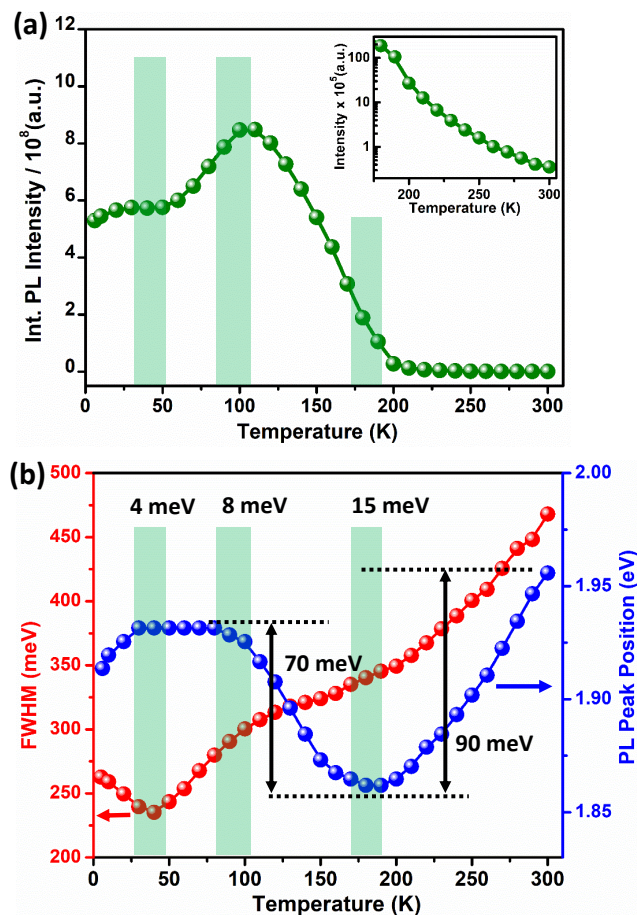
Figure A2.3 (a) Integrated PL intensity variation with temperature. Inset highlights the intensity changes for the temperature range 175 to 300 K. (b) Variation of the PL peak FWHM (red) and PL peak position (blue) with temperature. The temperature dependence of PL intensity, Peak position, and FWHM are in good correlation among themselves. The trends can be divided into four regimes (I to IV) separated by the transition regions marked by the green shaded area in Figures 4c and 4d.

A2.3.3 Fitting PL traces and calculation of FWHM at variable temperatures

The temperature-dependent PL spectra have a skewed Gaussian profile, so they were fitted using the Bigaussian function:

$$y = y_0 + He^{\frac{-(x-x_c)^2}{2w_1{}^2}}, x < x_c$$

$$y = y_0 + He^{\frac{-(x-x_c)^2}{2w_2{}^2}}, x > x_c \qquad (7)$$

where x and y are the wavelength and the PL intensity respectively, y_0 is the baseline correction, H is the peak intensity, x_c is the central wavelength, and w_1 and w_2 are parameters proportional to the width of the curves.

Comparing with the Gaussian function, the HWHM (half-width at half maximum), w', can be obtained as:

$$\frac{1}{2w_1{}^2} = \frac{2\ln(4)}{(2w')^2} \qquad (8)$$

$$w' = w_1\sqrt{\ln(4)}$$

FWHM of Bigaussian will be the sum of HWHMs of the 2 component functions;

$$\text{i.e, FWHM of Bigaussian} = (w_1 + w_2)\sqrt{\ln(4)} \qquad (9)$$

The FWHM decreases upon decreasing the temperature from 300 K to 50 K. Below 50 K, the FWHM shows a reverse trend. We also observe that there is a secondary blue-shifted peak of very low intensity appearing in the PL spectra below 50 K, which is most probably the reason for the increase in FWHM for these temperatures. A part of the area under the curve shifts to this secondary peak, resulting in a reduction in the peak intensity. But as the profile of the dominant peak, centered around 645 nm, remains the same, the FWHM is relocated to a lower position of the curve due to the reduction in the peak intensity. Since the width of a normal distribution increases towards the bottom, the value of the FWHM, therefore, increases for these temperatures. The normalized pseudo-color map of PL peaks at variable temperatures provided below represents these changes in FWHM clearly (Figure A2.4).

Anharmonicity and Dynamic-Disorder Driven Self Trapped Excitonic Emission in Pyridinium Lead Iodide Single Crystals
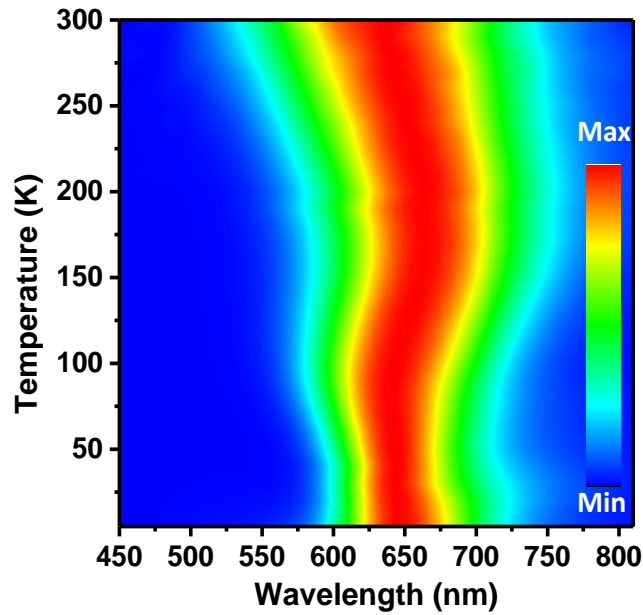

Figure A2.4: PL-temperature pseudo-color map of 1D PyPbI$_3$ single-crystals. With a decrease in temperature, the FWHM decreases till 50 K, below which it again starts to increase.

The PL peak position undergoes a steady red-shift on decreasing temperature from 300 K till ~200 K (blue data in Figure A2.3b). Below 200 K, the PL peak position blue-shifts till 100 K and then remains almost constant. The temperature dependence of the PL intensity, peak position, and FWHM are in good correlation with each other, as highlighted by the green shaded area in Figures A2.3a and A2.3b. It is worth noting that when the peak position shows an unusual behavior of red-shift (300-200 K) followed by a blue shift (200-100 K) as temperature changes from 300 K to 5K, the PLE edge shows a regular, continuous blue shift due to an increase in the bandgap (inset of Figure A2.2b). The increase in effective bandgap mainly stems from the change in phonon population distribution and other thermal effects such as lattice contraction on decreasing temperature.[6, 7] The PL (STE) Stokes shift shows a steady increase with the decrease in temperature as opposed to the trend observed for 3D perovskite systems $CH_3NH_3PbBr_3$ and $CsPbBr_3$ (inset of Figure A2.2b).[8] Here, the temperature dependence of the PL Stokes shift is dominated by the change in the effective bandgap.

The unusual trend in the PL properties observed upon decreasing the temperature suggests dynamic structural reorganizations or/and phase transition(s) with decreasing temperature in PyPbI$_3$.[9] The correlation between the PLE-edge and PLE-peak shown in Figure A2.5a also strongly suggests a possible transition between 150 and 200 K. A weak linear correlation between PLE-edge and PLE-peak in 300-200 K range mainly comes from the change in phonon

population with a decrease in temperature. A much stronger linear correlation below 150 K indicates a significant structural change leading to a steeper increase in the bandgap. A significant digression in radiative recombination dynamics in the same temperature range further strengthens the possibility of a phase transition between 150 and 200 K (Figure A2.5b, Figure A2.6 and Table A2.2).
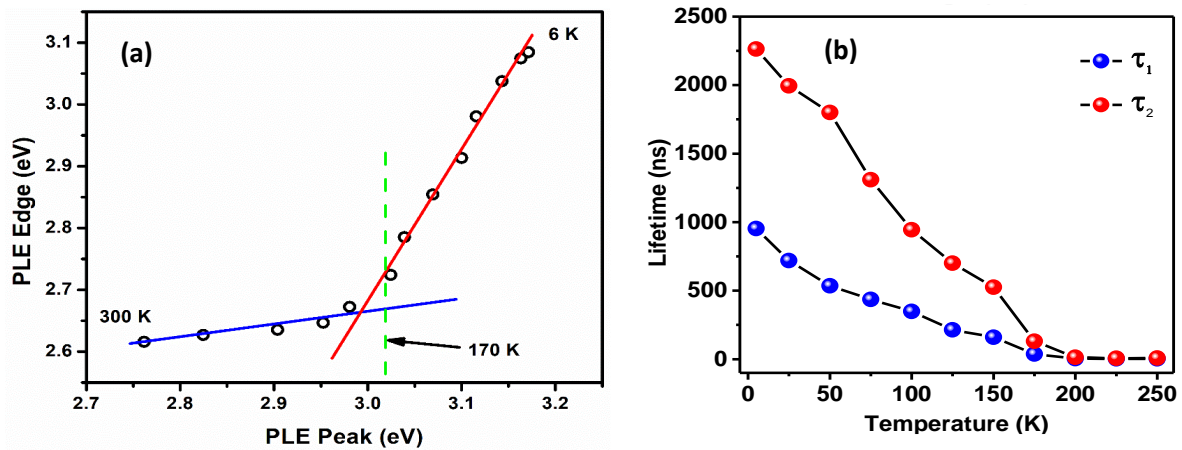

Figure A2.5: (a) Correlation diagram between PLE edge and PLE peak energies recorded in the temperature range of 300-5 K. Temperature-dependent (b) PL lifetime components.
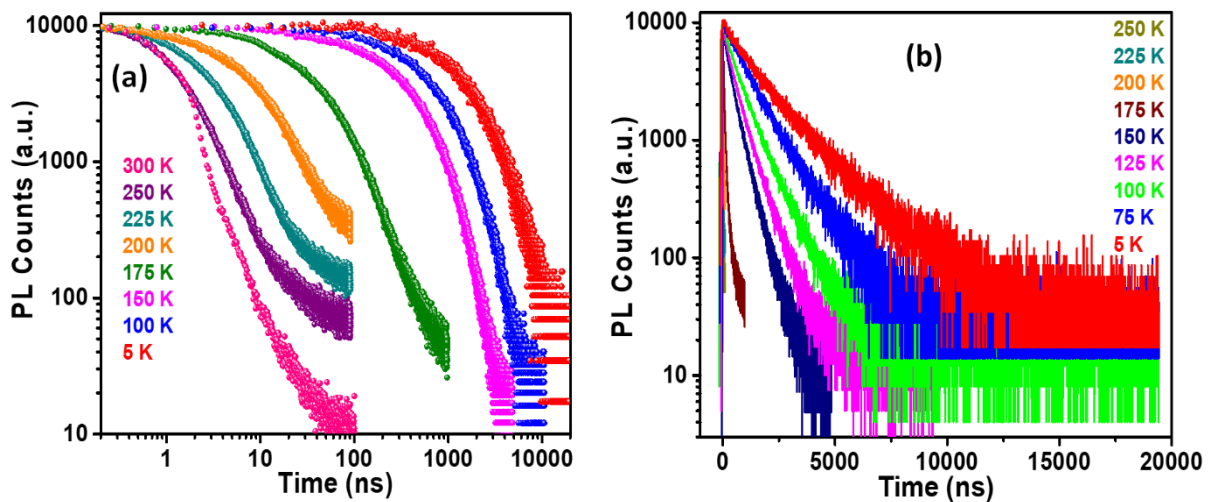
Figure A2.6: Variable temperature time-resolved PL spectra. (a) Log-log plot and (b) log-linear plot of temperature-dependent PL decay traces of PyPbI$_3$ crystals in the temperature range of 300 K to 5 K. The PL traces become longer with the decrease in temperature, reaching of the order of microseconds at 5 K.

Anharmonicity and Dynamic-Disorder Driven Self Trapped Excitonic Emission in Pyridinium Lead Iodide Single Crystals

The PL decay times have been fitted to bi-exponential function, and the average lifetime has been calculated using the following equation:

$$\tau_{av} = \frac{(A_1 \times \tau_1^2) + (A_2 \times \tau_2^2)}{(A_1 \times \tau_1) + (A_2 \times \tau_1)} \qquad (10)$$

Where τ_1 and τ_2 are the two decay components; A_1 and A_2 are their respective contributions, and τ_{av} is the average lifetime. Upon decreasing the temperature, the PL decay lifetime increases, as shown in Figure 5b of the main manuscript. Till 200 K, the lifetime increases slowly. A clear transition is observed around 170 K, below which the PL decay lifetime increases dramatically. PL lifetime increases from few nanoseconds at room temperature to ~2 microseconds at 5 K.

Table A2.2: The best-fit parameters of bi-exponential fitting of variable temperature time-resolved PL spectra shown in Figure A2.6:

Temp (K)	τ_1 (ns)	A_1	τ_2 (ns)	A_2	τ_{av} (ns)
5	953 ± 42	0.44 ± 0.03	2264 ± 49	0.56 ± 0.03	1938.2
25	720 ± 25	0.36 ± 0.02	1994 ± 25	0.63 ± 0.02	1776.1
50	536 ± 15	0.33 ± 0.01	1800 ± 16	0.66 ± 0.01	1636.2
75	436 ± 22	0.17 ± 0.06	1310 ± 29	0.83 ± 0.06	1254.2
100	348 ± 6	0.33 ± 0.01	945 ± 5	0.66 ± 0.01	852.2
125	214 ± 6	0.35 ± 0.01	700 ± 6	0.65 ± 0.01	631.3
150	160 ± 2	0.31 ± 0.0	525 ± 1	0.68 ± 0	480.5
175	37 ± 0	0.82 ± 0	131 ± 0	0.18 ± 0	78.1
200	3.9 ± 0	0.42 ± 0	13.9 ± 0	0.58 ± 0	12.2
225	2.3 ± 0	0.70 ± 0	6.5 ± 0	0.30 ± 0	4.6
250	1.6 ± 0	0.93 ± 0	8 ± 0	0.07 ± 0	3.3

Anharmonicity and Dynamic-Disorder Driven Self Trapped Excitonic Emission in Pyridinium Lead Iodide Single Crystals

---

We recorded heat capacity as a function of temperature to identify any phase transition at lower temperatures. The heat capacity data (Figure A2.7) indicates a phase transition in PyPbI$_3$ single crystal at ~170 K. To further validate the existence of phase transition in PyPbI$_3$, we performed temperature-dependent dielectric permittivity measurements in the range of 100-300 K. The plot of the real part of dielectric constant (ε') vs. T shows a sharp change in slope (between 150 and 200 K) around the phase transition, consistent with the heat capacity results. Moreover, a significant shift displayed by temperature steps from 1 MHz to 1 kHz indicates critical slowing down of the relaxation time. Similar trends were also observed in dielectric loss data, which yielded relatively low '*tan δ*' values at room temperature (Figure A2.7 inset, Figure A2.8).
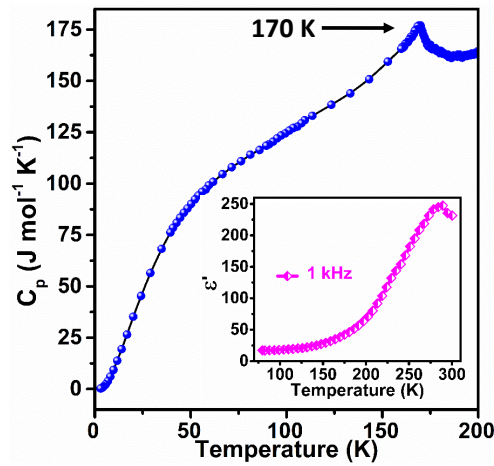
Figure A2.7: Temperature-dependent specific heat (C$_P$) plots of PyPbI$_3$ single crystals. The inset shows dielectric constant (ε') variation with the temperature at 1 kHz.
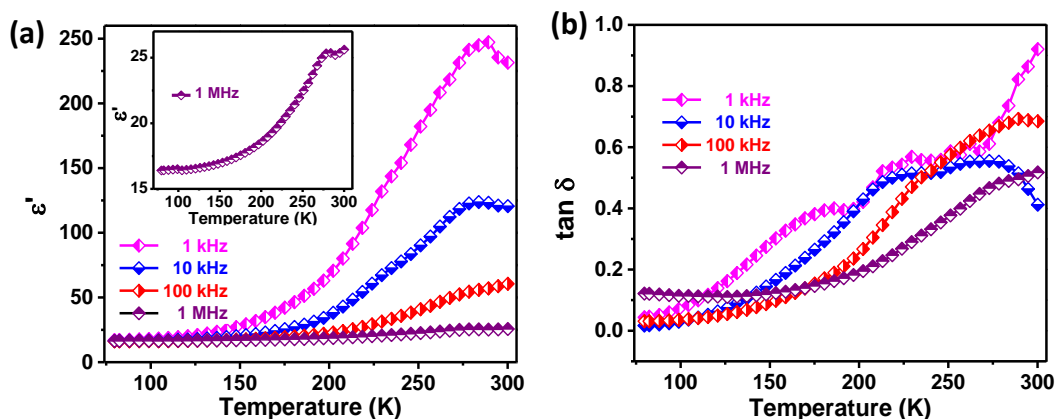
Figure A2.8: Temperature-dependent dielectric permittivity measurements in the range of 100-300 K. (a) Real part of dielectric constant (ε', inset shows 1 MHz variation with temperature). change in slope is observed around the phase transition. (b) dielectric loss data (tan δ) with temperature variation. Dielectric loss data yielded similar trends as observed in ε'.

Anharmonicity and Dynamic-Disorder Driven Self Trapped Excitonic Emission in Pyridinium Lead Iodide Single Crystals

To establish the nature of phase transition, we collected the SCXRD of $PyPbI_3$ at various low temperatures and established the structure at 100 K. The 100 K SCXRD structure of $PyPbI_3$ reveals that the space group of the crystal remains intact at *P*nma, albeit with marginal changes in the lattice parameters, indicating the existence of an isostructural phase transition.[10] A comparison of the unit cell parameters of $PyPbI_3$ at various temperatures (100, 150, 200, and 300 K) shows that the unit cell angles and the cell length along the *b*-axis remain almost unchanged from 100 K to 300 K. However, a noticeable change in the cell length along *a*- (increase) and *c*-axes (decrease) is observed around the transition temperature (170 K). The cell parameters at different temperatures are shown in Figure A2.9.
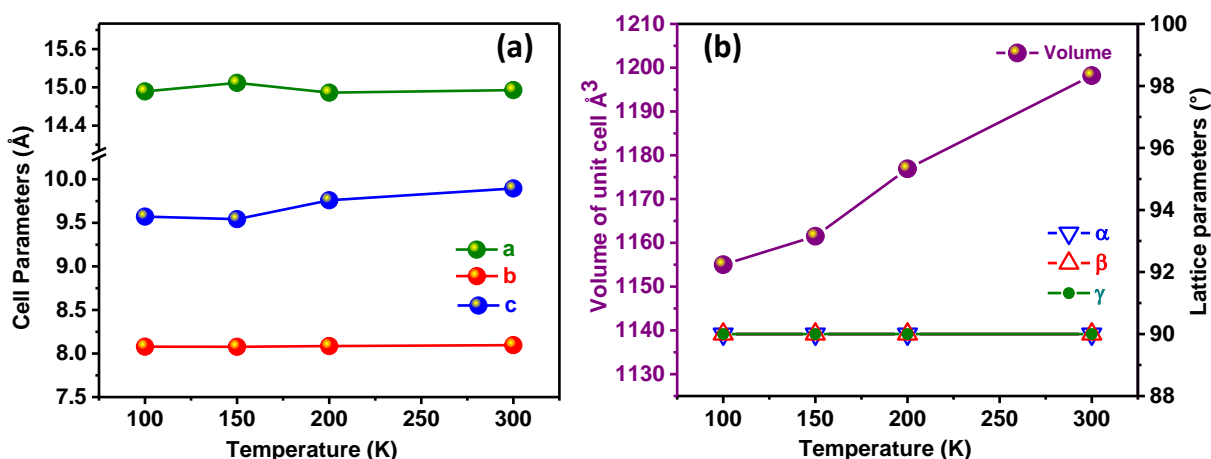
Figure A2.9: (a) Comparison of cell parameters at different temperatures. (b) Comparison of lattice parameters (angles) and volume of the unit cell at different temperatures.

The cell lengths do not undergo any drastic change with an increase in temperature from 100 K-300 K. The space group remains essentially same (*P*nma) throughout the whole temperature range. However, a noticeable variation in lattice parameters '*a*' and '*c*' is observed between 150-200 K, suggesting a structural reorganization. The volume of the unit cell also shows some variation from the usual expected thermal expansion trend at the same temperature range of 150-200 K. This corroborates well with the unusual trends observed in optical properties.

In addition, the distortion level parameters ($\Delta_{oct,}$ and σ^2_{oct}) calculated from the refined crystal structures at different temperatures (Section A2.3.4, Table A2.3 and Figure A2.10) also exhibit a significant deviation from the trend around the transition temperature. The distortion level is minimum at 150 K.

Anharmonicity and Dynamic-Disorder Driven Self Trapped Excitonic Emission in Pyridinium Lead Iodide Single Crystals

A2.3.4 Determination of distortion level

We have calculated the distortion level in lead iodide octahedra from the crystal structure using following equations:[11, 12]

$$\sigma^2_{oct} = \frac{1}{11} \sum_{i=1}^{11} (\alpha_i - 90)^2 \qquad (1)$$

$$\Delta_{oct} = \frac{1}{6} \sum_{i=1}^{6} \left[\frac{d_i - d_m}{d_m} \right]^2 \qquad (2)$$

Where σ^2_{oct} is octahedral bond angle variance, Δ_{oct} is bond length distortion, α_i represent the individual I-Pb-I bond angles, d_i represent individual Pb-I bond lengths, and d_m is the mean Pb-I bond distance.
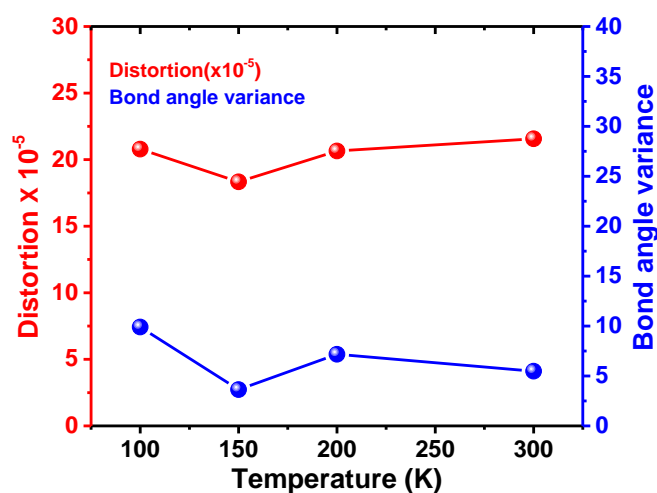
Figure A2.10: Variation of distortion level parameters with temperature. Minimum distortion is observed for structure at around 150 K.

Table A2.3: The distortion level parameters calculated for different temperatures are given in the following table.

Temp (K)	Δ_{oct}	σ^2_{oct}
100	7.43×10^{-05}	27.72367
150	2.73×10^{-05}	**24.44382**
200	5.38×10^{-05}	27.52876
300	4.11×10^{-05}	28.76058

Anharmonicity and Dynamic-Disorder Driven Self Trapped Excitonic Emission in Pyridinium Lead Iodide Single Crystals

We propose the mechanism responsible for the observed temperature-dependent PL properties in PyPbI$_3$ single crystals as the schematic shown in Figure A2.11. The existence of highly Stokes-shifted strong STE emission throughout the temperature range (300 to 5 K) suggests a strong exciton self-trapping facilitated by a strong exciton-phonon coupling evidenced by a large Huang-Rhys parameter (S = 31 at RT, see section A2.3.5 and Figure A2.12).[13] Photoexcitation into the FE (green) state causes significant carrier-phonon coupling leading to a comparatively stable STE (purple) state. The STE geometry is distorted along nuclear coordinate Q. Smaller anharmonicity at 200 K increases the fundamental phonon frequency resulting in a red-shift in PL peak. Below 200 K, the change in anharmonicity is insignificant, and the dynamic disorder is reduced, pushing the STE state (brown) to the left and higher in energy. This schematic does not incorporate the effect of the phase transition at 170K.
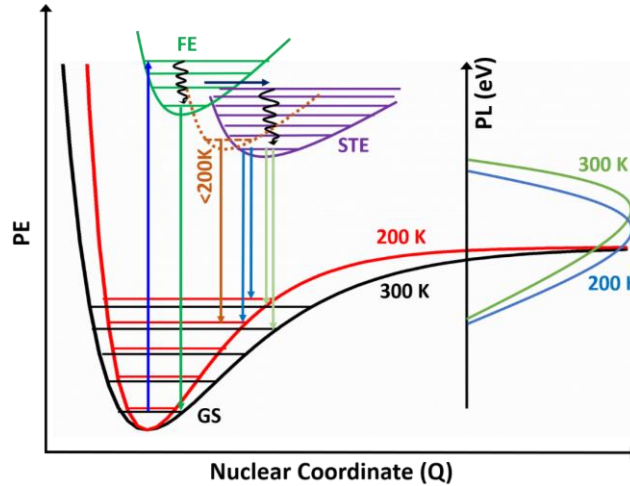
Figure A2.11: Schematic of potential energy surface leading to the observed temperature-dependent PL. GS, FE, and STE state represent the ground state, free excitonic, and self-trapped excitonic states, respectively.

A2.3.5 Calculation of Huang-Rhys Parameter (S Parameter)[13]

The S parameter was calculated using the following equation:

$$\Delta E_{stokes} = 2S\hbar\omega_{LO} = 2Sh\nu_{LO} \qquad (12)$$

$$\Delta E_{stokes} = E_{excitation} \text{-} E_{emission} \quad \text{at a particular temperature}$$

$\nu_{LO} = 3.17$ THz from the Raman spectrum at 300 K.

$$\text{Therefore, } S = \Delta E_{stokes}/2h\nu_{LO} \qquad (13)$$

Anharmonicity and Dynamic-Disorder Driven Self Trapped Excitonic Emission in Pyridinium Lead Iodide Single Crystals

We assume that ν_{LO} undergoes negligible changes with decrease in temperature.
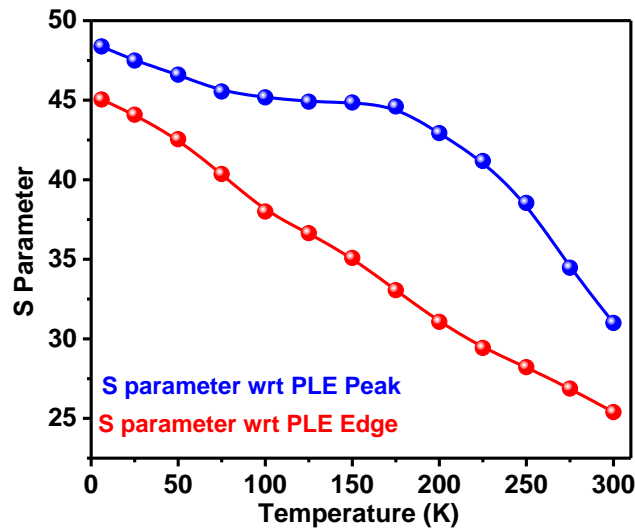

Figure A2.12: Temperature-dependent Huang-Rhys Parameter (S Parameter). The S parameter increases with decrease in temperature and reaches a maximum value of 48.5 at 5 K.

The FE emission appears only below 50 K, suggesting a minuscule thermal barrier (~4 meV) between the FE and STE states. The thermal barrier may even be comparable to the zero-point energy in the FE state. A significant Stokes shift (505 meV, with respect to the PLE edge, Figure A2.13) in FE emission recorded at 5 K indicates that the FE state is significantly distorted compared to the ground state.
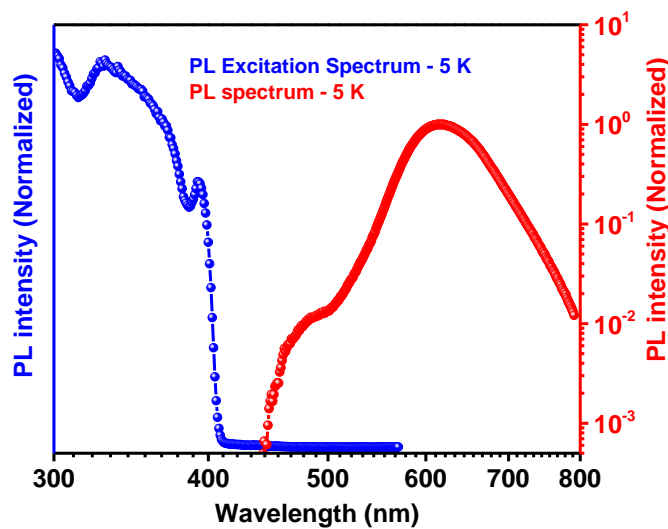
Figure A2.13: PLE and PL (log-scale) vs Wavelength (log-scale) at 5K. The shoulder peak at 5 K is red-shifted by ~85 nm from the PLE peak.

It is important to note that the Stokes shift for the STE peak is 1.17 eV with respect to the PLE edge at 5 K. As proposed in earlier literature,[14, 15] the STE is formed due to strong exciton-phonon interaction that leads to transient structural distortion along one or more nuclear coordinates (Q in Figure A2.11). We propose that Q is a linear combination of phonon modes that involve the vibrations of lead-iodide octahedra and the Py cation. The energy (13.1 meV) of the longitudinal optical (LO) phonon mode determined from fitting the FWHM of STE emission matches well with other Pb-iodide systems (see section A2.3.6, Figure A2.14, and Table A2.4).

A2.3.6 Fitting of variable temperatures FWHM

For semiconductors, the dependence of PL linewidth on temperature is governed by different kinds of interaction of the excitonic states with the phonon modes and impurities. The dependence of PL linewidth with temperature can be expressed by the equation:[16]

$$\Gamma(T) = \Gamma_0 + \Gamma_{ac} + \Gamma_{LO} + \Gamma_{imp}$$

$$= \Gamma_0 + \gamma_{ac}T + \gamma_{LO}\left(\frac{1}{e^{\frac{E_{LO}}{k_B T}}-1}\right) + \Gamma_{imp} \tag{11'}$$

where Γ_0 is a temperature-independent inhomogeneous broadening constant, Γ_{ac} and Γ_{LO} are homogenous broadening due to acoustic and longitudinal optical (LO) phonon scatterings, respectively, and Γ_{imp} is the term accounting for scattering due to ionized impurities. The constants γ_{ac} and γ_{LO} are the charge-carrier–phonon coupling strengths of acoustic and LO phonons, respectively, E_{LO} is the energy representative of the LO phonon mode, and k_B is the Boltzmann constant. The scattering due to ionized impurities do not play a major role, and therefore Γ_{imp} is taken to be 0.[16] The equation 11' reduces to:

$$\Gamma(T) = \Gamma_0 + \gamma_{ac}T + \gamma_{LO}\left(\frac{1}{e^{\frac{E_{LO}}{k_B T}}-1}\right) \tag{11}$$

Equation 11 was used to fit the temperature-dependent PL line-width (red trace in Figure A2.14a).

The parameters obtained using the fittings are tabulated in Table A2.4, along with the values of few previously reported lead halide and lead-free perovskites. We observe that the acoustic phonon coupling to the PL is negligible for our system ($\gamma_{ac} \sim 0$). Similar trend has been previously reported for few other perovskite systems.[16-18] In fact, several studies ignore the

Anharmonicity and Dynamic-Disorder Driven Self Trapped Excitonic Emission in Pyridinium Lead Iodide Single Crystals

acoustic phonon term while fitting the linewidth.[9, 19-22] The acoustic phonons, being much lower in energy compared to the LO phonon modes, have little impact on the PL linewidth. The E_{LO} obtained from the fit matches with the peak obtained in the Raman spectra of the sample (Figure A2.14b in SI). As can be seen from the Table A2.4, the γ_{LO} values of 3D and 2D perovskites are mostly in the range of 20 – 70 meV, and that of double perovskites are in the order of 10^2 meV. The value obtained for our sample, 134 meV, is similar to that of double perovskites due to strong exciton-phonon coupling, which is expected due to the 1D nature of the sample. The PL line-width trace from 200-300 K (cyan trace in Figure A2.14a) fitted well when considering only the LO phonon contribution in equation 11, i.e., $\left\{ \Gamma(T) = \Gamma_0 + \gamma_{LO} \left(\frac{1}{e^{\frac{E_{LO}}{k_B T}} - 1} \right) \right\}$, . This fitting was performed considering no phase transition takes place from 300 K to 200 K, and the phonon mode from the Raman spectrum at room temperature should be the LO phonon mode, as is evident from fit (Table A2.4 reveals the parameters, E_{LO} has been fixed to the dominant Raman mode).
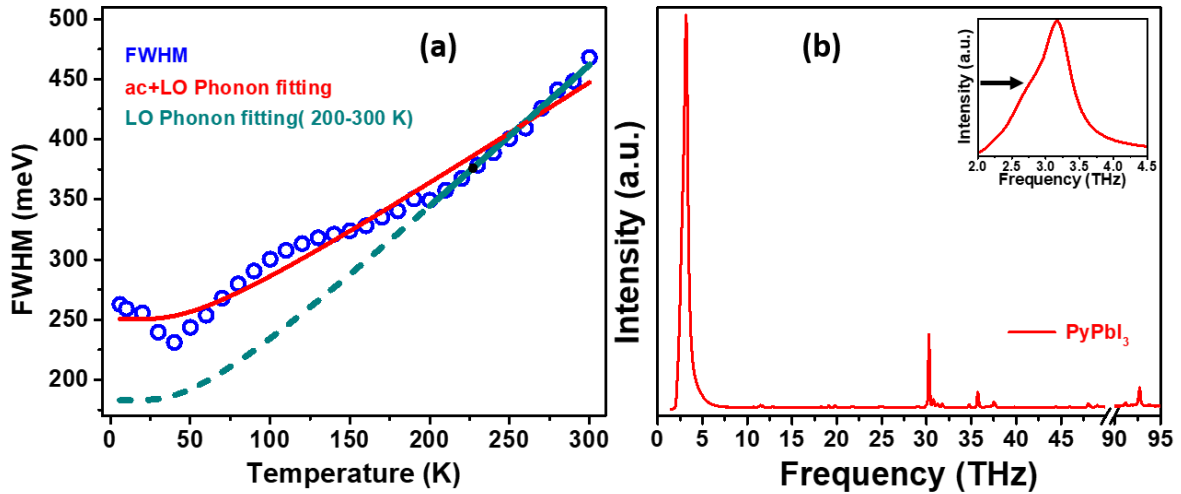
Figure A2.14: (a) Temperature-dependent PL peak FWHM (blue circles) and the corresponding fittings to account for coupling with phonon modes. Red trace for fitting with equation 11 for whole temperature range (5-300 K). For cyan trace, fitting done for 200-300 K with only LO phonon part of equation 11. (b) Raman spectrum of $PyPbI_3$ single-crystals. Inset shows zoomed-in portion around 2.7 THz. A clear broad phonon feature at 106 cm^{-1} (3.2 THz) and a shoulder at around 91 cm^{-1} (2.7 THz) in the room temperature Raman data.

Anharmonicity and Dynamic-Disorder Driven Self Trapped Excitonic Emission in Pyridinium Lead Iodide Single Crystals

Table A2.4: Comparison of parameters obtained using fitting Equation 11 for our sample with the reported perovskites:

Compound	γ_{LO} (meV)	E_{LO} (meV)	γ_{ac} (meV)	Reference
PyPbI$_3$ (5-300 K)	**134±39**	**13±3.1**	**~0**	This work
PyPbI$_3$(fitting from 200-300 K)	**185±5.4**	**13.1±0**		This work
CsPbBr$_3$	54 / 78 (higher/lower energy peak)		~0	[18]
MAPbBr$_3$	46 / 59 (higher/lower energy peak)		~0	[18]
	58	15.3	0.06	[16]
MAPbI$_3$	61	15.3	0.06	[16]
FAPbBr$_3$	40	11.5	0.06	[16]
FAPbI$_3$	40	11.5	0.06	[16]
	34.8	18	0.078	[23]
HA$_2$PbI$_4$	34.2 / 55.8 (phonon 1/phonon 2)	10.9 / 17	0.026	[24]
(EDBE)PbBr$_4$	130	12		[19]
(C$_6$H$_5$C$_2$H$_4$NH$_3$)PbI$_4$	70	13.7	0.03	[25]
BA-MAPb$_2$I$_7$	63.2	24.4	0.003	[26]
(C$_6$H$_8$N$_3$)$_2$Pb$_2$Br$_{10}$	150	18		[9]
(NH$_3$C$_2$H$_4$S$_2$C$_2$H$_4$NH$_3$)PbBr$_5$.NH$_4$	31	21.7		[20]
MASnI$_3$	53.8	21.6	~0	[17]
Cs$_2$AgBiBr$_6$	175	11.5		[21]
	226	22	0.081	[13]
(Benzyltriethylammonium)$_2$TeCl$_6$	295	38		[22]
(F$_2$CCh$_2$NH$_3$)$_2$CdBr$_4$	467	17.3	0.05	[27]
(C$_4$H$_{14}$N$_2$)$_2$In$_2$Br$_{10}$	178	24.2	0.000025	[28]

Anharmonicity and Dynamic-Disorder Driven Self Trapped Excitonic Emission in Pyridinium Lead Iodide Single Crystals

The LO mode has a major contribution from Pb-I stretching and I-Pb-I bending vibrations.[24, 29] According to the density functional theoretical (DFT) calculation of the PyPbI$_3$ single crystal, the conduction band wave function has the maximum contribution from the Py cation.[30] Hence, we anticipate that Q will have a significant contribution from the motion of the Py cation along with the vibrations of the octahedral core. The STE state can be further stabilized by the dynamic disorder (favourable alignments of the mobile dipoles, similar to the solvation of photo-excited fluorophore in polar solvent).[31] Rotational reorientation of polar Py cations should contribute mostly to such stabilization. The variation of PL peak position (STE) with temperature is dictated by the combination of the anharmonicity and dynamic disorder of the lattice.[8, 31, 32] The change in anharmonicity[33-35] due to cooling is mostly responsible for the observed red-shift from 300 K to 200 K (see Figure A2.11). However, at a low enough temperature, the rotational reorientation of Py cations will be significantly restricted, leading to a relative destabilization of the STE state and a blue-shift in the PL (as shown by the brown dotted curve in Figure A2.11). The effect of reduced dynamic disorder overwhelms the anharmonicity factor below 200 K resulting in the observed blue-shift in the PL peak position. At temperatures lower than 100 K, the rotational reorientation of Py cation would freeze, with no further change in PL peak position. The phase transition at 170 K is likely to alter even the GS potential energy surface contributing to the complexity in the emission properties observed at lower temperatures.

A2.4 Conclusion

We observe a broadband STE emission in PyPbI$_3$ single crystals due to strong exciton-phonon interaction. A negligible thermal barrier between FE and STE states ensures STE emission at all temperatures $\geq$5 K. The temperature evolution of STE emission is controlled by the relative contribution of high anharmonicity and dynamic disorder present in such 1D lead-halides. Temperature-dependent PL properties become more complicated due to an isostructural phase transition at 170 K. Photo-active materials derived from hybrid perovskitoids is an ever-growing area of research, and the observation of efficient THG and broadband STE emission in PyPbI$_3$ promises the practical utility of these compounds in high-tech optical and optoelectronic devices in the years to come.

A2.5 References

1. Kamminga, M. E.; de Wijs, G. A.; Havenith, R. W. A.; Blake, G. R.; Palstra, T. T. M., The Role of Connectivity on Electronic Properties of Lead Iodide Perovskite-Derived Compounds. *Inorg. Chem.* **2017,** *56* , 8408-8414.

2. Gapontsev, V. P.; Tyrtyshnyy, V. A.; Vershinin, O. I.; Davydov, B. L.; Oulianov, D. A., Third harmonic frequency generation by Type-I critically phase-matched LiB_3O_5 crystal by means of optically active quartz crystal. *Opt. Express* **2013,** *21*, 3715-3720.

3. Mao, L.; Guo, P.; Kepenekian, M.; Hadar, I.; Katan, C.; Even, J.; Schaller, R. D.; Stoumpos, C. C.; Kanatzidis, M. G., Structural Diversity in White-Light-Emitting Hybrid Lead Bromide Perovskites. *J. Am. Chem. Soc.* **2018,** *140*, 13078-13088.

4. Qi, Z.; Chen, Y.; Guo, Y.; Yang, X.; Zhang, F.-Q.; Zhou, G.; Zhang, X.-M., Broadband white-light emission in a one-dimensional organic–inorganic hybrid cadmium chloride with face-sharing $CdCl_6$ octahedral chains. *J. Mater. Chem. C* **2021,** *9*, 88-94.

5. Qi, Z.; Chen, Y.; Guo, Y.; Yang, X.; Gao, H.; Zhou, G.; Li, S.-L.; Zhang, X.-M., Highly efficient self-trapped exciton emission in a one-dimensional face-shared hybrid lead bromide. *Chem. Commun.* **2021,** *57*, 2495-2498.

6. Varshni, Y. P., Temperature dependence of the energy gap in semiconductors. *Physica* **1967,** *34*, 149-154.

7. Vainshtein, I. A.; Zatsepin, A. F.; Kortov, V. S., Applicability of the empirical Varshni relation for the temperature dependence of the width of the band gap. *Phys. Solid State* **1999,** *41*, 905-908.

8. Guo, Y.; Yaffe, O.; Hull, T. D.; Owen, J. S.; Reichman, D. R.; Brus, L. E., Dynamic emission Stokes shift and liquid-like dielectric solvation of band edge carriers in lead-halide perovskites. *Nat. Commun.* **2019,** *10*, 1175.

9. Biswas, A.; Bakthavatsalam, R.; Shaikh, S. R.; Shinde, A.; Lohar, A.; Jena, S.; Gonnade, R. G.; Kundu, J., Efficient Broad-Band Emission from Contorted Purely Corner-Shared One Dimensional (1D) Organic Lead Halide Perovskite. *Chem. Mater.* **2019,** *31*, 2253-2257.

10. He, L.; Liu, Y.; Shi, P.; Cai, H.; Fu, D.; Ye, Q., Energy Harvesting and Pd(II) Sorption Based on Organic–Inorganic Hybrid Perovskites. *ACS Appl. Mater. Interfaces* **2020,** *12*, 53799-53806.

Appendix 2

Anharmonicity and Dynamic-Disorder Driven Self Trapped Excitonic Emission in Pyridinium Lead Iodide Single Crystals

11. Cortecchia, D.; Neutzner, S.; Srimath Kandada, A. R.; Mosconi, E.; Meggiolaro, D.; De Angelis, F.; Soci, C.; Petrozza, A., Broadband Emission in Two-Dimensional Hybrid Perovskites: The Role of Structural Deformation. *J. Am. Chem. Soc.* **2017,** *139*, 39-42.

12. Wu, G.; Zhou, C.; Ming, W.; Han, D.; Chen, S.; Yang, D.; Besara, T.; Neu, J.; Siegrist, T.; Du, M.-H.; Ma, B.; Dong, A., A One-Dimensional Organic Lead Chloride Hybrid with Excitation-Dependent Broadband Emissions. *ACS Energy Lett.* **2018,** *3*, 1443-1449.

13. Steele, J. A.; Puech, P.; Keshavarz, M.; Yang, R.; Banerjee, S.; Debroye, E.; Kim, C. W.; Yuan, H.; Heo, N. H.; Vanacken, J.; Walsh, A.; Hofkens, J.; Roeffaers, M. B. J., Giant Electron–Phonon Coupling and Deep Conduction Band Resonance in Metal Halide Double Perovskite. *ACS Nano* **2018,** *12*, 8081-8090.

14. Hu, T.; Smith, M. D.; Dohner, E. R.; Sher, M.-J.; Wu, X.; Trinh, M. T.; Fisher, A.; Corbett, J.; Zhu, X. Y.; Karunadasa, H. I.; Lindenberg, A. M., Mechanism for Broadband White-Light Emission from Two-Dimensional (110) Hybrid Perovskites. *J. Phys. Chem. Lett.* **2016,** *7*, 2258-2263.

15. Smith, M. D.; Karunadasa, H. I., White-Light Emission from Layered Halide Perovskites. *Acc. Chem. Res.* **2018,** *51*, 619-627.

16. Wright, A. D.; Verdi, C.; Milot, R. L.; Eperon, G. E.; Pérez-Osorio, M. A.; Snaith, H. J.; Giustino, F.; Johnston, M. B.; Herz, L. M., Electron–phonon coupling in hybrid lead halide perovskites. *Nat. Commun.* **2016,** *7*, 11755.

17. Handa, T.; Aharen, T.; Wakamiya, A.; Kanemitsu, Y., Radiative recombination and electron-phonon coupling in lead-free $CH_3NH_3SnI_3$ perovskite thin films. *Phys. Rev. Mater.* **2018,** *2*, 075402.

18. Steele, J. A.; Puech, P.; Monserrat, B.; Wu, B.; Yang, R. X.; Kirchartz, T.; Yuan, H.; Fleury, G.; Giovanni, D.; Fron, E.; Keshavarz, M.; Debroye, E.; Zhou, G.; Sum, T. C.; Walsh, A.; Hofkens, J.; Roeffaers, M. B. J., Role of Electron–Phonon Coupling in the Thermal Evolution of Bulk Rashba-Like Spin-Split Lead Halide Perovskites Exhibiting Dual-Band Photoluminescence. *ACS Energy Lett.* **2019,** *4*, 2205-2212.

19. Dohner, E. R.; Jaffe, A.; Bradshaw, L. R.; Karunadasa, H. I., Intrinsic White-Light Emission from Layered Hybrid Perovskites. *J. Am. Chem. Soc.* **2014,** *136*, 13154-13157.

20. Bakthavatsalam, R.; Haris, M. P. U.; Shaikh, S. R.; Lohar, A.; Mohanty, A.; Moghe, D.; Sharma, S.; Biswas, C.; Raavi, S. S. K.; Gonnade, R. G.; Kundu, J., Ligand Structure Directed Dimensionality Reduction (2D →1D) in Lead Bromide Perovskite. *J. Phys. Chem. C* **2020,** *124*, 1888-1897.

21. Wright, A. D.; Buizza, L. R. V.; Savill, K. J.; Longo, G.; Snaith, H. J.; Johnston, M. B.; Herz, L. M., Ultrafast Excited-State Localization in $Cs_2AgBiBr_6$ Double Perovskite. *J. Phys. Chem. Lett.* **2021,** *12*, 3352-3360.

22. Biswas, A.; Bakthavatsalam, R.; Bahadur, V.; Biswas, C.; Mali, B. P.; Raavi, S. S. K.; Gonnade, R. G.; Kundu, J., Lead-free zero dimensional tellurium(iv) chloride-organic hybrid with strong room temperature emission as a luminescent material. *J. Mater. Chem. C* **2021,** *9*, 4351-4358.

23. Fang, H.-H.; Wang, F.; Adjokatse, S.; Zhao, N.; Even, J.; Antonietta Loi, M., Photoexcitation dynamics in solution-processed formamidinium lead iodide perovskite thin films for solar cell applications. *Light Sci. Appl.* **2016,** *5*, e16056-e16056.

24. Ni, L.; Huynh, U.; Cheminal, A.; Thomas, T. H.; Shivanna, R.; Hinrichsen, T. F.; Ahmad, S.; Sadhanala, A.; Rao, A., Real-Time Observation of Exciton–Phonon Coupling Dynamics in Self-Assembled Hybrid Perovskite Quantum Wells. *ACS Nano* **2017,** *11*, 10834-10843.

25. Gauthron, K.; Lauret, J. S.; Doyennette, L.; Lanty, G.; Al Choueiry, A.; Zhang, S. J.; Brehier, A.; Largeau, L.; Mauguin, O.; Bloch, J.; Deleporte, E., Optical spectroscopy of two-dimensional layered $(C_6H_5C_2H_4\text{-}NH_3)_2\text{-}PbI_4$ perovskite. *Opt. Express* **2010,** *18*, 5912-5919.

26. Paritmongkol, W.; Powers, E. R.; Dahod, N. S.; Tisdale, W. A., Two Origins of Broadband Emission in Multilayered 2D Lead Iodide Perovskites. *J. Phys. Chem. Lett.* **2020,** *11*, 8565-8572.

27. Luo, B.; Liang, D.; Sun, S.; Xiao, Y.; Lian, X.; Li, X.; Li, M.-D.; Huang, X.-C.; Zhang, J. Z., Breaking Forbidden Transitions for Emission of Self-Trapped Excitons in Two Dimensional $(F_2CHCH_2NH_3)_2CdBr_4$ Perovskite through Pb Alloying. *J. Phys. Chem. Lett.* **2020,** *11*, 199-205.

28. Zhou, L.; Liao, J.-F.; Huang, Z.-G.; Wei, J.-H.; Wang, X.-D.; Chen, H.-Y.; Kuang, D.-B., Intrinsic Self-Trapped Emission in 0D Lead-Free $(C_4H_{14}N_2)_2In_2Br_{10}$ Single Crystal. *Angew. Chem. Int. Ed.* **2019,** *58*, 15435-15440.

29. Yang, J.; Wen, X.; Xia, H.; Sheng, R.; Ma, Q.; Kim, J.; Tapping, P.; Harada, T.; Kee, T. W.; Huang, F.; Cheng, Y.-B.; Green, M.; Ho-Baillie, A.; Huang, S.; Shrestha, S.; Patterson, R.; Conibeer, G., Acoustic-optical phonon up-conversion and hot-phonon bottleneck in lead-halide perovskites. *Nat. Commun.* **2017,** *8*, 14120.

30. Selivanov, N. I.; Murashkina, A. A.; Kevorkyants, R.; Emeline, A. V.; Bahnemann, D. W., Pyridinium lead tribromide and pyridinium lead triiodide: quasi-one-dimensional perovskites with an optically active aromatic π-system. *Dalton Trans.* **2018,** *47*, 16313-16319.

31. Wang, F.; Fu, Y.; Ziffer, M. E.; Dai, Y.; Maehrlein, S. F.; Zhu, X. Y., Solvated Electrons in Solids—Ferroelectric Large Polarons in Lead Halide Perovskites. *J. Am. Chem. Soc.* **2021,** *143*, 5-16.

32. Munson, K. T.; Kennehan, E. R.; Doucette, G. S.; Asbury, J. B., Dynamic Disorder Dominates Delocalization, Transport, and Recombination in Halide Perovskites. *Chem* **2018,** *4*, 2826-2843.

33. Late, D. J.; Shirodkar, S. N.; Waghmare, U. V.; Dravid, V. P.; Rao, C. N. R., Thermal Expansion, Anharmonicity and Temperature-Dependent Raman Spectra of Single- and Few-Layer $MoSe_2$ and WSe_2. *ChemPhysChem* **2014,** *15*, 1592-1598.

34. Cuscó, R.; Gil, B.; Cassabois, G.; Artús, L., Temperature dependence of Raman-active phonons and anharmonic interactions in layered hexagonal BN. *Phys. Rev. B* **2016,** *94*, 155435.

35. Araujo, F. D. V.; Oliveira, V. V.; Gadelha, A. C.; Carvalho, T. C. V.; Fernandes, T. F. D.; Silva, F. W. N.; Longuinhos, R.; Ribeiro-Soares, J.; Jorio, A.; Souza Filho, A. G.; Alencar, R. S.; Viana, B. C., Temperature-dependent phonon dynamics and anharmonicity of suspended and supported few-layer gallium sulfide. *Nanotechnology* **2020,** *31*, 495702.

Thesis Summary and Future Outlook

Thesis Summary: small cations have big effects

In this thesis, we explored the big effects of the organic A-site cations in lead halide perovskites. In perovskites, the cation modifications incorporate changes in different aspects of applications. In 3D lead halide perovskites, formamidinium cation modifies the excited state properties compared to its all-inorganic Cs-based counterparts. This leads to distinct photovoltaic behavior due to the changes in the recombination mechanisms and the backscattering processes. Firstly, using time-resolved terahertz spectroscopy, we unraveled the recombination mechanisms, backscattering, and transport properties of $FAPbBr_3$ NC thin films. Frequency-averaged THz transients revealed information about the recombination dynamics and the effect of formamidinium cation on the excited state. Frequency resolved THz spectra till 6 THz was fitted with Drude Smith Anderson model to understand the complex mechanism of charge carrier transport. Backscattering of charge carriers is predominantly from the photo-induced lattice fluctuations governed by the Anderson model in addition to grain-boundary scattering processes governed by the Drude-Smith model. These backscattering processes affect the semiconducting properties, such as mobility and diffusion lengths.

We studied lower dimensional 1D $PyPbBr_3$ crystals and observed self-trapped excitonic emission. The fundamental understanding of this emission was unraveled by using optical Kerr effect (OKE) spectroscopy and DFT calculations. OKE spectroscopy reveals all the Raman active phonon modes that couple to the excitons, leading to the exciton self-trapping. DFT calculations help us visualize these phonon modes which get affected during the exciton self-trapping. A significant role of the pyridinium cation was observed in addition to the role of the lead bromide sublattice in the STE formation.

Interestingly, the lower dimensional perovskites show exciting non-linear behavior upon excitation with intense laser sources. Due to dimensionality reduction, which leads to quantum and dielectric confinement, the non-linear optical properties are highly enhanced as compared to their 3D counterparts. The optical stability under high fluences, also known as laser-induced damage threshold (LIDT), is also significantly improved. By cation engineering in 1D perovskites, we obtained wavelength-tunable THG output over a broad range. Selective enhancement of THG output due to band-edge resonance and significantly high LIDT values were observed in pyridinium and $DipaPbI_3$ single crystals. Mixed halide systems also depicted efficient THG up conversion with high LIDT. However, selective enhancement of THG output corresponding to the band-edge resonance was not observed. This behavior is due to distorted crystal lattices consisting of mixed bromide and iodide anions.
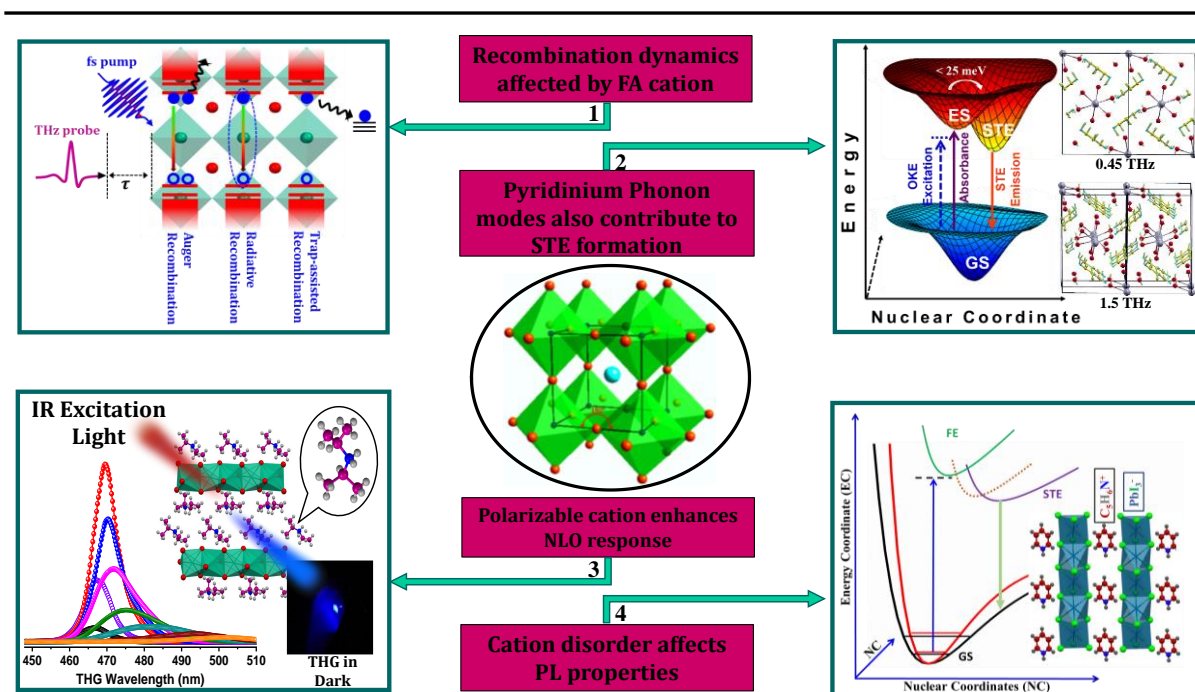
185

Figure S.1: Schematic of overall summary of the thesis representing the effects of cations on various properties of lead halide perovskites, Chapter 2 to Chapter 5, and Appendices 1 and 2.

Future Outlook: Perovskites can control the charge, light, and spin

Perovskites in lower dimensions have the capability of enormous functional and compositional diversity due to the choice of A-site cations. We can obtain an amazing mix of properties from both organic and inorganic constituents. For example, by exploring chiral A-site cations we can incorporate chirality into these lower-dimensional perovskites. Thus, we can synthesize perovskite systems that can show spin-dependent properties. Chiral molecules have selective handedness, while the electrons have spin selectivity. When electrons move through a chiral system, it observes a magnetic field acting upon itself. Thus, the chiral molecules can be used to filter the electrons based on their spin properties which is known as the spin filtering effect.

Numerous lower-dimensional chiral perovskite systems have been synthesized.[1] These systems can be used for spin-filtering, which is a very important aspect in quantum information technology. Various specialist ultrafast spectroscopic techniques, such as the magneto-optical Kerr effect and circularly polarized transient absorption, can be used to study the spin-quantum dynamics phenomena, which is an exciting emerging field.
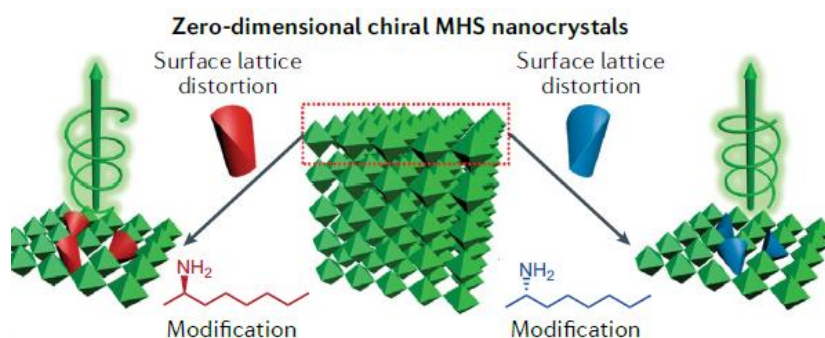
Figure F.1: Schematic showing the chiral effect in perovskites. The figure is reprinted from reference 1 with permission. Copyright © 2019, American Chemical Society.

References

1. Chen, W.; Zhang, S.; Zhou, M.; Zhao, T.; Qin, X.; Liu, X.; Liu, M.; Duan, P., Two-Photon Absorption-Based Upconverted Circularly Polarized Luminescence Generated in Chiral Perovskite Nanocrystals. *J. Phys. Chem. Lett.* **2019**, *10*, 3290-3295.

List of Publications

Included in Thesis

1. **Shabnum Maqbool**, Tariq Sheikh, Ziyad Thekkayil, Swati Deswal, Ramamoorthy Boomishankar, Angshuman Nag and Pankaj Mandal. Third Harmonic Upconversion and Self-Trapped Excitonic Emission in 1D Pyridinium Lead Iodide. *J. Phys. Chem. C* **2021**, *125*, 22674–22683.

2. **Shabnum Maqbool**, Ziyad Thekkayil, Pankaj Mandal. 1D Diisopropylammonium Lead Iodide Perovskite Shows Exceptional Third-Order Optical Nonlinearity and Stability. *Adv. Opt. Mater.* **2023,** just accepted**.**

3. **Shabnum Maqbool,** Sneha Banerjee, Swati Deswal, Prasenjit Ghosh, Pankaj Mandal. Probing the origins of Self Trapped Excitons in hybrid lead halide perovskites using time resolve Optical Kerr Effect Spectroscopy. (To be submitted).

4. **Shabnum Maqbool,** Garvit Bansal, Guruvi Reddy Yettapu, Ziyad Thekkayil, Pankaj Mandal. Ultrafast charge carrier dynamics in Formamidinium lead bromide nanocrystals using time-resolved Terahertz spectroscopy. (Manuscript under preparation).

5. **Shabnum Maqbool,** Ziyad Thekkayil, Pankaj Mandal. Interplay of Phase Stability and Polarizability in the Third Harmonic Up Conversion Process in Pyridinium Lead Mixed Halides (Manuscript under preparation).

Not Included in Thesis

1. Tariq Sheikh, **Shabnum Maqbool,** Pankaj Mandal and Angshuman Nag. Introducing Intermolecular Cation-π Interactions for Water-Stable Low Dimensional Hybrid Lead Halide Perovskites. *Angew. Chem. Int. Ed.* **2021**, *60*, 18265-1827.

2. Tariq Sheikh, **Shabnum Maqbool**, Parikshit Rajput, Pankaj Mandal, Angshuman Nag. Effect of Chirality on the Optical Properties of Layered Hybrid Perovskite R- and S-α-Methylbenzylammonium Lead Iodide. *Chem. Commun.* **2022**, *58*, 7650-7653.

3. Rayan Chakraborty, Parikshit Rajput, Gokul M A, **Shabnum Maqbool,** Ranjan Das, Atikur Rahman, Pankaj Mandal, and Angshuman Nag. Rational Design of Non-Centrosymmetric Hybrid Halide Perovskites. *J. Am. Chem. Soc.* **2023, 145,** 1378–1388.

Copyrights and Permission

Home | Help ⌄ | Live Chat | Sign in | Create Account

Third Harmonic Upconversion and Self-Trapped Excitonic Emission in 1D Pyridinium Lead Iodide

ACS Publications
Most Trusted. Most Cited. Most Read.

Author: Shabnum Maqbool, Tariq Sheikh, Ziyad Thekkayil, et al

Publication: The Journal of Physical Chemistry C

Publisher: American Chemical Society

Date: Oct 1, 2021

Copyright © 2021, American Chemical Society

PERMISSION/LICENSE IS GRANTED FOR YOUR ORDER AT NO CHARGE

This type of permission/license, instead of the standard Terms and Conditions, is sent to you because no fee is being charged for your order. Please note the following:

- Permission is granted for your request in both print and electronic formats, and translations.
- If figures and/or tables were requested, they may be adapted or used in part.
- Please print this page for your records and send a copy of it to your publisher/graduate school.
- Appropriate credit for the requested material should be given as follows: "Reprinted (adapted) with permission from {COMPLETE REFERENCE CITATION}. Copyright {YEAR} American Chemical Society." Insert appropriate information in place of the capitalized words.
- One-time permission is granted only for the use specified in your RightsLink request. No additional uses are granted (such as derivative works or other editions). For any uses, please submit a new request.

If credit is given to another source for the material you requested from RightsLink, permission must be obtained from that source.

BACK   CLOSE WINDOW

Searching for "Defect-Tolerant" Photovoltaic Materials: Combined Theoretical and Experimental Screening

ACS Publications
Most Trusted. Most Cited. Most Read.

Author: Riley E. Brandt, Jeremy R. Poindexter, Prashun Gorai, et al

Publication: Chemistry of Materials

Publisher: American Chemical Society

Date: Jun 1, 2017

Copyright © 2017, American Chemical Society

Shabnum Maqbool <shabnum.maqbool@students.iiserpune.ac.in>

Reuse of figures in thesis; non profit
2 messages

ACS Publications <support@services.acs.org>   Tue, Dec 27, 2022 at 9:51 AM
Reply-To: ACS Publications <acs@service-now.com>
To: shabnum.maqbool@students.iiserpune.ac.in

Dear Shabnum Maqbool,

Your permission requested is granted and there is no fee for this reuse. In your planned reuse, you must cite the ACS article as the source, add this direct link https://pubs.acs.org/doi/10.1021/nl5048779 and include a notice to readers that further permissions related to the material excerpted should be directed to the ACS.

If you need further assistance, please let me know.

Best regards,
Simran Mehra
~~~~~~~~~~~~~~~~~~~~~~~~~~~~~~~~
Simran Mehra
ACS Publications Support
Customer Services & Information
Website: https://acs.service-now.com/acs
Email: support@services.acs.org
Phone: 800-227-9919 | 202-872-(HELP) 4357

On Monday 26, December 04:14:55 PM EST, 'shabnum.maqbool@students.iiserpune.ac.in' wrote:

> Dear ACS Team,
>
> I would like to reuse two figures from the paper mentioned below in the introduction part of my thesis. I pledge to give the proper citations and credits.
> Details of figure and paper:
> Link to the paper: https://pubs.acs.org/doi/10.1021/nl5048779
> Title of the paper: Nanocrystals of Cesium Lead Halide Perovskites (CsPbX3, X = Cl, Br, and I): Novel Optoelectronic Materials Showing Bright Emission with Wide Color Gamut.
> Figure details: Figure number 2 and 3.
> Details of where the content will be used:
> Thesis Author: Shabnum Maqbool
>
> Thesis Title: Linear and Nonlinear Optical Properties and Ultrafast Dynamics of Hybrid Lead Halide
>
> Perovskites.
> Presentation date: February 2023.
> Institute: Indian Institute of Science Education and Research (IISER) Pune.
>
> Please grant me permission for the same. I would be highly thankful to you for this.
>
> Thanks and Regards
> Shabnum
>
> Shabnum Maqbool
> Terahertz Spectroscopy Lab
> Department of Chemistry
> IISER Pune

Ref:MSG0856997_YrRrFnnJouryIolCe0Cc

ACS Publications <support@services.acs.org>   Tue, Dec 27, 2022 at 9:53 AM
Reply-To: ACS Publications <acs@service-now.com>
To: shabnum.maqbool@students.iiserpune.ac.in

Dear Shabnum Maqbool,

Your permission requested is granted and there is no fee for this reuse. In your planned reuse, you must cite the ACS article as the source, add this direct link https://pubs.acs.org/doi/10.1021/acs.jpclett.1c01148 and include a notice to readers that further permissions related to the material excerpted should be directed to the ACS.

If you need further assistance, please let me know.

Best regards,
Simran Mehra
~~~~~~~~~~~~~~~~~~~~~~~~~~~~~~~~
Simran Mehra
ACS Publications Support
Customer Services & Information
Website: https://acs.service-now.com/acs
Email: support@services.acs.org
Phone: 800-227-9919 | 202-872-(HELP) 4357

On Monday 26, December 05:19:05 PM EST, 'Shabnum Maqbool <shabnum.maqbool@students.iiserpune.ac.in>' wrote:

Dear ACS Team,

I would like to reuse two figures from the paper mentioned below in the introduction part of my thesis. I pledge to give the proper citations and credits.
Details of figure and paper:
Link to the paper: **https://doi.org/10.1021/acs.jpclett.1c01148**
Title of the paper: Free Carriers versus Self-Trapped Excitons at Different Facets of Ruddlesden–Popper Two-Dimensional Lead Halide Perovskite Single Crystals
Figure details: Figure number 3.
Details of where the content will be used:
Thesis Author: Shabnum Maqbool

Thesis Title: Linear and Nonlinear Optical Properties and Ultrafast Dynamics of Hybrid Lead Halide

Perovskites.
Presentation date: February 2023.
Institute: Indian Institute of Science Education and Research (IISER) Pune.

Please grant me permission for the same. I would be highly thankful to you for this.

Thanks and Regards
Shabnum

Shabnum Maqbool
Terahertz Spectroscopy Lab
Department of Chemistry
IISER Pune

Ref:MSG0857001_dUmujG6sr3J0R8PIO2Qg

CCC

RightsLink

🏠
Home

❓
Help ∨

✉️
Email Support

👤
Sign in

👤➕
Create Account

Self-Assembly of Broadband White-Light Emitters

ACS Publications
Most Trusted. Most Cited. Most Read.

Author: Emma R. Dohner, Eric T. Hoke, Hemamala I. Karunadasa

Publication: Journal of the American Chemical Society

Publisher: American Chemical Society

Date: Feb 1, 2014

Copyright © 2014, American Chemical Society

PERMISSION/LICENSE IS GRANTED FOR YOUR ORDER AT NO CHARGE

This type of permission/license, instead of the standard Terms and Conditions, is sent to you because no fee is being charged for your order. Please note the following:

- Permission is granted for your request in both print and electronic formats, and translations.
- If figures and/or tables were requested, they may be adapted or used in part.
- Please print this page for your records and send a copy of it to your publisher/graduate school.
- Appropriate credit for the requested material should be given as follows: "Reprinted (adapted) with permission from {COMPLETE REFERENCE CITATION}. Copyright {YEAR} American Chemical Society." Insert appropriate information in place of the capitalized words.
- One-time permission is granted only for the use specified in your RightsLink request. No additional uses are granted (such as derivative works or other editions). For any uses, please submit a new request.

If credit is given to another source for the material you requested from RightsLink, permission must be obtained from that source.

BACK   CLOSE WINDOW

CCC
RightsLink

Home   Help ⌄   Email Support   Sign in   Create Account

White-Light Emission from Layered Halide Perovskites

ACS Publications
Most Trusted. Most Cited. Most Read.

Author: Matthew D. Smith, Hemamala I. Karunadasa

Publication: Accounts of Chemical Research

Publisher: American Chemical Society

Date: Mar 1, 2018

Copyright © 2018, American Chemical Society

PERMISSION/LICENSE IS GRANTED FOR YOUR ORDER AT NO CHARGE

This type of permission/license, instead of the standard Terms and Conditions, is sent to you because no fee is being charged for your order. Please note the following:

- Permission is granted for your request in both print and electronic formats, and translations.
- If figures and/or tables were requested, they may be adapted or used in part.
- Please print this page for your records and send a copy of it to your publisher/graduate school.
- Appropriate credit for the requested material should be given as follows: "Reprinted (adapted) with permission from {COMPLETE REFERENCE CITATION}. Copyright {YEAR} American Chemical Society." Insert appropriate information in place of the capitalized words.
- One-time permission is granted only for the use specified in your RightsLink request. No additional uses are granted (such as derivative works or other editions). For any uses, please submit a new request.

If credit is given to another source for the material you requested from RightsLink, permission must be obtained from that source.

BACK   CLOSE WINDOW

CCC

RightsLink

SPRINGER NATURE

Low-threshold amplified spontaneous emission and lasing from colloidal nanocrystals of caesium lead halide perovskites

Author: Sergii Yakunin et al

Publication: Nature Communications

Publisher: Springer Nature

Date: Aug 20, 2015

Copyright © 2015, The Author(s)

CCC
RightsLink

Home | Help ⌄ | Email Support | Sign in | Create Account

Chiral Lead Halide Perovskite Nanowires for Second-Order Nonlinear Optics

ACS Publications
Most Trusted. Most Cited. Most Read.

Author: Chunqing Yuan, Xinyue Li, Sergey Semin, et al

Publication: Nano Letters

Publisher: American Chemical Society

Date: Sep 1, 2018

Copyright © 2018, American Chemical Society

PERMISSION/LICENSE IS GRANTED FOR YOUR ORDER AT NO CHARGE

BACK   CLOSE WINDOW

Home | Help ⌄ | Live Chat | Sign in | Create Account

Two-Photon Absorption-Based Upconverted Circularly Polarized Luminescence Generated in Chiral Perovskite Nanocrystals

ACS Publications
Most Trusted. Most Cited. Most Read.

Author: Wenjie Chen, Shuai Zhang, Minghao Zhou, et al

Publication: Journal of Physical Chemistry Letters

Publisher: American Chemical Society

Date: Jun 1, 2019

Copyright © 2019, American Chemical Society

PERMISSION/LICENSE IS GRANTED FOR YOUR ORDER AT NO CHARGE

BACK   CLOSE WINDOW